University "G. d'Annunzio" of Chieti-Pescara

School of Advanced Study "G. d'Annunzio"

Research doctorate program in

Biomolecular and Pharmaceutical Sciences

Curriculum: Pharmaceutical Sciences and Biotechnologies

Cycle XXXVIII

Department of Pharmacy

Scientific Disciplinary Sector: Chem/08-A

Exploring Innovative and Conventional Approaches for Solid Lipid Nanoparticle Development

PhD student

Dr. Eleonora Chiara Toto

Tutor

Prof. Antonio Di Stefano

Head of PhD

Prof.ssa Assunta Pandolfi

Academic years 2022-2025

Index

Aims and objectives ***1***

Chapter 1.

Solid lipid nanoparticles (SLNs): features, fabrication, and applications ***3***

1.1. Introduction 4

1.2. Manufacturing techniques for SLNs 7

1.2.1. High-energy methods 7

1.2.2. Low energy methods 9

1.2.3. Organic solvents methods 10

1.3. Features of SLNs 12

1.3.1. General Components of SLNs 12

1.3.2. Structural organization and drug distribution 14

1.3.3. Characterization 15

1.4. Route of administration 18

1.4.1. Oral administration 18

1.4.2. Parenteral administration 18

1.4.3. Topical and transdermal applications 19

1.4.4. Ocular administration 19

1.5. Therapeutic Applications 20

1.5.1. SLNs for antimicrobial therapy 20

1.5.2. SLNs for neurodegenerative disorders 21

1.5.3. SLNs in cancer treatment 21

1.5.4. SLNs as carriers for biological drugs 22

1.5.5. SLNs for active delivery 24

Chapter 2.

Embracing New and Advanced Approaches for SLNs Production and Applications ***34***

2.1. From Classical Techniques to Microfluidics: Addressing the Limitations of Conventional SLNs Production 35

2.2. Co-/Multi-drug delivery systems 44

2.2.1 Trojan system 47

Chapter 3.

From Natural Extracts to Brain Targeting: Experimental Development of SLNs 55

3.1. Exploring the application of SLNs loaded with 56

Capsaicin-rich extract in Parkinson's disease 56

3.1.1. Introduction 56

3.1.2. Results and discussion 59

3.1.3 Experimental Section 70

3.1.4. Conclusion 76

3.2. Propolis-Loaded SLNs Targeting Pathogens 82

Associated with Gastrointestinal Diseases 82

3.2.1. Introduction 82

3.2.2. Results and discussion 85

3.2.3. Experimental Section 101

3.2.4. Conclusions 110

3.3. Lep(70-89) targeted SLNs as a platform for brain delivery 118

3.3.1 Introduction 118

3.3.2. Results and Discussion 121

3.3.3. Experimental Section 129

3.3.4. Conclusions and future perspectives 132

Chapter 4.

Experimental Investigation of Microfluidic and Hierarchical Structures 137

4.1. From Batch to Microfluidics Production of SLNs 138

4.1.1. Introduction 138

4.1.2. Results and Discussion 140

4.1.3. Experimental section 146

4.1.4. Conclusions 151

4.2. Bridging Microfluidics and Design of Experiments for the Development of SLNs-based Artificial Tears 154

4.2.1. Introduction 154

4.2.2. Results and discussion 157

4.2.3. Experimental Section 172

4.3.4. Conclusions 181

4.3. Exploring Nano-in-Micro Architectures: SLNs Incorporation into PLGA Microspheres 190

4.3.1 Introduction 190

4.3.2. Results and discussion 193

4.3.3. Experimental section 207

4.3.4. Conclusions and future perspectives 214

Conclusions ***220***

Aims and objectives

This PhD project focused on the design, production, and application of solid lipid nanoparticles (SLNs) as advanced drug delivery systems, following a progressive research pathway that moves from classical, well-established formulation methods toward more innovative and advanced manufacturing strategies, with a strong emphasis on translational pharmaceutical applications. The work integrates fundamental theoretical aspects of lipid nanocarriers with extensive experimental development, addressing both technological challenges and therapeutic needs.

Chapter 1 of this thesis was dedicated to establishing a solid theoretical background on SLNs. Fundamental concepts related to their composition, structural organization, physicochemical properties, drug incorporation mechanisms, and release behaviour were comprehensively analysed. In parallel, the wide range of SLNs applications across different administration routes and therapeutic areas was examined, highlighting their versatility as lipid-based nanocarriers.

Building on this consolidated knowledge, **Chapter 2** explored advanced and emerging strategies for SLNs production and application. Emphasis was placed on microfluidic technology, an innovative manufacturing approach capable of overcoming the limitations of conventional batch methods and enabling precise control over particle formation. In addition, the chapter introduced advanced delivery concepts such as co-delivery systems and hierarchical nano-in-micro architectures, discussed as strategic evolutions of SLNs toward more complex, multifunctional platforms. Together, these approaches were presented within a unified framework aimed at enhancing SLNs' manufacturability, functionality, and translational potential.

Hot topics:

The experimental core of the PhD encompassed multiple formulation case studies and is presented in Chapters 3 and 4. In particular, **Chapter 3** focused on the development of SLNs loaded with natural extract compounds, aiming to improve solubility, stability, bioavailability, and targeting efficiency, including strategies for brain delivery.

- *Chapter 3.1* describes the development of SLNs loaded with a capsaicin-rich extract (**CPS-ext SLNs**) as a delivery platform with potential relevance in Parkinson's disease.

- *Chapter 3.2* focuses on the development of SLNs loaded with propolis ethanolic extract (**PEE-SLNs**), aiming at combining antimicrobial and anti-inflammatory activity for the management of inflammatory bowel diseases (IBDs).
- *Chapter 3.3* investigates the development of SLNs functionalized with a leptin-derived peptide fragment (**ELM-Lep(70-89)**) as an active targeting platform for brain delivery.

Chapter 4 focused on the translation from conventional formulation approaches toward the innovative technologies previously introduced and was carried out through a collaborative effort between academia and industry. Chapter *4.1* was developed in collaboration with BSP Pharmaceuticals, and *Chapters 4.2* and *4.3* were the outcome of my visiting research period at the University Complutense of Madrid.

- *Chapter 4.1* provides an in-depth analysis of microfluidic techniques, where a **systematic screening** of formulation and process parameters was carried out to identify the critical variables governing particle size, polydispersity, and short-term stability.
- *Chapter 4.2* presents the integration of statistical optimization through **Response Surface Methodology** with microfluidic production. In this context, SLNs were optimized as components of advanced artificial tear formulations enriched with osmoprotectants and mucoadhesive polymers for the treatment of dry eye disease (DED) (**HA-SLNs**). These studies bridged nanotechnology and ocular physiology, combining physicochemical optimization with *in vitro* and *in vivo* tolerance assessments.
- *Chapter 4.3* investigates hierarchical nano-in-micro delivery systems, known also as **Trojan systems**. SLNs were incorporated into PLGA microspheres to create long-acting intraocular delivery platforms capable of co-delivering multiple therapeutic agents, thereby contributing to the rational treatment of chronic ocular diseases.

This PhD covered a broad yet coherent set of topics ranging from fundamental SLN science to advanced manufacturing technologies and complex drug delivery systems, with a strong emphasis on translational relevance and pharmaceutical applicability.

Chapter 1.

Solid lipid nanoparticles (SLNs): features, fabrication, and applications

1.1. Introduction

Nanotechnology-based drug delivery systems (DDS) have witnessed remarkable growth over the past few decades, profoundly transforming the landscape of pharmaceutical sciences [1, 2]. The reduction of material dimensions to the nanometer scale (typically 1-1000 nm) results in a significant increase in surface area and reactivity, leading to improved physicochemical properties [3, 4]. Materials within this size range are generally referred to as nanoparticles (NPs) (**Figure 1**). Although the concept of "nano" can be defined simply in terms of size, it encompasses a broad range of applications across scientific disciplines.

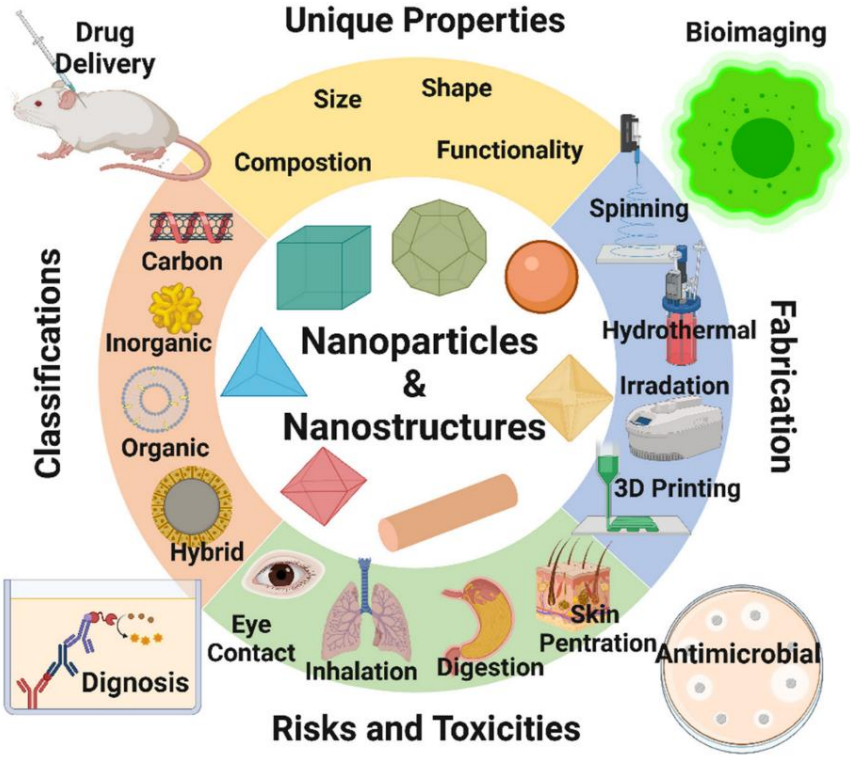


Figure 1. Summary of the recent topic on nanoparticles and nanostructured materials and their applications in bioimaging, biosensing, drug delivery, tissue engineering, antimicrobial, and agro-food sectors [5].

In modern pharmaceutical research, nanotechnology has revolutionized drug delivery approaches**,** offering innovative tools to refine the pharmacokinetic (ADME) and pharmacodynamic behaviour of therapeutic agents [6, 7]. Owing to their tunable size, surface charge, and chemical composition, NPs can markedly enhance drug solubility, stability, and bioavailability while minimizing systemic toxicity and immunogenicity [8]. Through precise surface engineering, NPs can be functionalized with ligands that enable

site-specific targeting, reduce off-target effects, while allowing a controlled or sustained release of the encapsulated drug [9]. As a result, nanotechnology has opened the possibility to overcome many of the limitations of conventional formulations, paving the way for more effective and personalized therapies [10]. Advances in nanotechnology, combined with developments in proteomics, genomics, and bioinformatics, have further expanded the possibilities for designing nanosystems capable of addressing previously intractable therapeutic challenges [11]. The overall performance of any DDS depends not only on the drug's physicochemical properties, such as solubility, crystallinity, hydrophilic-lipophilic balance (HLB), and toxicity, but also on the route of administration, absorption mechanisms, metabolism, and elimination [12]. Hence, formulation design plays a crucial role in determining the bioavailability and therapeutic effectiveness of active pharmaceutical ingredients (APIs).

Widely investigated nanocarriers, such as liposomes, polymeric NPs, solid lipid nanoparticles (SLNs), nanostructured lipid carriers, dendrimers, micelles, and metallic nanoparticles, have greatly contributed to the advancement of nanotechnology-based DDS and the development of innovative therapies [13, 14]. These are only a few of the most widely studied examples, since the NPs developed so far can be broadly classified, based on the chemical nature of their components and structural organization, into three main categories: inorganic, polymeric, and lipid-based NPs [15].

Inorganic NPs are composed of inorganic materials, such as gold, silver, iron, and silica. Due to the intrinsic characteristics of these materials, inorganic NPs may have distinct electrical, physical, optical, or magnetic features, including, for example, the photothermal effects of gold NPs or superparamagnetic behaviour of iron oxide NPs [16-17]. Although they display excellent stability and have shown promising potential in applications such as photothermal therapy, bioimaging, and diagnostics, their clinical use remains limited because of their low aqueous solubility and potential cytotoxicity [18, 19]. Conversely, polymeric NPs are prepared from a wide variety of natural or synthetic polymers. They include structures like dendrimers, polymeric micelles, nanospheres, and polymersomes. These nanosystems can encapsulate both hydrophobic and hydrophilic compounds with different molecular weights, ranging from small molecules to macromolecules like proteins [20]. The advantages of polymeric NPs include biodegradability, biocompatibility, and the ability to co-deliver multiple therapeutic

agents. Furthermore, they can be engineered to deliver drugs to specific tissues or cells [21-23]. Nevertheless, limitations such as particle aggregation, residual toxicity, and complex manufacturing processes still pose challenges to their widespread clinical translation [1]. Lipid-based NPs have been extensively investigated due to their excellent biocompatibility, high drug-loading capacity, formulation simplicity, and intrinsic ability for self-assembly. Lipids can interact favorably with biological membranes and cross physiological barriers such as the blood-brain barrier (BBB), making them particularly suitable for encapsulating lipophilic drugs that often exhibit poor aqueous solubility and limited bioavailability [24]. Lipidic NPs encompass various systems, including emulsions, liposomes, and SLNs, which are produced from physiological or synthetic lipids selected for their biocompatibility, low toxicity, and ability to integrate with biological membranes. Although traditional carriers like liposomes have demonstrated remarkable therapeutic potential, their limited stability, high production costs, and scalability issues have driven the development of more advanced lipid-based systems, most notably SLNs [25, 26]. Introduced in the mid-1990s, SLNs emerged as a next-generation platform combining the advantages of polymeric nanoparticles and liposomes while minimizing their respective drawbacks. The main advantages of SLNs compared with liposomes and polymeric nanoparticles are summarized in **Table 1**, highlighting their superior stability, preparation flexibility, and potential for targeted drug delivery [27]. For these reasons, this thesis investigates SLNs as a versatile and promising nanocarrier across multiple applications and administration routes.

Table 1. Benefits of SLNs with respect to liposomes and polymeric NPs [28].

Points to consider	Benefits over liposomes	Benefits over polymeric NPs
Organ distribution	SLNs show higher bioactivity in the spleen. Liposomes are mainly active in the liver due to differences in formulation flexibility.	Unlike polymeric NPs, SLNs do not show significant accumulation in non-target organs (e.g. spleen, liver), reducing the risk of unwanted side effects.
Flexibility in the selection of preparation method	SLNs can be prepared using solvent-free methods, allowing scalable and reproducible production processes	SLNs can be produced by aqueous-based homogenization methods that are simple, scalable, and suitable for industrial production.
Target ability	Both surface-modified liposomes and SLNs can be used for site-specific delivery; however, liposomes face multiple cellular barriers that limit efficient gene delivery.	Surface-modified SLNs enable site-specific delivery of drugs and biomolecules (proteins, DNA, RNA), whereas polymeric NPs often require complex synthetic tailoring to achieve similar targeting performance

1.2. Manufacturing techniques for SLNs

Extensive research on SLNs production has led to the development of multiple well-established preparation techniques, which can be broadly categorized into three main groups: high-energy, low-energy, and solvent-based methods. High-energy methods rely on mechanical equipment capable of generating intense shear and pressure forces to reduce particle size, with high-pressure homogenization being the most widely used technique. Low-energy methods achieve SLNs formation without extensive energy input, often exploiting spontaneous emulsification phenomena. Finally, solvent-based methods that utilize organic solvents during nanoparticle formation can be operated under either high- or low-energy conditions depending on the system design [29].

1.2.1. High-energy methods

High-pressure homogenization

High-pressure homogenization (HPH) includes two types of methods: hot homogenization and cold homogenization. Both methods involve a preliminary step of dissolving or dispersing the drug in solid lipid melt. The HPH method employs a high-pressure piston chamber connected to a narrow homogenization gap. The applied pressure, typically ranging from 100 to 2,000 bar, forces the pre-emulsion through the valve, where intense shear stress, turbulence, and cavitation break down the droplets into submicron or nanometric sizes [30].

Hot homogenization: Temperatures higher than the melting point of the lipid are used for this process and can subsequently be considered as the homogenization of an emulsion. An aqueous surfactant is used for the combination of lipid and drug at the same temperature. A device for high shear mixing is used to prepare a hot pre-emulsion, resulting in an emulsion of oil in water type. Then, the product is left for cooling, and this leads to the initiation of lipid crystals and then the formation of SLNs (**Figure 2A**) [31].

Cold homogenization: To address problems with hot homogenization processes like thermolabile drugs that cannot handle high temperature, drug loss during its distribution in the aqueous phase, and complex crystalline structure of lipid cold homogenization mechanism has been introduced. Therefore, the molten lipid and bioactive component mixture cools down before being crushed into microparticles of 50 to 100 μm, employing

a ball mill. Following that, the powder is dispersed in an aqueous stabilizing medium (**Figure 2B)** [32].

Ultrasonication technique

This method requires the addition of homogenization or stirring steps to avoid particle size growth due to a broader particle size distribution. The ultrasonication splits droplets depending on the creation, development, and implosive collapse of bubbles. The primary disadvantage of the ultrasonication method is the possibility of metal contamination (**Figure 2C**) [33].

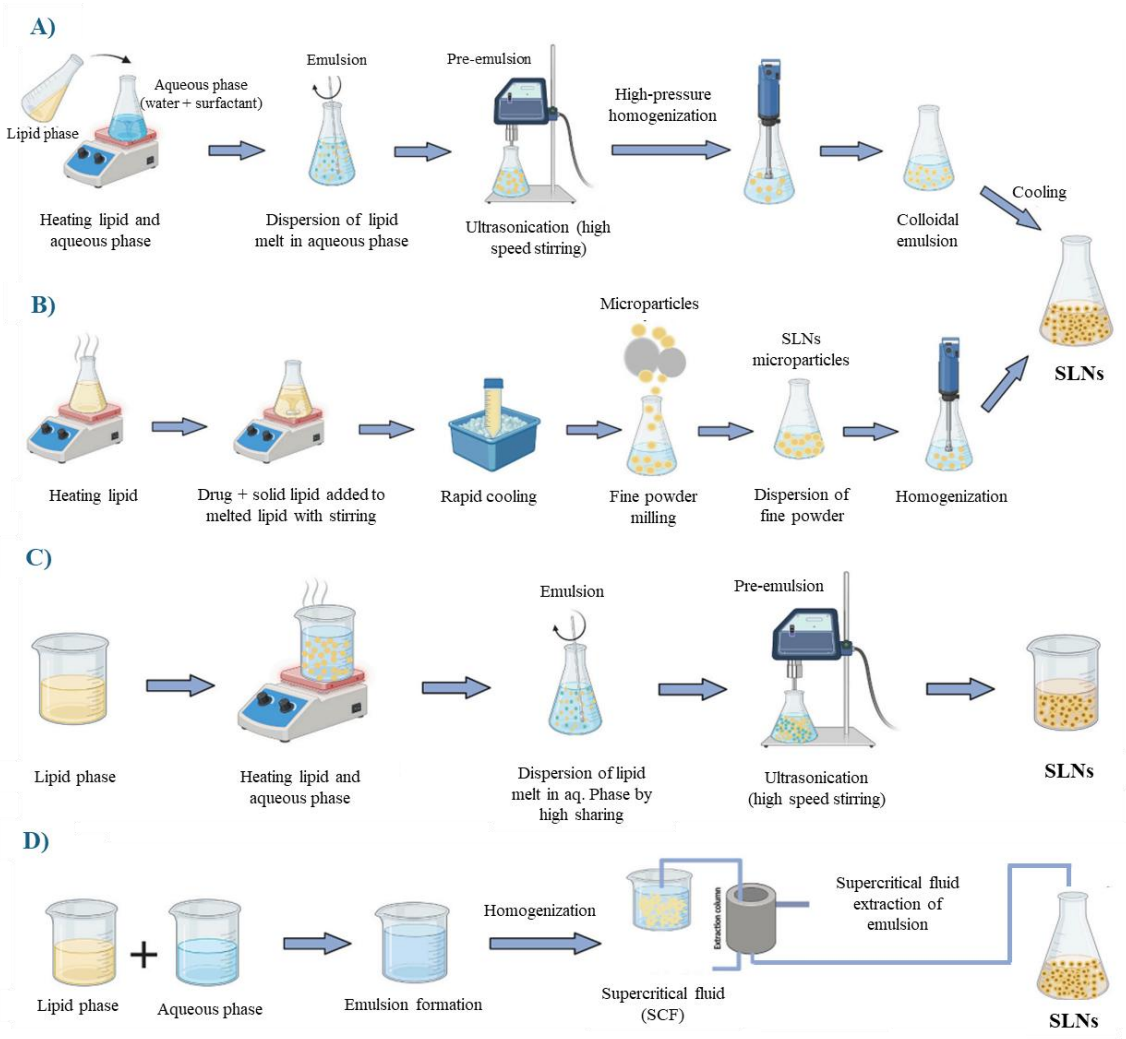


Figure 2. High-energy mechanical methods for the preparation of SLNs: **(A)** hot homogenization, **(B)** cold homogenization, **(C)** ultrasonication, **(D)** supercritical fluid.

Supercritical fluid technique

In this technique, SLNs are obtained from gas-saturated solutions (GSS) by adjusting pressure and temperature parameters to optimize solvent power, liquid-like density, and gas-like transport properties. Initially, the lipids are melted in the presence of GSS and subsequently dissolved in the supercritical fluid under ambient pressure. The resulting saturated solution is then rapidly expanded through an atomizing nozzle, where the supercritical fluid quickly evaporates, yielding fine, dry SLNs particles. The major advantage of this process lies in its solvent-free nature, which enables the direct formation of SLNs in powder form within the nanometer size range (**Figure 2D**) [34].

1.2.2. Low energy methods

Micro emulsion

This method relies on the spontaneous production of microemulsions because of the high stabilizer/lipid ratio. In this process, the solid lipid is first melted using indirect heating. An aqueous phase is then prepared by dissolving surfactants in water. When the hot lipid melt is combined with the aqueous phase under continuous stirring, microemulsions are formed spontaneously. This technique is straightforward and repeatable, as well as solvent-free and scalable. The massive volume of water required to dilute microemulsions and the excessive stabilizer consumption are two of its drawbacks (**Figure 3A**) [35, 36].

Double emulsion

Generally used to produce SLNs incorporating hydrophilic compounds. The active component is included in the melted combination of lipids to create a transparent W/O microemulsion, which is then dispersed into an aqueous medium containing a hydrophilic stabilizer to generate a double emulsion W/O/W. The double emulsion technique is the most frequently used, however, it produces larger SLNs (**Figure 3B**) [37].

Phase inversion temperature

The phase inversion temperature (PIT) method involves emulsification at the inversion temperature followed by rapid cooling to form a fine O/W nanoemulsion. In this process, the oil phase (solid lipids and nonionic surfactant) and the aqueous phase (usually containing NaCl) are heated to above the surfactant transition temperature. Under constant stirring, the aqueous phase is added dropwise to form a W/O emulsion, which

inverts upon cooling to yield an O/W nanoemulsion. The method relies on temperature-dependent nonionic stabilizers, allowing droplet size reduction through sequential inversion between W/O and O/W states. This low-energy, solvent-free technique is simple and reproducible, though the resulting emulsions may show limited stability, often requiring multiple temperature cycles [38].

Membrane contactor

The membrane contactor method involves pressing a molten blend of lipids through a porous hydrophobic membrane (usually 0.05 μm pore diameter) into the aqueous medium comprising the stabilizer. The particle size can be controlled by adjusting parameters such as lipid concentration, lipid-phase pressure, and aqueous crossflow velocity. Smaller SLNs are obtained when the aqueous phase temperature is maintained below the lipid's melting point, allowing rapid solidification. The significant benefit of this approach is that it allows continuous nanoparticle manufacturing. However, this technique has drawbacks in that it necessitates a complex operation, and membranes are susceptible to being clogged [39, 40].

Coacervation

This is the solvent-free technique to produce SLNs by the acidification of salt micelles. In this method, the acidification of micellar salt solutions induces the precipitation of free fatty acids from their micelles through proton transfer between the acid and soap solutions. As a result, spherical NPs with sizes typically ranging from 250 to 500 nm are formed. This technique does not require complex or expensive equipment; however, it is not appropriate for pH-sensitive pharmaceutical compounds [41].

1.2.3. Organic solvents methods

Solvent Emulsification-Evaporation

In this technique, lipid and drug are dissolved in a non-water-miscible organic solvent (e.g. cyclohexane, dichloromethane, toluene, chloroform) followed by emulsification using high-speed homogenizers in an aqueous process. The coarse emulsion is quickly passed through a microfluidizer to increase the efficiency of emulsification. By mechanical mixing at room temperature or reduced pressures (e.g., rotatory evaporators), the organic solvent content disappears, leaving SLNs precipitates (**Figure 3C**) [42].

Solvent emulsification diffusion

In this method, water-miscible organic solvents are used (e.g., methyl acetate, isopropyl acetate, benzyl alcohol, ethyl acetate). The initial saturation of both aqueous and oil phases maintains the initial thermodynamic balance of both phases [43].

Solvent injection

This approach and the solvent emulsification-diffusion method have similar underlying concepts. However, using a needle, the organic medium is rapidly injected into the aqueous solution maintained continuous mechanical stirring. This allows the rapid migration of organic phase into the water phase, leading to nanoparticles precipitation [44].

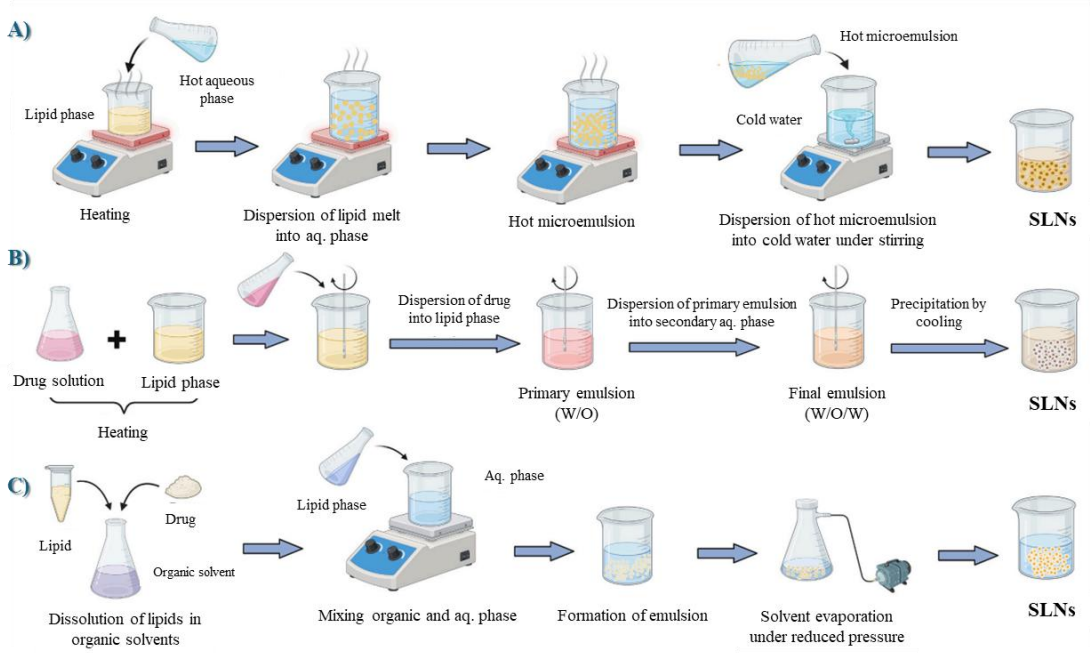


Figure 3. Emulsion and solvent-based methods: **(A)** the microemulsion, **(B)** the double emulsion, **(C)** solvent emulsification-evaporation.

1.3. Features of SLNs

1.3.1. General Components of SLNs

The biological performance of lipid NPs is strongly influenced by their overall composition and the nature of the excipients used. SLNs are typically composed of solid lipids, surfactants, and surface-modifying agents when necessary [45]. The functional roles of SLNs components can be summarized as follows:

- Solid lipids form the lipid matrix or core of the SLNs, determining structural stability, crystallinity, and drug release behaviour.
- Surfactants and co-surfactants stabilize the lipid suspension, maintain a uniform particle size distribution, and prevent particle growth or aggregation.
- Surface modifiers provide specific functionalities such as targeted delivery, stealth behaviour, or enhanced biocompatibility, thereby influencing *in vivo* performance.

The selection of suitable excipients depends on their physicochemical properties, stability, and safety, as well as their ability to support the desired drug loading and release characteristics. In general, the term *lipid* is used broadly and includes triglycerides, partial glycerides, fatty acids, and waxes. Various classes of emulsifiers differing in charge and molecular weight have been employed to stabilize lipid dispersions, with combinations of emulsifiers often providing superior prevention of particle agglomeration. **Table 2** lists the main lipids commonly employed in SLNs formulations [46].

Table 2. Lipids and emulsifiers used for the preparation of SLNs [47].

Triglycerides	Hard fat types	Emulsifiers/coemulsifiers
Tricaprin	Witepsol® W 35	Brij 78
Trilaurin	Witepsol® H 35	Brij 99
Trimyristin	Witepsol® H 42	Egg lecithin
Tripalmitin	Witepsol® H 85	Phosphatidylcholine
Tristearin	Glyceryl monostearate (Imwitor® 900)	Poloxamer 188
Softisan® 142	Glyceryl behenate (Compritol® 888 ATO)	Poloxamer 182
	Glyceryl palmitostearate (Precirol® ATO 5)	Poloxamer 407
	Cetyl palmitate	Poloxamine 908
	Stearic acid	Polysorbate 20
	Palmitic acid	Polysorbate 60
	Decanoic acid	Polysorbate 80
	Behenic acid	Sodium cholate
		Sodium glycocholate
		Soybean lecithin

Surface modifiers and ligands

The concept of surface modification in lipid-based nanocarriers emerged as a second-generation advancement following the first developments in nanotechnology-based drug delivery. Initially introduced in the 1970s with liposomes, lipid vesicles showed promise for encapsulating both hydrophilic and lipophilic drugs but suffered from rapid clearance by the mononuclear phagocyte system. This limitation led to the development of stealth liposomes in the late 1980s, achieved by coating their surface with hydrophilic polymers such as polyethylene glycol (PEG) [48]. The success of PEGylation in prolonging circulation time and reducing opsonization inspired similar approaches for SLNs. Over time, lipid excipients were chemically modified with functional groups, such as carboxyl, amine, or maleimide moieties, allowing covalent ligand attachment and enabling actively targeted delivery (**Figure 4**) [49]. Surface modification now represents a crucial strategy to tailor the biological behaviour of SLNs, enhance stability, and enable specific targeting [50].

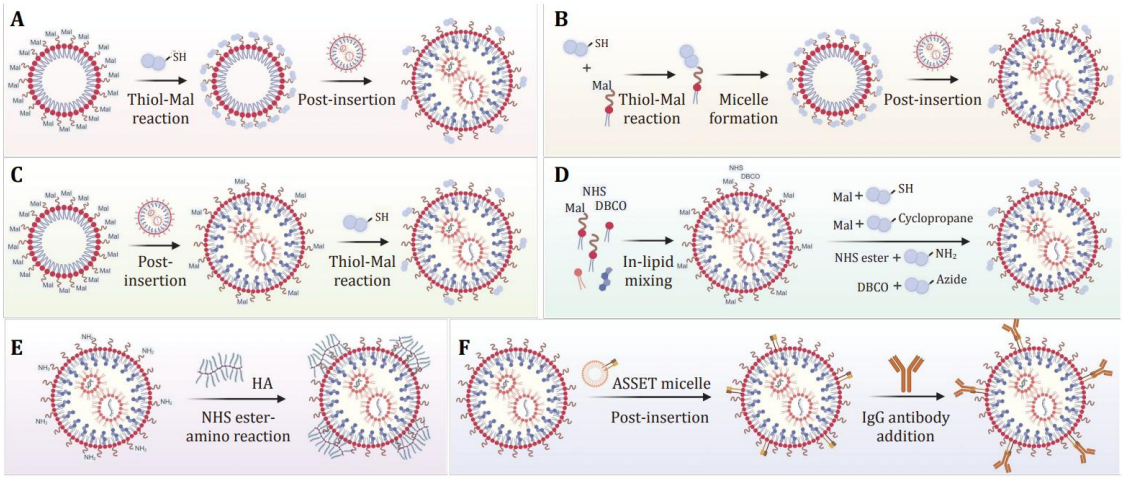


Figure 4. Schematic representation of the main chemical strategies used for the surface functionalization of SLNs. **(A-C)** Thiol-maleimide coupling for ligand conjugation via direct insertion or post-insertion methods. **(D)** In-lipid mixing and click-chemistry-based approaches, including NHS-ester/amine, DBCO-azide, and maleimide-thiol reactions. **(E)** Covalent attachment of hyaluronic acid (HA) to amine groups on the nanoparticle surface through NHS-ester activation. **(F)** Post-insertion of ASSET micelles followed by antibody conjugation (e.g., IgG) for active targeting. These strategies enable stable and versatile ligand incorporation on solid lipid nanoparticles, improving receptor-specific targeting and therapeutic performance [49].

Ligand coupling further extends the functionality of surface-engineered SLNs by enabling *active targeting* through specific molecular recognition (**Table 3**) [51]. Ligands such as folic acid (FA), transferrin (Tf), lactoferrin, mannose, and peptides are covalently

attached to lipid-PEG linkers using chemistries including amide bond formation (via EDC/NHS activation), Michael addition to maleimide-terminated PEG chains, or Schiff-base condensation with aldehyde groups [52, 53]. For example, FA-PEG-DSPE and Tf-PEG-SA conjugates have been extensively used to direct SLNs toward overexpressed folate or transferrin receptors in tumor cells, while mannose and hyaluronic acid moieties target macrophages and CD44 receptors, respectively [54]. More sophisticated strategies have employed antibodies, aptamers, or small peptides to improve cellular selectivity and intracellular delivery. The density, orientation, and spacer length of ligands are critical design factors that influence binding affinity and uptake efficiency.

Table 3. Examples of organic reaction-based surface conjugation to lipid [99].

Cojugation method	Target ligands	Surface modifier lipid	Receptor	Disease
Amidation	Hyaluronic Acid	Amine-labeled lipid	CD44	Cancer
EDC/NHS coupling	Anti-EGFR	Carboxyl-labeled-lipid	ROCK1	Gallbladder carcinoma
Thiol maleimide reaction	Folate	Maleimide-labeled lipid	4T1	Breast cancer
NHS-Amidation	Anti-PDL1	NHS-labeled lipid	PDL1	Melanoma
Thiol-azide click chemistry	scFv46.1	DBCO-labeled lipid	RMT	Brain injury and disease

1.3.2. Structural organization and drug distribution

The release behaviour of SLNs strongly depends on the type of lipid matrix and on the spatial distribution of the active compound within the particle [55]. Three principal models have been proposed to describe typical drug distribution patterns in SLNs.

In the drug-enriched shell matrix model (**Figure 5A**), the drug is concentrated in the outer shell. This occurs when the API concentration in the melted lipid is low, leading the lipid to crystallize first during cooling and to push the drug toward the surface [56]. This structure generally results in an initial burst release and is advantageous for formulations requiring rapid therapeutic action or enhanced skin penetration in topical delivery [57]. The homogeneous matrix (**Figure 5B**) is characterized by a uniform molecular dispersion of the drug within the lipid phase, achieved through optimized drug-to-lipid ratios and high-pressure homogenization, either hot or cold [58]. This configuration promotes a more controlled and sustained drug release profile, suitable for prolonged therapeutic effects. In contrast, the drug-enriched core matrix (**Figure 5C**) forms when the drug is close to its saturation solubility in the lipid melt; upon cooling, the drug recrystallizes

before the lipid, creating a dense drug core surrounded by a lipid shell [59]. This arrangement allows for prolonged and modulated drug release, as the lipid barrier slows diffusion and can be tuned by modifying the composition and crystallization properties of the lipid matrix.

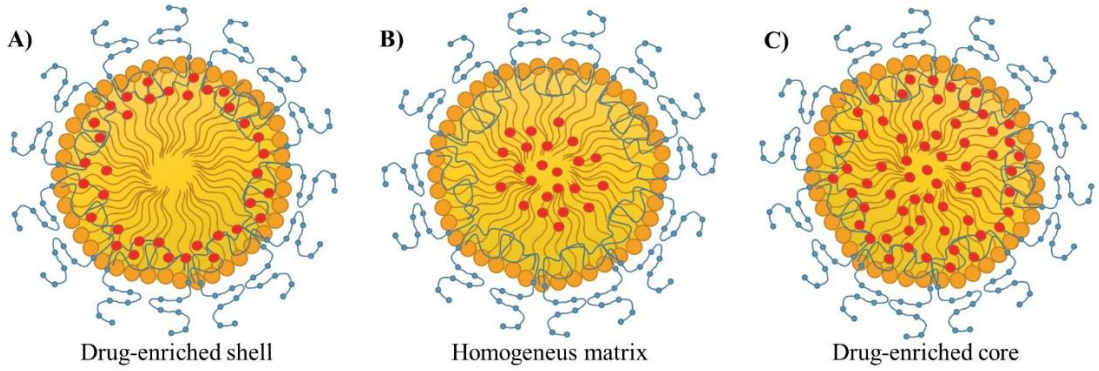


Figure 5. SLNs' drug incorporation models.

1.3.3. Characterization

The characterization of SLNs with respect to key physicochemical parameters is fundamental for their successful development. Over the years, research has helped to identify the most critical parameters and their acceptable ranges. Evaluating these criteria provides an initial understanding of the formulation's long-term stability and its safety profile.

Surface charge and particle size

Particle diameter is one of the most important characteristics of NPs. It may influence important material properties, including reactivity, dissolution rate, colloidal dispersion stability, and delivery efficiency. The most frequently used method for calculating the particle size of SLNs dispersed in a liquid medium is Dynamic Light Scattering (DLS). It measures the fluctuations in the intensity of scattered light caused by the Brownian motion of particles in suspension; from these fluctuations, the hydrodynamic diameter is calculated using the Stokes-Einstein equation. The DLS provides rapid, non-destructive measurements [60].

ζ-potential analysis is a crucial parameter for assessing the surface charge and colloidal stability of SLNs. It represents the electrical potential at the slipping plane of particles suspended in a liquid medium and is typically determined by electrophoretic light

scattering (ELS). The magnitude and sign of the ζ-potential indicate the degree of electrostatic repulsion between particles: values higher than ±30 mV generally suggest good physical stability, as strong repulsive forces prevent aggregation. On the contrary, low ζ--potential values may lead to particle agglomeration and reduced shelf-life. In addition, ζ--potential measurements provide valuable information about surface modifications, the adsorption of surfactants, and possible interactions between the lipid matrix and incorporated bioactive compounds [61].

Crystallinity and polymorphism

The evaluation of crystallinity degree of SLNs is essential for understanding their physical stability and drug release behaviour. The degree of crystallinity directly influences the loading capacity and retention of the incorporated drug, as highly ordered lipid lattices tend to expel the active compound during storage [62]. Moreover, polymorphic transitions ($\alpha \rightarrow \beta' \rightarrow \beta$) can lead to alterations in lattice packing and affect stability over time. Differential Scanning Calorimetry (DSC) and X-ray Diffraction (XRD) are complementary techniques employed to determine the thermal transitions and polymorphic forms of the lipid matrix. These analyses provide valuable insights into structural organization and allow prediction of long-term stability. Additional spectroscopic techniques, such as Infrared (IR) and Raman spectroscopy, are also applied to investigate the molecular and structural properties of lipid components [63].

Entrapment efficiency and drug loading

Lipid and aqueous phase separation is a key step in determining the amount of drug entrapped per unit weight of lipid nanocarrier. Ultrafiltration, centrifugation, and dialysis are commonly employed to achieve this separation. Both drug loading (%DL) and entrapment efficiency (%EE) are determined through quantitative analytical methods, such as UV-visible spectrophotometry or high-performance liquid chromatography (HPLC), after separation of the unencapsulated drug from the formulation. The drug loading capacity and entrapment efficiency of SLNs depend on several factors, including the solubility and polymorphic state of the lipid matrix. High lipid solubility of the drug is required for adequate loading, as solubility typically decreases during the cooling step of nanoparticle formation. The presence of mono- and diglyceride components in the lipid phase enhances drug solubilization, whereas lipids forming highly ordered crystalline

lattices tend to expel the drug. The difference between these two parameters lies only in their calculation: (%EE) expresses the proportion of the total drug successfully encapsulated within the SLNs, while (%DL) refers to the amount of drug loaded per unit weight of lipid material. These parameters are fundamental indicators of formulation performance and stability, as changes in lipid crystallinity or drug-lipid interactions over time may alter both values [64].

Morphological characterization

The morphological characterization of SLNs is essential, as particle shape and surface structure greatly influence biological behaviour, including circulation time, biodistribution, cellular uptake, and overall therapeutic efficacy. Understanding morphology helps establish structure-function relationships and predict *in vivo* performance. Techniques such as Transmission and Scanning Electron Microscopy (TEM, SEM) are commonly used to assess shape and surface features, while Atomic Force Microscopy (AFM) and Cryo-TEM provide detailed topographical and internal structural information [65].

In vitro drug release study

In vitro release studies are crucial for elucidating the release mechanism and kinetics, as well as for predicting *in vivo* performance. Drug release from SLNs generally occurs through a diffusion-controlled mechanism; depending on drug distribution within the lipid matrix, SLNs may exhibit a biphasic release profile, an initial burst release of surface-associated drug followed by a sustained or controlled phase, or a more uniform, prolonged release if the drug is homogeneously incorporated within the core. Several factors influence the release behaviour, including the method of preparation, drug-lipid compatibility, solubility of the drug in the lipid, type and concentration of surfactant, composition of the lipid matrix, and particle size. These studies are particularly important when developing formulations with specific release targets, such as gastroresistant systems, where release is evaluated under simulated gastric (SGF) and intestinal (SIF) fluids [66].

1.4. Route of administration

The *in vivo* fate of SLNs primarily depends on the route of administration and on their interactions with the biological environment, including the adsorption of biomolecules onto the particle surface and the potential desorption of SLN components into surrounding tissues. Owing to their composition, which is based on physiological or physiologically related lipids and waxes, SLNs generally follow endogenous pathways of transport and metabolism, strongly influencing their biodistribution and degradation behaviour. Enzymatic degradation represents a key mechanism governing SLN fate, with lipases playing a major role. These enzymes, widely distributed throughout organs and tissues, catalyze the hydrolysis of ester bonds within the lipid matrix, leading to the formation of partial glycerides, glycerol, and free fatty acids. Lipase activity is typically initiated at the oil-water interface, where enzyme adsorption induces conformational changes that expose the catalytic site ("lid opening"). In vitro studies have demonstrated that the rate of SLN degradation by pancreatic lipases is highly dependent on formulation parameters, particularly the nature of the lipid matrix and the surfactant used for stabilization, highlighting the critical role of formulation design in determining the metabolic fate of SLNs [67].

1.4.1. Oral administration

Oral administration represents a convenient route for drug delivery, but it poses major challenges for peptide- and protein-based therapeutics such as insulin, mainly due to enzymatic degradation and poor intestinal permeability [68]. SLNs have shown great potential to overcome these limitations, as their lipid matrix can protect the encapsulated molecules from gastrointestinal degradation and improve absorption. Zhang *et al.* developed stearic acid-octaarginine-modified SLNs for oral insulin delivery, demonstrating partial protection of insulin from enzymatic digestion *in vitro* and a significant hypoglycemic effect *in vivo* in diabetic rats [69].

1.4.2. Parenteral administration

The parenteral route is crucial in the management of severe or acute conditions requiring rapid therapeutic action. SLNs are suitable carriers for intravenous administration, as they can reduce local irritation and improve the solubility of poorly water-soluble drugs such

as camptothecin or doxorubicin. Yang *et al.* developed camptothecin-loaded SLNs via high-pressure homogenization and observed higher AUC/dose and mean residence time compared to camptothecin solution, particularly in the brain and organs of the reticuloendothelial system, indicating improved tissue distribution and brain targeting [67]. Similarly, intravenous administration of paclitaxel (PTX)- and doxorubicin (DOX)-loaded SLNs, especially when PEGylated, resulted in enhanced uptake, prolonged circulation, and reduced cardiotoxicity compared to free drug formulations [70].

1.4.3. Topical and transdermal applications

SLNs have been reported to penetrate the stratum corneum and enhance the delivery of encapsulated drugs into the viable layers of the skin. Their solid lipid matrix enables sustained drug release, ensuring a prolonged local drug supply while limiting systemic absorption. In addition, SLNs exhibit occlusive properties due to film formation on the skin surface, which reduces transepidermal water loss (TEWL), increases skin hydration, and contributes to the alleviation of atopic eczema symptoms and improvement of skin appearance. Importantly, this occlusive effect also facilitates drug permeation by increasing stratum corneum hydration. Compared with conventional oil-in-water creams, SLN-based topical formulations have been shown to increase stratum corneum thickness and further enhance drug penetration, highlighting their ability to modulate skin permeation profiles [71].

1.4.4. Ocular administration

Due to the complex anatomy and physiological barriers of the eye, ocular drug delivery remains a major challenge. Therefore, the development of efficient nanoscale delivery systems capable of improving ocular bioavailability while minimizing local and systemic toxicity is of great interest. SLNs have emerged as promising carriers for ophthalmic administration owing to their biocompatibility and ability to enhance corneal penetration. Satyanarayana *et al.* developed bimatoprost-loaded SLNs for glaucoma management, achieving sustained drug release, improved corneal permeation, and enhanced intraocular bioavailability compared to conventional eye drops [72]. Beyond topical application, SLNs have also shown strong potential for intravitreal administration, where prolonged drug retention and reduced injection frequency are key goals. In an *in vivo* study, Parra-Sánchez *et al.* demonstrated that bevacizumab-loaded SLNs (BVZ-SLNs) ensured

sustained intravitreal release, reduced vascular density, and decreased lesion depth in a laser-induced CNV rat model. Importantly, BVZ-SLNs achieved therapeutic outcomes comparable to, or better than, those of standard Avastin®, while using markedly lower drug doses and without inducing retinal damage. These findings confirm the versatility of SLNs as effective carriers for both anterior- and posterior-segment ocular delivery [73].

1.5. Therapeutic Applications

Since their initial introduction, SLNs have garnered increasing scientific attention, with ongoing efforts devoted to expanding their therapeutic applications (**Figure 6**). This increasing body of research has confirmed the high versatility and adaptability of SLNs as an effective drug delivery platform.

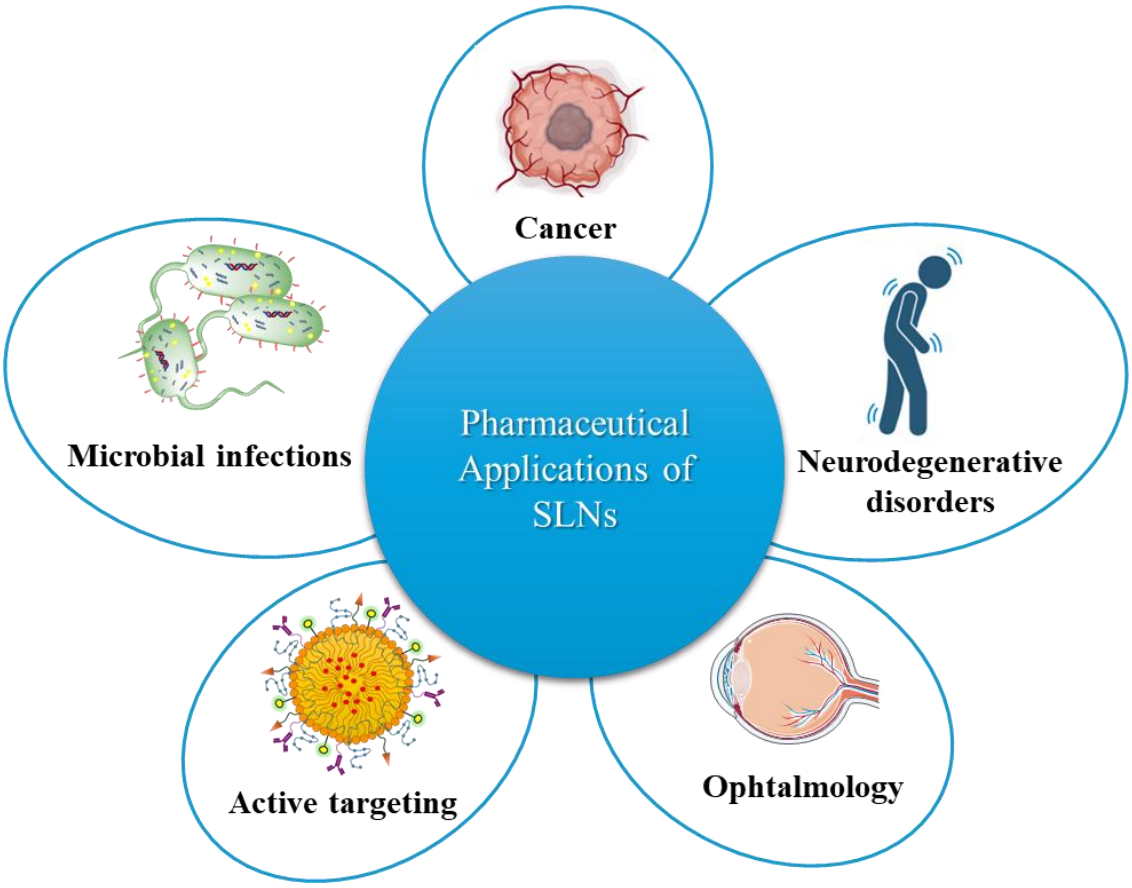


Figure 6. Therapeutic applications of SLNs.

1.5.1. SLNs for antimicrobial therapy

Antibiotic resistance represents one of the major challenges in modern medicine, leading to an urgent need for innovative therapeutic strategies. It has been reported that the

incorporation of antibiotics into SLNs can significantly enhance their therapeutic performance by improving solubility, stability, and bioavailability while reducing enzymatic degradation and resistance development [75]. As demonstrated by Arana *et al.*, SLNs can enhance antibiotic efficiency through improved membrane permeability, reduced efflux pump activity, and increased intracellular accumulation [76]. Moreover, several studies have shown enhanced antimicrobial efficacy of SLN formulations against intracellular pathogens such as *Brucella melitensis* and *Salmonella enterica* [77], as well as improved eradication of biofilm-forming bacteria like *Staphylococcus epidermidis* [78].

1.5.2. SLNs for neurodegenerative disorders

The pharmacological management of neurodegenerative diseases such as Alzheimer's, Parkinson's, and Huntington's disease is often hindered by the presence of the blood-brain barrier (BBB), which restricts the entry of therapeutic molecules into the central nervous system (CNS). SLNs have been reported as a promising nanocarrier system to overcome this limitation, owing to their biocompatibility and capacity to enhance brain uptake through mechanisms such as adsorptive- or receptor-mediated transcytosis [79].
As demonstrated by Satapathy *et al.* [1], SLNs significantly enhance the permeation of drugs across the BBB, resulting in higher brain bioavailability and improved therapeutic efficacy. For instance, nicotinamide- and curcumin-loaded SLNs have shown increased CNS accumulation and marked neuroprotective effects in Alzheimer's disease models [79, 80]. Similarly, bromocriptine and ropinirole-loaded SLNs exhibited improved BBB permeability and bioavailability, resulting in superior dopaminergic activity and sustained pharmacological action in Parkinson's disease [81]. Furthermore, curcumin- and rosmarinic acid-loaded SLNs demonstrated enhanced antioxidant activity and neuronal protection in models of Huntington's disease [82].

1.5.3. SLNs in cancer treatment

Conventional chemotherapeutic agents often suffer from poor aqueous solubility, low bioavailability, and severe systemic toxicity, which limit their therapeutic efficacy. SLNs have been extensively investigated to overcome these drawbacks by improving the pharmacokinetic profile, protecting the drug from premature degradation, and allowing sustained release at the tumor site. Their small size facilitates passive tumor targeting

through the enhanced permeability and retention (EPR) effect, while the lipid matrix enables high drug encapsulation efficiency and controlled release kinetics [83].

It has been reported that paclitaxel-loaded SLNs significantly increased drug accumulation in tumor tissues and produced a prolonged antitumor effect compared to free paclitaxel formulations [84]. Similarly, doxorubicin-loaded SLNs exhibited improved bioavailability, reduced systemic toxicity, and enhanced cytotoxicity against various cancer cell lines [85]. Cisplatin and etoposide-loaded SLNs have also demonstrated sustained drug release and superior tumor growth inhibition in preclinical models, highlighting their potential as efficient carriers for lipophilic anticancer agents [86, 87].

1.5.4. SLNs as carriers for biological drugs

Biological drugs, including nucleic acids, peptides, proteins, and antibodies, represent a rapidly growing class of therapeutics with high selectivity and potency. However, their therapeutic application is often hampered by poor stability, enzymatic degradation, and low membrane permeability. These limitations underline the need for efficient carrier systems capable of protecting biological molecules and improving their delivery to target cells. SLNs have emerged as a versatile platform for this purpose, combining biocompatibility, biodegradability, and the ability to encapsulate both hydrophilic and hydrophobic biomolecules while providing controlled release and targeted distribution.

Gene delivery

Gene therapy offers great promise for treating a variety of genetic and acquired disorders, but its success largely depends on the safety and efficiency of the vector. Compared with viral systems, SLNs provide a safer, non-immunogenic, and more stable alternative for nucleic acid transport. Their cationic surface facilitates electrostatic interaction with negatively charged DNA or RNA, leading to stable complex formation and efficient transfection [88].

It has been reported that cationic SLNs (cSLNs) can deliver plasmid DNA and small interfering RNA (siRNA) effectively, achieving high transfection rates with minimal cytotoxicity. For instance, Botto *et al.* demonstrated the ability of cSLNs to deliver shNUPR1 plasmids to hepatocellular carcinoma cells, achieving superior transfection efficiency and cell compatibility compared with conventional non-viral vectors [89].

Similarly, Penumarthi *et al.* formulated DNA-SLN complexes capable of transfecting dendritic cells, while maintaining low cytotoxicity and high structural stability [90].

Protein and peptide delivery

The delivery of proteins and peptides poses major challenges due to their hydrophilic nature and vulnerability to enzymatic degradation. SLNs offer protection by encapsulating these molecules within a lipid matrix, thus improving their stability and bioavailability. Hong *et al.* demonstrated that ion-pair formation between hydrophilic peptides such as leuprolide or insulin and lipophilic counterions enhanced their encapsulation efficiency in SLNs. Protein- and peptide-loaded SLNs have also shown favorable pharmacokinetic profiles and high tolerability, providing controlled release and improved therapeutic performance compared with conventional formulations [91].

Antibody delivery

Among biologics, monoclonal antibodies (mAbs) are particularly challenging to formulate due to their large molecular size, structural complexity, and limited permeability across biological barriers such as the blood–brain barrier (BBB). Encapsulation into SLNs has been proposed as a strategy to improve their stability, bioavailability, and tissue penetration.

Battaglia *et al.* developed bevacizumab-loaded SLNs using a fatty acid coacervation method, achieving stable incorporation of the antibody through hydrophobic ion pairing with dioctyl sulfosuccinate (AOT). The encapsulated bevacizumab maintained its biological activity and exhibited a 100-200-fold increase in efficacy *in vitro* compared with the free drug. Moreover, BVZ-loaded SLNs enhanced antibody transport across an *in vitro* BBB model, suggesting potential use for glioblastoma therapy [92]. Similarly, Ozgenc *et al.* designed trastuzumab-loaded SLNs using high-shear homogenization and sonication. The resulting nanoparticles (<100 nm) showed high entrapment efficiency (>90%) and sustained release. Radiolabeled formulations demonstrated high stability and biocompatibility, while *in vitro* studies revealed improved cytotoxicity and uptake in HER2-positive breast cancer cells compared with free trastuzumab. *In vivo* studies further confirmed prolonged circulation and enhanced tumor accumulation [93].

1.5.5. SLNs for active delivery

Active targeting involves the surface modification of nanocarriers with specific ligands, such as antibodies, peptides, or polysaccharides, that can selectively recognize receptors overexpressed in pathological tissues. This strategy enhances cellular uptake through receptor-mediated endocytosis, improving drug accumulation at the target site while reducing systemic toxicity. Although initially developed for oncology, where ligands like folic acid or transferrin have been used to enhance tumor targeting, active targeting is also highly valuable in other therapeutic areas [94].

For instance, Shilpi *et al*. demonstrated that lactoferrin-conjugated SLNs loaded with rifampicin significantly improved pulmonary drug delivery in tuberculosis. The surface functionalization enabled receptor-mediated uptake by alveolar epithelial cells and macrophages, resulting in a threefold increase in lung drug accumulation and reduced systemic distribution compared with non-functionalized SLNs [95]. In the field of neurodegenerative diseases, Dal Magro *et al.* developed apolipoprotein E-modified SLNs (SLN-mApoE) that efficiently crossed the blood-brain barrier through receptor-mediated transcytosis, achieving higher brain bioavailability and prolonged residence time without inducing inflammatory effects [96]. Similarly, Maretti *et al.* designed mannosylated SLNs for the treatment of tuberculosis, showing that mannose-functionalized nanoparticles exhibited strong affinity for macrophage mannose receptors, promoting faster cellular internalization and sustained intracellular drug release [97]. More recently**,** Jain *et al.* formulated chondroitin sulfate-modified SLNs loaded with diacerein for the treatment of osteoarthritis, exploiting the natural affinity of chondroitin sulfate for articular cartilage. This system resulted in higher drug concentration in the joint, improved cartilage regeneration, and reduced systemic exposure compared with unmodified SLNs [98].

References

1. Mitchell, M.J., M.M. Billingsley, R.M. Haley, M.E. Wechsler, N.A. Peppas, R. Langer, Engineering precision nanoparticles for drug delivery. *Nature reviews drug discovery*, **2021**. 20(2): p. 101-124.
2. Lu, H., S. Zhang, J. Wang, Q. Chen, A review on polymer and lipid-based nanocarriers and its application to nano-pharmaceutical and food-based systems. *Frontiers in nutrition*, **2021**. 8: p. 783831.
3. Egwu, C.O., C. Aloke, K.T. Onwe, C.I. Umoke, J. Nwafor, R.A. Eyo, J.A. Chukwu, G.O. Ufebe, J. Ladokun, D.T. Audu, Nanomaterials in drug delivery: strengths and opportunities in medicine. *Molecules*, **2024**. 29(11): p. 2584.
4. Sim, S., N. Wong, Nanotechnology and its use in imaging and drug delivery (review*). Biomed Rep,* **2021**. 14 (5): 42.
5. Harish, V., D. Tewari, M. Gaur, A.B. Yadav, S. Swaroop, M. Bechelany, A. Barhoum, Review on Nanoparticles and Nanostructured Materials: Bioimaging, Biosensing, Drug Delivery, Tissue Engineering, Antimicrobial, and Agro-Food Applications. *Nanomaterials*, **2022**. 12(3): p. 457.
6. Abdifetah, O., K. Na-Bangchang, Pharmacokinetic studies of nanoparticles as a delivery system for conventional drugs and herb-derived compounds for cancer therapy: a systematic review. *International journal of Nanomedicine*, **2019**: p. 5659-5677.
7. Li, S.D., L. Huang, Pharmacokinetics and biodistribution of nanoparticles. *Mol Pharm*, **2008**. 5(4): p. 496-504.
8. Zielińska, A., F. Carreiró, A.M. Oliveira, A. Neves, B. Pires, D.N. Venkatesh, A. Durazzo, M. Lucarini, P. Eder, A.M. Silva, Polymeric nanoparticles: production, characterization, toxicology and ecotoxicology. *Molecules*, **2020**. 25(16): p. 3731.
9. Béduneau, A., P. Saulnier, J.-P. Benoit, Active targeting of brain tumors using nanocarriers. *Biomaterials*, **2007**. 28(33): p. 4947-4967.
10. Mitchell, M.J., R.K. Jain, R. Langer, Engineering and physical sciences in oncology: challenges and opportunities. *Nature Reviews Cancer*, **2017**. 17(11): p. 659-675.
11. Yadollahpour, A., Nanotechnology and Biomarkers in Precision Medicine: Advances and Perspectives. *Curr Top Med Chem*, **2021**. 21(14): p. 1199-1201.
12. Patra, J.K., G. Das, L.F. Fraceto, E.V.R. Campos, M.D.P. Rodriguez-Torres, L.S. Acosta-Torres, L.A. Diaz-Torres, R. Grillo, M.K. Swamy, S. Sharma, S. Habtemariam, H.S. Shin, Nano based drug delivery systems: recent developments and future prospects. *J Nanobiotechnology*, **2018**. 16(1): p. 71.

13. Allen, T.M., P.R. Cullis, Liposomal drug delivery systems: from concept to clinical applications. *Advanced drug delivery reviews*, **2013**. 65(1): p. 36-48.
14. Anselmo, A.C., S. Mitragotri, A review of clinical translation of inorganic nanoparticles. *The AAPS journal*, **2015**. 17(5): p. 1041-1054.
15. Boztepe, T., G.R. Castro, I.E. León, Lipid, polymeric, inorganic-based drug delivery applications for platinum-based anticancer drugs. *Int J Pharm*, **2021**. 605: p. 120788.
16. Hu, X., Y. Zhang, T. Ding, J. Liu, H. Zhao, Multifunctional gold nanoparticles: a novel nanomaterial for various medical applications and biological activities. *Frontiers in bioengineering and biotechnology*, **2020**. 8: p. 990.
17. Xu, W., T. Yang, S. Liu, L. Du, Q. Chen, X. Li, J. Dong, Z. Zhang, S. Lu, Y. Gong, Insights into the Synthesis, types and application of iron Nanoparticles: The overlooked significance of environmental effects. *Environment International*, **2022**. 158: p. 106980.
18. Arias, L.S., J.P. Pessan, A.P.M. Vieira, T.M.T.d. Lima, A.C.B. Delbem, D.R. Monteiro, Iron oxide nanoparticles for biomedical applications: a perspective on synthesis, drugs, antimicrobial activity, and toxicity. *Antibiotics*, **2018**. 7(2): p. 46.
19. Ghosn, Y., M.H. Kamareddine, A. Tawk, C. Elia, A. El Mahmoud, K. Terro, N. El Harake, B. El-Baba, J. Makdessi, S. Farhat, Inorganic nanoparticles as drug delivery systems and their potential role in the treatment of chronic myelogenous leukaemia. *Technology in cancer research & treatment*, **2019**. 18: p. 1533033819853241.
20. Caldorera-Moore, M., J.E. Vela Ramirez, N.A. Peppas, Transport and delivery of interferon-α through epithelial tight junctions via pH-responsive poly (methacrylic acid-grafted-ethylene glycol) nanoparticles. *Journal of drug targeting*, **2019**. 27(5-6): p. 582-589.
21. Valcourt, D.M., M.N. Dang, M.A. Scully, E.S. Day, Nanoparticle-mediated co-delivery of Notch-1 antibodies and ABT-737 as a potent treatment strategy for triple-negative breast cancer. *ACS nano*, **2020**. 14(3): p. 3378-3388.
22. Le, Q.-V., J. Suh, J.J. Choi, G.T. Park, J.W. Lee, G. Shim, Y.-K. Oh, In situ nanoadjuvant-assembled tumor vaccine for preventing long-term recurrence. *ACS nano*, **2019**. 13(7): p. 7442-7462.
23. Nguyen, H.V., K. Campbell, G.F. Painter, S.L. Young, G.F. Walker, Nanoparticle system based on amino-dextran as a drug delivery vehicle: immune-stimulatory CpG-oligonucleotide loading and delivery. *Pharmaceutics*, **2020**. 12(12): p. 1150.

24. Salunkhe, S.S., N.M. Bhatia, M.S. Bhatia, Implications of formulation design on lipid-based nanostructured carrier system for drug delivery to brain. *Drug Delivery*, **2016**. 23(4): p. 1306-1316.
25. Duan, Y., A. Dhar, C. Patel, M. Khimani, S. Neogi, P. Sharma, N.S. Kumar, R.L. Vekariya, A brief review on solid lipid nanoparticles: Part and parcel of contemporary drug delivery systems. *RSC advances*, **2020**. 10(45): p. 26777-26791.
26. Sastri, K.T., G.V. Radha, S. Pidikiti, P. Vajjhala, Solid lipid nanoparticles: Preparation techniques, their characterization, and an update on recent studies. *Journal of applied pharmaceutical science*, **2020**. 10(6): p. 126-141.
27. Paliwal, R., S.R. Paliwal, R. Kenwat, B.D. Kurmi, M.K. Sahu, Solid lipid nanoparticles: A review on recent perspectives and patents. *Expert opinion on therapeutic patents*, **2020**. 30(3): p. 179-194.
28. Pandey, S., F. Shaikh, A. Gupta, P. Tripathi, J.S. Yadav, A recent update: solid lipid nanoparticles for effective drug delivery. *Advanced Pharmaceutical Bulletin*, **2021**. 12(1): p. 17.
29. Gordillo-Galeano, A., C.E. Mora-Huertas, Solid lipid nanoparticles and nanostructured lipid carriers: A review emphasizing on particle structure and drug release. *European Journal of Pharmaceutics and Biopharmaceutics*, **2018**. 133: p. 285-308.
30. Lippacher, A., R. Müller, K. Mäder, Investigation on the viscoelastic properties of lipid based colloidal drug carriers. *International journal of pharmaceutics*, **2000**. 196(2): p. 227-230.
31. Lander, R., W. Manger, M. Scouloudis, A. Ku, C. Davis, A. Lee, Gaulin homogenization: a mechanistic study. *Biotechnology progress*, **2000**. 16(1): p. 80-85.
32. Müller, R.H., S. Benita, B.H. Böhm, Emulsions and nanosuspensions for the formulation of poorly soluble drugs. *CRC Press,* **1998**.
33. Xie, S., L. Zhu, Z. Dong, X. Wang, Y. Wang, X. Li, W. Zhou, Preparation, characterization and pharmacokinetics of enrofloxacin-loaded solid lipid nanoparticles: influences of fatty acids. *Colloids and Surfaces B: Biointerfaces*, **2011**. 83(2): p. 382-387.
34. Andrade, L.N., D.M.L. Oliveira, M.V. Chaud, T.F.R. Alves, M. Nery, C.F. da Silva, J.K.C. Gonsalves, R.S. Nunes, C.B. Corrêa, R.G. Amaral, E. Sanchez-Lopez, E.B. Souto, P. Severino, Praziquantel-Solid Lipid Nanoparticles Produced by Supercritical Carbon Dioxide Extraction: Physicochemical Characterization, Release Profile, and Cytotoxicity. *Molecules*, **2019**. 24(21): p. 3881.

35. Gasco, M.R., Method for producing solid lipid microspheres having a narrow size distribution. *Google Patents*, **1993**.
36. Malik, M.A., M.Y. Wani, M.A. Hashim, Microemulsion method: A novel route to synthesize organic and inorganic nanomaterials: 1st Nano Update. *Arabian journal of Chemistry*, **2012**. 5(4): p. 397-417.
37. Li, Z., L. Yu, L. Zheng, F. Geng, Studies on crystallinity state of puerarin loaded solid lipid nanoparticles prepared by double emulsion method. *Journal of thermal analysis and calorimetry*, **2010**. 99(2): p. 689-693.
38. Friberg, S.E., R.W. Corkery, I.A. Blute, Phase inversion temperature (PIT) emulsification process. *Journal of chemical & engineering data*, **2011**. 56(12): p. 4282-4290.
39. Charcosset, C., A. El-Harati, H. Fessi, Preparation of solid lipid nanoparticles using a membrane contactor. *Journal of controlled release*, **2005**. 108(1): p. 112-120.
40. Laouini, A., V. Andrieu, L. Vecellio, H. Fessi, C. Charcosset, Characterization of different vitamin E carriers intended for pulmonary drug delivery. *International journal of pharmaceutics*, **2014**. 471(1-2): p. 385-390.
41. Battaglia, L., M. Gallarate, R. Cavalli, M. Trotta, Solid lipid nanoparticles produced through a coacervation method. *Journal of microencapsulation*, **2010**. 27(1): p. 78-85.
42. Sjöström, B., B. Bergenståhl, Preparation of submicron drug particles in lecithin-stabilized o/w emulsions I. Model studies of the precipitation of cholesteryl acetate. *International journal of pharmaceutics*, **1992**. 88(1-3): p. 53-62.
43. Paliwal, R., S. Rai, B. Vaidya, K. Khatri, A.K. Goyal, N. Mishra, A. Mehta, S.P. Vyas, Effect of lipid core material on characteristics of solid lipid nanoparticles designed for oral lymphatic delivery. *Nanomedicine: Nanotechnology, Biology and Medicine*, **2009**. 5(2): p. 184-191.
44. Duong, V.A., T.T. Nguyen, H.J. Maeng, Preparation of Solid Lipid Nanoparticles and Nanostructured Lipid Carriers for Drug Delivery and the Effects of Preparation Parameters of Solvent Injection Method. *Molecules*, **2020**. 25(20).
45. Doktorovova, S., R. Shegokar, E.B. Souto, Role of excipients in formulation development and biocompatibility of lipid nanoparticles (SLNs/NLCs). *Nanostructures for novel therapy*, **2017**. p. 811-843.
46. Queiroz, M.d.C.V., L.A. Muehlmann, Characteristics and Preparation of Solid Lipid Nanoparticles and Nanostructured Lipid Carriers. *Journal of Nanotheranostics*, **2024**. 5(4): p. 188-211.

47. Mehnert, W., K. Mäder, Solid lipid nanoparticles: production, characterization and applications. *Advanced drug delivery reviews*, **2012**. 64: p. 83-101.
48. Allen, T.M., P.R. Cullis, Liposomal drug delivery systems: from concept to clinical applications. *Adv Drug Deliv Rev*, **2013**. 65(1): p. 36-48.
49. Priya, S., V.M. Desai, G. Singhvi, Surface Modification of Lipid-Based Nanocarriers: A Potential Approach to Enhance Targeted Drug Delivery. *ACS Omega*, **2023**. 8(1): p. 74-86.
50. Seo, Y., H. Lim, H. Park, J. Yu, J. An, H.Y. Yoo, T. Lee, Recent Progress of Lipid Nanoparticles-Based Lipophilic Drug Delivery: Focus on Surface Modifications. *Pharmaceutics*, **2023**. 15(3): p. 772.
51. Lin, Y., Q. Cheng, T. Wei, Surface engineering of lipid nanoparticles: targeted nucleic acid delivery and beyond. *Biophys Rep*, **2023**. 9(5): p. 255-278.
52. Patel, D., J. Solanki, M.M. Kher, A. Azagury, A review: surface engineering of lipid-based drug delivery systems. *Small*, **2024**. 20(43): p. 2401990.
53. Singh, R., S. Srinivas, M. Kumawat, H.K. Daima, Ligand-based surface engineering of nanomaterials: Trends, challenges, and biomedical perspectives. *OpenNano*, **2024**. 15: p. 100194.
54. Han, E.L., S. Tang, D. Kim, A.M. Murray, K.L. Swingle, A.G. Hamilton, K. Mrksich, M.S. Padilla, R. Palanki, J.J. Li, Peptide-functionalized lipid nanoparticles for targeted systemic mRNA delivery to the brain. *Nano Letters*, **2024**. 25(2): p. 800-810.
55. Ganesan, P., D. Narayanasamy, Lipid nanoparticles: Different preparation techniques, characterization, hurdles, and strategies for the production of solid lipid nanoparticles and nanostructured lipid carriers for oral drug delivery. *Sustainable Chemistry and Pharmacy*, **2017**. 6: p. 37-56.
56. Ghasemiyeh, P., S. Mohammadi-Samani, Solid lipid nanoparticles and nanostructured lipid carriers as novel drug delivery systems: applications, advantages and disadvantages. *Res Pharm Sci*, **2018**. 13(4): p. 288-303.
57. Mishra, V., K.K. Bansal, A. Verma, N. Yadav, S. Thakur, K. Sudhakar, J.M. Rosenholm, Solid Lipid Nanoparticles: Emerging Colloidal Nano Drug Delivery Systems. *Pharmaceutics*, **2018**. 10(4): p. 191.
58. Pardeshi, C., P. Rajput, V. Belgamwar, A. Tekade, G. Patil, K. Chaudhary, A. Sonje, Solid lipid based nanocarriers: An overview / Nanonosači na bazi čvrstih lipida: Pregled. *Acta Pharmaceutica*, **2012**. 62(4): p. 433-472.

59. Uner, M., G. Yener, Importance of solid lipid nanoparticles (SLN) in various administration routes and future perspectives. *Int. J. Nanomedicine*, **2007**. 2(3): p. 289-300.
60. Ramos, A.P., Dynamic light scattering applied to nanoparticle characterization, in Nanocharacterization techniques. *Elsevier*, **2017**. p. 99-110.
61. Clogston, J.D., A.K. Patri, Zeta potential measurement, in Characterization of nanoparticles intended for drug delivery. *Springer,* **2010**. p. 63-70.
62. Schubert, M., B. Schicke, C. Müller-Goymann, Thermal analysis of the crystallization and melting behaviour of lipid matrices and lipid nanoparticles containing high amounts of lecithin. *International journal of pharmaceutics*, **2005**. 298(1): p. 242-254.
63. López-Lorente, Á.I., B. Mizaikoff, Recent advances on the characterization of nanoparticles using infrared spectroscopy. *TrAC Trends in Analytical Chemistry*, **2016**. 84: p. 97-106.
64. Lv, Y., H. He, J. Qi, Y. Lu, W. Zhao, X. Dong, W. Wu, Visual validation of the measurement of entrapment efficiency of drug nanocarriers. *International journal of pharmaceutics*, **2018**. 547(1-2): p. 395-403.
65. Truong, N.P., M.R. Whittaker, C.W. Mak, T.P. Davis, The importance of nanoparticle shape in cancer drug delivery. *Expert opinion on drug delivery*, **2015**. 12(1): p. 129-142.
66. D'Souza, S., A review of in vitro drug release test methods for nano-sized dosage forms. *Advances in pharmaceutics*, **2014**. 2014(1): p. 304757.
67. Yang, S., J. Zhu, Y. Lu, B. Liang, C. Yang, Body distribution of camptothecin solid lipid nanoparticles after oral administration. *Pharmaceutical research*, **1999**. 16(5): p. 751-757.
68. Dwivedi, P., R. Kumar Tekade, N. Kumar Jain, Nanoparticulate carrier mediated intranasal delivery of insulin for the restoration of memory signaling in Alzheimer's disease. *Current Nanoscience*, **2013**. 9(1): p. 46-55.
69. Zhang, Z.-H., Y.-L. Zhang, J.-P. Zhou, H.-X. Lv, Solid lipid nanoparticles modified with stearic acid–octaarginine for oral administration of insulin. *International journal of nanomedicine*, **2012**: p. 3333-3339.
70. Arranja, A., L.F. Gouveia, P. Gener, D.F. Rafael, C. Pereira, S. Schwartz Jr, M.A. Videira, Self-assembly PEGylation assists SLN-paclitaxel delivery inducing cancer cell apoptosis upon internalization. *International journal of pharmaceutics*, **2016**. 501(1-2): p. 180-189.
71. Souto, E.B., R. Müller, Cosmetic features and applications of lipid nanoparticles (SLN®, NLC®). *International journal of cosmetic science*, **2008**. 30(3): p. 157-165.

72. Satyanarayana, S.D., A.S. Abu Lila, A. Moin, E.H. Moglad, E.-S. Khafagy, H.F. Alotaibi, A.J. Obaidullah, R.N. Charyulu, Ocular Delivery of Bimatoprost-Loaded Solid Lipid Nanoparticles for Effective Management of Glaucoma. *Pharmaceuticals*, **2023**. 16(7): p. 1001.
73. Parra-Sánchez, Á., G. Martínez-Navarrete, G. Accomasso, G. Chindamo, D. Chirio, E. Peira, S. Sapino, A. Bernabeu-Zornoza, A. Gombau-García, M. Gallarate, A novel bevacizumab delivery system using solid lipid nanoparticles for potential wet age-related macular degeneration treatment: An in vivo study. *International Journal of Pharmaceutics*, **2025**. 673: p. 125379.
74. Mohamed, R.A., H.A. Abass, M.A. Attia, O.A. Heikal, Formulation and evaluation of metoclopramide solid lipid nanoparticles for rectal suppository. *J Pharm Pharmacol*, **2013**. 65(11): p. 1607-21.
75. Severino, P., E.F. Silveira, K. Loureiro, M.V. Chaud, D. Antonini, M. Lancellotti, V.H. Sarmento, C.F. da Silva, M.H.A. Santana, E.B. Souto, Antimicrobial activity of polymyxin-loaded solid lipid nanoparticles (PLX-SLN): Characterization of physicochemical properties and in vitro efficacy. *European Journal of Pharmaceutical Sciences*, **2017**. 106: p. 177-184.
76. Arana, L., L. Gallego, I. Alkorta, Incorporation of antibiotics into solid lipid nanoparticles: a promising approach to reduce antibiotic resistance emergence. *Nanomaterials*, **2021**. 11(5): p. 1251.
77. Hosseini, S.M., R. Abbasalipourkabir, F.A. Jalilian, S.S. Asl, A. Farmany, G. Roshanaei, M.R. Arabestani, Doxycycline-encapsulated solid lipid nanoparticles as promising tool against Brucella melitensis enclosed in macrophage: a pharmacodynamics study on J774A. 1 cell line. *Antimicrobial Resistance & infection control*, **2019**. 8(1): p. 62.
78. Bazzaz, B.S.F., B. Khameneh, H. Zarei, S. Golmohammadzadeh, Antibacterial efficacy of rifampin loaded solid lipid nanoparticles against Staphylococcus epidermidis biofilm. *Microbial pathogenesis*, **2016**. 93: p. 137-144.
79. Satapathy, M.K., T.-L. Yen, J.-S. Jan, R.-D. Tang, J.-Y. Wang, R. Taliyan, C.-H. Yang, Solid Lipid Nanoparticles (SLNs): An Advanced Drug Delivery System Targeting Brain through BBB. *Pharmaceutics*, **2021**. 13(8): p. 1183.
80. Kakkar, V., I.P. Kaur, Evaluating potential of curcumin loaded solid lipid nanoparticles in aluminium induced behavioural, biochemical and histopathological alterations in mice brain. *Food and chemical toxicology*, **2011**. 49(11): p. 2906-2913.

81. Esposito, E., M. Fantin, M. Marti, M. Drechsler, L. Paccamiccio, P. Mariani, E. Sivieri, F. Lain, E. Menegatti, M. Morari, R. Cortesi, Solid lipid nanoparticles as delivery systems for bromocriptine. *Pharm Res*, **2008**. 25(7): p. 1521-30.
82. Sandhir, R., A. Yadav, A. Mehrotra, A. Sunkaria, A. Singh, S. Sharma, Curcumin nanoparticles attenuate neurochemical and neurobehavioural deficits in experimental model of Huntington's disease. *Neuromolecular Med*, **2014**. 16(1): p. 106-18.
83. Ghasemiyeh, P., S. Mohammadi-Samani, Solid lipid nanoparticles and nanostructured lipid carriers as novel drug delivery systems: applications, advantages and disadvantages. *Research in pharmaceutical sciences*, **2018**. 13(4): p. 288-303.
84. Li, R., J.S. Eun, M.K. Lee, Pharmacokinetics and biodistribution of paclitaxel loaded in pegylated solid lipid nanoparticles after intravenous administration. *Arch Pharm Res*, **2011**. 34(2): p. 331-7.
85. Kang, K.W., M.-K. Chun, O. Kim, R.K. Subedi, S.-G. Ahn, J.-H. Yoon, H.-K. Choi, Doxorubicin-loaded solid lipid nanoparticles to overcome multidrug resistance in cancer therapy. *Nanomedicine: Nanotechnology, Biology and Medicine*, **2010**. 6(2): p. 210-213.
86. Wang, J., R. Zhu, X. Sun, Y. Zhu, H. Liu, S.-L. Wang, Intracellular uptake of etoposide-loaded solid lipid nanoparticles induces an enhancing inhibitory effect on gastric cancer through mitochondria-mediated apoptosis pathway. *International journal of nanomedicine*, **2014**: p. 3987-3998.
87. Aldawsari, H.M., S. Singh, Rapid Microwave-Assisted Cisplatin-Loaded Solid Lipid Nanoparticles: Synthesis, Characterization and Anticancer Study. *Nanomaterials*, **2020**. 10(3): p. 510.
88. de Garibay, A., M. Solinís, A. del Pozo-Rodríguez, P. Apaolaza, J. Shen, A. Rodríguez-Gascón, Solid lipid nanoparticles as non-viral vectors for gene transfection in a cell model of fabry disease. *Journal of Biomedical Nanotechnology*, **2015**. 11(3): p. 500-511.
89. Botto, C., G. Augello, E. Amore, M.R. Emma, A. Azzolina, G. Cavallaro, M. Cervello, M.L. Bondì, Cationic solid lipid nanoparticles as non viral vectors for the inhibition of hepatocellular carcinoma growth by RNA interference. *Journal of biomedical nanotechnology*, **2018**. 14(5): p. 1009-1016.
90. Penumarthi, A., D. Parashar, A.N. Abraham, C. Dekiwadia, I. Macreadie, R. Shukla, P.M. Smooker, Solid lipid nanoparticles mediate non-viral delivery of plasmid DNA to dendritic cells. *Journal of Nanoparticle Research*, **2017**. 19(6): p. 210.

91. Yuan, H., S.-P. Jiang, Y.-Z. Du, J. Miao, X.-G. Zhang, F.-Q. Hu, Strategic approaches for improving entrapment of hydrophilic peptide drugs by lipid nanoparticles. *Colloids and surfaces B: Biointerfaces*, **2009**. 70(2): p. 248-253.
92. Battaglia, L., M. Gallarate, E. Peira, D. Chirio, I. Solazzi, S.M.A. Giordano, C.L. Gigliotti, C. Riganti, C. Dianzani, Bevacizumab loaded solid lipid nanoparticles prepared by the coacervation technique: preliminary in vitro studies. *Nanotechnology*, **2015**. 26(25): p. 255102.
93. Ozgenc, E., M. Karpuz, E. Arzuk, M. Gonzalez-Alvarez, M.B. Sanz, E. Gundogdu, I. Gonzalez-Alvarez, Radiolabeled Trastuzumab Solid Lipid Nanoparticles for Breast Cancer Cell: in Vitro and in Vivo Studies. *ACS Omega*, **2022**. 7(34): p. 30015-30027.
94. Nag, O.K., J.B. Delehanty, Active Cellular and Subcellular Targeting of Nanoparticles for Drug Delivery. *Pharmaceutics*, **2019**. 11(10): p. 543.
95. Shilpi, S., V.D. Vimal, V. Soni, Assessment of lactoferrin-conjugated solid lipid nanoparticles for efficient targeting to the lung. *Progress in biomaterials*, **2015**. 4(1): p. 55-63.
96. Dal Magro, R., F. Ornaghi, I. Cambianica, S. Beretta, F. Re, C. Musicanti, R. Rigolio, E. Donzelli, A. Canta, E. Ballarini, ApoE-modified solid lipid nanoparticles: A feasible strategy to cross the blood-brain barrier. *Journal of Controlled Release*, **2017**. 249: p. 103-110.
97. Maretti, E., L. Costantino, F. Buttini, C. Rustichelli, E. Leo, E. Truzzi, V. Iannuccelli, Newly synthesized surfactants for surface mannosylation of respirable SLN assemblies to target macrophages in tuberculosis therapy. *Drug delivery and translational research*, **2019**. 9(1): p. 298-310.
98. Jain, A., S.K. Mishra, P.R. Vuddanda, S.K. Singh, R. Singh, S. Singh, Targeting of diacerein loaded lipid nanoparticles to intra-articular cartilage using chondroitin sulfate as homing carrier for treatment of osteoarthritis in rats. *Nanomedicine: Nanotechnology, Biology and Medicine*, **2014**. 10(5): p. e1031-e1040.
99. Menon, I., Zaroudi, M., Zhang, Y., Aisenbrey, E., & Hui, L. Fabrication of active targeting lipid nanoparticles: Challenges and perspectives, **2022**. *Materials Today Advances*, *16*, 100299.

Chapter 2.
Embracing New and Advanced Approaches for SLNs Production and Applications

2.1. From Classical Techniques to Microfluidics: Addressing the Limitations of Conventional SLNs Production

In the first chapter, the fundamental concepts, key features, and major advantages of SLNs were discussed, providing the scientific basis for their use as advanced drug delivery systems. Since their introduction in the mid-1990s, decades of research have consolidated the physicochemical principles, preparation strategies, and therapeutic potential of SLNs across multiple administration routes, establishing them as a well-recognized nanocarrier platform within pharmaceutical nanotechnology.

Despite this extensive development, the practical implementation of SLNs still relies predominantly on classical preparation techniques, such as high-pressure homogenization, solvent-based methods, and microemulsions. Although these approaches have enabled the formulation of a wide range of SLN systems, they are often associated with intrinsic limitations, including suboptimal control over particle size and polydispersity, batch-to-batch variability, solvent-related concerns, and limited reproducibility [1]. High-pressure homogenization, for instance, may lead to polydisperse particle populations due to non-uniform shear forces, while solvent-based techniques raise concerns related to residual organic solvents in the final product. Similarly, microemulsion-based methods, despite their scalability, may suffer from lipid crystallization during storage, which can promote drug expulsion and reduce encapsulation efficiency. Overall, inadequate control over particle size and morphology remains a major weakness of conventional SLN preparation procedures, with direct implications for drug distribution, therapeutic efficacy, and formulation reliability [2]. Most notably, the intrinsic difficulty in scaling up these methods represents a critical barrier to the broader industrial translation of SLNs. These challenges collectively underscore the need for enhanced manufacturing strategies that can improve scalability, uniformity, and standardization in SLN production [3, 4].

In this context, microfluidic technology has emerged as a groundbreaking and promising alternative for the fabrication of nanocarriers, including SLNs [5]. By precisely regulating fluid dynamics and mixing conditions within microscale channels, microfluidic platforms enable the production of nanoparticles with highly uniform and tunable sizes, improved reproducibility, and enhanced encapsulation efficiencies compared with conventional

techniques [6-9]. Beyond these performance benefits, microfluidics also reduces reagent consumption and solvent use, as the confined microenvironment requires only minimal volumes, leading to lower waste generation and more sustainable, cost-effective formulation processes [10, 11]. Recent studies have demonstrated the versatility of MFT in producing SLNs encapsulating peptides, proteins, enzymes, and chemotherapeutics, achieving higher loading efficiencies, improved stability, and enhanced biological performance when compared to classical approaches. Anderluzzi *et al.* developed tristearine-based SLNs for the delivery of ovalbumin, using a benchtop NanoAssemblr^{TM} instrument [12]. More specialised formulations have also been reported, including iRGD-functionalized paclitaxel-loaded SLNs for tumour targeting, manufactured through 3D-printed microfluidic chips [13]. Sommonte *et al*. developed lysozyme-loaded SLNs using a 3D-printed microfluidic device as well, demonstrating efficient encapsulation of a biologic enzyme while preserving its structural stability and activity [14]. Taken together, these studies consistently highlight the ability of microfluidic platforms to produce SLN formulations with suitable physicochemical features. However, given that the application of microfluidics to SLN fabrication has only recently emerged, the number of available studies remains limited, and further investigations are needed to establish its robustness, scalability, and translational potential fully.

Fundamentals of microfluidic technique

Microfluidics exploits the unique behaviour of fluids at the microscale to achieve precise control over chemical processes and material fabrication. These systems handle extremely small volumes (10^{-9} to 10^{-18} L) and create environments dominated by enhanced surface effects and rapid mass and heat transfer, by confining reactions within microchannels, usually tens to hundreds of micrometers in size [15-17]. A defining characteristic of microfluidic operation is the predominance of laminar flow, resulting from the low Reynolds numbers at this scale. Fluids move in parallel layers with minimal turbulence, and mixing occurs primarily through molecular diffusion, enabling highly controlled and predictable interactions between reagent streams [18]. The high surface-to-volume ratio further influences wetting, contact angles, and overall fluid dynamics, which are critical for device performance [19]. Cooperatively, these features enable the precise regulation of mixing rates, reaction times, and temperature, making microfluidics an ideal platform

for the production of precise nanocarriers [20, 21]. Through the accurate regulation of flow rates and channel architectures, microfluidic systems can generate nanoparticles with highly uniform sizes and low polydispersity, ensuring excellent reproducibility, an essential requirement for clinical translation and regulatory compliance. Furthermore, microfluidics reduces energy and solvent consumption, contributing to more environmentally and economically sustainable manufacturing processes [22, 23].

Preparation of SLNs using microfluidic techniques

The microfluidic preparation of drug-loaded SLNs is based on the controlled mixing of two distinct solutions: an organic phase containing the molten lipid dissolved in a water-miscible solvent, and an aqueous phase containing a stabilizing surfactant. These solutions are introduced into a microfluidic mixer via high-precision pumps, where they meet under laminar flow conditions.

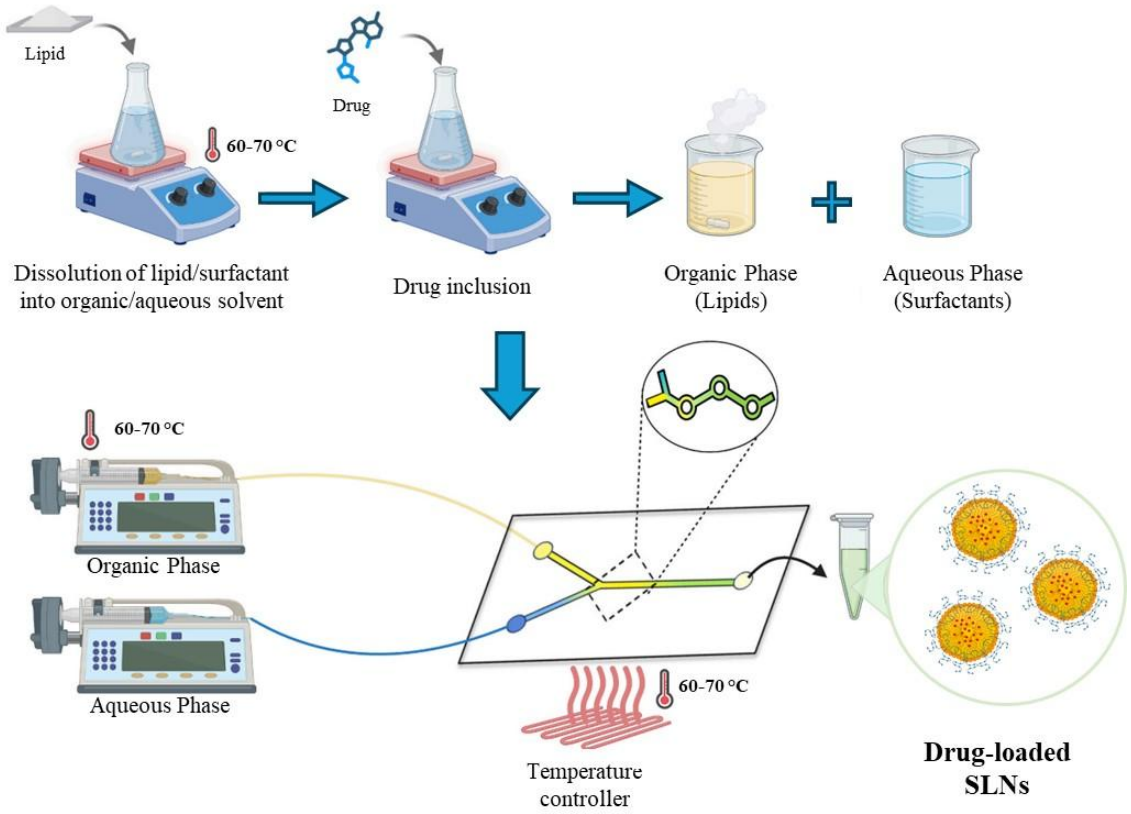


Figure 7. Set up for the preparation of SLNs via microfluidic systems. The microfluidic mixing chip is heated to maintain temperature during SLNs production [24].

Rapid diffusion of the solvent into the aqueous stream induces supersaturation, triggering the co-precipitation and self-assembly of the lipid into SLNs. After formation, the crude

dispersion containing residual solvent and unencapsulated drug is collected for purification and downstream characterization.

Temperature regulation during mixing is essential to maintain the lipid in a molten state for uniform mixing, particularly when using solid lipids that require melting for proper dissolution and homogeneous mixing with the aqueous phase. In continuous-flow microfluidic systems, both the organic and aqueous streams are typically maintained at elevated and constant temperatures (over the temperature of solid lipid fusion) to prevent premature lipid solidification and ensure stable, uninterrupted processing throughout the device, as shown in **Figure 1**.

Key parameters in microfluidic SLNs production

The preparation of SLNs by MFT depends on several interdependent parameters that must be accurately controlled to tailor the final nanoparticle properties, as summarized in **Figure 2**.

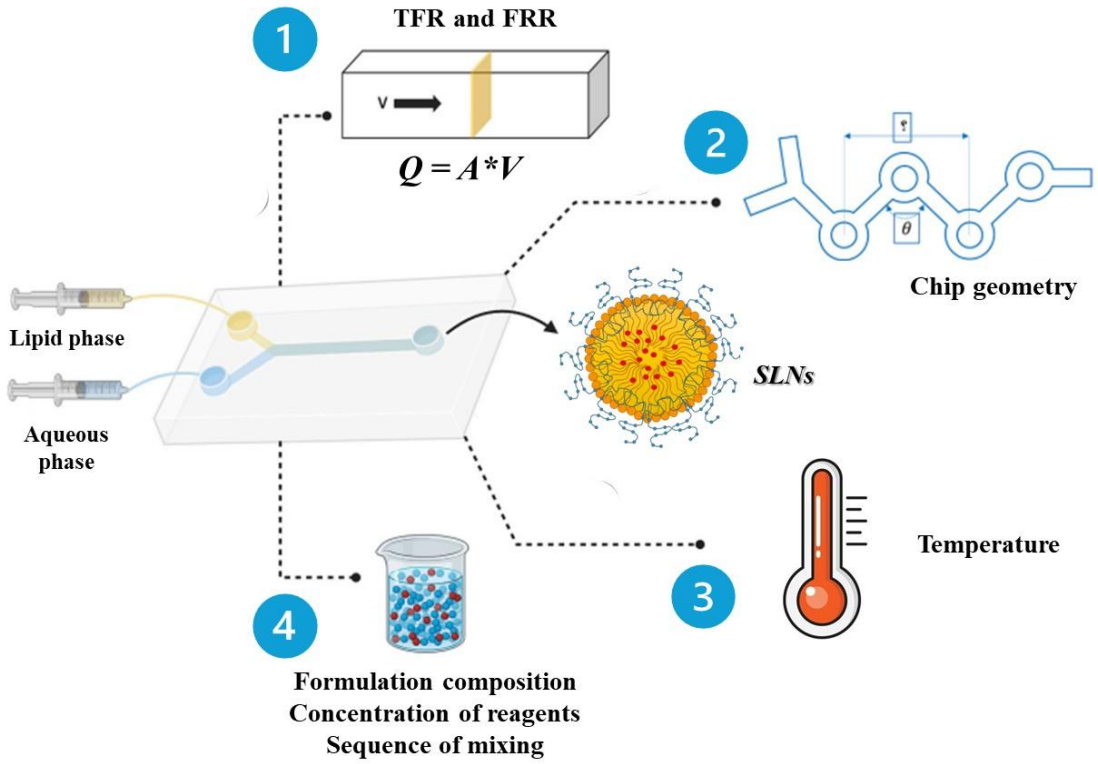


Figure 8. Key parameters in SLNs preparation through microfluidics.

Among these, flow conditions play a central role: in microfluidic devices, fluid behaviour is regulated by the volumetric flow rate (Q), defined by external pumping and the microchannel cross-sectional area (A), where $Q = A \times V$. Two derived parameters, the

total flow rate (TFR) and the flow rate ratio (FRR), are particularly important, as they determine mixing efficiency, residence time, and the degree of supersaturation during nanoprecipitation. Both govern nucleation and growth processes, enabling the fine-tuning of SLN characteristics [25, 26]. Higher TFRs can promote rapid mixing but reduce residence time, whereas the FRR governs solvent-antisolvent interactions and directly influences nucleation and growth, ultimately determining nanoparticle size [7, 27]. Device geometry is another critical parameter. Features such as channel dimensions, junction design, and integrated mixing structures modulate fluid dynamics and enhance chaotic advection, improving mixing efficiency and ensuring uniform particle formation with low polydispersity [28]. Temperature and pressure within the device also affect final formulation features: temperature determines lipid solubility and reaction kinetics, while pressure regulates flow behaviour, with higher pressures often producing smaller nanoparticles due to faster mixing and reduced aggregation time [29].

Formulation-related factors, like lipid or polymer concentration, drug payload, and the sequence of phase introduction, further influence the physicochemical properties of the resulting SLNs, as these parameters affect supersaturation, self-assembly, and encapsulation efficiency [30]. Collectively, these parameters, flow dynamics, device architecture, temperature, pressure, and formulation composition, must be simultaneously optimized to achieve predictable and reproducible microfluidic production of SLNs.

Materials and fabrication methods of microfluidic chips

Materials used for microfluidic chip fabrication critically influence fluid behaviour at the microscale and, consequently, the properties of the resulting nanomaterials. Interactions between channel surfaces and flowing solutions can affect drug concentration, mixing efficiency, and final SLN characteristics, especially during continuous processing [31]. Microfluidic devices can be fabricated from several materials, selected based on durability, chemical resistance, transparency, biocompatibility, and suitability for surface modification. Common materials include poly(dimethylsiloxane) (PDMS), appreciated for its low cost and ease of fabrication but limited by hydrophobicity, absorption of lipids and drugs, and swelling in organic solvents [32]; glass, which offers excellent chemical inertness, hydrophilicity, and resistance to solvents, temperature, and pressure [33]; thermoplastics such as polymethyl methacrylate (PMMA), polycarbonate, polylactic acid

(PLA), polyvinyl chloride (PVC), and cyclic olefin copolymer (COC) offering good mechanical stability and biocompatibility; and stainless steel, widely employed in industrial pharmaceutical equipment due to its outstanding solvent and thermal resistance, making it ideal for high-pressure or continuous-flow reactors [34].

These materials can be shaped into microfluidic devices using a variety of fabrication techniques, including hot embossing, injection molding, and micromilling for thermoplastics, photolithography and soft lithography for PDMS and glass-based devices, and laser ablation, wet etching, or dry etching for precise patterning of glass and silicon substrates [35-37]. Additive manufacturing (3D printing) has recently emerged as a powerful and flexible alternative, allowing rapid prototyping of complex three-dimensional channel architectures at low cost, as demonstrated in recent SLN studies employing 3D-printed microfluidic devices [38].

Microfluidic mixer design

As already introduced, the design of the microfluidic mixer is a critical determinant in SLN formation, as the channel geometry and mixing strategy directly govern solvent-antisolvent interactions, nucleation kinetics, and the resulting nanoparticle attributes. Over the years, several mixer configurations have been developed to enhance control over diffusion, shear, and chaotic advection within microchannels, each offering distinct advantages in terms of mixing efficiency. The most widely used microfluidic mixer designs for SLN production, their diversity and functional relevance are summarized below, and represented in **Figure 3**.

Hydrodynamic Flow Focusing (HFF)

Uses a central organic lipid stream, focused by two lateral aqueous streams. Mixing occurs by diffusion at the compressed interface, enabling precise control of nucleation and particle size [39].

Staggered Herringbone Micromixers (SHM)

Incorporate asymmetric V-shaped grooves on the channel floor or ceiling to generate chaotic advection. This geometry enhances transverse mixing and rapidly increases interfacial area [40].

T- and Y-junction Mixers

Simple passive mixers in which the organic and aqueous streams meet at a T- or Y-shaped intersection. Mixing occurs primarily by diffusion under laminar flow, although higher Reynolds numbers can introduce mild turbulence [41].

Baffle and Bifurcating Mixers

Use internal structures such as obstacles, baffles, or repeated channel splits to enhance mixing by altering flow patterns and increasing contact between phases. These designs improve nanoprecipitation efficiency and enable better control of particle size and encapsulation by promoting repeated stretching and folding of fluid streams [42].

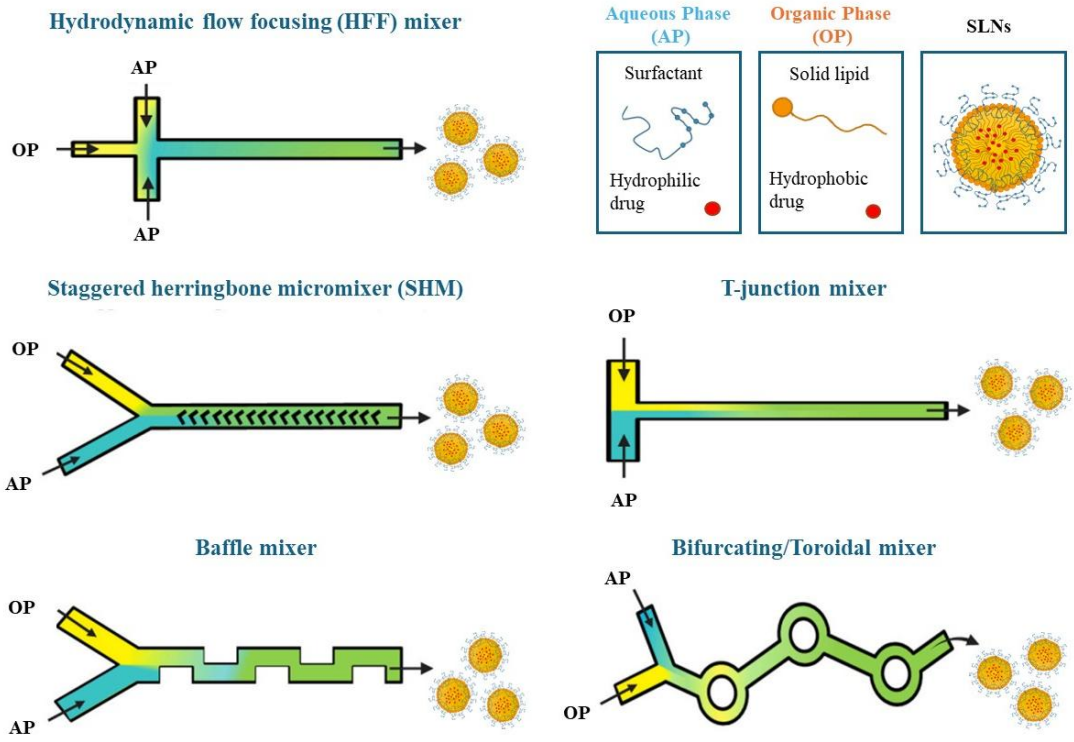


Figure 9. Representative microfluidic mixer channel geometries for nanocarrier preparation.

Post-production purification

During microfluidic production, formulations contain significant amounts of organic solvent, such as ethanol, which must be removed to meet safety requirements and ensure nanoparticle stability. Ultracentrifugal filters, dialysis, spin-column purification, and tangential flow filtration (TFF) are the main purification strategies employed. Anderluzzi *et al*. performed a comprehensive study comparing dialysis, spin-column purification, and

TFF. All three methods proved effective in reducing ethanol content to below 1%, with both dialysis and TFF achieving residual levels below 0.5%, in line with ICH guidelines for Class 3 solvents. However, the efficiency of nanoparticle recovery varied considerably among the techniques: spin columns and dialysis preserved almost the entire SLNs yield, whereas TFF resulted in lower recovery, likely due to particle losses during filtration. Despite this drawback, TFF offers important advantages in terms of scalability, processing speed, and robustness, making it a viable option for larger-scale or continuous manufacturing. [12].

Comparative performance: microfluidic vs. conventional SLNs

A critical measure of success for any drug delivery platform is its performance in a biological context. While direct head-to-head *in vivo* studies comparing the pharmacokinetics and biodistribution of SLNs prepared by microfluidic versus bulk methods are still an emerging area of research, a growing body of evidence from *in vitro* and comparative formulation studies strongly suggests the superiority of the microfluidic approach. The enhanced control over nanoparticle physicochemical properties afforded by microfluidics directly translates to improved biological performance. The preparation method of SLNs, whether bulk or microfluidic, plays a pivotal role in determining SLNs' physicochemical properties, such as size, PDI, encapsulation efficiency, and surface characteristics. These attributes, in turn, influence pharmacokinetics, biodistribution, and therapeutic efficacy. **Table 1** contrasts the key performance characteristics of SLNs prepared using microfluidic platforms versus conventional bulk methods.

Table 1. Comparative analysis of key performance indicators for SLNs prepared by microfluidic vs. conventional method [24].

Performance parameter	Microfluidic production	Conventional production
Particle size and PDI	Highly uniform size (often around 100-200 nm) and low PDI (typically)	Larger size, higher PDI (>0.3), broader distribution, and inadequate control over final size. Example: LZ SLNs: 180.21 ± 7.46 nm
Morphology	Uniform spherical or turtle-like structures (e.g., solid core spherical; peculiar turtle-like surface in lysozyme SLNs via cryoEM)	Irregular and not extremely spherical morphology, structure consists of denser lipidic concentric lamellae with a diffuse core
Encapsulation efficiency	Higher encapsulation efficiency due to uniform and rapid mixing, ensuring optimal drug incorporation. Examples: PTX-SLN: 54 ± 3 % SFN-SLN: 79 ± 1 % Cur-SLNs: over 60 %	Often low and variable, example: PTX-SLN: 42 ± 1.5 % SFN-SLN: 65 ± 2.4 %. Cur-SLNs: ~40 %

Drug release profile	Tunable and sustained release profiles, often with an initial burst effect followed by prolonged release, and release can be triggered by enzymes (e.g., lipase). Examples: PTX-SLNs: 10 % in 6 h (without lipase), 100 % in 72 h (with lipase), BDNF-SLNs: 20 % in the first 4 h (without lipase), steady within 72 h, DZX-SLNs: 97.3 % released within 96 h in the presence of human serum, OVA-loaded SLNs: up to 90 % released within the first 24 h (rapid release	Conventional prepared SLNs showed no drug release for PTX and SFN in 120 h when tested without human serum
Cytotoxicity and biocompatibility	High biocompatibility: empty SLNs show >80 % cell viability at high concentrations and are non-hemolytic (<5 % at appropriate dilutions), Exenatide-loaded SLNs maintained over 85 % cell viability up to 20 μg/mL of exenatide.	Methods like microemulsion require high surfactant levels, raising potential toxicity concerns
Cellular uptake	Uniform particles enable effective surface functionalization for targeted uptake (e.g., with iRGD peptide), SLNs (especially with sizes between 120 and 200 nm) can bypass the reticuloendothelial system (RES) absorption, extending circulation time and improving delivery to target sites	Lower due to size
Pharmacokinetics	More consistent due to high uniformity and excellent colloidal stability in plasma	More variable due to polydispersity and potential for aggregation in biological fluids
Therapeutic efficacy	Demonstrates enhanced cytotoxicity against cancer cells compared to free drug and shows superior anti-inflammatory effects in neuroinflammation models. Examples: iRGD-functionalized SLNs demonstrated enhanced anti-cancer activity of paclitaxel by increasing cytotoxicity and providing more efficient tumor targeting and penetration in both 2D and 3D tumor models, BDNF-SLNs showed an enhanced decrease in nitrite production and NOS mRNA levels in an in vitro neuroinflammatory model (TBI-like model) compared to plain BDNF, DZX-SLNs led to a significantly greater improvement in cell viability and a discernible reduction in mitochondrial ROS production in frataxin-deficient fibroblasts	Efficacy can be compromised by lower drug loading, poor stability, and uncontrolled release

2.2. Co-/Multi-drug delivery systems

Having explored microfluidics as an innovative and highly controlled method for SLN production, attention can now shift toward another frontier in advanced drug-delivery design: co-delivery and multi-drug platforms. These systems represent an evolution of conventional nanocarriers, enabling the coordinated administration of multiple therapeutic agents through a single formulation and addressing complex pathological mechanisms more effectively.

Traditionally, combination therapy refers to the use of two or more drugs acting through different mechanisms to achieve superior therapeutic outcomes compared with monotherapy [43]. After gaining prominence in oncology, where combined regimens significantly improved clinical responses and survival, it has become a standard strategy in various pathological case, such as hypertension, dyslipidemia, infectious diseases, neurological disorders, and dermatological conditions [44-47]. Its success relies on the potential for synergistic or additive effects, enabling lower doses of each agent to be used while enhancing efficacy and reducing overall toxicity [48]. Traditional combination therapy typically involves the separate administration of individual drugs; however, limitations such as mismatched pharmacokinetics, differential biodistribution, and uncontrolled exposure have driven a shift toward co-delivery systems, in which multiple therapeutic molecules are incorporated into a single micro- or nano-drug delivery platform [49].

Therefore, researchers have progressively shifted toward co-encapsulation approaches, recognizing that integrating multiple bioactive agents into a single carrier offers substantial advantages. Co-delivery systems are particularly impactful in oncology, where monotherapies frequently fail due to poor tissue penetration, tumor heterogeneity, and the emergence of drug resistance [50]. Importantly, co-delivery technologies emerged from the convergence of drug delivery science and gene therapy, enabling the simultaneous encapsulation of agents with different physicochemical and biological properties and achieving true combination chemotherapy within a single system [51]. This strategy is particularly relevant in oncology, where monotherapy frequently fails to produce durable responses due to poor treatment penetration, tumor heterogeneity, and the rapid emergence of drug resistance [52]. In contrast, dual or multi-agent nanocarriers can deliver chemotherapeutics, gene-silencing molecules, metabolic modulators, or

immunotherapeutics in a coordinated manner, improving tumor regression and overcoming classical resistance pathways [53].

Beyond oncology, co-delivery is increasingly recognized as a versatile approach in many fields, since it can address multifactorial disease mechanisms by acting on several pathways at once [54]. Nevertheless, the development of effective co-delivery systems remains challenging: co-encapsulating multiple compounds with different solubilities, stabilities, or interaction profiles requires sophisticated carrier design and careful optimization of formulation parameters. Despite the formulation challenges associated with loading multiple compounds, such as differences in solubility, stability, and molecular interactions, co-delivery remains a rapidly expanding field. Multi-drug delivery platforms now represent a significant evolution of combination therapy, capable of harmonizing biodistribution, release kinetics, and pharmacodynamics, ultimately enabling more effective, safer, and rationally designed treatments for complex diseases. .

Co-delivery strategies in cancer therapy

In oncology, co-delivery platforms have shown particular promise in addressing the intrinsic complexity of tumor biology and the limitations of conventional combination regimens, as briefly discussed above. Several studies demonstrate that integrating multiple anticancer agents within the same nanocarrier enhances therapeutic cooperation and improves tumor targeting. For example, transferrin-modified SLNs simultaneously transporting doxorubicin and plasmid DNA achieved superior antitumor effects in A549 lung cancer models, combining chemotherapeutic cytotoxicity with gene-expression modulation and benefiting from receptor-mediated targeting to tumor cells [55]. Similarly, Yu *et al*. explored the co-delivery of paclitaxel and siRNA within cationic SLNs, demonstrating a coordinated intracellular release, efficient gene silencing, and significantly enhanced inhibition of tumor growth, highlighting the advantage of suppressing drug-resistance pathways while delivering a cytotoxic payload [56].

Co-delivery strategies in neurodegenerative treatment

In neurodegenerative diseases, co-delivery strategies have emerged as an effective way to modulate the multiple interacting pathways involved in neuronal dysfunction. As emphasized by Angelova *et al*., combining neurotrophic mediators with antioxidant or anti-inflammatory compounds enhances neuronal survival and synaptic repair by

simultaneously targeting TrkB signaling, oxidative stress, and mitochondrial damage, key drivers of disorders such as Alzheimer's, Parkinson's, and retinal degeneration [57]. Recent developments in ocular neuroprotection further illustrate the benefit of multi-drug delivery. Aragón-Navas *et al.* demonstrated that PLGA microspheres co-loaded with dexamethasone, ursodeoxycholic acid, and GDNF provided sustained, simultaneous release of anti-inflammatory, anti-apoptotic, and neurotrophic cues, ultimately improving retinal ganglion cell function and preserving neuroretinal structure in a chronic glaucoma model [58]. Similar synergistic outcomes were reported by Arranz-Romera *et al.,* where dual-delivery systems combining ketorolac and ursodeoxycholic acid achieved enhanced neuroprotection by concurrently reducing inflammation and stabilizing mitochondrial integrity in retinal tissues. Moreover, the co-incorporation of different drugs into a single microcarrier reduces the amount of PLGA required for intraocular administration compared to equivalent dosing of single drug-loaded formulations, so reducing the risk of PLGA-associated retinal stress [59]. Nassar *et al*. designed a thermosensitive hydrogel for vascular injury treatment, exploring the co-delivery of metformin and levofloxacin. This study highlighted how multi-target platforms can modulate angiogenesis, oxidative stress, and inflammation mechanisms closely intertwined with neurodegenerative processes in the eye [60].

Co-delivery strategies to overcome antimicrobial multidrug resistance

The rapid rise of antimicrobial resistance (AMR) has intensified interest in co-delivery approaches capable of simultaneously targeting bacterial viability, membrane integrity, and host inflammatory responses. As highlighted by Lyu *et al*., combining antibiotics with gene-regulatory agents offers a powerful multi-target strategy: their tetrahedral framework DNA nanoplatform co-delivering levofloxacin and miR-146 achieved potent antibacterial activity against *Staphylococcus aureus* and *Escherichia coli* while markedly suppressing NF-κB-mediated inflammation, ultimately accelerating wound closure in infected *in vivo* models [61]. A different but complementary approach is described by Güleç-Güngör *et al.*, who formulated liposomes co-loaded with azithromycin and nisin. These dual-loaded vesicles enhanced skin penetration, decreased MIC values, and achieved superior inhibition of resistant *Staphylococcus aureus* strains compared to single-drug liposomes, demonstrating that combining antibiotics with antimicrobial

peptides can reduce required doses and limit resistance development [62]. Further evidence of a synergistic benefit is provided by Ng *et al.*, who demonstrated that pairing membrane-disrupting polycarbonate polymers with conventional antibiotics, such as doxycycline, significantly reduced MICs by more than an order of magnitude against the difficult-to-treat *Pseudomonas aeruginosa* [63].

2.2.1 Trojan system

Nano-in-micro (NiM) systems, also referred to as Trojan systems, represent a multiscale drug-delivery strategy and can be considered a functional evolution of conventional co-delivery approaches. Whereas classical co-delivery embeds multiple therapeutic agents within a single nanosystem, it remains constrained by rapid clearance, limited loading capacity, and the need for physicochemical compatibility between co-encapsulated molecules. NiM architectures overcome these limitations by decoupling the roles of retention and targeting across two size domains, embedding nanoparticles within microstructures. From a technological standpoint, Trojan systems expand the design space for co-delivery strategies, enabling the combination of fast- and slow-release profiles within the same platform and allowing fine control over the burst effect according to the therapeutic needs of specific diseases or individual patients. Microscale carriers are well-suited to provide prolonged drug release following administration, while nanoscale carriers protect labile molecules from degradation, reduce premature clearance, and efficiently reach target tissues [64].

The integration of these two components has led to a new generation of hierarchical drug-delivery systems. In Trojan designs, microparticles are loaded with nanoparticles that, in turn, carry the active compound. Once administered, the microparticles gradually release the nanoparticles over extended periods, safeguarding those still entrapped from external degradation. After release, nanoparticles migrate toward the target cells, are internalized, and ultimately discharge the therapeutic payload intracellularly. This multistep process maximizes the efficacy of the administered agents by minimizing premature loss and ensuring that each component performs its function at the appropriate biological level. This sequential release mechanism has provided the foundational rationale for the design of hierarchical delivery systems. As described by Anton *et al.*, Trojan particles were originally conceived to resolve anatomical and physiological barriers, such as poor deep-

tissue diffusion or pulmonary and ocular clearance, by concentrating nanosystems at the administration site and enabling their subsequent diffusion to target cells [65]. This hierarchical concept not only preserves but extends co-delivery capabilities by enabling multi-level co-delivery. For instance, Zarubova *et al*. demonstrated that alginate microparticles can release gentamicine-loaded PLGA nanoparticles together with vascular endothelial growth factor (VEGF), thereby promoting simultaneous antibacterial activity and angiogenesis in infected wounds. These findings demonstrate how NiM platforms coordinate multiple therapeutic pathways within a single system [66]. Similarly, Reshmi *et al*. designed NiM scaffolds in which gemtamicin and vitamin B12-loaded montmorillonite nanosheets were incorporated into electrospun poly (ε-ca prolactone)-based microfibers. This hierarchical system enhances fibroblast adhesion, supports sustained and pH-responsive release (vitamin B12 and gentamicin up to 15 days), and demonstrates antibacterial activity, highlighting its potential for tissue engineering and controlled drug delivery applications [67].

NiM systems represent a particularly advanced application in ocular drug delivery, where they can solve the classical “penetration-retention paradox”: nanoparticles are small enough to traverse ocular barriers but are cleared rapidly, whereas microparticles exhibit long residence times but lack penetration capacity. As reviewed by Huang *et al*., NiM devices strategically combine these properties, enabling prolonged intraocular retention with subsequent nanoparticle migration toward retinal tissues [68]. Likewise, Bravo-Osuna *et al*. emphasize the suitability of Trojan microparticles for intravitreal delivery, where microscale carriers protect the drug and provide multi-week release, allowing the released nanoparticles to reach the retina and deliver the therapeutic payload with high precision [69].

Collectively, these studies position NiM/Trojan systems as a next-generation evolution of co-delivery: a hierarchical, programmable, and highly versatile platform that enhances drug stability, modulates spatiotemporal release, improves tissue penetration, and enables coordinated multi-pathway therapeutic interventions across various clinical contexts.

References

1. Subroto, E., R. Andoyo, R. Indiarto, Solid lipid nanoparticles: review of the current research on encapsulation and delivery systems for active and antioxidant compounds. *Antioxidants*, **2023**. 12(3): p. 633.
2. Bukke, S.P.N., C. Venkatesh, S. Bandenahalli Rajanna, T.S. Saraswathi, P.K. Kusuma, N. Goruntla, N. Balasuramanyam, S. Munishamireddy, Solid lipid nanocarriers for drug delivery: design innovations and characterization strategies—a comprehensive review. *Discover applied sciences*, **2024**. 6(6): p. 279.
3. Daneshmand, S., S. Golmohammadzadeh, M.R. Jaafari, J. Movaffagh, M. Rezaee, A. Sahebkar, B. Malaekeh-Nikouei, Encapsulation challenges, the substantial issue in solid lipid nanoparticles characterization. *Journal of cellular biochemistry*, **2018**. 119(6): p. 4251-4264.
4. Musielak, E., A. Feliczak-Guzik, I. Nowak, Optimization of the Conditions of Solid Lipid Nanoparticles (SLN) Synthesis. *Molecules*, **2022**. 27(7): p. 2202.
5. Khoshnood, A., S. Iranpour, S. Khaksari, S.A.M. Shaegh, K. Abnous, S.M. Taghdisi, Liposome/AZIF-8 Janus nanoplatforms: Promising nanocarriers for improving chemotherapeutic outcomes in breast cancer treatment. *International Journal of Pharmaceutics*, **2025**: p. 125702.
6. Bezelya, A., B. Küçüktürkmen, A. Bozkır. *Microfluidic devices for precision nanoparticle production*. in *Micro*. 2023. MDPI.
7. Osouli-Bostanabad, K., S. Puliga, D.R. Serrano, A. Bucchi, G. Halbert, A. Lalatsa, Microfluidic manufacture of lipid-based nanomedicines. *Pharmaceutics*, **2022**. 14(9): p. 1940.
8. Liu, D., S. Cito, Y. Zhang, C.F. Wang, T.M. Sikanen, H.A. Santos, A versatile and robust microfluidic platform toward high throughput synthesis of homogeneous nanoparticles with tunable properties. *Adv Mater*, **2015**. 27(14): p. 2298-304.
9. Fontana, F., M.P. Ferreira, A. Correia, J. Hirvonen, H.A. Santos, Microfluidics as a cutting-edge technique for drug delivery applications. *Journal of Drug Delivery Science and Technology*, **2016**. 34: p. 76-87.
10. Gdowski, A., K. Johnson, S. Shah, I. Gryczynski, J. Vishwanatha, A. Ranjan, Optimization and scale up of microfluidic nanolipomer production method for preclinical and potential clinical trials. *Journal of nanobiotechnology*, **2018**. 16(1): p. 12.
11. Liu, Z., F. Fontana, A. Python, J.T. Hirvonen, H.A. Santos, Microfluidics for production of particles: mechanism, methodology, and applications. *Small*, **2020**. 16(9): p. 1904673.

12. Anderluzzi, G., Y. Perrie, Microfluidic manufacture of solid lipid nanoparticles: A case study on tristearin-based systems. *Drug Delivery Letters*, **2020**. 10(3): p. 197-208.
13. Arduino, I., Z. Liu, R.M. Iacobazzi, A.A. Lopedota, A. Lopalco, A. Cutrignelli, V. Laquintana, L. Porcelli, A. Azzariti, M. Franco, H.A. Santos, N. Denora, Microfluidic preparation and in vitro evaluation of iRGD-functionalized solid lipid nanoparticles for targeted delivery of paclitaxel to tumor cells. *Int J Pharm*, **2021**. 610: p. 121246.
14. Sommonte, F., I. Arduino, R.M. Iacobazzi, M. Tiboni, F. Catalano, R. Marotta, M. Di Francesco, L. Casettari, P. Decuzzi, A.A. Lopedota, N. Denora, Microfluidic assembly of "Turtle-Like" shaped solid lipid nanoparticles for lysozyme delivery. *Int J Pharm*, **2023**. 631: p. 122479.
15. Shepherd, S.J., D. Issadore, M.J. Mitchell, Microfluidic formulation of nanoparticles for biomedical applications. *Biomaterials*, **2021**. 274: p. 120826.
16. Nguyen, N.-T., S.T. Wereley, S.A.M. Shaegh, *Fundamentals and applications of microfluidics*. 2019: Artech house.
17. Liu, Y., L. Sun, H. Zhang, L. Shang, Y. Zhao, Microfluidics for drug development: from synthesis to evaluation. *Chemical reviews*, **2021**. 121(13): p. 7468-7529.
18. Fan, J., S. Li, Z. Wu, Z. Chen, *Diffusion and mixing in microfluidic devices*, in *Microfluidics for pharmaceutical applications*. 2019, Elsevier. p. 79-100.
19. Xie, X., Y. Wang, S.-Y. Siu, C.-W. Chan, Y. Zhu, X. Zhang, J. Ge, K. Ren, Microfluidic synthesis as a new route to produce novel functional materials. *Biomicrofluidics*, **2022**. 16(4).
20. Zhang, H., J. Yang, R. Sun, S. Han, Z. Yang, L. Teng, Microfluidics for nano-drug delivery systems: from fundamentals to industrialization. *Acta Pharmaceutica Sinica B*, **2023**. 13(8): p. 3277-3299.
21. Shen, Y., H. Gwak, B. Han, Advanced manufacturing of nanoparticle formulations of drugs and biologics using microfluidics. *Analyst*, **2024**. 149(3): p. 614-637.
22. Garg, S., G. Heuck, S. Ip, E. Ramsay, Microfluidics: a transformational tool for nanomedicine development and production. *Journal of drug targeting*, **2016**. 24(9): p. 821-835.
23. Fabozzi, A., F. Della Sala, M. di Gennaro, M. Barretta, G. Longobardo, N. Solimando, M. Pagliuca, A. Borzacchiello, Design of functional nanoparticles by microfluidic platforms as advanced drug delivery systems for cancer therapy. *Lab on a Chip*, **2023**. 23(5): p. 1389-1409.

24. Javid-Naderi, M.J., S.A. Mousavi Shaegh, Advanced microfluidic techniques for the preparation of solid lipid nanoparticles: Innovations and biomedical applications. *Int J Pharm X*, **2025**. 10: p. 100399.
25. Prakash, G., A. Shokr, N. Willemen, S.M. Bashir, S.R. Shin, S. Hassan, Microfluidic fabrication of lipid nanoparticles for the delivery of nucleic acids. *Advanced drug delivery reviews*, **2022**. 184: p. 114197.
26. Jaradat, E., E. Weaver, A. Meziane, D.A. Lamprou, Microfluidics Technology for the Design and Formulation of Nanomedicines. *Nanomaterials*, **2021**. 11(12): p. 3440.
27. Mudugamuwa, A., U. Roshan, S. Hettiarachchi, H. Cha, H. Musharaf, X. Kang, Q.T. Trinh, H.M. Xia, N.T. Nguyen, J. Zhang, Periodic Flows in Microfluidics. *Small*, **2024**. 20(50): p. e2404685.
28. Liu, Y., G. Yang, Y. Hui, S. Ranaweera, C.X. Zhao, Microfluidic nanoparticles for drug delivery. *Small*, **2022**. 18(36): p. 2106580.
29. Maeki, M., Y. Fujishima, Y. Sato, T. Yasui, N. Kaji, A. Ishida, H. Tani, Y. Baba, H. Harashima, M. Tokeshi, Understanding the formation mechanism of lipid nanoparticles in microfluidic devices with chaotic micromixers. *PLoS One*, **2017**. 12(11): p. e0187962.
30. Vogelaar, A., S. Marcotte, J. Cheng, B. Oluoch, J. Zaro, Use of Microfluidics to Prepare Lipid-Based Nanocarriers. *Pharmaceutics*, **2023**. 15(4): p. 1053.
31. Gimondi, S., H. Ferreira, R.L. Reis, N.M. Neves, Microfluidic devices: a tool for nanoparticle synthesis and performance evaluation. *ACS nano*, **2023**. 17(15): p. 14205-14228.
32. Dangla, R., F. Gallaire, C.N. Baroud, Microchannel deformations due to solvent-induced PDMS swelling. *Lab on a Chip*, **2010**. 10(21): p. 2972-2978.
33. Aralekallu, S., R. Boddula, V. Singh, Development of glass-based microfluidic devices: A review on its fabrication and biologic applications. *Materials & Design*, **2023**. 225: p. 111517.
34. Banejad, A., M. Passandideh-Fard, H. Niknam, M.J.M. Hosseini, S.A.M. Shaegh, Design, fabrication and experimental characterization of whole-thermoplastic microvalves and micropumps having micromilled liquid channels of rectangular and half-elliptical cross-sections. *Sensors and Actuators A: Physical*, **2020**. 301: p. 111713.
35. Alghannam, F., M. Alayed, S. Alfihed, M.A. Sakr, D. Almutairi, N. Alshamrani, N. Al Fayez, Recent Progress in PDMS-Based Microfluidics Toward Integrated Organ-on-a-Chip Biosensors and Personalized Medicine. *Biosensors*, **2025**. 15(2): p. 76.

36. Aldaghestani, Y., R. Homsi, A. Alazzam, A. Schiffer, 3D printed microfluidic devices for nanoparticle fabrication: a review. *Progress in Additive Manufacturing*, **2025**: p. 1-20.
37. Konstantinova, T., M. Andronic, D. Baklykov, V. Stukalova, D. Ezenkova, E. Zikiy, M. Bashinova, A. Solovev, E. Lotkov, I. Ryzhikov, Deep multilevel wet etching of fused silica glass microstructures in BOE solution. *Scientific Reports*, **2023**. 13(1): p. 5228.
38. Tiboni, M., M. Tiboni, A. Pierro, M. Del Papa, S. Sparaventi, M. Cespi, L. Casettari, Microfluidics for nanomedicines manufacturing: An affordable and low-cost 3D printing approach. *Int J Pharm*, **2021**. 599: p. 120464.
39. Lu, M., A. Ozcelik, C.L. Grigsby, Y. Zhao, F. Guo, K.W. Leong, T.J. Huang, Microfluidic Hydrodynamic Focusing for Synthesis of Nanomaterials. *Nano Today*, **2016**. 11(6): p. 778-792.
40. Cheung, C.C.L., W.T. Al-Jamal, Sterically stabilized liposomes production using staggered herringbone micromixer: Effect of lipid composition and PEG-lipid content. *Int J Pharm*, **2019**. 566: p. 687-696.
41. Chen, D., Z. Liu, L. Guo, L. Yang, Y. Zhao, M. Yang, Controlled preparation of lipid nanoparticles in microreactors: Mixing time, morphology and mRNA delivery. *Chemical Engineering Journal*, **2025**. 505: p. 159318.
42. Gamage, S.S., T. Huang, N. O'Brien-Simpson, D.E. Heath, A.J. O'Connor, Microfluidics enables rapid and facile fabrication of multi-component antimicrobial nanoparticles. *Chemical Engineering Journal*, **2025**. 520: p. 165807.
43. Ataide, J.A., J.C. Coco, M. Dos Santos É, V. Beraldo-Araujo, J.R.A. Silva, K.C. de Castro, A.M. Lopes, N. Filipczak, S.S.K. Yalamarty, V.P. Torchilin, P.G. Mazzola, Co-Encapsulation of Drugs for Topical Application-A Review. *Molecules*, **2023**. 28(3).
44. Smith, D.K., R.P. Lennon, P.B. Carlsgaard, Managing Hypertension Using Combination Therapy. *Am Fam Physician*, **2020**. 101(6): p. 341-349.
45. Goldberg, A.C., Combination therapy of dyslipidemia. *Current Treatment Options in Cardiovascular Medicine*, **2007**. 9(4): p. 249-258.
46. van Griensven, J., M. Boelaert, Combination therapy for visceral leishmaniasis. *The Lancet*, **2011**. 377(9764): p. 443-444.
47. Conway, D., J.A. Cohen, Combination therapy in multiple sclerosis. *The Lancet Neurology*, **2010**. 9(3): p. 299-308.
48. Kim, M.R., T. Feng, Q. Zhang, H.Y.E. Chan, Y. Chau, Co-encapsulation and co-delivery of peptide drugs via polymeric nanoparticles. *Polymers*, **2019**. 11(2): p. 288.

49. Tundisi, L.L., J.A. Ataide, J.S.R. Costa, D. de Freitas Coêlho, R.B. Liszbinski, A.M. Lopes, L. Oliveira-Nascimento, M.B. de Jesus, A.F. Jozala, C. Ehrhardt, Nanotechnology as a tool to overcome macromolecules delivery issues. *Colloids and Surfaces B: Biointerfaces*, **2023**. 222: p. 113043.
50. Handali, S., E. Moghimipour, M. Rezaei, Z. Ramezani, M. Kouchak, M. Amini, K.A. Angali, S. Saremy, F.A. Dorkoosh, A novel 5-Fluorouracil targeted delivery to colon cancer using folic acid conjugated liposomes. *Biomed Pharmacother*, **2018**. 108: p. 1259-1273.
51. Cervantes, A., M. Alsina, J. Tabernero, J. Infante, P. LoRusso, G. Shapiro, L. Paz-Ares, R. Falzone, J. Hill, J. Cehelsky, Phase I dose-escalation study of ALN-VSP02, a novel RNAi therapeutic for solid tumors with liver involvement. *Journal of Clinical Oncology*, **2011**. 29(15_suppl): p. 3025-3025.
52. Gong, J., T. Shi, J. Liu, Z. Pei, J. Liu, X. Ren, F. Li, F. Qiu, Dual-drug codelivery nanosystems: An emerging approach for overcoming cancer multidrug resistance. *Biomedicine & pharmacotherapy*, **2023**. 161: p. 114505.
53. Wu, J., H. Zhang, X. Hu, R. Liu, W. Jiang, Z. Li, Y. Luan, Reduction-sensitive mixed micelles assembled from amphiphilic prodrugs for self-codelivery of DOX and DTX with synergistic cancer therapy. *Colloids and Surfaces B: Biointerfaces*, **2018**. 161: p. 449-456.
54. Gong, C.-X., F. Liu, K. Iqbal, Multifactorial hypothesis and multi-targets for Alzheimer's disease. *Journal of Alzheimer's Disease*, **2018**. 64(s1): p. S107-S117.
55. Han, Y., P. Zhang, Y. Chen, J. Sun, F. Kong, Co-delivery of plasmid DNA and doxorubicin by solid lipid nanoparticles for lung cancer therapy. *Int J Mol Med*, **2014**. 34(1): p. 191-6.
56. Yu, Y.H., E. Kim, D.E. Park, G. Shim, S. Lee, Y.B. Kim, C.W. Kim, Y.K. Oh, Cationic solid lipid nanoparticles for co-delivery of paclitaxel and siRNA. *Eur J Pharm Biopharm*, **2012**. 80(2): p. 268-73.
57. Angelova, A., B. Angelov, Dual and multi-drug delivery nanoparticles towards neuronal survival and synaptic repair. *Neural regeneration research*, **2017**. 12(6): p. 886-889.
58. Aragón-Navas, A., M.J. Rodrigo, I. Munuera, D. Garcia-Herranz, M. Subías, P. Villacampa, J. García-Feijoo, L. Pablo, E. Garcia-Martin, R. Herrero-Vanrell, Multi-loaded PLGA microspheres as neuroretinal therapy in a chronic glaucoma animal model. *Drug Delivery and Translational Research*, **2025**. 15(5): p. 1660-1684.

59. Arranz-Romera, A., S. Esteban-Pérez, D. Garcia-Herranz, A. Aragón-Navas, I. Bravo-Osuna, R. Herrero-Vanrell, Combination therapy and co-delivery strategies to optimize treatment of posterior segment neurodegenerative diseases. *Drug discovery today*, **2019**. 24(8): p. 1644-1653.
60. Liu, D., Q. Wu, Y. Zhu, Y. Liu, X. Xie, S. Li, H. Lin, W. Chen, F. Zhu, Co-delivery of metformin and levofloxacin hydrochloride using biodegradable thermosensitive hydrogel for the treatment of corneal neovascularization. *Drug Delivery*, **2019**. 26(1): p. 522-531.
61. Lyu, X., H. Wu, Y. Chen, Y. Sun, X. Cai, S. Li, Y. Lin, A Multifunctional Nanocomplex as miRNA/Antibiotic Co-Delivery System Based on Tetrahedral Framework DNA: Application to Infected Wound Healing. *Small*, **2024**. 20(49): p. 2406629.
62. Gelen-Gungor, D., Ş. Nigiz, C. Özkul, H. Eroğlu, E. Nemutlu, K. Ulubayram, Y. Mao, B. Michniak-Kohn, İ. Eroğlu, Co-delivery of Azithromycin and nisin through liposomes for skin infection to reduce antimicrobial drug resistance. *International Journal of Pharmaceutics*, **2025**. p. 125764.
63. Ng, V.W.L., X. Ke, A.L. Lee, J.L. Hedrick, Y.Y. Yang, Synergistic co-delivery of membrane-disrupting polymers with commercial antibiotics against highly opportunistic bacteria. *Advanced Materials*, **2013**. 25(46): p. 6730-6736.
64. Carvalho, S.G., A.M. Dos Santos, A.L. Polli Silvestre, A.G. Tavares, M. Chorilli, M.P. Daflon Gremião, Multifunctional systems based on nano-in-microparticles as strategies for drug delivery: advances, challenges, and future perspectives. *Expert Opinion on Drug Delivery*, **2023**. 20(9): p. 1231-1249.
65. Anton, N., A. Jakhmola, T.F. Vandamme, Trojan microparticles for drug delivery. *Pharmaceutics*, **2012**. 4(1): p. 1-25.
66. Zarubova, J., M.M. Hasani-Sadrabadi, L. Bacakova, S. Li, Nano-in-micro dual delivery platform for chronic wound healing applications. *Micromachines*, **2020**. 11(2): p. 158.
67. Reshmi, C., S.P. Sundaran, T. Subija, S. Athiyanathil, "Nano in micro" architecture composite membranes for controlled drug delivery. *Applied Clay Science*, **2018**. 166: p. 262-275.
68. Huang, Y., D. Yan, W. Ouyang, J. Hu, Z. Liu, Recent Achievements and Perspectives in Smart Nano-in-Micro Platforms for Ocular Disease Treatment. *International Journal of Nanomedicine*, **2025**. p. 7579-7612.
69. Esteban-Pérez, S., I. Bravo-Osuna, V. Andrés-Guerrero, I.T. Molina-Martínez, R. Herrero-Vanrell, Trojan Microparticles Potential for Ophthalmic Drug Delivery. *Curr Med Chem*, **2020**. 27(4): p. 570-582.

Chapter 3.

From Natural Extracts to Brain Targeting: Experimental Development of SLNs

3.1. Exploring the application of SLNs loaded with Capsaicin-rich extract in Parkinson's disease

3.1.1. Introduction

Parkinson's disease (PD) is a fast-growing neurodegenerative disorder, widespread primarily in the geriatric population, associated with motor dysfunctions (rigidity, tremor, and gradualness of movement) depending on the progressive degeneration of nigrostriatal dopamine (DA) neurons. Despite the major advances in this field, the aetiology of PD remains an unsolved issue and a PD model useful to estimate the effect of drugs on the disease progression is lacking [1]. Most of the existing PD treatments are based on the restoration of dopaminergic tone in the striatal nucleus but they often result inadequate [2]. Existing therapeutics are ineffective and intended to mitigate cognitive and behavioural symptoms. In fact, to date, there is no successful treatment capable of inverting the disease course, freezing the cognitive impairment, and other symptoms, affecting the patient's quality of life [3]. One of the major limiting factors of available PD pharmacological treatments is the poor brain bioavailability due to the blood-brain barrier (BBB), which restricts central nervous system (CNS) targeting. Moreover, neuropsychiatric side effects represent a further criticism of conventional synthetic drugs [4]. Recently, plant-derived natural products and plant extracts have been investigated for their therapeutic potential. They claim simple accessibility, affordability, safety, and neurodegenerative-protecting properties [5]. Among them, Capsaicin (CPS), chemically composed of an aromatic ring and a hydrophobic chain connected through a polar amide group [6], is an alkaloid belonging to the vanilloid family, extracted from chili pepper (**Figure 1**). CPS possesses anti-cancer, analgesic, antioxidant, antimicrobial, antifungal, cardioprotective, and anti-obesity activities [7, 8]. Moreover, its beneficial effect in the prevention and management of neurodegenerative diseases is also proven. In a 1-methyl-4-phenyl-1,2,3,6-tetrahydropyridine (MPTP) mouse model of PD, CPS displayed the capability in inhibiting brain inflammation and oxidative stress by activation of the transient receptor potential vanilloid subtype 1 (TRPV1), highly expressed in the brain, which modulates neuronal function and controls motor behaviour. Indeed, TRPV1 receptors stimulation led to a sequence of events that involve astrocyte activation and result in increased DA levels in the striatum [9]. Literature data show that CPS when

intraperitoneally administered in PD mouse model can increase the number of dopaminergic neurons in the substantia nigra, also shifting the microglial cells to an anti-inflammatory state [10-12]. Furthermore, dietary CPS increases dopamine content in the transgenic *Drosophila* expressing human α-synuclein, reducing the markers of oxidative stress, and enhancing free radical scavenging [13]. Notwithstanding literature data highligh the effectiveness of CPS, its applicability is hampered by poor water solubility, pungency-induced irritation, off-target effects, a high degree of first-pass metabolism, and low bioavailability [14]. Several studies have been reported regarding the development of novel formulations that ameliorate CPS-associated drawbacks, including liposomes, hydrogels, and nanoformulations. For example, CPS-loaded alginate nanoparticles loaded in polycaprolactone-chitosan nanofibers exhibit an improved prolonged release of CPS from 120 h to 500 h [15]. While CPS-loaded folic acid-conjugated lipid nanoparticles prevented rapid RES uptake prolonging their blood circulation time [16]. Kunjiappan and coworkers reported CPS-loaded solid lipid nanoparticles with anticancer efficacy on human hepatocellular carcinoma *in vitro* [17]. Notably, nanotechnology has been explored as a useful strategy to modify poor physico-chemical properties and facilitate transport across the BBB [18-20]. Among various colloidal systems, solid lipid nanoparticles (SLNs) have received special interest due to many features that make them particularly captivating as alternative drug carriers, being able to trap and safeguard drugs in the biocompatible core [21,22]. SLNs may represent a valid delivery platform since possessing countless advantages mostly due to the reduced nanosized dimensions that allow bypassing the liver and spleen filtration prolonging blood circulation and allowing them to reach the site of interest [23]. Drug-loaded SLNs highlight sustained release features, and, due to biodegradable constituents, lower toxicity than polymeric nanoparticles [22]. Since evidence of herbal-extract nanoformulations reaching the central nervous system (CNS) exists but only a few examples of nanoformulations loaded with CPS-extract are described, in the present work, we reported the preparation of SLNs loaded with a CPS-extract obtained from *Capsicum annuum* fruits and we evaluated their potential applicability in the treatment of CNS disorders. To improve the drug-likeness profile of CPS, CPS-extract SLNs were purposed for a potential oral administration. They were prepared, characterized for their physicochemical properties as well as entrapment efficiency, drug release, and evaluated for the *in vitro* biological activity assessed by

dichloro-dihydro-fluorescein diacetate (DCFH-DA) assay on retinoic acid/phorbol 12-myristate 13-acetate (RA/PMA) differentiated SH-SY5Y neuroblastoma cell line. According to our findings, there is no literature data, on drug delivery systems based on SLNs loaded with CPS-extract for application in the field of neurodegenerative disorders.

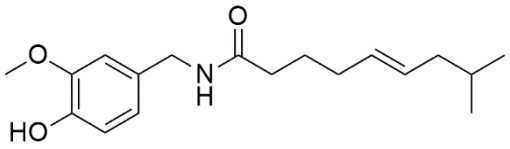


Figure 1. Chemical structure of Capsaicin.

3.1.2. Results and discussion

CPS extraction and quantification

CPS identification was performed by HPLC using the optimized chromatographic conditions by comparing the retention times and chromatograms of CPS in the extract samples with those of reference standards. **Figure 2** shows a chromatogram of the CPS-extract where the highest peak represents the CPS detected at a wavelength of 280 nm. CPS resulted well separated from dihydrocapsaicin (DHC) and nordihydrocapsaicin (*n*-DHC) with retention times of 9.39, 13.68, and 8.63 min, respectively.

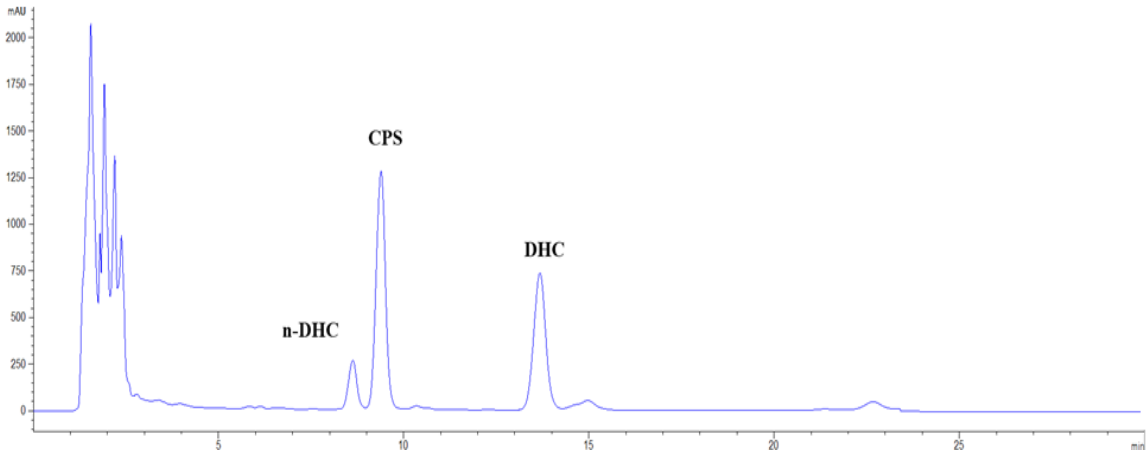


Figure 2. HPLC chromatogram of CPS-extract.

The calibration curve of CPS showed a linear relationship within the range of the considered concentrations (2.5-50 µg/mL) with a high correlation coefficient (R^2 = 0.9991). The LOD and LOQ, calculated considering the regression equation (y = 13.601x - 9.5392), were 3.07 and 9.29 µg/mL, respectively. CSP, as the most abundant extract constituent, was found in a percentage of 52% over those of *n*-DHC (9%) and DHC (39%).

CPS-extract SLNs preparation and characterization

CPS-extract SLNs were proposed to overcome CPS biopharmaceutical limitations and increase its targeting in the brain. SLNs were successfully formulated using SA as solid lipid, which was emulsified with the aqueous phase containing Brij 78. Brij 78 is a non-ionic surfactant possessing an attractive hydrophyl-lipophyl balance (HLB) value suitable to form oil-in-water (o/w) microemulsions. The lipid/surfactant phase and the

lipid/extract ratios were 1:0.3 and 1:1.5, respectively. These ratios guaranteed the best physico-chemical properties and a CPS-extract solubilization up to 800 μg/mL. Indeed, based on preformulation studies by raising both the lipid and extract amounts, large and highly polydisperse particles were obtained, also macroscopically characterized by turbidity and precipitates (data not shown). In previous work, the effect of SA and Brij 78 was evaluated in a systematic study, which highlighted a close correlation between their concentrations and both size and EE% of the resulting SLNs. The particle size was optimized by using a surfactant: lipid ratio of 0.38:1 [18]. The strong dependency of particle size from the surfactant is due to the lack of self-emulsifying property of stearic acid in aqueous media. This aspect was well-established by several investigations [34].

CPS-extract SLNs appeared as a homogenous suspension, orange-coloured. They showed a hydrodynamic diameter of 208.2 nm, slightly bigger compared to the empty SLNs (178.11 nm). ζ-potential measurements revealed appreciable negative surface charge with values lower than -20 mV for both blank and CPS-extract SLNs (-28.7 and -27.9 mV before and after loading, respectively) (**Table 1**). This negative charge is conferred by the SA, organized in the lipid core with the lipophilic hydrocarbon chains, which exposes the -COOH group, expected in its dissociation form at physiological pH, into the aqueous phase. These results suggest good electrostatic stabilization since it is well established that ζ-potential values ranging from +30 and -30 mV indicate physically stable dispersions able to avoid particle aggregation through van der Waals interactions [35, 36]. The increase in size, after CPS-extract loading, may confirm the high encapsulation (86%) even if a small amount of CPS-extract is supposed to be adsorbed on the particle surface as suggested by the slight decrease of the negative charge in the loaded formulation. Low PDI values of 0.02 and 0.17, before and after loading, suggest uniform and monodisperse formulations characterized by a narrow size distribution [37]. Moreover, CPS-extract SLNs showed an EE% of 86.27, with a recovery, after freeze drying of 61% (**Table 1**). The high EE% may be explained by strong hydrophobic interactions established between the fatty acid chains and alkyl chains present in the solid lipid core and the CPS-extract, respectively. Additional intermolecular hydrogen bonds between the Brij 78 hydroxyl groups and the capsaicinoids phenolic and amide groups further immobilize the cargo in the nanostructure. These results suggest physico-chemical properties suitable for the proposed brain delivery. Indeed, particle size, PDI, and ζ-

potential are key parameters affecting nanoparticle uptake via transcellular, paracellular transport, and/or nonspecific uptake mechanisms. It has been demonstrated that negatively charged NPs may have a unique ability to penetrate the electrostatic BBB. In our case, we also tried to increase the plasma half-life producing particles with a size close to 200 nm corresponding to the best size for an engineered long-circulatory particle which also enables to cross tight endothelial cells of the BBB [22, 38, 39]. Additionally, we propose a surface coating with the hydrophilic surfactant Brij 78, commonly employed in Nps manufacturing to confer them stealth features. Since its amphiphilic nature, Brij 78 in aqueous media self-assemblies and forms a steric barrier, composed of hydrophilic PEG chains, which shields particles from opsonization, and clearance mechanisms mediated by the reticuloendothelial system (RES) [40]. Beyond this RES escaping, Brij 78 may increase the CPS delivery on the CNS since its ability to open tight junctions without any alteration on the BBB parameters, as confirmed by *in situ* brain perfusion studies [41, 42]. These results are supported by several studies described in the literature. In some works, the effect of surfactants has been investigated as a hopeful strategy to prevent aggregation, modify SLN's features, and increase brain drug distribution. In the field of neurodegenerative disorders, andrographolide-loaded SLNs were proposed as potential brain delivery systems [43]. *In vivo* studies performed on healthy rats demonstrated the ability of this kind of formulation to overcome the BBB as confirmed by the fluorescent nanoparticle's detection in the brain parenchyma [39, 41]. Brij 78 also promoted in paclitaxel loaded-Nps an improvement of the brain drug distribution related to their ability to circumvent BBB P-gp efflux transporters [44].

Table 1. Physico-chemical features of CPS-extract SLNs.

	Size (nm)	PDI	ζ-potential (mV)	EE %	Recovery %
Empty SLNs	178.11 ± 1.94	0.02 ± 0.001	-28.7 ± 0.76	-	-
CPS-extract SLNs	208.2 ± 10.74	0.17 ± 0.002	-27.9 ± 0.47	86.27 ± 5.14	61

Thermal analysis

DSC is a thermal analysis widely used for the characterization of drug-loaded NPs in terms of crystallinity degree, drug-lipid interactions, and polymorphism. DSC thermograms of the bulk materials and both empty and CPS-extract SLNs are shown in

Figure 3, and the phenomenological data, including onset temperature (T_{onset}), melting temperature, and melting enthalpy (ΔH), are reported in **Table 2**. CPS-extract showed a wide endothermic thermal event from 113 °C, associated with water evaporation. The well-known sharp endothermic melting peak close to 65 °C of the pure CPS, representing its crystalline nature, is not detectable in the CPS-extract, probably due to its amorphization occurring during the extraction. Both Brij 78 and SA displayed an endothermic transition at 42 °C and 68 °C, respectively. Compared to the bulk materials, CPS-extract SLNs showed a broader peak with a lower onset temperature [45, 46]. The wider peak, at lower onset temperature, and the ΔH decline both suggest a less ordered crystal state which may be due to CPS-extract/lipid matrix interactions [47].

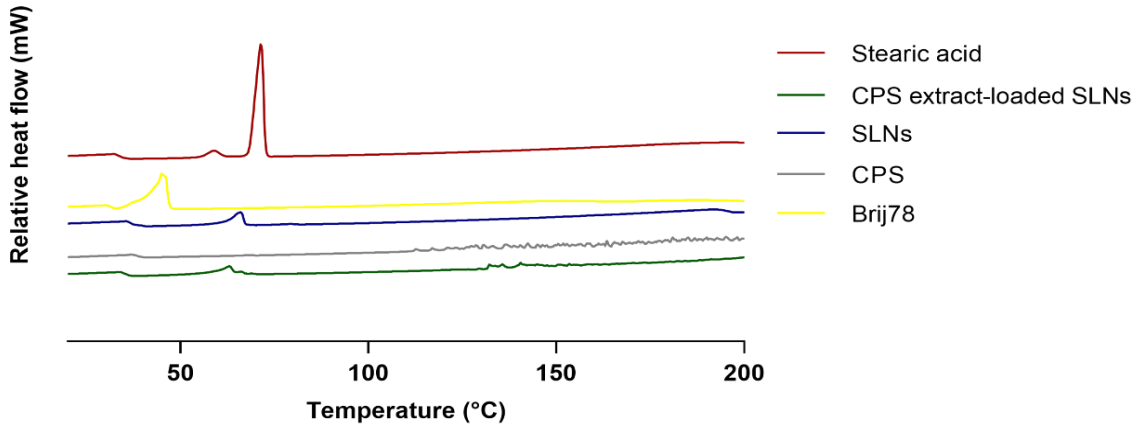


Figure 3. Thermal analysis of starting materials and CPS-extract SLNs.

Table 2. DSC parameters of CPS-extract SLNs and their constituents.

	T_{onset} (°C)	T_m (°C)	ΔH (J/g)
Stearic Acid	68.375	71.333	206.469
Brij78	42.096	45.666	145.932
CPS-extract	113.004	120.066	38.912
CPS-extract SLNs	58.577	63.000	40.174
Empty SLNs	62.137	66.000	68.857

Stability studies of CPS-extract SLNs

To define the formulation stability their physico-chemical properties were assessed for 30 days at different storage conditions. No significant effects were observed in CPS-extract SLNs stored at 25 and 4 ± 2 °C. As shown in **Figure 4A**, their initial size, after 2 days,

slightly increased to around 300 and 250 nm for formulation stored at 25 and 4 °C, respectively. After these initial changes, these values remained almost stable for a period of at least 30 days, suggesting that SLNs do not lose their integrity but simply undergo a slight structural rearrangement preserving their stability. Concerning the ζ-potentials, the surface charge resulted almost unchanged over 30 days, further supporting the maintained integrity. The residual CPS was also quantified after the incubation period and no significant changes were detected since the drug quantity resulted slightly reduced of around 10%. These results agree with previous work which proved the good storage shelf-life and storage stability of SLNs loaded herbal extracts [48].

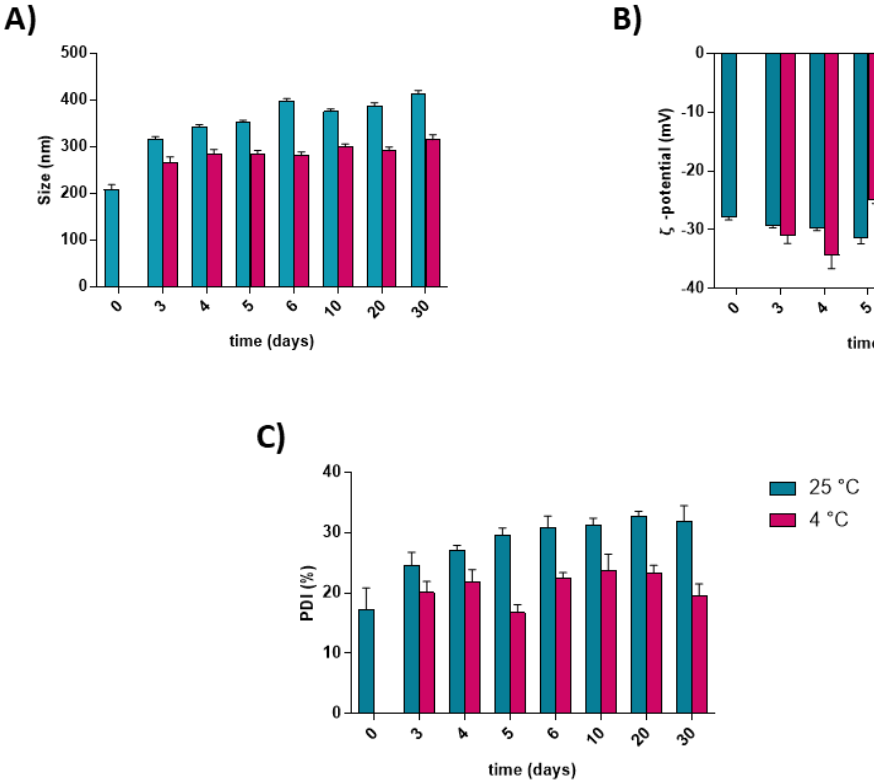


Figure 4. CPS-extract SLNs stability in the preparation media at different temperatures. Evaluation in terms of particle size (**A**), ζ-potential (**B**), and PDI (**C**) over a period of 30 days. Each value represents the mean ± SD (n = 3).

In vitro drug release

The release rate of CPS from SLNs was studied at room temperature. As shown in **Figure 5**, after 24 h it has reached the maximum release of almost 90%. The release profile is characterized by a gradual release that provides, within 9 h, the release of approximately 80% of CPS, probably adsorbed on the outer layer of the lipid matrix or interacting with

the surfactant shell of the SLNs. After this period, the release rate becomes slower most likely because this phase involves the innermost CPS-extract, included in the core, which needs to cross the lipid matrix through a diffusion process and hindering effect due to the surrounding shell of solid lipid [16]. The release profile may be justified by the high affinity between CPS aromatic moiety and SA involved each other in hydrophobic interactions responsible for the hold back of the CPS-extract thus delaying its release into the aqueous medium. Considering the high affinity with the lipids, CPS-extract may result homogeneously dispersed in the matrix in either an amorphous cluster or molecularly dispersed phase (adsorbed on the SLNs surface and entrapped in the core), a recurring pattern for highly lipophilic drugs incorporated into SLNs [48, 49]. The *in vitro* drug release data were fitted into different empirical models including zero-, first-order, Higuchi, and Korsmeyer-Peppas kinetic models (**Figure 6**) [29]. The corresponding kinetic parameters (R^2, k, and n), obtained from the investigated fit models, are reported in **Table 3**. The highest R^2 value allowed us to define the kinetic which better describes the CPS release from the SLNs. Based on the results the CPS-extract release was best fitted into the Korsmeyer–Peppas model ($R^2 = 0.9721$). Furthermore, the n value being > 0.5 but lower than 1 allows us to define an anomalous, non-Fickian diffusion release, controlled by both diffusion and lipid erosion mechanisms, implied in the control of drug release rate from the lipid core and through the interfacial film formed by the surfactant [50]. These results agree with previously published data involving drug-loaded SLNs where the best fit into the Korsmeyer-Peppas model, with n values ranging from 0.43 to 0.85, were found [51, 52]. The CPS release kinetic from CPS-extract SNLs may result in a decrease of its unwanted burning and pungency, in part due to the reduced content (~ 50% of CPS) in the entrapped extract, and because of the gradual release that can counteract the undesired effects after a proposed oral administration.

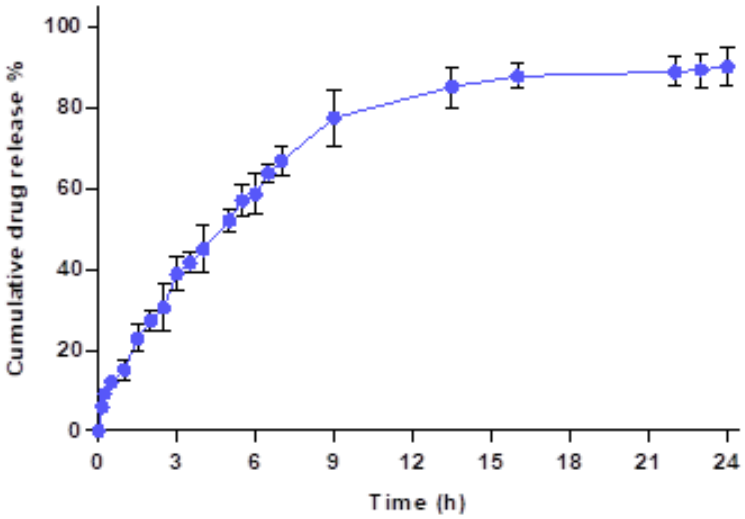


Figure 5. Release profile of CPS from CPS-extract SLNs.

Table 3. Kinetic parameters of the *in vitro* release of CPS-extract from SLNs.

Zero Order		First Order		Higuchi		Korsmeyer-Peppas		
$Q_t=Q_0-k_0t$		$log\ Q_t=logQ_0+k_1t/2.303$		$Q_t=k_Ht^{1/2}$		$M_t/M_\infty=kt^n$		
R^2	k_0 (h^{-1})	R^2	k_1 (h^{-1})	R^2	k_H($h^{-1/2}$)	R^2	K (h^{-n})	*N*
0.7698	3.5279	0.4133	0.0999	0.9342	20.622	0.9439	16.9590	0.6225

Qt: amount of active agent released on time *t*; Q_0: initial amount of drug dissolved (equal to zero).
K_0, k_1, k_H, k: constants for the zero-, first-order kinetics, Higuchi and Korsmeyer-Peppas models, respectively.
M_∞ amount of drug at the equilibrium state; M_t amount of drug released over time t.
n: exponent release, related to the drug release mechanism.
The constant values of zero order and Higuchi correspond to the slopes of the lines. The constant value for first-order model is obtained from the equation: slope=k/2.303 [28].

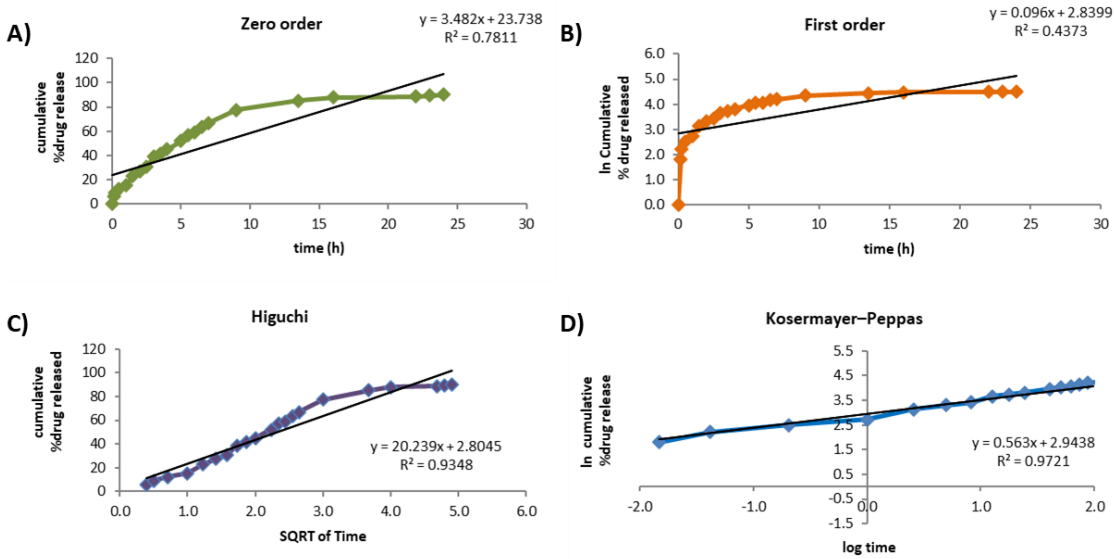


Figure 6. Kinetic analysis of drug release: (**A**) Zero-order kinetic, (**B**) First-order kinetic, (**C**) Higuchi, and (**D**) Korsmeyer–Peppas.

PAMPA assays

PAMPA assay is based on the evaluation of the passive diffusion through an artificial membrane made of PBL mimicking the physicochemical microenvironment of the BBB. Results revealed that the permeability of both CPS and CPS-extract are low with *Pe* values of $0.35 \pm 0.04 \times 10^{-6}$ and $1.78 \pm 0.05 \times 10^{-6}$ cm/s, respectively. For this reason, SLNs were selected as a well-known approach suitable to increase their permeability. Indeed, CPS permeability increased when included in SLNs (**Table 4**). As expected, dopamine and diazepam, selected as standard compounds, showed low ($Pe < 2 \times 10^{-6}$ cm/s) and high permeability ($Pe > 4 \times 10^{-6}$ cm/s), respectively. PAMPA-BBB represents an *in vitro* assay extremely helpful in the early stages of preformulation studies since it considers the worst case, underestimating the effective *in vivo* BBB crossing in which more events may allow the active drug uptake [30].

Table 4. PAMPA-BBB permeability assays [a]

	PAMPA-BBB permeability ***Pe*** **(10^{-6} cm/s)**	**Classification[c]**
	pH 7.4 [b]	
CPS	0.35 ± 0.04	CNS -
CPS-extract	1.78 ± 0.05	CNS -
CPS-extract SLNs	4.05 ± 0.21	CNS +/-

[a] SD range is within ± 8% for all the experiments (each data point represents the mean of three repeats); [b] pH of both donor and acceptor compartments; [c] CNS + (high BBB permeation): $Pe > 4.0 \times 10^{-6}$ cm/s; CNS +/- (discrete BBB permeation): *Pe* from 4.0×10^{-6} cm/s to 2.0×10^{-6} cm/s; CNS- (low BBB permeation): $Pe < 2.0 \times 10^{-6}$ cm/s [30].

Biological assays

CPS protects against oxidative insults and alleviates behavioural deficits occurring in PD [10]. Since oxidative stress is one of the key biochemical abnormalities involved in the progression of PD, [53] it is important to identify specific substances that have an antioxidant and protective effect. Here, we investigated the antioxidant effects of CPS, CPS-extract, CPS-extract SLNs in SH-SY5Y human neuroblastoma cells. To define the appropriate concentration range, the cytotoxic effects of the selected compounds were determined by the MTT test (**Figure 7**). Thus, dose-response experiments were performed in both UC (**Figure 7A**) and DC (**Figure 7B**), in concentrations of 1 and 0.1 μM to verify whether, 24 and 48 h after incubation, the compounds had any effect on the cell vitality

[54]. The concentration of 0.1 μM was selected to evaluate both antioxidant and neuroprotective activity since it did not interfere with SH-SY5Y cell vitality.

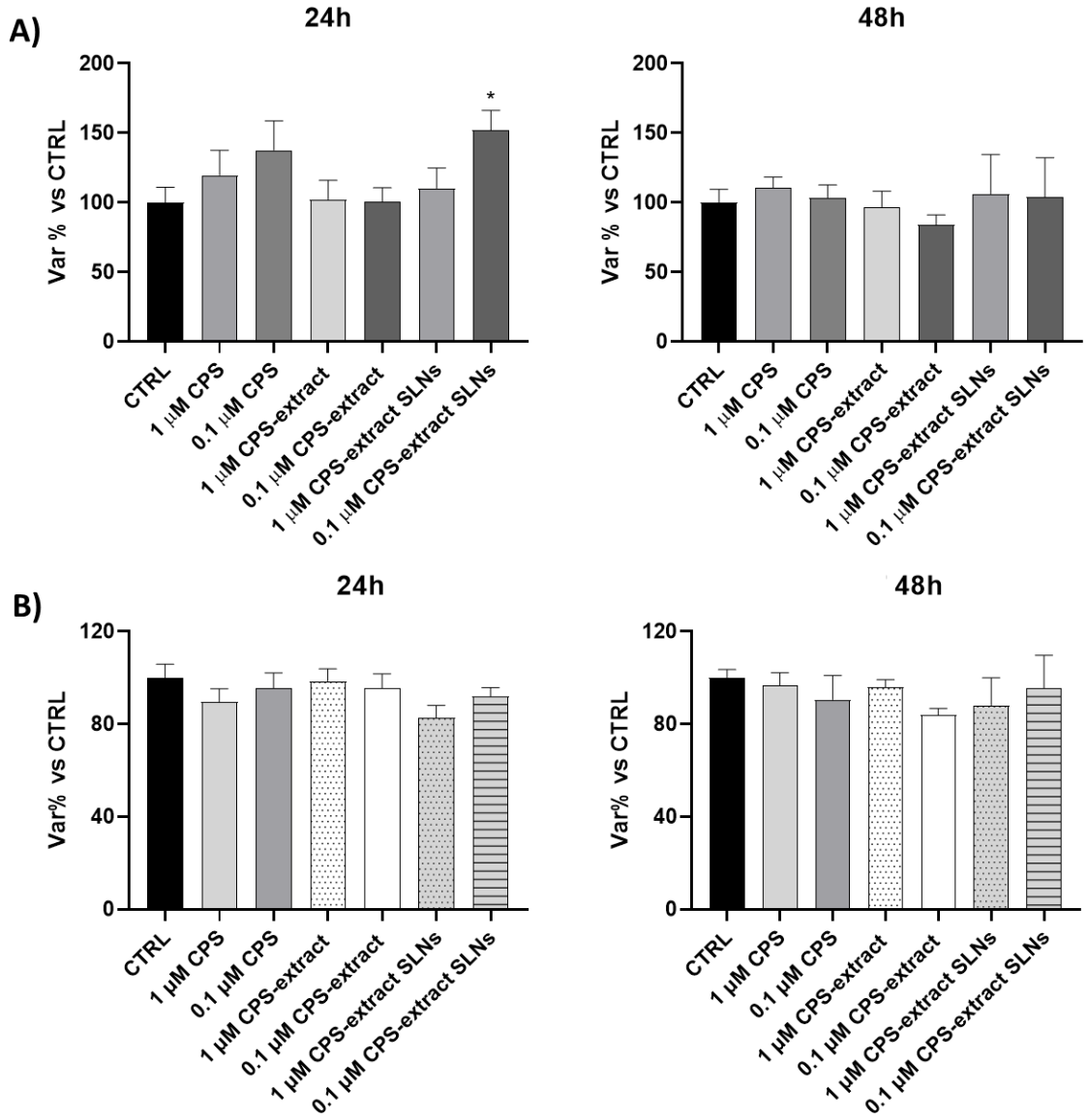


Figure 7. Dose-response effects of CPS, CPS-extract, CPS-extract SLNs in undifferentiated (**A**) and differentiated (**B)** SH-SY5Y human neuroblastoma cells. The cells were incubated for 24 and 48 h with 1 and 0.1 μM concentrations of the compounds. CTRL: cells w/o compounds. The values are reported as means ± SEM of the percentage variation with respect to CTRL of three different experiments (n=16). *p < 0.05.

The neuroprotective and antioxidative capacity of CPS, CPS-extract, CPS-extract SLNs against oxidative stress was evaluated by using the human neuroblastoma cell line SH-SY5Y. H_2O_2 was used as a toxic insult on SH-SY5Y cells for the generation of exogenous

free radicals to obtain an *in vitro* model of PD. Thus, differentiated SH-SY5Y cells were pre-treated with CPS, CPS-extract, CPS-extract SLNs for 24 h and then exposed to H_2O_2 (25-150-300 μM) for another 24 h. Cell viability was detected using MTT assay as shown in **Figure 8**. All the tested samples showed a protective effect against H_2O_2. Moreover, our results indicate that CPS can protect almost completely from the toxic effect of H_2O_2 at all concentrations, maintaining the viability like controls or cells treated with the unentrapped CPS-extract. Otherwise, CPS, CPS-extract, CPS-extract SLNs efficiently counteract the effect of 25 μM H_2O_2, although they exert a partial protective effect on cell viability even at higher H_2O_2 concentrations. The neuroprotection results were more pronounced in presence of the extract instead of pure CPS. This effect could be related to the synergic action of other polyphenols contained in the extract, that, in combination, more efficiently subverts the damage induced by the H_2O_2.

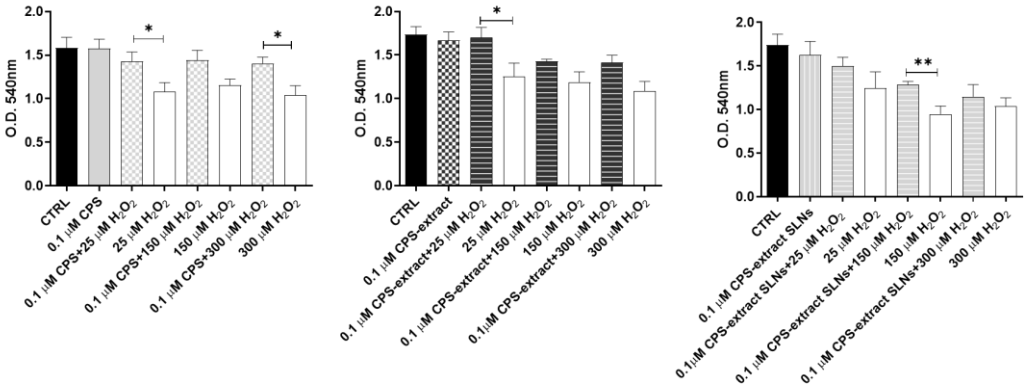


Figure 8. MTT assay in differentiated and H_2O_2-lesioned SH-SY5Y human neuroblastoma cells in the presence of 0.1 μM CPS, CPS-extract, CPS-extract SLNs. The means ± SEM derived from three different experiments ($n = 16$). *$p < 0.05$; **$p < 0.005$.

To measure ROS and the cell capability to counteract this insult, H_2DCFDA was used as a specific probe for direct measuring the redox state of a cell. Based on previous results, the concentration of 25 μM H_2O_2 was selected to evaluate the ability of CPS, CPS-extract, CPS-extract SLNs to reduce oxidant levels. Our data showed that all the compounds in the presence of H_2O_2 exerted an antioxidant action, keeping free radical levels lower than the control treated with H_2O_2 and like the control. Moreover, treated SH-SY5Y displayed ROS levels lower than the control (**Figure 9**), confirming antioxidant and neuroprotective capabilities.

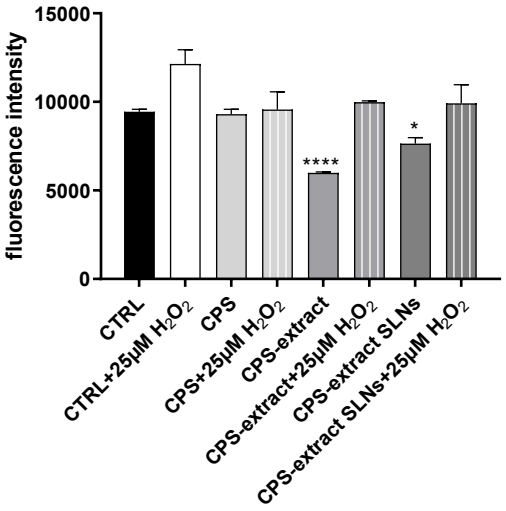


Figure 9. ROS measurement by H_2DCFDA fluorescence in differentiated SH-SY5Y human neuroblastoma cells exposed to 0.1 μM CPS, CPS-extract, CPS-extract SLNs 24 h before with 25 μM H_2O_2. CTRL: cells w/o compounds. The values are reported as means ± SEM of the fluorescence intensity, derived from three different experiments ($n = 8$). *$p < 0.05$; **** $p < 0.0001$.

Furthermore, the antioxidant effects of CPS, CPS-extract, CPS-extract SLNs were assessed also by NBT assay (**Figure 10**). The formazan concentration deriving from NBT reduction is determined using a spectrophotometer, such that more formazan indicates that more O_2^- had reduced NBT. In the presence of potent antioxidant substances, the superoxide is detoxified by the scavenger action, which decreases the amount of NBT reduced, allowing the detection of a reduced amount of formazan. Our results showed a significant decrease of O_2^- levels after 24 h of incubation in the presence of CPS, CPS-extract, CPS-extract SLNs at 0.1 μM.

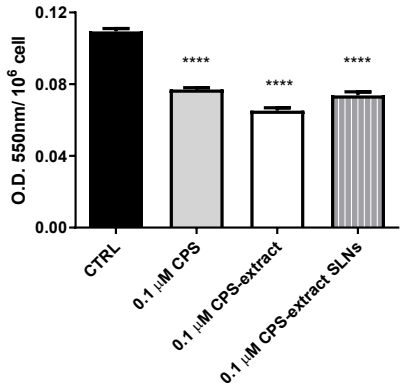


Figure 10. NBT assay in differentiated SH-SY5Y human neuroblastoma cells, in the presence of 0.1 μM CPS, CPS-extract, CPS-extract SLNs, after 24 h of incubation. Mean values ± SEM were derived from three independent experiments ($n = 5$; **** $p < 0.0001$, Unpaired t-test). CTRL: cells w/o compounds *vs* treated cells for 24 h.

Taking together these results, CPS-extract SLNs possessed favorable features and a significant protective effect in reducing ROS increments. This evidence suggests that the proposed formulation may be considered a suitable nanomedical tool to manage PD also through the modulation of gut inflammation, closely associated with the pathogenesis of this neurodegenerative disease [55].

3.1.3 Experimental Section

Materials

Stearic acid (SA), polyoxyethylen (20) stearyl ether (Brij 78), ethanol, capsaicin standard, tween 80, dodecane, dopamine, diazepam, Dulbecco's Modified Eagle's medium, heat-inactivated fetal bovine serum, penicillin, streptomycin, L-glutamine, retinoic acid, phorbol 12-myristate 13-acetate. 3-[4,5-dimethylthiazol-2-yl]-2,5-diphenyltetrazolium bromide, hydrogen peroxide, nitro blue tetrazolium chloride, 2',7'-dichlorofluorescin diacetate (H_2DCF-DA), dimethyl sulfoxide (DMSO), Milli-Q water, methanol, acetonitrile, MultiScreen-IP PAMPA filter plate and 96-well polytetrafluoroethylene (PTFE) plate were purchased from Sigma-Aldrich (St. Louis, MO, USA). Porcine polar brain lipid (PBL) extract was acquired from Avanti Polar Lipids, Inc. CPS was extracted from *Capsicum annuum* fruits.

***Capsicum annuum* extraction**

CPS was extracted from *Capsicum annuum* L. fruits collected in Pescara, Italy (42.4618° N, 14.2161° E). After the peduncle and seeds separation, fruits were dried under atmosphere conditions until reaching a constant weight and then powdered using an electric blender. The finely triturated powder (400 Mesh) was stored at -20 °C before being subjected to the extraction procedure, accomplished by hot maceration in ethanol, under vigorous stirring for 3h at 50 ± 0.5 °C. The dark red extraction mixture was filtered, dried, and characterized by High-Performance Liquid Chromatography (HPLC) analysis.

Chromatographic conditions

The chromatographic analyses were performed using an Agilent 1260 Infinity II HPLC (Agilent, Santa Clara, CA, USA) consisting of a 1260 Infinity II Quaternary Pump (model G7111A), 1260 Infinity II auto-sampler (model G7129A), a 1260 Infinity II Multicolumn Thermostat (model G7116A), and a 1260 Infinity II Diode Array Detector (model

G7115A) equipped with a Poroshell 120 EC-C18 column (150 x 4.6 mm i.d., particle size 4 μm, Agilent, Santa Clara, USA) operating at 20 °C. The samples were analyzed in isocratic elution mode using a mixture of acetonitrile (A) and water (B) 50:50 *v/v*, for 30 min, at a flow rate of 0.8 mL/min, with a UV detector set at 280 nm. Starting from a CPS stock solution in methanol (10 mg/mL), a series of dilutions, in the range of 2.5-50 μg/mL, were used for the calibration curve. The LOD and LOQ were determined based on the equations: LOD = 3.3 × σ/S and LOQ = 10 × σ/S, where σ is the standard deviation of the intercept with y-axis and S the slope [24].

Preparation of CPS-extract SLNs

Preformulation studies for CPS-extract SLNs were performed using different CPS-extract/lipid ratios (1:2, 1.5:1, 2:1 *w/w*). To select the best formulation, physico-chemical features such as the mean particle size, polydispersity index (PDI), and ζ-potential were considered. SLNs were prepared according to a procedure that involved first an emulsification phase followed by the evaporation and the subsequent solidifying step [18]. Briefly, SA (33.6 mg) was dissolved in 2.5 mL of pure ethanol under stirring at 40 ± 2 °C. Simultaneously, an aqueous phase (24 mL), containing Brij 78 (12.68 mg) as surfactant, was heated at 70 ± 2 °C. Under mechanical stirring (400 rpm), the organic phase was added drop by drop to the aqueous phase. The so-obtained lipid emulsion was left at 70 ± 2 °C under stirring for the complete organic solvent removal and then diluted with an equal volume of cold water to allow the nanoparticle solidification. In CPS-extract SLNs, the SA and the CPS-extract, containing 2% *w/w* of CPS (44 mg), were both dissolved in the organic phase. To remove the unentrapped drug, the final suspension was filtered through a 1.20 μm syringe filter (Minisart Plus).

Physico-chemical properties of CPS-extract SLNs

Formulations were characterized in terms of particle size and PDI by dynamic light scattering (DLS, Anton Paar Litesizer 500 Graz, Austria). Samples were diluted 1:10 with Milli-Q water in a 1.5-mL disposable cuvette. Samples were thermostated for 2 min at 25 °C before each measurement which was performed at 25 °C in back scattering mode (175°). Results reported as mean hydrodynamic diameter were obtained from three repetitions per sample in triplicate. The ζ-potential was measured by the electrophoretic light scattering (AntonPaar Litesizer 500, Graz, Austria). The samples were conditioned

in an electrophoretic Omega cuvette Mat. No. 225288 at 25 °C, applying a potential of 200.0 V. The ζ-potential values of CPS-extract, empty and extract-loaded SLNs were calculated from the electrophoretic mobility obtained from 12 repeated analyses via the conversion of electrophoretic mobility according to the method used by Helmholtz-von Smoluchowski.

Encapsulation efficiency (EE%)

The EE% was determined by a direct method. 100 µL of CPS-extract SLNs as colloidal dispersion was added to 900 µL of methanol, vortexed, and sonicated to allow the nanoparticle disruption. The obtained solution was filtered through a 0.45 µm syringe filter and analyzed by HPLC, to quantify the entrapped CPS [25]. The EE% was obtained by the ratio of the found and theoretical amount of CPS encapsulated in SLNs. The yield of the preparation process of SLNs was calculated as the weight of the product obtained after the freeze-drying compared to the weight of the different components used during the formulation set-up. The encapsulation efficiency percentage (EE %) was calculated by using the **Equation (1)**:

$$EE\ \% = \left(\frac{Wf}{Wt}\right) * 100 \qquad \textbf{(1)}$$

where *Wf* is the amount of CPS found and *Wt* is the total amount of loaded CPS [26].

Differential scanning calorimetry (DSC)

DSC analysis was performed using an instrument PerkinElmer Inc. (Waltham, MA, USA) in the temperature ranging from 20 to 200 °C in hermetically sealed aluminum capsules. Briefly, the pan was filled with 5 mg of each sample, and heated with a scan rate of 10 °C/min. An empty pan with a cover was used as a reference. The DSC measurements were carried out for the following samples: (a) SA; (b) CPS-extract; (c) Brij 78; (d) empty SLNs; and (e) CPS-extract SLNs.

Storage stability of CPS-extract SLNs

Formulation stability was determined after incubation at 25 ± 2 °C and 4 ± 2 °C over a period of 30 days. The formulations were stored in a colorless glass, sealed vial. At each time point (0, 3, 4, 5, 6, 10, 20, 30 days) the formulations were assessed in terms of physico-chemical parameters such as size, ζ-potential, PDI, and EE%.

***In vitro* release profile**

CPS release was determined using a dialysis bag (Pur-A-Lyzer Mega 12000 kDa MWCO, Sigma-Aldrich, St. Louis, MO, USA), which guarantees the CPS-extract diffusion, avoiding the SLNs passage. 15 mL of the CPS-extract SLNs were introduced in the dialysis bag and maintained at 37 ± 0.5 °C, under continuous stirring at 500 rpm to ensure homogeneity of the system. Experiments were performed under sink conditions using 600 mL of release medium composed of 200 mM phosphate buffer solution (PBS, pH 7.4) enriched with 0.05% of Tween 80. At predefined time intervals, aliquots (100 µL) of the incubated CPS-extract SLNs were sampled from the dialysis bag, diluted 1:10 with methanol, and following the same procedure used for the EE% determination, CPS was quantified by HPLC. The cumulative release was calculated by determining the residual CPS quantity in the donor compartment (*n*=3), following the **Equation (4)**:

$$Cumulative\ percentage\ release\ \% = \left(\frac{Volume\ of\ sample\ withdrawn\ (mL)}{Bath\ volume}\right) * P(t-1) + Pt \quad \textbf{(4)}$$

where Pt = percentage released at time t and P (t-1) is the percentage released before t [27]. The zero-, first order, Higuchi, and Korsmeyer-Peppas models were applied to ascertain the CPS release kinetic from the SLNs. The best-fitting one was defined considering the highest regression values (R^2) of the analyzed release data. Moreover, the *n* value, obtained from the slope of the equation referring to the Korsmeyer-Peppas model, was employed to define the release mechanism of CPS as well [28].

Parallel Artificial Membrane Permeation Assay (PAMPA)

The PAMPA method was used to evaluate the CPS BBB permeability. Analyses were performed using a 96-well, MultiScreen-IP PAMPA filter plate as donor, and a 96-well polytetrafluoroethylene (PTFE) acceptor plate as receiving. Donor wells were treated with a lipid solution prepared in *n*-dodecane (2% *w/v*) based on porcine polar brain lipid (PBL) extract (from Avanti Polar Lipids, Inc.). Donor solution consisting of CPS, CPS-extract, and CPS-extract SLNs were diluted with PBS (pH 7.4) supplemented with DMSO (5% *v/v*) to reach a final CPS concentration of 100 µg/mL. The acceptor solution had the same composition as the donor but without the investigated compounds. The system was assembled by setting 300 µL of the donor and acceptor solutions between an artificial

membrane, previously coated, with a solution (5 μL) of the phospholipid mixture. After 18 h of incubation, concentrations in each donor and acceptor well were quantified by HPLC, and the effective permeability coefficient (*Pe*, cm/s) was calculated as previously reported [29]. To assess the suitability and reliability of the system, dopamine, and diazepam were used as reference compounds with low and high BBB permeability, respectively [30].

Biological studies

SH-SY5Y Cell Culture

Human SH-SY5Y neuroblastoma cells (EGACC, Sigma–Aldrich, UK) were grown in Dulbecco's Modified Eagle's medium supplemented with 10% heat-inactivated fetal bovine serum, penicillin (100 U/mL), streptomycin (100 μg/mL), and 1% L-glutamine. The cells were maintained at 37 °C in a 5% CO_2 humidified atmosphere. To obtain a dopaminergic phenotype, the SH-SY5Y cells were treated with retinoic acid (RA)/ phorbol 12-myristate 13-acetate (PMA). In detail, the medium was supplemented with RA (10 μM) for 3 days; then the medium was removed and replaced with a growth medium containing PMA (80 nM) for a subsequent 3 days.

MTT assay

2700 cells/well were seeded in a final volume of 200 μL growth medium in 96-well plates. The undifferentiated cells (UC) and the differentiated cells (DC) were incubated with CPS, CPS-extract, and CPS-extract SLNs at two different concentrations (1 and 0.1 μM). After 24 and 48 h of incubation, the cells both UC and DC were assessed for viability by using a colorimetric assay of 3-[4,5-dimethylthiazol-2-yl]-2,5-diphenyltetrazolium bromide (MTT) test as described by Cacciatore *et al*. [31]. For experiments with the neurotoxin H_2O_2, the differentiated SH-SY5Y cells were pretreated with CPS, CPS-extract, and CPS-extract SLNs at 0.1 μM for 24 h and then exposed to 25, 150, and 300 μM H_2O_2 for further 24 h. Cell viability was revealed using the MTT assay.

Intracellular Reactive Oxygen Species (ROS) Measurement

Intracellular ROS were quantified by the 2',7'-dichlorodihydrofluorescein diacetate (H_2DCFDA Cat. No. D6883; Sigma) as described by Sozio et al., 2013 [32], using a Synergy H1, BioTek a microplate reader fluorometer. Briefly, the differentiated SH-SY5Y

cells were treated with CPS, CPS-extract, and CPS-extract SLNs at 0.1 μM for 24 h. After the incubation with 10 μM of permeable fluorescent and chemiluminescent probes, the cells were treated with 25 μM H_2O_2 for immediate fluorescence measurement.

Nitro blue tetrazolium chloride (NBT) assay

The differentiated SH-SY5Y cells were treated with CPS, CPS-extract, and CPS-extract SLNs at 0.1 μM for 24 h and then 10^6 cells were detached, centrifuged for 5 min at 1200 rpm, and resuspended in 1 mL of 0.9% NaCl with 1 mg/mL of NBT (Sigma-Aldrich, Milan, Italy). The spectrophotometric NBT (Nitro blue tetrazolium chloride, assay, conventionally used to determine the production of $O_2^{-\bullet}$ and based on the reduction of NBT in Nitro blue-formazan in the presence of O_2, was performed according to Di Stefano *et al*. [33].

Statistical Analysis

The results of the biological analysis are presented as the mean ± SEM of three different experiments (each $n = 8$). The statistical analysis (unpaired *t*-tests) was carried out using GraphPad Prism Software, version 9.3.1 (GraphPad Software, La Jolla, California, USA), comparing treated cells with respect to the control.

3.1.4. Conclusion

In this study, the feasibility of SLNs for CPS extract delivery was assessed. The optimized CPS-extract SLNs, prepared using SA and Brij 78, showed advantageous physicochemical properties, suitable for the intended purpose, and provided a gradual release of CPS, increasing its bioavailability in the brain. Moreover, biological studies revealed that CPS as well as the derived formulation tested, at sufficiently low and physiological concentrations used, provides a significant antioxidant capacity by protecting dopaminergic-like cells from oxidant insults. This preliminary data indicates that CPS-extract SLNs represent a promising strategy to overcome the BBB as suggested by the PAMPA-BBB assays. These results warrant further efforts to clarify the uptake mechanisms in greater detail. Proof of the concept will involve an investigation of CPS-extract SLNs *in vivo* neuroprotective profile.

All the contents of the work discussed in this chapter have been published as follows:
Marinelli L., Dimmito M.P., Cacciatore I., **Toto E.C.**, Di Rienzo A., Palmerio F., Puca V., Di Filippo E.S., Fulle S., Di Stefano A. *Solid lipid nanoparticles for efficient delivery of capsaicin-rich extract: Potential neuroprotective effects in Parkinson's disease* (2024) Journal of Drug Delivery Science and Technology, 91, art. no. 105097. DOI: 10.1016/j.jddst.2023.105097.

References

1. Z. Mari, T.A. Mestre, The Disease Modification Conundrum in Parkinson's Disease: Failures and Hopes*, Front. Aging Neurosci*, **2022.** 14, p. 1-7.
2. A. Di Stefano, B. Mosciatti, G. M. Cingolani, G. Giorgioni, M. Ricciutelli, I. Cacciatore, P. Sozio, F. Claudi, Dimeric L-dopa derivatives as potential prodrugs. *Bioorganic Med. Chem*. Lett. **2001.** 11, p. 1085-1088.
3. T.K. Lee, E.L. Yankee, A review on Parkinson's disease treatment, *Neuroimmunol. Neuroinflammation,* **2022.** 8, p. 222.
4. B.D. Li, Z.Y. Bi, J.F. Liu, W.J. Si, Q.Q. Shi, L.P. Xue, J. Bai, Adverse effects produced by different drugs used in the treatment of Parkinson's disease: A mixed treatment comparison, *CNS Neurosci. Ther*, **2017.** 23, p. 827-842.
5. F. Pohl, P.K.T. Lin, The potential use of plant natural products and plant extracts with antioxidant properties for the prevention/treatment of neurodegenerative diseases: In vitro, in vivo and clinical trials, *Molecules*, **2018**. 23.
6. M. Ilie, C. Caruntu, M. Tampa, S.-R. Georgescu, C. Matei, C. Negrei, R.-M. Ion, C. Constantin, M. Neagu, D. Boda, Capsaicin: Physicochemical properties, cutaneous reactions and potential applications in painful and inflammatory conditions (Review), *Experimental and Therapeutic Medicine,* **2019.** 916-925.
7. S. Basith, M. Cui, S. Hong, S. Choi. Harnessing the Therapeutic Potential of Capsaicin and Its Analogues in Pain and Other Diseases, *Molecules,* **2016**. 21, p. 966.
8. A. Akhtar, A. Andleeb, T.S. Waris, M. Bazzar, A.R. Moradi, N.R. Awan, M. Yar, Neurodegenerative diseases and effective drug delivery: A review of challenges and novel therapeutics, *J. Control. Release*, **2021**. 330, p. 1152-1167,
9. Y.C. Chung, J.Y. Baek, S.R. Kim, H.W. Ko, E. Bok, W.H. Shin, S.Y. Won, B.K. Jin, Capsaicin prevents degeneration of dopamine neurons by inhibiting glial activation and oxidative stress in the MPTP model of Parkinson's disease, *Exp. Mol. Med,* **2017**. 49, p e298-9.
10. J. Liu, H. Liu, Z. Zhao, J. Wang, D. Guo, Y. Liu, Regulation of Actg1 and Gsta2 is possible mechanism by which capsaicin alleviates apoptosis in cell model of 6-OHDA-induced Parkinson's disease, *Biosci. Rep*, **2020.** 40, p. 1-12.
11. E. Bok, Y.C. Chung, K.S. Kim, H.H. Baik, W.H. Shin, B.K. Jin, Modulation of M1/M2 polarization by capsaicin contributes to the survival of dopaminergic neurons in the lipopolysaccharide-lesioned substantia nigra in vivo, *Exp. Mol. Med,* **2018**. 50.
12. O.M.E. Abdel-Salam, A.A. Sleem, M.A.E.B.M. Sayed, E.R. Youness, N. Shaffie, Capsaicin Exerts Anti-convulsant and Neuroprotective Effects in Pentylenetetrazole-Induced Seizures,

Neurochem. Res, **2020**. 45, p. 1045-1061.

13. Y.H. Siddique, F. Naz, S. Jyoti, Effect of capsaicin on the oxidative stress and dopamine content in the transgenic drosophila model of Parkinson's disease, *Acta Biol. Hung,* **2018.** 69, p. 115-124.
14. W.D. Rollyson, C.A. Stover, K.C. Brown, H.E. Perry, C.D. Stevenson, C.A. McNees, J.G. Ball, M.A. Valentovic, P. Dasgupta, Bioavailability of capsaicin and its implications for drug delivery, *J. Control. Release,* **2014**. 196, p. 96-105.
15. A.R. Ahmady, A. Solouk, S. Saber-Samandari, S. Akbari, H. Ghanbari, B.E. Brycki, Capsaicin-loaded alginate nanoparticles embedded polycaprolactone-chitosan nanofibers as a controlled drug delivery nanoplatform for anticancer activity, *Journal of Colloid and Interface Science*, **2023**. 638, p. 616-628.
16. L.Y. Zhuang, H. Zhang, N. Tian, W. Dang, S. Wu, Capsaicin-loaded folic acid-conjugated lipid nanoparticles for enhanced therapeutic efficacy in ovarian cancers, Biomedicine & Pharmacotherapy, **2017**. 91, p. 999-1005.
17. S. Kunjiappan, M. Sankaranarayanan, B.K. Kumar, P. Pavadai, E. Babkiewicz, P. Maszczyk, E. Glodkowska-Mrowka, S. Arunachalam, S. R. K. Pandian, V. Ravishankar, S. Baskararaj, S. Vellaichamy, L. Arulmani and T. Panneerselvam. Capsaicin-loaded solid lipid nanoparticles: design, biodistribution, in silico modeling and in vitro cytotoxicity evaluation, *Nanotechnology,* **2021**. 32, 095101.
18. S. Laserra, A. Basit, P. Sozio, L. Marinelli, E. Fornasari, I. Cacciatore, M. Ciulla, H. Türkez, F. Geyikoglu, A. Di Stefano, Solid lipid nanoparticles loaded with lipoyl–memantine codrug: Preparation and characterization, *Int. J. Pharm,* **2015**. 485, p. 183-191.
19. R. Ben Khalifa, I. Cacciatore, M.P. Dimmito, M. Ciulla, R. Grande, V. Puca, I. Robuffo, V. De Laurenzi, L. Chekir-Ghedira, A. Di Stefano, L. Marinelli, Multiple lipid nanoparticles as antimicrobial drug delivery systems, *J. Drug Deliv. Sci. Technol*., **2022**. 67, 102887.
20. N.H. Khan, M. Mir, E.E. Ngowi, U. Zafar, M.M.A.K. Khakwani, S. Khattak, Y.K. Zhai, E.S. Jiang, M. Zheng, S.F. Duan, J.S. Wei, D.D. Wu, X.Y. Ji, Nanomedicine: A Promising Way to Manage Alzheimer's Disease, *Front. Bioeng. Biotechnol*., **2021**. 9.
21. Y. Duan, A. Dhar, C. Patel, M. Khimani, S. Neogi, P. Sharma, N. Siva Kumar, R.L. Vekariya, A brief review on solid lipid nanoparticles: Part and parcel of contemporary drug delivery systems, *RSC Adv.*, **2020**. 10, p. 26777-26791.
22. M.K. Satapathy, T. Yen, J. Jan, R. Tang, J. Wang, R. Taliyan, C. Yang, Solid Lipid Nanoparticles (SLNs): An Advanced Drug Delivery System Targeting Brain through BBB, *Pharmaceutics*, **2021.** p. 1-36.

23. Y.Y.C. Tam, S. Chen, P.R. Cullis, Advances in lipid nanoparticles for siRNA delivery, *Pharmaceutics*, **2013**. 5, p. 498-507.
24. D.W.G. Harron, Technical Requirements for Registration of Pharmaceuticals for Human Use: The ICH Process, *The Textbook of Pharmaceutical Medicine*, **2013.** 1994, p. 447-460,
25. Y. Shi, M.J. van Steenbergen, E.A.Teunissen, L. Novo, S. Gradmann, M. Baldus, C.F. van Nostrum, W.E. Hennink. Π-π stacking increases the stability and loading capacity of thermosensitive polymeric micelles for chemotherapeutic drugs. *Biomacromolecules,* **2013**. 14, p. 1826-37.
26. G. Quiram, F. Montagner, K.L. Palmer, M.C. Stefan, K.E. Washington, D.C. Rodrigues, Novel Chlorhexidine-Loaded Polymeric Nanoparticles for Root Canal Treatment, *J. Funct. Biomater.,* **2018**. 9, p. 29.
27. A.R. Chandrasekaran, C.Y. Jia, C.S. Theng, T. Muniandy, S. Muralidharan and S.A. Dhanaraj, In vitro studies and evaluation of metformin marketed tablets-Malaysia, *J. Appl. Pharm. Sci.,* **2011.** 01, p. 214-217.
28. M.L. Bruschi, Mathematical models of drug release, Strategies to Modify the Drug Release from Pharmaceutical Systems, *Woodhead Publishing*, **2015**. p. 63-86.
29. P.K. Mante, N.O. Adomako, P. Antwi, N.K. Kusi-Boadum, N. Osafo, Solid-lipid nanoparticle formulation improves antiseizure action of cryptolepine, *Biomed. Pharmacother,* **2021**. 137, p. 11135.
30. L. Di, E.H. Kerns, K. Fan, O.J. McConnell, G.T. Carter, High-throughput artificial membrane permeability assay for blood-brain barrier, *Eur. J. Med. Chem,* **2003**. 38, p. 223-232.
31. I. Cacciatore, E. Fornasari, L. Baldassarre, C. Cornacchia, S. Fulle, E.S. Di Filippo, T. Pietrangelo, F. Pinnen, A potent (R)-alpha-bis-lipoyl derivative containing 8-hydroxyquinoline scaffold: Synthesis and biological evaluation of its neuroprotective capabilities in SH-SY5Y human neuroblastoma cells, *Pharmaceuticals*, **2013**. 6, p. 54-69.
32. P. Sozio, L.S. Cerasa, S. Laserra, I. Cacciatore, C. Cornacchia, E.S. Di Filippo, S. Fulle, A. Fontana, A. Di Crescenzo, M. Grilli, M. Marchi, A. Di Stefano, Memantine-sulfur containing antioxidant conjugates as potential prodrugs to improve the treatment of Alzheimer's disease, *Eur. J. Pharm. Sci.,* **2013**. 49, p. 187-198.
33. A. Di Stefano, L. Marinelli, P. Eusepi, M. Ciulla, S. Fulle, E.S. Di Filippo, L. Magliulo, G. Di Biase, I. Cacciatore, Synthesis and biological evaluation of novel selenyl and sulfur-L-Dopa derivatives as potential anti-Parkinson's disease agents, *Biomolecules,* **2019**. 9, p. 1-13.
34. S. Kumar, J.K. Randhawa, Solid lipid nanoparticles of stearic acid for the drug delivery of paliperidone, *RSC Adv,* **2015**. 5, p. 68743-68750.

35. R.M. Shah, F. Malherbe, D. Eldridge, E.A. Palombo, I.H. Harding, Physicochemical characterization of solid lipid nanoparticles (SLNs) prepared by a novel microemulsion technique, *J. Colloid Interface Sci*., **2014.** 428, p. 286-294.
36. M.R. Aji Alex, A.J. Chacko, S. Jose, E.B. Souto, Lopinavir loaded solid lipid nanoparticles (SLN) for intestinal lymphatic targeting, *Eur. J. Pharm. Sci.,* **2011.** 42,11-18.
37. P. Adhikari, P. Pal, A.K. Das, S. Ray, A. Bhattacharjee, B. Mazumder, Nano lipid-drug conjugate: An integrated review, *Int. J. Pharm*., **2017**. 529, p. 629-641.
38. H. Yuan, J. Miao, Y.Z. Du, J. You, F.Q. Hu, S. Zeng, Cellular uptake of solid lipid nanoparticles and cytotoxicity of encapsulated paclitaxel in A549 cancer cells, *Int. J. Pharm*., **2008**. 348, 137-145.
39. J.A. Loureiro, S. Andrade, A. Duarte, A.R. Neves, J.F. Queiroz, C. Nunes, E. Sevin, L. Fenart, F. Gosselet, M.A.N. Coelho, M.C. Pereira, N. Latruffe, Resveratrol and grape extract-loaded solid lipid nanoparticles for the treatment of Alzheimer's disease, *Molecules*, **2017.** 221, p. 16.
40. A.C. Correia, A.R. Monteiro, R. Silva, J.N. Moreira, J.M. Sousa Lobo, A.C. Silva, Lipid nanoparticles strategies to modify pharmacokinetics of central nervous system targeting drugs: Crossing or circumventing the blood-brain barrier (BBB) to manage neurological disorders, *Adv. Drug Deliv. Rev.*, **2022**. 189, p. 114485.
41. G. Tosi, T. Musumeci, B. Ruozi, C. Carbone, D. Belletti, R. Pignatello, M. Angela, G. Puglisi, The "fate" of polymeric and lipid nanoparticles for brain delivery and targeting: Strategies and mechanism of blood e brain barrier crossing and trafficking into the central nervous system*, J. Drug Deliv. Sci. Technol.,* **2016**. 32, p. 66-76.
42. S.-H. Hsu, S. A. Al-Suwayeh, C.-C. Chen, C.-H. Chi, J.-Y. Fang, PEGylated Liposomes Incorporated with Nonionic Surfactants as an Apomorphine Delivery System Targeting the Brain: In Vitro Release and In Vivo Real-time Imaging, *Curr. Nanosci*., **2011**. 7, p. 191-199.
43. S. Shrivastava, C.D. Kaur, Development of andrographolide-loaded solid lipid nanoparticles for lymphatic targeting: Formulation, optimization, characterization, in vitro, and in vivo evaluation, *Drug Deliv. Transl. Res.,* **2023**. 13, p. 658-674.
44. J.M. Koziara, P.R. Lockman, D.D. Allen, R.J. Mumper, Paclitaxel nanoparticles for the potential treatment of brain tumors, *J. Control. Release*, **2004**. 99, p. 259-269.
45. V. Teeranachaideekul, T. Chantaburanan, V.B. Junyaprasert, Influence of state and crystallinity of lipid matrix on physicochemical properties and permeation of capsaicin-loaded lipid nanoparticles for topical delivery, J. *Drug Deliv. Sci. Technol.,* **2017**. 39, p. 300-307.

46. P. Anantaworasakul, W. Chaiyana, B.B. Michniak-Kohn, W. Rungseevijitprapa, C. Ampasavate, Enhanced transdermal delivery of concentrated capsaicin from chili extract-loaded lipid nanoparticles with reduced skin irritation, *Pharmaceutics*, **2020**. 22.
47. D.Z. Hou, C.S. Xie, K.J. Huang, C.H. Zhu, The production and characteristics of solid lipid nanoparticles (SLNs), *Biomaterials,* **2003**. 24, p. 1781-1785.
48. D.A. Campos, A.R. Madureira, B. Sarmento, M.M. Pintado, A.M. Gomes, Technological stability of solid lipid nanoparticles loaded with phenolic compounds: Drying process and stability along storage, *J. Food Eng.,* **2017**. 196, p. 1-10.
49. Mishra V, Bansal KK, Verma A, Yadav N, Thakur S, Sudhakar K, Rosenholm JM. Solid Lipid Nanoparticles: Emerging Colloidal Nano Drug Delivery Systems. *Pharmaceutics*. **2018**. 18, p. 191.
50. Wu K.W., Sweeney C., Dudhipala N., Lakhani P., Chaurasiya N.D., Tekwani B.L., Majumdar S. Primaquine Loaded Solid Lipid Nanoparticles (SLN), Nanostructured Lipid Carriers (NLC), and Nanoemulsion (NE): Effect of Lipid Matrix and Surfactant on Drug Entrapment, in vitro Release, and ex vivo Hemolysis. *AAPS Pharm. Sci. Tech.*, **2021**. 22, p. 240.
51. J. Xu, B. Xu, D. Shou, X. Xia, Y. Hu, Preparation and evaluation of vancomycin-loaded N-trimethyl chitosan nanoparticles, *Polymers (Basel*), **2015**. 7, p. 1850-1870.
52. H. Amekyeh, N. Billa, Lyophilized drug-loaded solid lipid nanoparticles formulated with beeswax and theobroma oil, Molecules, **2021.** 26, p. 1-13.
53. Z.X. Zhao, J.F. Wang, L.L. Wang, X.M. Yao, Y.L. Liu, Y. Li, S. Chen, T. Yue, X.T. Wang, W.F. Yu, Y.M. Liu, Capsaicin Protects Against Oxidative Insults and Alleviates Behavioural Deficits in Rats with 6-OHDA-Induced Parkinson's Disease via Activation of TRPV1, *Neurochem. Res*., **2017**. 42, p. 3431-3438.
54. J.C. Stockert, A. Blázquez-Castro, M. Cañete, R.W. Horobin, Á. Villanueva, MTT assay for cell viability: Intracellular localization of the formazan product is in lipid droplets, *Acta Histochem*., **2012**. 114, p. 785-796.
55. Q.Q. Chen, C. Haikal, W. Li, J.Y. Li. Gut Inflammation in Association with Pathogenesis of Parkinson's Disease. *Front. Mol. Neurosci*., **2019**. 12, p. 218.

3.2. Propolis-Loaded SLNs Targeting Pathogens Associated with Gastrointestinal Diseases

3.2.1. Introduction

Propolis is a resinous natural product composed of a complex mixture of substances, including plant resins, waxes, honey, pollen, and royal jelly, which honeybees collect from the flowers and bark of certain trees and plants. It functions as a protective barrier against environmental threats and microbial contamination [1, 2]. Due to its broad spectrum of pharmacological activities - including antibacterial, antiviral, antifungal, anti-inflammatory, and anticancer - propolis has gained significant attention as a health supplement and functional ingredient in foods, beverages, and traditional medicine [3]. Renewed scientific interest has been directed toward characterizing the chemical composition and bioactivity of propolis, which, however, varies considerably depending on botanical and geographical origins.

Notably, propolis has shown antimicrobial activity against *Helicobacter pylori (H. pylori)*, *Fusobacterium nucleatum (F. nucleatum)*, and *Clostridium difficile (C. difficile)*, pathogens implicated in gut dysbiosis and in the development or exacerbation of gastrointestinal (GI) as well as inflammatory bowel diseases (IBDs). *H. pylori* has been recognized as a key pathogen implicated in GI disorders such as gastritis, peptic ulcer, and gastric cancer. *H. pylori* eradication is challenged given its genetic variability, its ability of both forming biofilms and of entering in the Viable But Not Culturable (VBNC) state, and the subsequent rise in antimicrobial resistance. Consequently, the therapy against *H. pylori* infection includes at least two antimicrobials for a long-term period. In detail, the first-line recommended treatment in areas of high (>15%) or unknown clarithromycin resistance is Bismuth Quadruple Therapy (BQT) for 14 days consisting of proton pump inhibitor (PPI), bismuth salt, tetracycline and metronidazole [4]. Since the World Health Organization (WHO) has identified *H. pylori* as a group I carcinogen, considerable efforts have been made to develop a strategy to counteract this pathogen. In this context, propolis has shown antimicrobial activity against bacteria responsible for gut dysbiosis, highlighting its potential as a natural therapeutic agent for managing GI disorders, including those associated with IBD [5,6]. Propolis antimicrobial activity is primarily attributed to polyphenolic compounds that interact with microbial proteins

through hydrogen bonding and ionic interactions, leading to conformational disruption and loss of function [7]. These mechanisms are particularly promising in the context of rising antimicrobial resistance (AMR), as propolis has been shown to act synergistically with conventional antibiotics, enhancing efficacy while reducing the required dosage and associated side effects [8]. Additionally, it has been demonstrated that synergistic effects of propolis occur when combined with antimicrobial agents against both drug-sensitive and drug-resistant bacterial strains [9].

IBD affects over 2 million individuals in Europe and 1.5 million in North America, with high healthcare costs, many of which are related to long-term pharmacological interventions [10-12]. Dysbiosis-related infections by *C. difficile*, *F. nucleatum*, and *H. pylori* may aggravate IBD symptoms, contributing to severe pain, mucosal inflammation, disruption of intestinal barrier integrity, and increased susceptibility to recurrent infections [13-17]. Moreover, *C. difficile* and *F. nucleatum* are pathogens of great clinical relevance, given that the former causes severe infectious colitis that leads to significant morbidity and mortality worldwide [18], while the latter, in addition to being an oral pathogen, has been correlated with colorectal cancer [19].

However, despite its promising bioactivity, the clinical translation of propolis is hampered by poor water solubility, chemical instability, low bioavailability, and rapid GI metabolism. These limitations hinder propolis absorption and distribution in conventional dosage forms, markedly reducing its therapeutic efficacy. Overcoming these drawbacks requires advanced delivery systems to ensure that its bioactive components reach target sites in adequate concentrations [20].

Various strategies have been explored to improve propolis solubility, stability, and bioavailability - including emulsions, liposomes, and polymeric nanoparticles - but many of these systems present limitations such as the use of organic solvents, poor scalability, or insufficient protection of labile constituents [21].

Solid lipid nanoparticles (SLNs) have emerged as a promising alternative, offering several advantages: protection of encapsulated bioactives from degradation, enhanced bioavailability, improved permeability across mucosal and dermal barriers, and the possibility to avoid organic solvents during preparation. Furthermore, their membrane-mimicking properties make them particularly suitable for encapsulating lipophilic natural agents such as those found in propolis [22].

While several studies have investigated propolis-loaded nanoparticles, there is still a lack of research on SLN-based systems specifically developed for GI conditions such as IBD. Therefore, this study aimed to develop and characterize SLNs loaded with propolis ethanolic extract (PEE) obtained by using raw propolis collected in Chieti (42° 20′ 53.8″ N, 14° 09′ 53.8″ E), to overcome limitations of propolis. The experimental work involved screening multiple formulations, optimizing physicochemical characteristics, and performing a comprehensive characterization, including release profile, stability, permeability, antimicrobial and anti-inflammatory activities, and *in vivo* safety evaluation [23].

3.2.2. Results and discussion

PEE characterization

PEE was obtained using an ethanolic maceration, a method suitable for preserving the integrity of thermolabile phenolic compounds. The extraction efficiency % reached 74%, indicating that a considerable portion of bioactive constituents was effectively extracted into the ethanolic phase.

To characterize PEE, HPLC analyses were performed using the optimized conditions reported in the experimental section. In **Figure 10**, the chromatogram of PEE confirmed the presence of several bioactive compounds, including caffeic acid, ferulic acid, quercetin, caffeic acid phenethyl ester (CAPE), chrysin, and galangin, identified by comparing their retention times with those of analytical standards (RT = 11.78, 17.96, 34.84, 47.81, 49.97, and 51.07 min, respectively). These findings are consistent with previous literature data describing the rich phenolic profile of propolis [45].

Among the identified compounds, chrysin was the most abundant in PEE, representing 5.78%. Its well-known antioxidants, anti-inflammatory, and antimicrobial properties suggest a potential application in these fields [46].

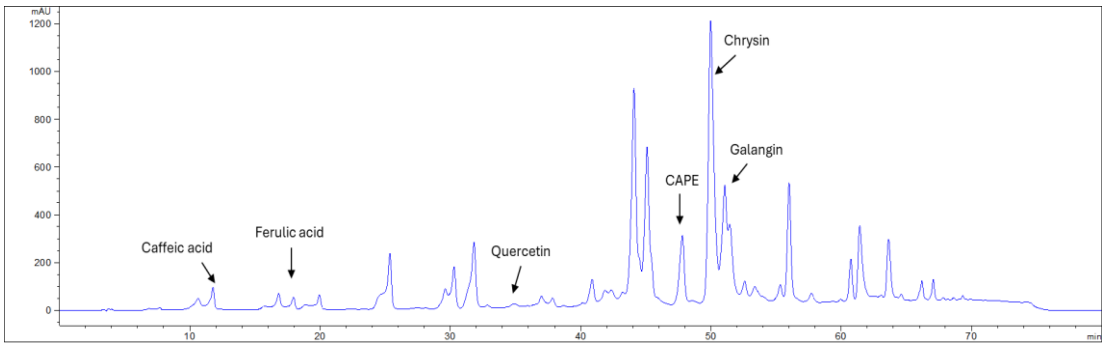


Figure 10. Chromatograms of PEE obtained by HPLC analysis: caffeic acid; ferulic acid; quercetin; CAPE; chrysin; galangin.

TPC and TFC were evaluated through the Folin-Ciocalteau and Aluminium chloride methods, respectively. TPC and TFC were found to be 583.64 ± 73.39 mg GAE/g and 153 mg Q/g, respectively [47]. These high concentrations are consistent with literature values and confirm that phenolic and flavonoids represent the most abundant constituents in the PEE [48]. The slightly higher value observed in this study can be explained by the natural variability in propolis composition, which is strongly influenced by its

geographical and botanical origins and consequently affects its phytochemical profile [49, 50].

PEE-SLNs preparation and characterization

The preformulative phase involved the development of eleven distinct SLNs by systematically varying key parameters, including the lipid-to-extract ratio, lipid-to-surfactant ratio, and total lipid content. The objective was to identify the most suitable composition for optimal formulation. Each preparation was characterized in terms of critical physicochemical parameters, including particle size, PDI, ζ-potential, and EE%, with the latter calculated in terms of chrysin, the major constituent of PEE (Table 5). Brij 78, SL, and TS were selected as core excipients to ensure nanoparticle stability, enhance encapsulation efficiency, enable controlled release, and promote biocompatibility and intestinal absorption [51]. The solid-state nature of the lipid components at physiological temperature facilitates the entrapment and stabilization of PEE constituents, which are prone to hydrolytic and oxidative degradation. The solid lipid matrix forms a protective core, improving the chemical stability and bioavailability of the encapsulated PEE. Brij 78 contributes to the stabilization of the hydrophobic PEE constituents by reducing interfacial tension during emulsification, promoting uniform nanoparticle formation, and preventing aggregation during storage. Its optimal hydrophilic-lipophilic balance allows the formation of a stable interfacial film, further contributing to colloidal stability [52, 53].

Among the initial formulations (PEE-SLN1 to PEE-SLN5), PEE-SLN4, prepared with a lipid-to-PEE ratio of 1:6 and a lipid-to-surfactant ratio of 1:2.5, emerged as the most promising. It exhibited favorable physicochemical properties: a mean particle size of 187.79 nm, suitable for intestinal delivery; a low PDI of 0.16, indicative of a monodisperse population; a ζ-potential of -26.30 mV, reflecting good electrostatic stability; and an EE% of 41.18%. To further enhance EE%, additional formulations were developed by increasing the absolute quantities of lipids and surfactants, while maintaining their relative ratios.

All the formulations demonstrated suitable physicochemical characteristics, with particle sizes ranging from 139 to 460 nm and negative surface charges. Notably, PEE-SLN10 exhibited optimal properties, with a particle size of 161.71 nm, a PDI of 0.14, a ζ-potential

of -23.13 mV, and the highest EE% corresponding to 86.08%. The enhanced properties of this formulation could be attributed to an optimal balance of lipophilic and amphiphilic components, which promotes the effective incorporation of PEE within the lipid matrix. In contrast, further increases in lipid and Brij 78 concentrations (PEE-SLN11) led to a significant decline in EE%, likely due to unfavorable interactions among formulation components.

PEE-SLN10 was thus selected as the optimized formulation, representing the best compromise among size, surface charge, and EE%. Formulations with lower lipid/surfactant ratios (*e.g.*, PEE-SLN1 and PEE-SLN2) resulted in larger particles with poor EE%, while those with very small particle sizes (*e.g.*, PEE-SLN3) showed low EE% and weak surface charge, suggesting limited stability. Intermediate formulations (PEE-SLN4 to PEE-SLN8) presented acceptable size and ζ-potential values but failed to reach the encapsulation levels achieved by PEE-SLN10.

Variations in ζ-potential (**Table 5**) were strongly influenced by lipid and surfactant concentrations as well as EE%. Formulations with higher Brij 78 content or lower lipid-to-PEE ratios (*e.g.*, PEE-SLN3, PEE-SLN6) exhibited reduced surface charge due to the protective effect of non-ionic surfactants. On the other hand, intermediate Brij 78 levels combined with balanced lipid-to-PEE ratios (*e.g.*, PEE-SLN4, PEE-SLN5, PEE-SLN7) produced more negative ζ-potentials (-26 to -27 mV), indicative of enhanced electrostatic stabilization. In formulations with higher EE% (PEE-SLN10 and PEE-SLN11), partial surface adsorption of PEE contributed to reduced surface charge, consistent with saturation of the lipid matrix.

Chrysin EE% was closely dependent on formulation composition. Higher lipid-to-PEE ratios favored retention of the extract within the lipid core, minimizing drug loss during nanoparticle solidification. While excessive PEE content disrupted lipid matrix organization, impairing encapsulation. Brij 78 improved EE% by facilitating emulsification and nanoparticle stabilization; however, at high concentrations, it competed with the drug for incorporation into the lipid domains, thereby reducing EE%. These findings are consistent with previous studies on polyphenol-loaded nanocarriers, where drug solubility within the lipid phase and partitioning behaviour at the oil-water interface were identified as key determinants of EE% [54].

Table 5. Preformulative studies considering various lipids: PEE, lipid: Brij 78 ratios, and increasing amounts of lipids.

Formulation	Lipid: PEE ratio	Lipid: Brij78 ratio	TS (mg)	SL (mg)	Brij 78 (mg)	PEE (mg)	Size (nm)	PDI	ζ-potential (mV)	EE%
PEE-SLN1	2:1.0	1:2.5	20	4	50	10	328.66 ± 2.06	0.17 ± 0.03	-25.46 ± 0.76	21.13
PEE-SLN2	1:1.5	1:2.5	20	4	50	30	322.17 ± 11.28	0.16 ± 0.02	-24.70 ± 0.27	15.87
PEE-SLN3	1:3.0	1:2.5	20	4	50	60	105.50 ± 3.22	0.25 ± 0.01	-7.10 ± 1.60	13.11
PEE-SLN4	1:6.0	1:2.5	20	4	50	120	187.79 ± 3.75	0.16 ± 0.02	-26.30 ± 0.65	41.18
PEE-SLN5	1:7.0	1:2.5	20	4	50	240	205.20 ± 2.50	0.19 ± 0.02	-26.90 ± 0.80	37.57
PEE-SLN6	1:6.0	1:1.0	20	4	20	120	177.02 ± 2.89	0.19 ± 0.02	-5.10 ± 1.00	50.23
PEE-SLN7	1:6.0	1:2.0	20	4	40	120	187.51 ± 4.70	0.18 ± 0.05	-27.30 ± 0.90	67.48
PEE-SLN8	1:6.0	2:5.0	20	4	100	120	200.69 ± 1.65	0.21 ± 0.03	-16.80 ± 0.92	68.66
PEE-SLN9	1:6.0	1:2.5	40	8	110	120	139.09 ± 0.15	0.20 ± 0.03	-19.13 ± 1.07	29.45
PEE-SLN10	1:6.0	1:2.5	80	16	220	120	161.71 ± 3.35	0.14 ± 0.05	-23.13 ± 0.15	86.08
PEE-SLN11	1:6.0	1:2.5	120	24	330	120	455.70 ± 20.96	0.21 ± 0.02	-8.70 ± 0.68	54.00

All the measurements were performed in triplicate. Values are reported as means ± SD.

Regarding the TPC and TFC, after encapsulation of PEE into SLNs, they both consistently decreased to 117.43 ± 77.39 mg GAE/g and 24.9 mg Q/g, respectively, compared to the values found in the free extract (**Table 6).** Although a reduction in phenolic and flavonoid content was observed after encapsulation into SLNs, the resulting formulation still retained measurable quantities of bioactive compounds, indicating that a fraction of phenolics and flavonoids was effectively retained within the SLNs.

Table 6. TPC and TFC contents of PEE and PEE-SLN10.

Sample	TPC (mgGAE/g)	TFC (mgQE/g)
PEE	583.64 ±73.39	153 ± 20.2
PEE-SLN10	117.43 ±77.39	24.9 ± 4.6

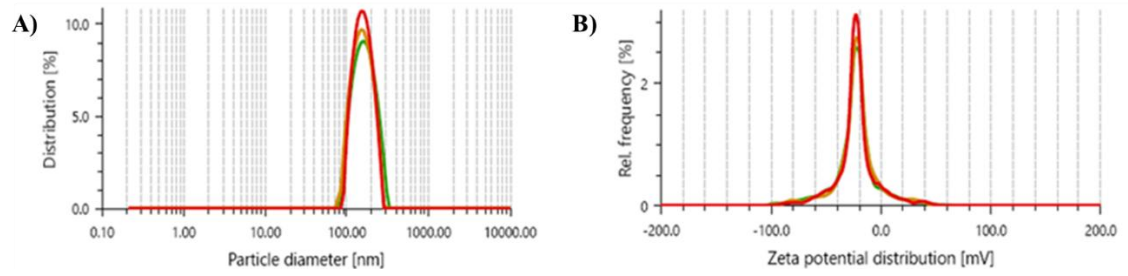


Figure 12. Particle diameter **(A)** and ζ-potential **(B)** measurements for PEE-SLN10.

The size and the morphology of PEE-SLN10 were assessed by TEM analysis. As depicted in **Figure 13**, the particle structure is nearly spherical. The figure highlights the successful development of nanoparticles having a homogenous size distribution, in agreement with the low PDI reported in **Table 5**.

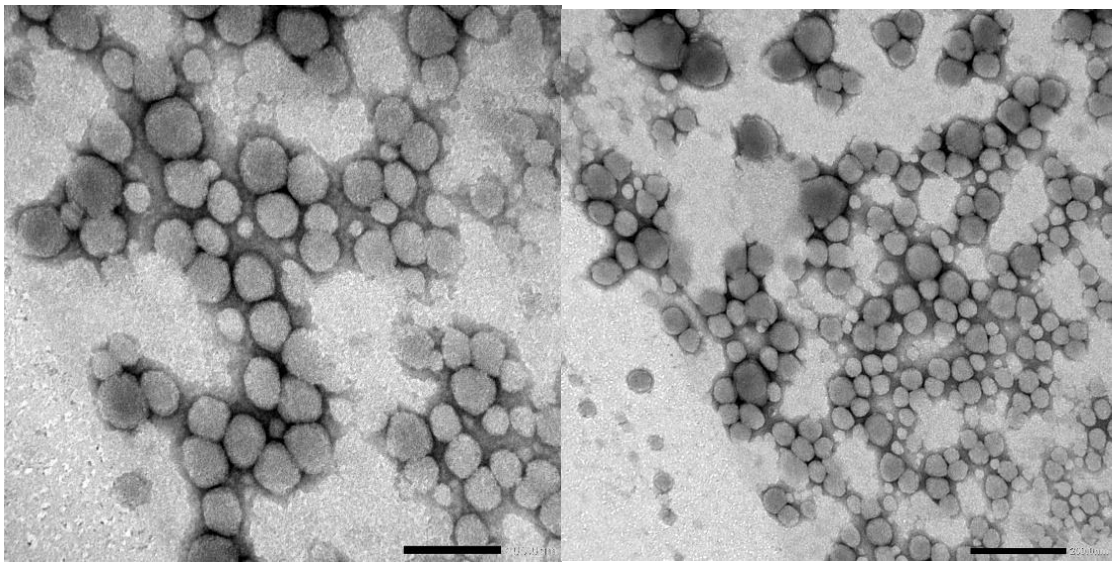


Figure 13. Structure of the PEE-SLN10 obtained by the TEM analysis (bars refers to 100.00 nm and 200.00 nm, on left and right, respectively).

Differential scanning calorimetry (DSC)

DSC analysis was performed to investigate the thermal behaviour of raw propolis and PEE-SLN10. The thermogram of the starting material, TS, exhibited a sharp endothermic peak at 55.66 °C with a high enthalpy value (ΔH) of 161.46 J/g, confirming its crystalline state. The raw propolis exhibited a broad endothermic peak at approximately 47.85°C with a ΔH of 67.58 J/g, a value related to the melting of waxes and resins contained (**Table 7**). In contrast, the DSC curve of the PEE-SLN10 showed a sharper endothermic peak at a higher temperature (49.46 °C) but with a significantly reduced enthalpy (ΔH =

17.95 J/g) as reported in **Figure 14**. The disappearance of the representative melting peak of raw propolis and TS in the thermogram of PEE-SLN10, as well as the shift of endothermic peaks of SLN10-unloaded, suggests that PEE is efficiently encapsulated within the lipid matrix. Moreover, the marked decrease in ΔH indicates a reduction in the overall crystallinity of the system due to the incorporation of PEE, which destabilizes the lipid structure. These results confirm the successful loading and the formation of a less crystalline lipid arrangement, which could potentially enhance the controlled release [55].

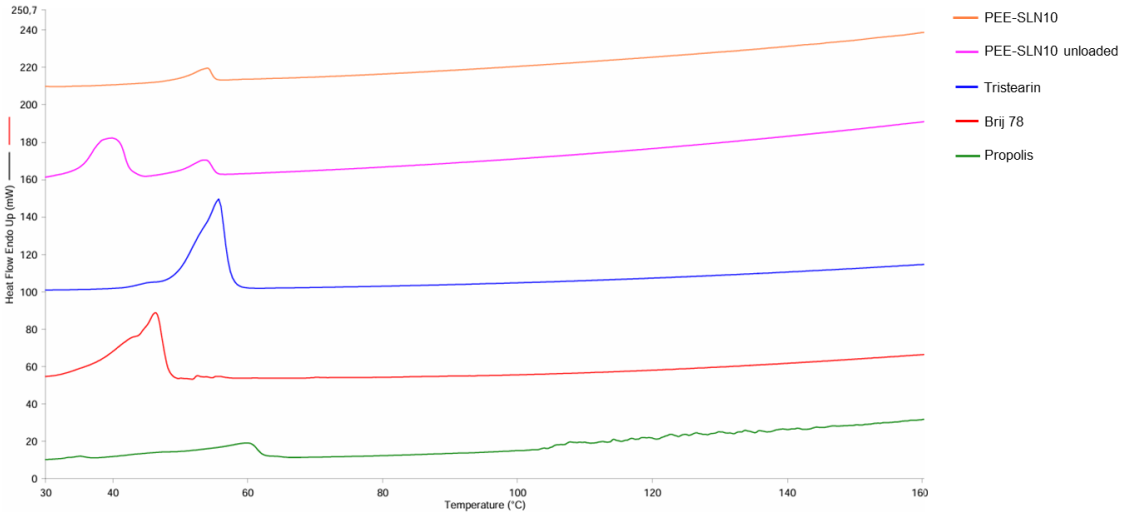


Figure 14. Thermal analysis of PEE-SLN10 (orange line), SLN-10 unloaded (pink line), tristearin (blu line), Brij 78 (red line), and propolis (green line).

Table 7. DSC data of T_{onset}, $T_{melting}$, enthalpy (ΔH), and area of propolis, PEE-SLN10, SLN-10 unloaded, tristearin, and Brij 78.

	T_{onset} (°C)	**$T_{melting}$ (°C)**	**ΔH (J/g)**	**Area (mJ)**
Propolis	47.85	59.78	67.58	540.70
PEE-SLN10	49.46	54.01	17.95	157.95
SLN-10 unloaded	34.62	39.75	105.10	756.73
	49.07	53.52	27.22	196.02
Tristearin	49.90	55.66	161.46	741.72
Brij 78	41.27	46.25	181.06	1430.41

PEE-SLN10 stability studies

The stability profile of the PEE-SLN10 was assessed in three different conditions: over time, in simulated body fluids, and in accelerated stress conditions (40-90 °C). During long-term storage, the SLNs keep size and PDI values, suggesting preserved colloidal stability (**Figure 15**). However, a shift in ζ-potential was observed on day 112, becoming less negative. This variation may be representative of destabilization phenomena,

responsible for modification of the SLNs' surface composition, maybe due to rearrangement or partial degradation of surface-associated components, without compromising overall structural integrity. These modifications alter the electrostatic environment without compromising the structural integrity of the SLNs, indicating that while the core remains stable, the surface properties and potentially the biological interactions may evolve over time. Regarding the EE% after storage over time, no significant drug leakage was observed for PEE-SLN10, with drug expulsion not exceeding 10%.

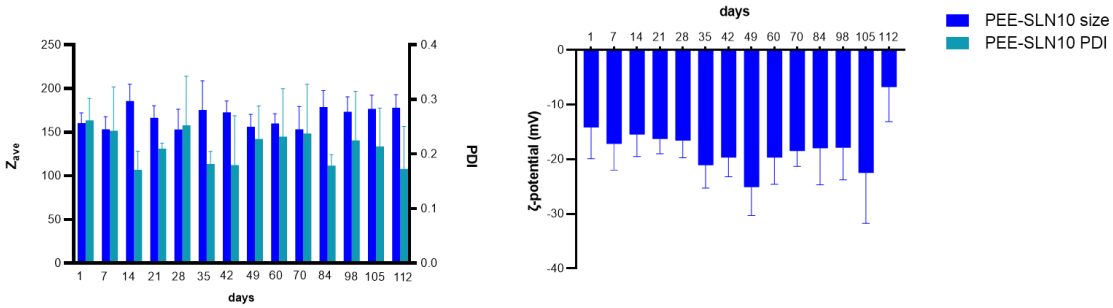


Figure 15. Storage stability of PEE-SLN10.

In simulated GI fluids, the PEE-SLN10 remained stable, with only slight variations in size (**Figure 16**). When analyzed in SIF, an increase in diameter was observed at t0 (reaching a value of approximately 200 nm), suggesting that interactions between the SLNs and the simulated fluid occur. The diameter slightly decreases over time, maintaining the overall initial value. As in the case of SIF, in SGF, the nanoparticles increased in diameter after 2 h, reaching a size of about 300 nm, with no possibility of detection at 6 h. The observed behaviour of PEE-SLN10, characterized by SGF instability, may represent a key advantage for this formulation, since it allows the loaded active compounds to be promptly released at the gastric level and act against pathogens involved in diseases affecting the stomach, ensuring a site-specific targeting.

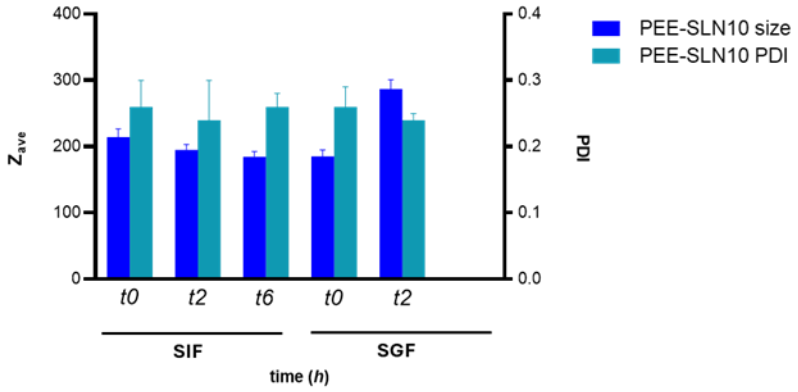


Figure 16. SIF and SGF stability of PEE-SLN10.

Moreover, in accelerated conditions (**Figure 17**), PEE-SLN10 demonstrated good thermal stability in the range of 40-90 °C, resisting heat-induced destabilization and suggesting compatibility with common processing and storage conditions. Together, these findings confirm the favorable physicochemical features of the PEE-SLN10 and their potential applicability in scale-up processes.

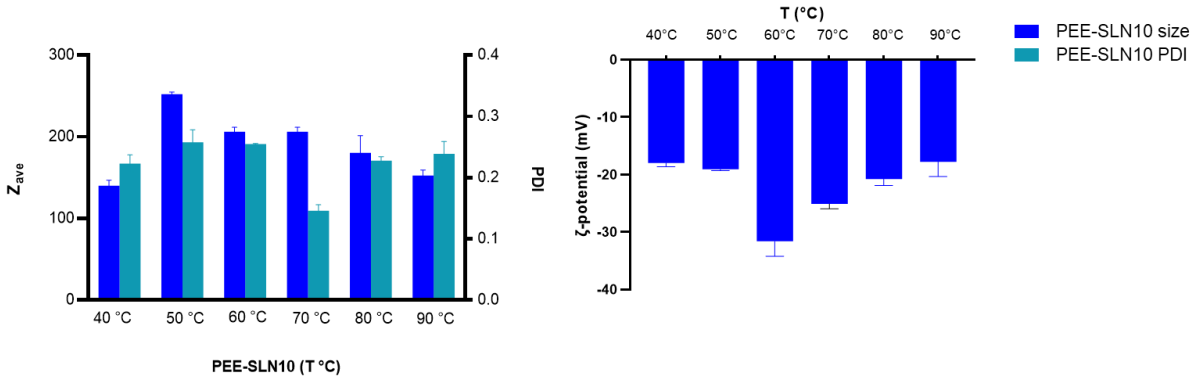


Figure 17. Thermal stability of PEE-SLN10.

In vitro release studies

The *in vitro* release profile of PEE-SLN10 was evaluated based on the release of chrysin, one of the most abundant flavonoids found in PEE, selected as a marker, to study the release pattern (**Figure 18**). Results indicated that PEE-SLN10 promoted a gradual release of chrysin, in contrast to free PEE, which ensures its immediate availability. Notably, the PEE-SLN10 displayed a biphasic release profile, characterized by a gradual release of approximately 20% during the first 2 h in SGF, likely due to surface-associated chrysin and destabilization phenomena due to the instability involving the nanoparticles

in the media. This initial phase was followed by a more sustained release phase in SIF, indicating the controlled diffusion of chrysin from the lipid matrix. This controlled behaviour may offer significant pharmacokinetic advantages, such as prolonged intestinal residence time, which translates to enhanced absorption of chrysin, otherwise limited by its poor solubility and rapid degradation [56, 57]. Overall, the formulation demonstrates preferential efficacy against gastric bacteria, due to the rapid release under gastric conditions, while still retaining a fraction of the active compound capable of a slower, sustained release that may contribute to antibacterial activity at the intestinal site. This biphasic behaviour can therefore be considered as a dual-targeting strategy, with a preferential impact in the stomach and a complementary, although less pronounced, effect in the intestine.

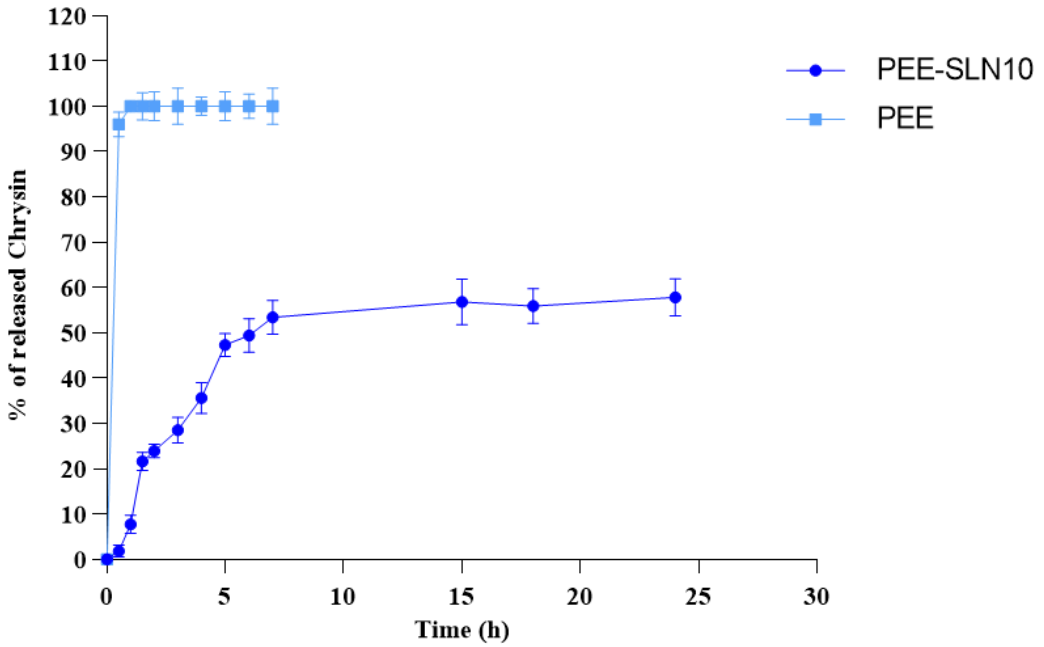


Figure 18. Release profile of chrysin from PEE and PEE-SLN10 in SGF and SIF.

The release profile of phenolic compounds from PEE-SLN10 exhibited biphasic behaviour, characterized by an initial limited release followed by a marked increase upon the change of release medium (**Figure 19**). In SGF, approximately 20% of flavonoids and 10% of total polyphenols were released within the first 2 h. Upon transition to SIF, the release significantly increased, reaching about 50% for flavonoids and 40% for polyphenols. This behaviour can be attributed to the stability of the lipid matrix in the acidic gastric environment, which limits the release and its subsequent degradation in the

presence of intestinal enzymes. Moreover, the higher release percentage of flavonoids compared to polyphenols may be explained by their greater solubility in SIF. These results are in agreement with the stability in simulated GI-fluids.

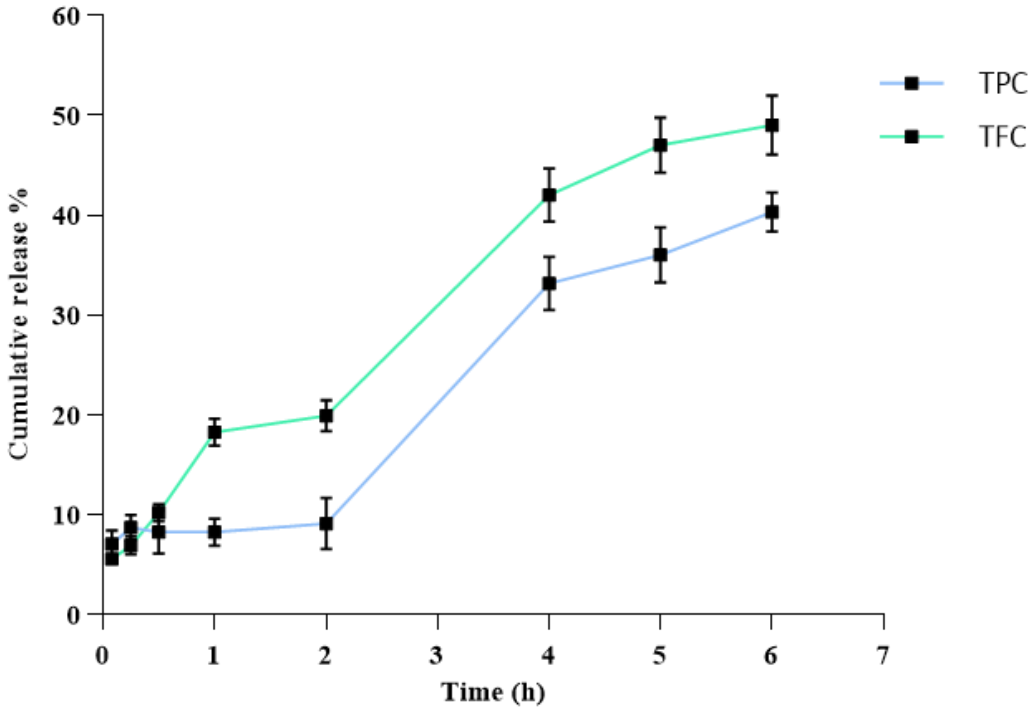


Figure 19. Release profile in terms of polyphenols and flavonoids from PEE-SLN10 in SGF and SIF.

Permeability studies

PAMPA studies

PEE-SLN10 was tested in the PAMPA model under pH conditions simulating various segments of the GI tract. The permeation behaviour of chrysin was evaluated to assess the SLNs' ability to enhance passive diffusion. The use of this *in vitro* method enables the identification of passive permeability mechanisms, independent of cellular uptake or active transport, thereby revealing the intrinsic permeability properties of the formulation. According to our results (**Table 8**), PEE showed moderate permeability to cross the model membrane with an apparent permeability (*Pe*) of 0.12×10^{-6} cm/s, suggesting poor passive absorption. In contrast, PEE-SLN10 exhibited higher permeability values corresponding to 0.30×10^{-6} cm/s, suggesting that the lipid system can enhance the transport of chrysin.

Even though both values are still below the typical permeability threshold (1×10^{-6} cm/s), PEE-SLN10 revealed an increased permeability compared to free extract, potentially improving its bioavailability.

A possible explanation for this behaviour may be attributed to improved solubilization, combined with favorable membrane interactions, and to the protective effects exerted by the lipid matrix versus free PEE. This matrix could enhance the solubility of poorly water-soluble chrysin, thereby increasing the concentration gradient that drives passive diffusion across the artificial membrane of the PAMPA system, potentially fluidizing the membrane and facilitating the transfer of chrysin.

These data agree with those reported regarding SLNs loaded with plant extracts [28]. This enhancement is generally attributed to improved solubility, protection of labile phytochemicals from degradation, and increased diffusivity across lipid-mimetic membranes. Our results highlight the potential of lipid-based systems as carriers for polyphenolic compounds with low oral absorption.

Table 8. PAMPA-GI permeability assays in terms of chrysin[a].

	PAMPA-GI permeability (*Pe* 10^{-6} cm/s)	**Classification[c]**	**PAMPA-GI permeability (*Pe* 10^{-6} cm/s)**	**Classification[c]**
	pH 5[b]		**pH 7[b]**	
PEE	0.12 (± 0.03)	GI -	0.07 (± 0.02)	GI -
PEE-SLN10	0.30 (± 0.06)	GI -	0.24 (± 0.05)	GI -
SLN10 unloaded	-	-	-	-

[a]Each experiment was conducted in triplicate, and is expressed as mean ±SD.
[b]pH of both donor and acceptor compartments.
[c]GI + (high GI permeation): $Pe > 1.5 \times 10^{-6}$ cm/s; GI - (low GI permeation): $Pe < 1.5 \times 10^{-6}$ cm/s.

Permeability studies using EpiIntestinal™

To extend the permeability assessment under a more biomimetic environment, chrysin transport was evaluated using the EpiIntestinal™ tissue model. As reported in Figure 20, the P*app* of chrysin was determined to be 3.22×10^{-7} cm/s, indicating low-to-moderate translocation across the intestinal epithelium. Even if the permeability value from PEE-SLN10 remains low, the *Papp* resulted in improvement compared to free PEE. This suggests that the lipid system could facilitate crossing across the epithelial surface, improving the poor physicochemical properties of chrysin. This low improvement in *Papp* value could be due to the aggregation of particles at the epithelial surface, which may create a steric barrier, thereby limiting chrysin's interactions with the membrane

interface. Beyond physical barriers at the epithelial surface, active efflux transporters and intracellular retention mechanisms may further limit chrysin permeability.

To further improve the chrysin permeability from PEE-SLNs, mucoadhesive coatings could be explored. This coating could enhance residence time at the mucosal site, which prolongs drug release and absorption. This mucoadhesion is achieved through interactions between the coating polymer and mucus glycoproteins, with common coating materials including chitosan and hyaluronic acid. The enhanced mucoadhesion facilitates extended exposure of the drug to the mucosa, increasing the probability of cellular uptake and penetration [58].

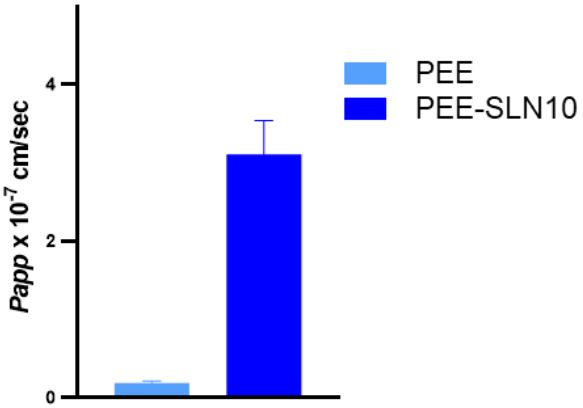


Figure 20. Values of apparent permeability coefficients of chrysin from PEE and PEE-SLN10.

Biological studies

MIC and MBC determination of PEE and PEE-SLN10 vs Fusobacterium nucleatum ATCC 25586, Clostridioides (Clostridium) difficile ATCC 700057, and Helicobacter pylori ATCC 700684 (CLA^R)

PEE-SLN10 was tested against *F. nucleatum*, *C. difficile,* and *H. pylori* CLA^R reference strains (Table 9). PEE, PEE-SLN10, and SLN10 unloaded displayed no antimicrobial activity against these two anaerobic bacteria while showing MIC value at 0.06 µg/mL against *H. pylori*. Possible explanations for these different results could be related to the key differences between the chosen pathogens, such as the fact that *H. pylori* is a microaerophilic bacterium, whereas *F. nucleatum* and *C. difficile* are strict anaerobes. These different growth conditions could influence the efficacy of both PEE and PEE-SLN10 in inhibiting bacterial growth. Moreover, given that *H. pylori* is a Gram-negative bacterium, whereas *C. difficile* is a Gram-positive bacterium, there are differences in cell

wall structure. *F. nucleatum* and *H. pylori* are both Gram-negative bacteria and can resist compound entry via different types of efflux pumps and porins, but mechanisms vary due to their different environments [59-62]. This result demonstrated that the obtained formulation was able to increase the antimicrobial activity compared to the free PEE. This behaviour could be related to the improved protection guaranteed to PEE from the lipid matrix that can enhance mechanisms responsible for PEE's active compounds. Indeed, as previously described by Asadi *et al.,* bioactive compounds such as chrysin can bind and inhibit *H. pylori* urease, exerting antimicrobial activity [63]. The lack of antimicrobial activity against the two anaerobes selected for this study could be related to the fact that these bacteria do not produce this enzyme. Moreover, polyphenols' hydroxyl groups may interact with microbial cell membranes, proteins, and organelles, exerting antimicrobial activity, as well as bacterial detachment, as reported previously. These interactions may interfere with metabolic pathways, leading to damage to proteins and nucleic acids as well as bacterial cell disruption [64-67].

Table 9. MIC and MBC determination of PEE, PEE-SLN10, and SLN10 unloaded versus *Fusobacterium nucleatum* ATCC 25586, *Clostridioides* (*Clostridium*) *difficile* ATCC 700057, and *Helicobacter pylori* ATCC 700684 via viability assays and the colony-forming unit count, respectively. Amoxicillin (AMX), vancomycin (VAN), clarithromycin (CLA), and metronidazole (MTZ) were used as positive controls.

	Fusobacterium nucleatum **ATCC 25586**		***Clostridioides* (*Clostridium*) *difficile*** **ATCC 700057**		***Helicobacter pylori*** **ATCC 700684**	
Compound	**MIC (µg/mL)**	**MBC (µg/mL)**	**MIC (µg/mL)**	**MBC (µg/mL)**	**MIC (µg/mL)**	**MBC (µg/mL)**
PEE	>128	>128	>128	>128	32	64
PEE-SLN10	>128	>128	>128	>128	0.06	0.25
SLN10 unloaded	>128	>128	>128	>128	0.06	0.25
AMX	0.03	0.06	-	-	-	-
VAN	-	-	2	4	-	-
MTZ	-	-	-	-	0.5	1
CLA	-	-	-	-	8	16

***In vivo* toxicity studies using the *G. mellonella* model**

PEE-SLN10 was selected for toxicity tests in the *G. mellonella* model. As mentioned in the experimental section, the compound concentration was increased 10-fold above the MIC value. *G. mellonella* larvae were also infected with PEE, SLN10 unloaded, TS, SL, and Brij 78 as controls to evaluate their toxicity *in vivo* model. As shown in Figure 21, no larvae died during the follow-up period of four days after treatment, demonstrating that the compounds are non-toxic at the concentration tested. While the *G. mellonella* model offers a cost-effective, rapid, and ethically favorable platform for *in vivo* screening, including preliminary assessments of toxicity, it does have physiological differences compared to mammalian systems. Although it does not replicate the full complexity of mammalian metabolism or adaptive immune responses, it provides valuable initial insights that can pose the bases for subsequent studies in higher-order models.

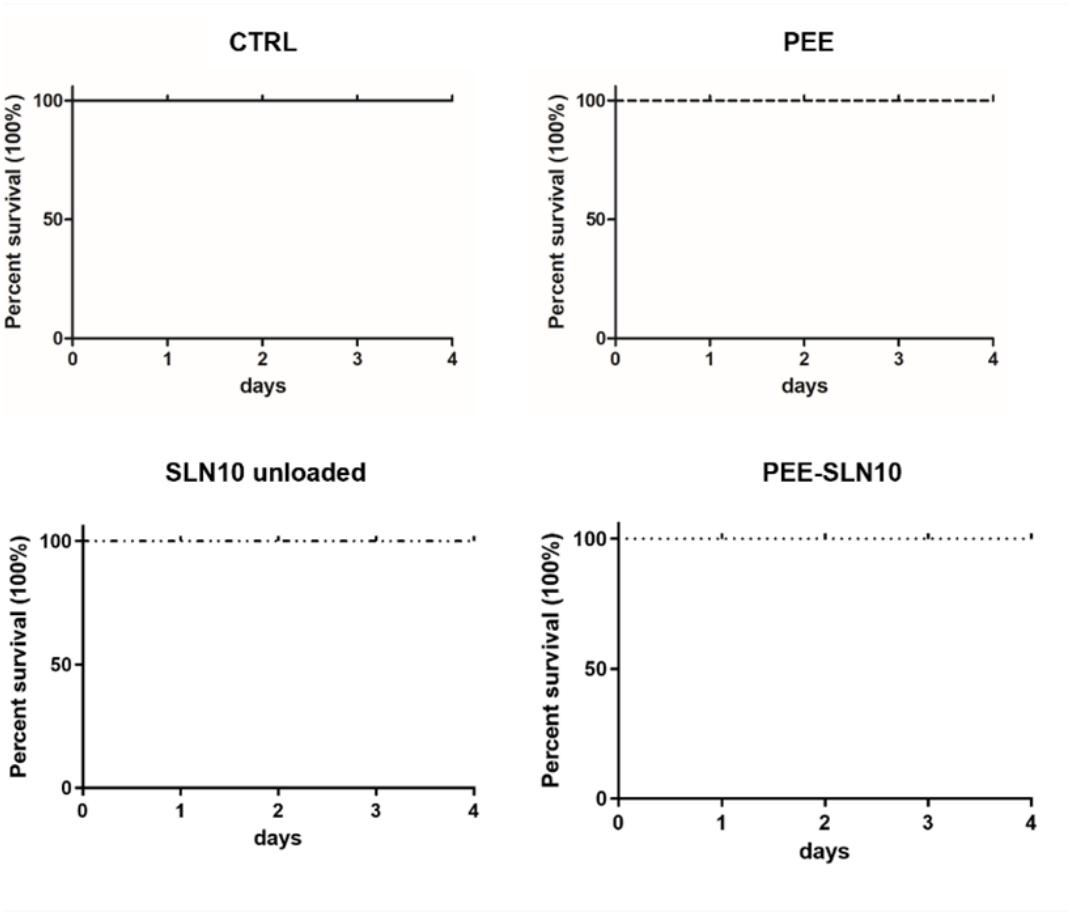


Figure 21. Survival curves related to the toxicity of PEE, TS, SL, and Brij 78 in the *G. mellonella in vivo* model.

Cell metabolic activity

Under basal conditions, the PEE and PEE-SLN10 are not effective on the cell metabolic activity of macrophages up to the concentration of 2 µg/mL after 24 h of treatment. After this concentration, a significant dose-dependent decrease in cell metabolic activity is registered compared to the untreated control. Notably, a dramatic decrease (around 80 %) in the percentage of metabolically active cells is assessed in the presence of PEE-SLN10 and SLN10 unloaded (**Figure 22a**). Under pro-inflammatory conditions, the stimulation with LPS significantly increases cell metabolic activity, as expected (**Figure 22b**). The PEE, as well as PEE-SLN10 and SLN10 unloaded, significantly decreased cell metabolic activity of LPS-stimulated macrophages, counteracting the effect of LPS alone. As for basal conditions, the cell metabolic activity of LPS-stimulated cells is significantly decreased in the higher range of concentrations [68].

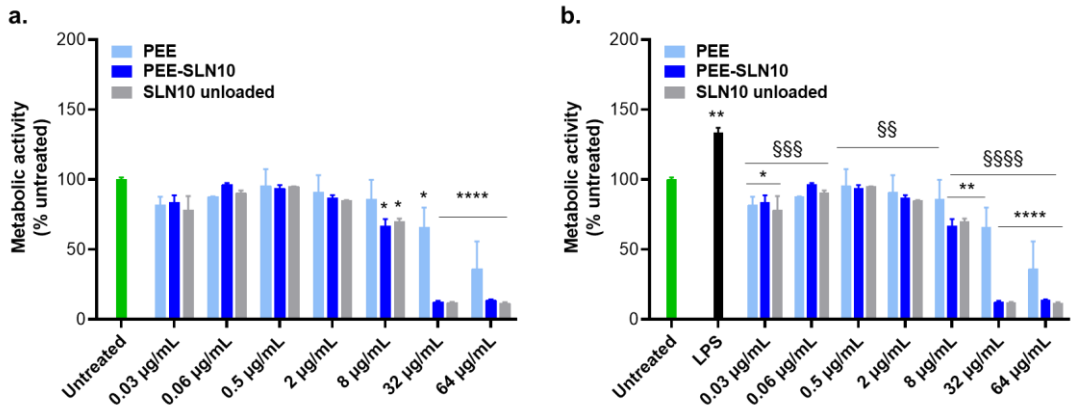


Figure 22. Cell metabolic activity of macrophages after 24 h of treatment. Bar graphs represent the percentages of cell metabolic activity under basal (a) and pro-inflammatory conditions (b). The untreated control (untreated) was set as 100 %. LPS = cells stimulated with 0.5 µg/mL LPS. *p<0.01, **p<0.001 and ****p<0.00001 between samples and untreated; §§p<0.001, §§§p<0.0001 and §§§§p<0.00001 between samples and LPS.

Generation of superoxide anions under pro-inflammatory conditions in the presence of the PEE and PEE-SLN10

To assess the potential anti-inflammatory activity of PEE and PEE-SLN10, a cellular model of inflammation was established by stimulating cells with lipopolysaccharide (LPS). LPS is a well-known endotoxin capable of triggering a pro-inflammatory response, leading to an imbalance in the cellular redox state and the overproduction of reactive oxygen species (ROS), including superoxide anions. This oxidative stress

condition is closely associated with tissue damage in chronic inflammatory diseases. As expected, stimulation with LPS markedly altered the redox equilibrium, resulting in a significant increase in superoxide anion levels compared with the untreated control (Figure 23). When PEE was administered in parallel with LPS, the production of superoxide anions displayed a dose-dependent behaviour. At concentrations of 32 and 64 µg/mL, the mean fluorescence intensities (MFIs) were significantly higher than those observed with LPS alone, suggesting that in its free form, PEE might not effectively counteract, and could even slightly exacerbate, oxidative stress under these experimental conditions.

In contrast, treatment with PEE-SLN10 in the presence of LPS resulted in a slight but consistent reduction of MFIs compared to LPS alone. This effect became more evident at higher concentrations (32-64 µg/mL), where the generation of superoxide anions was significantly decreased. The encapsulation of PEE within SLNs appears to enhance its capacity to modulate redox imbalance, possibly by improving cellular uptake, ensuring a more sustained release of active constituents, and protecting them from premature degradation. Overall, these findings indicate that while free PEE does not exert a protective effect against LPS-induced oxidative stress, its encapsulation in SLNs markedly improves its ability to decrease the production of superoxide anions.

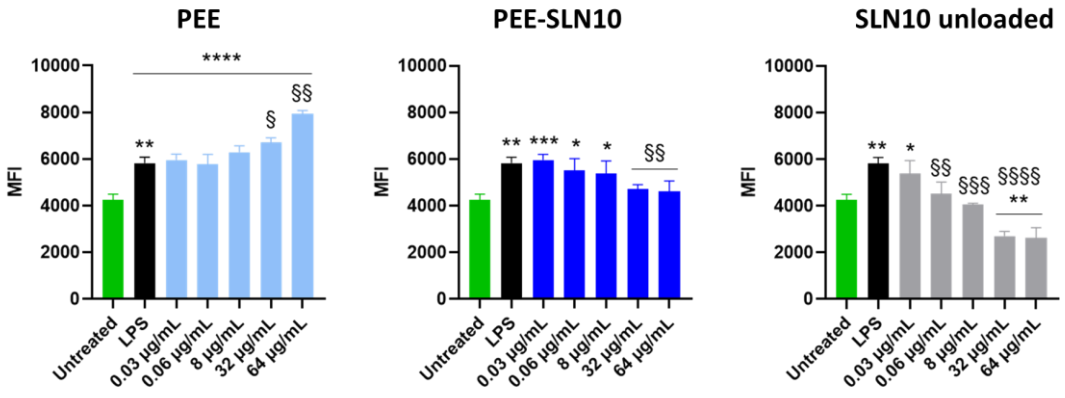


Figure 23. Generation of superoxide anions from LPS-stimulated macrophages after 24 h of treatment. Bars show mean fluorescence intensities (MFIs), which are proportional to the generation of superoxide anions. Untreated = untreated control. LPS = cells stimulated with 0.5 µg/mL LPS. *p<0.01, **p<0.001, ***p<0.0001 and ****p<0.00001 between samples and untreated; §p<0.01, §§p<0.001, §§§p<0.0001 and §§§§p<0.00001 between samples and LPS.

3.2.3. Experimental Section

Materials

All the reagents, unless otherwise specified, were purchased from Merck KGaA, Darmstadt, Germany. Tristearin (TS), Phosphatidylethanolamine (soy lecithin, SL), stearyl ether (Brij 78), ethanol, dodecane, dimethyl sulfoxide (DMSO), Milli-Q water, methanol, acetonitrile, MultiScreen-IP PAMPA filter plate and 96-well polytetrafluoroethylene (PTFE) plate, and fetal bovine serum were purchased from Sigma-Aldrich (St. Louis, MO, USA). EpiIntestinal^{TM} tissue model was purchased from MatTek, a Bico company, Bratislava, Slovakia. Propolis Ethanolic Extract (PEE) was obtained from raw Propolis collected in Chieti (42° 20′ 53.8″ N, 14° 09′ 53.8″ E), Italy. Columbia agar base, bacto yeast extract, Campygen, Brain Heart Infusion broth, and defibrinated horse blood were purchased from Oxoid Limited, Hampshire, UK. AlamarBlue (AB) was purchased from Thermo Fisher Scientific, Waltham, MA, USA, and Cell Proliferation Kit II XTT from Roche Diagnostic, Mannheim, Germany.

Propolis ethanolic extract (PEE) preparation

PEE was prepared by a maceration method [24]. Before the extraction, raw propolis was frozen at -20 °C, and homogenized by grinding using an electric blender. Grounded raw propolis (10 g) was added to 40 g of EtOH (96% *v/v*) in a dark glass bottle, and left under stirring for 72 h, at room temperature. Then, the mixture was filtered, collected, dried under vacuum, and stored in a round-bottom flask at 4 °C. The extraction efficiency was calculated following **Equation (3)**:

$$\text{Extraction Efficiency} = m_s/m_t \times 100 \qquad \textbf{(3)}$$

where m_t is the total amount of raw propolis, and m_s represents the weight of dried extract.

PEE characterization

High-Performance Liquid Chromatography (HPLC) analysis of PEE

The chromatographic analyses were performed for the PEE characterization in terms of their main constituents by using an Agilent 1260 Infinity II HPLC (Agilent, Santa Clara, CA, USA) consisting of a 1260 Infinity II Quaternary Pump (model G7111A), 1260 Infinity II auto-sampler (model G7129A), a 1260 Infinity II Multicolumn Thermostat (model G7116A), and a 1260 Infinity II Diode Array Detector (model G7115A) equipped

with an Hypersil C_{18} (250 mm, 4.6 μm, 150 mm) operating at 20 °C. The samples were analyzed in gradient elution mode using a mixture of water enriched with 2% of acetic acid (A) and acetonitrile and water (1:1) enriched with 0.5% of acetic acid (B), and acetonitrile (C). The following gradient was selected: 0-30 min, 75-45% A and 25-55% B; 60 min, 20% A and 80% B; 70-73 min, 100% C; 83-85 min, 75% A and 15% B. The flow rate was 0.8 mL/min, with the UV detector set at 280 nm [25].

Determination of total phenolic content (TPC) and flavonoid content of PEE

TPC in PEE was determined spectrophotometrically using the Folin-Ciocalteu method [26]. Briefly, 0.1 mL of PEE was mixed with 2.5 mL of distilled water, 0.1 mL of Folin-Ciocalteu reagent, and 0.5 mL of 20% sodium carbonate. The obtained mixture was left for 2 h at room temperature, and the absorbance was measured at 760 nm. TPC was calculated by using the calibration curve of gallic acid (GAE), in the concentration range 0.015-1 mg/mL, and the obtained amounts were expressed in mg of gallic acid equivalents GAE per g (GAE/g) of PEE.

The TFC in PEE was determined spectrophotometrically using the aluminum chloride method ($AlCl_3$) [27]. Briefly, 500 μL of 2% $AlCl_3$ in EtOH were added to 500 μL of PEE, and the mixture was left at room temperature for 1 h. The absorbance was then measured at 450 nm. TFC was calculated by using the calibration curve of quercetin (Q) in the concentration range 0.9-62.5 μg/mL, and the obtained amounts were expressed as equivalent Q per g (mg Q/g) of PEE.

Preparation of PEE-SLNs

PEE-SLNs were prepared using a slightly modified emulsification–evaporation–solidification method based on the procedure previously described by Marinelli *et al* [28]. The organic phase was prepared by dissolving TS and SL in EtOH under stirring (400 rpm), at 55 ± 2 °C. While the aqueous phase was prepared by dissolving the Brij 78 in Milli-Q water under stirring (500 rpm) and heating to 70 ± 2 °C. Next, the organic phase was added dropwise to the aqueous phase, which was subsequently concentrated to 24 mL, by evaporation of the organic solvent at 70 ± 2 °C. Next, the emulsion was quickly added to 24 mL of Milli-Q water on an ice bath under stirring (500 rpm) and left to equilibrate for 30 min, obtaining a final volume of 48 mL. The suspension was then subjected to centrifugation (6000 rpm, room temperature), and the supernatant was

collected and used for further characterizations. For the PEE-SLNs, the same procedure was followed; the PEE was dissolved in the organic phase containing TS and SL.

Characterization of PEE-SLNs

Mean particle size and polydispersity index (PDI) of PEE-SLNs were determined by dynamic light scattering (DLS, Anton Paar Litesizer 500 Graz, Austria). Samples were analyzed by diluting the PEE-SLNs with Milli-Q water (1:10) in a 1.5-mL disposable cuvette and were analyzed at 25 °C. The results regarding the mean hydrodynamic diameter were obtained from three different experiments. The ζ-potential was evaluated by the electrophoretic light scattering (AntonPaar Litesizer 500, Graz, Austria). The samples were conditioned in an electrophoretic Omega cuvette Mat. No. 225288 at 25 °C, applying a potential of 200.0 V. The ζ-potential values of PEE-SLNs and unloaded SLNs were calculated by the electrophoretic mobility obtained from 12 repeated analyses according to the method used by Helmholtz-von Smoluchowski.

Entrapment efficiency percentage (EE%) of PEE-SLNs

The EE% was determined using the direct method and is expressed in terms of chrysin content. 200 µL of PEE-SLNs, as a colloidal dispersion, was added to 1800 µL of EtOH (1:10), vortexed, and sonicated to allow the nanoparticle disruption. The resulting solution was filtered through a 0.45 µm syringe filter and analyzed by HPLC. The EE% was calculated by using **Equation (2):**

$$EE\% = \left(\frac{Wf}{Wt}\right) x\ 100 \qquad \textbf{(2)}$$

where W_f is the amount of chrysin found and W_t is the theoretical amount of loaded chrysin contained in the PEE.

Morphology of PEE-SLNs

The morphology of PEE-SLN10 was assessed using a transmission electron microscope (TEM) Philips 268 D (FEI, Eindhoven, The Netherlands). The samples were treated with negative staining. Formvar and carbon-coated copper grids (200 mesh; TAABLab.UK) were floated, film side down, on 20 µL of each sample for 20 s. Then the grids were marked with 20 µL of 2% (*w/v*) uranyl acetate and gently touched to filter paper to remove excess sample/water.

Differential scanning calorimetry (DSC)

20 µL aluminum pans containing 5-10 mg of crude propolis, tristearin, Brij 78, and lyophilized PEE-SLN10 and SLN10 unloaded, were closed by pressing and analyzed using a differential scanning calorimeter (DSC, Diamond-Perkin Elmer). The samples were placed in the DSC furnace, and thermograms were recorded by subjecting the sample to a thermal program using a heating rate of 10 °C/min in the temperature range of 30 to 160 °C under nitrogen purge gas maintained at a flow rate of 20 mL/min. An empty aluminum pan was used as a reference [29].

Heat and storage stabilities

Heat stability of freshly prepared PEE-SLN10 was evaluated by pouring the formulation into a glass tube and immersing it in a preconditioned oil bath set at different temperatures (40 °C, 50 °C, 60 °C, 70 °C, 80 °C, 90 °C) and letting to stand for 20 min. Next, all the formulations were cooled down to room temperature and analyzed in terms of particle size, PDI, and ζ-potential [30].

For the evaluation of storage stability, PEE-SLN10 were incubated at 25 ± 2 °C over a period of 112 days. The formulation was stored in a dark glass sealed vial. At each time point (0, 7, 14, 30, 40, 50, 60, 90, 112 days), the formulations were assessed in terms of physicochemical parameters such as particle size, PDI, and ζ-potential [31].

Simulated Gastric Fluid (SGF) and Simulated Intestinal Fluid (SIF) stability

The stability of PEE-SLN10 and unloaded SLN10 was evaluated in the simulated GI fluids. The suspensions were incubated in the Simulated Gastric Fluid (SGF, pH 1.2) and in the Simulated Intestinal Fluid (SIF, pH 6.8). The SGF was composed of 2 g of NaCl, 3.2 g of pepsin, 7 mL of HCl, 36.5% *v/v*, and 1000 mL of water. The SIF was composed of 6.8 g of monobasic potassium phosphate (KH_2PO_4) with 10 g of pancreatin (pH was adjusted to 6.8 by using NaOH). Approximately 0.5 mL of each SLNs' suspension was added to 5 mL of the simulated fluid and then incubated for 2 h in the SGF or 6 h in the SIF at 37 °C. Afterwards, the particle size and PDI were measured at different time intervals [32].

In vitro release study of PEE-SLN10 in SGF and SIF in terms of chrysin

The *in vitro* release profile, in terms of chrysin, selected as a marker compound, from PEE and PEE-SLN10, was evaluated using a dialysis cassette Slide-A-Lyzer™ Gamma Irradiated (MWCO 10 kDa). PEE and PEE-SLN10 were separately introduced into the dialysis cassette and placed in the dissolution apparatus filled with SGF for the first 2 h, and then the medium was replaced with SIF and left for 24 h [33]. At predefined time intervals (0.5 h, 1 h, 1.5 h, 2 h, 3 h, 4 h, 5 h, 6 h, 7 h, 15 h, 18 h, 24 h), aliquots of 200 µL of the formulations were withdrawn from the membrane and mixed with 1800 µL of EtOH, vortexed, and sonicated to promote SLN disruption. The samples were then filtered through 0.45 µm syringe filters and quantified for chrysin content by HPLC.

In vitro release study of PEE-SLN10 in SGF and SIF in terms of TPC and TFC

The *in vitro* release profile, in terms TPC and TFC, from PEE-SLN10, was evaluated using a dialysis cassette Slide-A-Lyzer™ Gamma Irradiated (MWCO 10 kDa). PEE-SLN10 were introduced into the dialysis cassette and placed in the dissolution apparatus filled with SGF for the first 2 h, and then the medium was replaced with SIF and left for 6 h [33]. At predefined time intervals (0.08 h, 0.25 h, 0.5 h, 1 h, 2 h, 4 h, 5 h, and 6 h), aliquots were withdrawn from the receiving media for TPC and TFC, respectively, and were analyzed as reported in below sections.

Permeation studies

Parallel Artificial Membrane Permeability Assay (PAMPA)

PAMPA was used to evaluate GI permeability. Analyses were performed using a 96-well, MultiScreen-IP PAMPA filter plate, and a 96-well polytetrafluoroethylene (PTFE) acceptor plate as donor and receiving, respectively. Donor wells were pre-treated with 5 µL of a lipid solution consisting of lecithin in dodecane (2% *w/v*). Subsequently, 150 µL of donor solutions, composed of either PEE or PEE-SLN10, were added to the donor compartments. PEE was diluted in PBS (pH 5.0 or 7.0) containing Cremophor EL (0.1% *v/v*) to match the chrysin concentration present in the PEE-SLN10 formulation. After 4 h of incubation, chrysin concentrations in both donor and acceptor wells were quantified by HPLC, and the effective permeability coefficient (*Pe*, cm/s) was calculated as previously described [28].

Permeation studies on EpiIntestinal^{TM} tissue model

The permeation studies were performed by using the EpiIntestinal^{TM} tissue model mounted on a vertical diffusion system (Hanging Top system). The furnished kit consists of individual tissues cultured in specific inserts, characterized by a tissue diameter of 9 mm (surface area = 0.6 cm^2), an underlying microporous membrane with a pore size of 0.4 µm. For the permeation studies, fresh tissues were used following standard experimental protocols provided by MaTtek.

Upon receiving the EpiIntestinal^{TM} kit, tissues were incubated overnight in 12-well plates, Hanging Top system, containing 5 mL of pre-warmed SMI-100-MM medium (37 °C, 5% CO_2). After the incubation period, the tissues were fixed in the permeation device and put into 12-well plates containing 5 mL of receiving solution, composed of SMI-100-MM. PEE and PEE-SLN10 (100 µL, 168 µg/mL in terms of chrysin) were added to the tissue and incubated at 37 °C and 5% CO_2. At 3 h, aliquots (1 mL) were withdrawn, replaced with an equal volume of fresh medium. At 24 h, all the receiving solutions were collected, filtered through 0.45 µm syringe filters, and all the samples were analyzed by HPLC. The experiment was performed in triplicate [34].

Biological studies

Antimicrobial activities of PEE-SLNs

H. pylori ATCC 700684 clarithromycin-resistant (CLA^R), *F. nucleatum* ATCC 25586, and *Clostridioides (Clostridium) difficile* ATCC 700057 purchased from ATCC were chosen as reference strains and were stored at -80 °C. The strains were thawed at room temperature and cultivated as follows. *H. pylori* was plated on Columbia agar base (CA; Oxoid Limited, Hampshire, UK) supplemented with 10% horse serum (Sigma Aldrich, St. Louis, MO, USA) and 0.25% bacto yeast extract (Oxoid Limited, Hampshire, UK) and incubated at 37 °C for 72 h in a microaerophilic atmosphere (Campygen; Oxoid Limited, Hampshire, UK) [31]; *F. nucleatum* and *C. difficile* were plated on Fastidious Anaerobe Agar (FAA, Lab M, Heywood, UK) plus 5% of defibrinated horse blood (Oxoid Limited, Hampshire, UK) for 72 h in a anaerobic atmosphere (whitley a25 anaerobic workstation; Don Whitley Scientific Limited, UK) [35].

PEE-SLN10 was tested against the abovementioned bacteria. The antibacterial activity was carried out via the broth microdilution method in 96-well plates (Eppendorf,

Hamburg, Germany) according to Clinical & Laboratory Standards Institute guidelines [36]. *H. pylori* were cultivated in Brain Heart Infusion broth (BHI; Oxoid Limited, Hampshire, UK) plus 5% of fetal bovine serum (FBS; Sigma Aldrich, St. Louis, MO, USA) as previously described [37], whereas *F. nucleatum* and *C. difficile* were cultivated in Fastidious Anaerobe Broth (FAB, Lab M, Heywood, UK). The results obtained were confirmed by using the alamarBlue (AB) (Thermo Fisher Scientific, Waltham, MA, USA) viability assay as previously described [38, 39] for *H. pylori* and via XTT (Cell Proliferation Kit II XTT, Roche Diagnostic, Mannheim, Germany) for the anaerobic bacteria [40]. PEE, PEE-SLN10, and SLN-10 unloaded, were diluted in the abovementioned broths and were used in the range of 0.125-128 μg/mL. Controls consisting of: (*i*) *bacterial* broth cultures in the medium without the addition of the tested compound; (*ii*) *bacterial* broth cultures in the medium plus 4.74% (*v/v*) of H_2O without the addition of the tested compound; (*iii*) bacterial broth cultures in the medium plus 2.35% (*v/v*) of EtOH without the addition of TS; (*iv*) bacterial broth cultures with the reference antimicrobials (as positive control); (*v*) media with the tested compound; (*vi*) just media. Two independent experiments were performed in triplicate. The initial bacterial inoculum was 2-8 × 10^5 CFU/mL for *H. pylori* and 1 × 10^6 CFU/mL for anaerobes [41]. The 96-well plates were incubated at 37 °C for 72 h for *H. pylori* and 48 h for the anaerobes. The minimum inhibitory concentration (MIC) was defined as the lowest concentration of the sample, resulting in a detectable colorimetric change in the assays [37-42]. Subsequently, the minimum bactericidal concentration (MBC) was determined, starting from the wells stained with alamarBlue: 100 μL of the bacterial suspensions into the wells corresponding to both MIC and subsequent concentrations were seeded on the selected agar plates and incubated at 37 °C for 3-5 days in the appropriate conditions. The MBC was defined as the lowest concentration of the tested compound capable of killing the initial bacterial inoculum beyond 99.9%.

Evaluation of *in vivo* toxicity using the *Galleria mellonella* model

The *in vivo* toxicity of PEE-SLN10 was tested using the greater wax moth, *Galleria mellonella*. *G. mellonella* larvae were kindly provided by Prof. Maria Luisa Dindo (Department of Agricultural and Food Science, University of Bologna) and stored in the dark at 20 °C. Larvae weighing 200-250 mg were selected for the experiments. As

previously reported [8], we considered a dilution factor within the larvae; therefore, the compound concentration was increased 10-fold before administering to the animal: the final dose of PEE SLN10 was 0.024 mg/kg, while that of PEE was 12.8 mg/kg.

PEE-SLN10 and PEE were properly diluted in DPBS (Sigma Aldrich, St. Louis, MO, USA) starting from the stock solutions. Each larva was injected with 10 µL into the third left proleg using a Hamilton syringe (Hamilton, Nevada, USA). The experimental groups were: (*i*) larvae treated with 0.024 mg/kg of PEE SLN10 and 12.8 mg/kg of PEE; (*ii*) larvae treated with TS, SL, and Brij 78 at the same concentrations contained in PEE-SLN10 and (*iii*) larvae treated with SLN10 unloaded; and (*iv*) untreated larvae (not injected). 10 Larvae were enrolled for each experimental group. Two independent experiments were performed. After the injection, larvae were housed in Petri dishes, stored at 35 °C for 4 days, and monitored daily to evaluate mortality [43].

Cell cultures

Undifferentiated human monocytes (CRL-9855™) were purchased from ATCC® and sub-cultured in RPMI 1640 (Merck, Darmstadt, Germany) supplemented with 10% heat-inactivated fetal bovine serum (FBS), 1% penicillin/streptomycin, and 1% sodium pyruvate (all from Gibco, Invitrogen, Life Technologies, Carlsbad, CA, USA) at 37 °C and 5% CO_2. For differentiation into macrophages, monocytes were seeded into 96 multi-well culture plates (0.5×10^4 cells/well) or 6 multi-well culture plates (0.5×10^5 cells/well) and stimulated with 100 ng/mL of phorbol-12-myristate-13-acetate (PMA, Merck, Darmstadt, Germany, stock solution 1 mM in DMSO) in complete RPMI for 48 h at 37 °C and 5% CO_2.

Cell metabolic activity

Undifferentiated monocytes were seeded (5×10^3 cells/well) in 96 multi-well culture-treated plates (Corning™ Falcon™, Glendale, USA) and differentiated as described previously in this section. Then, the differentiation medium was discarded after 48 h and replaced with a fresh one containing complete RPMI (untreated cells) or extracts or formulations (range 0.03-64 µg/mL) for 24 h. To establish an inflamed environment, macrophages were stimulated with 0.5 µg/mL lipopolysaccharide (LPS) from *E. coli*, purchased from Merck, Darmstadt, Germany, stock solution 1 mg/mL in water, and exposed in parallel to extracts or formulations (range 0.03-64 µg/mL) for 24 h. At the

established time point (24 h), the exposure media were replaced by fresh RPMI containing 3-(4,5-dimethylthiazol-2-yl)-2,5-diphenyltetrazolium bromide (MTT) 0.5 mg/mL (Merck, Darmstadt, Germany) and processed as elsewhere reported [44]. The optical density in each well was measured using a spectrophotometer (Thermo Fisher Scientific, Waltham, MA, USA) at a wavelength of 540 nm. Each experiment was performed three times in triplicate per experimental condition (n = 9).

Detection of Mitochondrial Superoxide Anions

The intracellular generation of mitochondrial superoxide anions was determined after 24 h using the oxidation-sensitive fluorescent probe MitoSOX™ (MitoSOX™ Red Mitochondrial Superoxide Indicator, Invitrogen, Thermo Fisher Scientific, Waltham, MA, USA). Undifferentiated monocytes were seeded (0.5×10^5 cells/well) in a 6 multi-well tissue culture-treated plate (Corning™ Falcon™, Glendale, USA) and differentiated into macrophages as previously described. Then, the growth medium was removed and replaced with fresh medium mixed with PEE and PEE-SLN10. After the exposure time (24 h), cells were incubated with MitoSOX Red at a final concentration of 1 µM (stock solution in DMSO 1 mM) in the exposure medium for 30 min at 37 °C and 5% CO_2 in the dark. Next, stained cells were trypsinized, harvested, and washed. Cell suspensions were analyzed using a CytoFLEX flow cytometer (Beckman Coulter, Indianapolis, IN, USA) equipped with a 488 nm laser with the fluorescence channel FL-2/PE in a linear mode. Relative fluorescence emissions of gated cells by means of their forward and side scatter properties (FSC/SSC) were analyzed with the CytExpert software (Beckman Coulter, Indianapolis, IN, USA), and they were expressed as mean fluorescence intensity ratios on the unstained control (set as 1, not shown). Each experiment was performed three times in duplicates per experimental condition (n = 6).

Statistical analysis

Statistics were performed using one-way analysis of variance (ANOVA) followed by Tukey's multiple comparison test by means of the Prism 8.0 software (GraphPad, San Diego, CA, USA). Results are presented as mean values ± standard deviations. Values of $p \leq 0.05$ were considered statistically significant.

3.2.4. Conclusions

SLNs represent a promising strategy to overcome the main limitations associated with the therapeutic use of PEE, including poor solubility and instability. The optimized PEE-SLN10 ensured effective encapsulation of key polyphenolic compounds, enabling gradual release, enhanced permeability, and improved physicochemical stability under stress induced by the contact with body fluids and thermal stress. According to our findings, the encapsulation of PEE into PEE-SLN10 improved the extracts' activity by protecting the extract from degradation; this translates into improved antimicrobial activity as well as improved ability to modulate oxidative stress, suggesting potential indirect benefits on biological efficacy. These results highlight that the main advantage of the nanocarrier system lies in the improved stability, permeability, and delivery of PEE bioactives. PEE-SLN10 shows promise as a gastric-targeted delivery system for *H. pylori* treatment, with potential for further optimization for intestinal applications. However, future research will focus on broadening the panel of gastrointestinal pathogens, including both Gram-positive and Gram-negative strains, and elucidating the mechanisms underlying the antimicrobial activity, especially against *H. pylori*. Overall, the findings support the potential of SLNs as a biocompatible platform for the delivery of polyphenolic compounds, providing a rationale for further *in vivo* pharmacokinetic and mechanistic investigations.

All the contents of the work discussed in this chapter have been submitted to the *Journal of Functional Food* as follows: Dimmito M.P., Puca V., Di Stefano A., **Toto E.C**., Corfiati G., Appignani M., Grande R., Marinacci B., Gallorini M., Santolo F., Robuffo I., Cacciatore I., Marinelli L., Propolis-Loaded Solid Lipid Nanoparticles Targeting Pathogens Associated with Gastrointestinal Diseases.

References

1. Wojtacka, J. Propolis Contra Pharmacological Interventions in Bees. *Molecules* **2022**, 27, 4914.
2. Pasupuleti, V. R.; Sammugam, L.; Ramesh, N.; Gan, S. H. Honey, Propolis, and Royal Jelly: A Comprehensive Review of Their Biological Actions and Health Benefits. *Oxid Med Cell Longev*. **2017**.
3. Osés, S. M.; Pascual-Maté, A.; Fernández-Muiño, M. A.; López-Díaz, T. M.; Sancho, M. T. Bioactive Properties of Honey with Propolis. *Food Chem.* **2016**, 196, 1215-1223.
4. Malfertheiner, P.; Megraud, F.; Rokkas, T.; Gisbert, J.P.; Liou, J.M.; Schulz, C.; Gasbarrini, A.; Hunt, R.H.; Leja, M.; O'Morain, C.; Rugge, M.; Suerbaum, S.; Tilg, H.; Sugano, K.; El-Omar, E.M. European Helicobacter and Microbiota Study group. Management of Helicobacter pylori infection: the Maastricht VI/Florence consensus report. *Gut* **2022**, 327745.
5. Pahlavani, N.; Malekahmadi, M.; Firouzi, S.; Firouzi, S.; Rostami, D.; Sedaghat, A.; Moghaddam, A.B.; Ferns, G.A.; Navashenaq, J.G.; Reazvani, R.; Safarian, M.; Ghayour-Mobarhan, M. Molecular and Cellular Mechanisms of the Effects of Propolis in Inflammation, Oxidative Stress and Glycemic Control in Chronic Diseases. *Nutr. Metab. (Lond.)* **2020**, 17, 65.
6. Song, M. Y.; Lee, D. Y.; Kim, E. H. Anti-Inflammatory and Anti-Oxidative Effect of Korean Propolis on Helicobacter pylori-Induced Gastric Damage In Vitro. *J. Microbiol.* **2020**, 58(10), 878–885.
7. Nichitoi, M.M.; Josceanu, A.M.; Isopescu, R.D.; Isopencu, G.O.; Geana, E.I.; Ciucure, C.T.; Lavric, V. Polyphenolics profile effects upon the antioxidant and antimicrobial activity of propolis extracts. *Scientific reports* **2021**, 11(1), 20113.
8. Wojtyczka, R. D.; Kępa, M.; Idzik, D.; Kubina, R.; Kabała-Dzik, A.; Dziedzic, A.; Wąsik, T. J. In Vitro Antimicrobial Activity of Ethanolic Extract of Polish Propolis against Biofilm Forming Staphylococcus epidermidis Strains. *Evid. Based Complement. Alternat. Med.* **2013**, 590703.
9. Belmehdi, O.; Bouyahya, A.; Jekő, J.; Cziáky, Z.; Zengin, G., Sotkó, G., El Baaboua, A., Senhaji, N. S., & Abrini, J. (2021). Synergistic interaction between propolis extract, essential oils, and antibiotics against Staphylococcus epidermidis and methicillin resistant Staphylococcus aureus. *International Journal of Secondary Metabolite*, **2021**, 8(3), 195-213.
10. Di Rienzo, A.; Marinelli, L.; Dimmito, M.P.; Toto, E.C.; Di Stefano, A.; Cacciatore, I. Advancements in Inflammatory Bowel Disease Management: From Traditional Treatments

to Monoclonal Antibodies and Future Drug Delivery Systems. *Pharmaceutics* **2024**, 16, 1185.

11. Ciulla, M.; Marinelli, L.; Di Biase, G.; Cacciatore, I.; Santoleri, F.; Costantini, A.; Dimmito, M.P.; Di Stefano, A. Healthcare Systems across Europe and the US: The Managed Entry Agreements Experience. *Healthcare* **2023**, 11, 447.
12. World Health Organization. WHO Publishes List of Bacteria for Which New Antibiotics Are Urgently Needed. Available at: Https://Www.Who.Int/News/Item/27-02-2017-Who-Publishes-List-of-Bacteria-for-Which-New-Antibiotics-Are-Urgently-Needed. Accessed 20 February 2021.
13. Spigaglia, P.; Mastrantonio, P.; Barbanti, F. Antibiotic Resistances of Clostridium difcile; *Springer: Cham, Switzerland*, **2018**, 137–159.
14. Strauss, J.; Kaplan, G.G.; Beck, P.L.; Rioux, K.; Panaccione, R.; Devinney, R.; Lynch, T.; Allen-Vercoe E. Invasive potential of gut mucosa-derived Fusobacterium nucleatum positively correlates with IBD status of the host. *Inflamm Bowel Dis.* **2011**, 17(9), 1971-8.
15. Wang, W.; Chen, L.; Zhou, R.; Wang, X.; Song, L.; Huang, S.; Wang, G.; Xia B. Increased proportions of Bifidobacterium and the Lactobacillus group and loss of butyrate-producing bacteria in inflammatory bowel disease. *J. Clin Microbiol.* **2014**, 52(2), 398-406.
16. Nitzan, O.; Elias, M.; Chazan, B.; Raz, R.; Saliba, W. Clostridium difficile and Inflammatory Bowel Disease: Role in Pathogenesis and Implications in Treatment. World *J. Gastroenterol.* **2013**, 19(43), 7577–7585.
17. Zhang, L.; Zhao, M.; Fu, X. Gastric Microbiota Dysbiosis and Helicobacter pylori Infection. *Front. Microbiol.* **2023**, 14, 1153269.
18. Czepiel, J.; Dróżdż, M.; Pituch, H.; Kuijper, E.J.; Perucki, W.; Mielimonka, A.; Goldman, S.; Wultańska, D.; Garlicki, A.; Biesiada, G. Clostridium difficile infection: review. *Eur. J. Clin. Microbiol. Infect. Dis*. **2019**, 38(7), 1211-1221.
19. Wang, N.; Fang, J.Y. Fusobacterium nucleatum, a key pathogenic factor and microbial biomarker for colorectal cancer. *Trends Microbiol*. **2023**, 31(2), 159-172.
20. Mendez-Pfeiffer, P.; Juarez, J.; Hernandez, J.; Taboada, P.; Virués, C.; Valencia, D.; Velazquez, C. Nanocarriers as drug delivery systems for propolis: A therapeutic approach. *Journal of Drug Delivery Science and Technology*, **2021**, 65, 102762.
21. Borges, A.; de Freitas, V.; Mateus, N.; Fernandes, I.; Oliveira, J. Solid Lipid Nanoparticles as Carriers of Natural Phenolic Compounds. *Antioxidants* **2020**, 9, 998.

22. Satapathy, M.K.; Yen, T.L.; Jan, J.S.; Tang, R.D.; Wang, J.Y.; Taliyan, R.; Yang, C.H. Solid Lipid Nanoparticles (SLNs): An Advanced Drug Delivery System Targeting Brain through BBB. *Pharmaceutics*. **2021**, 13(8), 1183.
23. Gonçalves, C. C.; Hernandes, L.; Bersani-Amado, C. A.; Franco, S. L.; Silva, J. F.; Natali, M. R. Use of Propolis Hydroalcoholic Extract to Treat Colitis Experimentally Induced in Rats by 2,4,6-Trinitrobenzenesulfonic Acid. *Evidence-Based Complementary and Alternative Medicine* **2013**, 853976.
24. Bankova, V.; Trusheva, B.; Popova, M. Propolis extraction methods: a review. *Journal of Apicultural Research*, **2021**, *60*(5), 734-743.
25. Bo Bozkuş, T. N.; Değer, O.; Yaşar, A. Chemical characterization of water and ethanolic extracts of Turkish propolis by HPLC-DAD and GC-MS. *Journal of Liquid Chromatography & Related Technologies*, **2021**, 44(1-2), 77-86.
26. Escriche I.; Juan-Borrás M. Standardizing the analysis of phenolic profile in propolis. *Food Res Int.* **2018**, 106, 834-841.
27. Ordoñez A.A.L.; Gomez J.D.; Vattuone M.A.; lsla M.I.; Antioxidant activities of Sechium edule (Jacq.) Swartz extracts, Food Chemistry, **2006**, 97, 3, 452-458.
28. Marinelli, L.; Dimmito, M.P.; Cacciatore, I., Toto E.C.; Di Rienzo A.; Palmerio F.; Puca V.; Di Filippo E.S.; Fulle, S.; Di Stefano A. Solid lipid nanoparticles for efficient delivery of capsaicin-rich extract: potential neuroprotective effects in Parkinson's disease. *J Drug Deliv Sci Technol*. **2024**, 91,105097.
29. Amin, A. A.; Mahmoud, K. F.; Salama, M. F.; Longo, V.; Pozzo, L.; Seliem, E. I.; Ibrahim, M. A. Characterization and stability evaluation of Egyptian propolis extract nano-capsules and their application. *Sci. Rep.* **2023**, 13, 16065.
30. Soleimanian, Y., Goli, S. A. H., Varshosaz, J., & Maestrelli, F. β-Sitosterol lipid nano carrier based on propolis wax and pomegranate seed oil: Effect of thermal processing, pH, and ionic strength on stability and structure. *European Journal of Lipid Science and Technology*, **2019,** 121(1), 1800347.
31. Silva, A.C.; Kumar, A.; Wild, W.; Ferreira, D.; Santos, D.; Forbes B. Long-term stability, biocompatibility and oral delivery potential of risperidone-loaded solid lipid nanoparticles. *Int J Pharm.* **2012**, 15, 436, 798-805.
32. Shi, L.L.; Lu, J.; Cao, Y.; Liu, J.Y.; Zhang, X.X.; Zhang, H.; Cui, J.H., Cao Q.R. Gastrointestinal stability, physicochemical characterization and oral bioavailability of chitosan or its derivative-modified solid lipid nanoparticles loading docetaxel. *Drug Dev Ind Pharm.* **2017**, 43(5), 839-846. doi: 10.1080/03639045.2016.1220571.

33. Wu, J.; Chen, J.; Wei, Z.; Zhu, P.; Li, B.; Qing, Q.; Chen, H.; Lin, W.; Lin, J.; Hong, X.; et al. Fabrication, Evaluation, and Antioxidant Properties of Carrier-Free Curcumin Nanoparticles. *Molecules* **2023**, *28*, 1298. https://doi.org/10.3390/molecules28031298.
34. Turco, L.; Santori, N.; Buratti, F. M.; Dorne, J. C. M.; Testai, E. Congeners-Specific Intestinal Absorption Of Microcystins In An *In Vitro* 3D Human Intestinal Epithelium: The Role Of Influx/Efflux Transporters. *Frontiers in toxicology*, **2022**, *4*, 883063.
35. Pignatelli, P.; Iezzi, L.; Pennese, M.; Raimondi, P.; Cichella, A.; Bondi, D.; Grande, R.; Cotellese, R.; Di Bartolomeo, N.; Innocenti, P.; Piattelli, A.; Curia, M.C. The Potential of Colonic Tumor Tissue *Fusobacterium nucleatum* to Predict Staging and Its Interplay with Oral Abundance in Colon Cancer Patients. *Cancers (Basel).* **2021**, 13, 1032.
36. Puca, V.; Turacchio, G.; Marinacci, B.; Supuran, C.T.; Capasso, C.; Di Giovanni, P.; D'Agostino, I.; Carradori, S.; Grande, R. Antimicrobial and Antibiofilm Activities of Carvacrol, Amoxicillin and Salicylhydroxamic Acid Alone and in Combination vs. *Helicobacter pylori:* Towards a New Multi-Targeted Therapy. *Int. J. Mol. Sci.* **2023**, 24, 24(5), 4455.
37. Clinical and Laboratory Standard Institute [CLSI] (**2007**). Performance Standards for Antimicrobial Susceptibility Testing. Seventeenth Informational Supplement M100–S17, Vol. 27. Wayne, PA: Clinical and Laboratory Standard Institute.
38. Marinelli, L.; Ciulla, M.; Ritsema, J.A.S.; van Nostrum, C.F.; Cacciatore, I.; Dimmito, M.P.; Palmerio, F.; Orlando, G.; Robuffo, I.; Grande, R.; et al. Preparation, Characterization, and Biological Evaluation of a Hydrophilic Peptide Loaded on PEG-PLGA Nanoparticles. *Pharmaceutics* **2022**, 14, 1821.
39. Ben Khalifa, R.; Cacciatore, I.; Dimmito, M.P.; Ciulla, M.; Grande, R.; Puca, V.; Robuffo, I.; De Laurenzi, V.; Chekir-Ghedira, L.; Di Stefano, A.; Marinelli, L. Multiple Lipid Nanoparticles as Antimicrobial Drug Delivery Systems. *J. Drug Deliv. Sci. Technol*. **2022**, *67*, 102887.
40. Vitale, I.; Spano, M.; Puca, V.; Carradori, S.; Cesa, S.; Marinacci, B.; Sisto, F.; Roos, S.; Grompone, G.; Grande R. Antibiofilm activity and NMR-based metabolomic characterization of cell-free supernatant of Limosilactobacillus reuteri DSM 17938. *Front Microbiol.* **2023**, *20 (14)*, 1128275.
41. Clinical and Laboratory Standard Institute [CLSI] (2018). Methods for Antimicrobial Susceptibility Testing of Anaerobic Bacteria. CLSI M11, ninth edition.
42. Marinacci, B.; D'Agostino, I.; Angeli, A.; Carradori, S.; Melfi, F.; Grande, R.; Corsiani, M.; Ferraroni, M. Agamennone, M.; Tondo, A.R.; Zara, S.; Puca, V.; Pellegrini, B.; Vagaggini,

C.; Dreassi, E.; Patrauchan, M.A.; Capasso, C.; Nicolotti, O.; Carta F.; Supuran, C.T. Inhibition of *Pseudomonas aeruginosa* Carbonic Anhydrases, Exploring Ciprofloxacin Functionalization Toward New Antibacterial Agents: An In-Depth Multidisciplinary Study. *J. Med. Chem.* **2024**, 14, 67, 19077-19102.

43. Gallorini, M.; Marinacci, B.; Pellegrini, B.; Cataldi, A.; Dindo, M.L.; Carradori, S.; Grande R. Immunophenotyping of hemocytes from infected Galleria mellonella larvae as an innovative tool for immune profiling, infection studies and drug screening. *Sci. Rep.* **2024**, 8, 14(1), 759. doi: 10.1038/s41598-024-51316-z.
44. Kahraman, H.A.; Tutun, H.; Kaya, M.M.; Usluer, M.S.; Tutun, S.; Yaman, C.; Sevin, S.; Keyvan, E. Ethanolic extract of Turkish bee pollen and propolis: phenolic composition, antiradical, antiproliferative and antibacterial activities. *Biotechnology & Biotechnological Equipment*, **2022**, 36, 1, 45-56.
45. Kosalec, I.; Bakmaz, M.; Pepeljnjak, S. Analysis of propolis from the continental and Adriatic regions of Croatia. *Acta pharmaceutica*, **2003**, 53(4), 275-285.
46. İzol, E.; Bursal, E.; Yapici, İ.; Yilmaz, M.; Yilmaz, İ.; Gülçin, I. Chemical Content by LC–MS/MS, Antiglaucoma, and Antioxidant Activity of Propolis Samples From Different Regions of Türkiye, *Journal of Food Biochemistry*, **2024**, 7488590.
47. Tumbarski, Y.; Ivanov, I.; Todorova, M.; Apostolova, S.; Tzoneva, R.; Nikolova, K. Phenolic Content, Antioxidant Activity and In Vitro Anti-Inflammatory and Antitumor Potential of Selected Bulgarian Propolis Samples. *Biomedicines.* **2025**, 13(2), 334. .
48. Nichitoi, M.M.; Josceanu, A.M.; Isopescu, R.D.; Isopencu, G.O.; Geana, E.I.; Ciucure, C.T.; Lavric, V. Polyphenolics profile effects upon the antioxidant and antimicrobial activity of propolis extracts. *Sci. Rep.* **2021**, 11(1), 20113.
49. Moreira, L.; Dias, L. G.; Pereira, J. A.; Estevinho, L. Antioxidant properties, total phenols, and pollen analysis of propolis samples from Portugal. *Food and chemical toxicology: an international journal published for the British Industrial Biological Research Association* **2008**, 46(11), 3482–3485.
50. Silva, A.M.; Rocha, B.; Moreira, M.M., Delerue-Matos, C., das Neves, J., & Rodrigues, F. Biological activity and chemical composition of propolis extracts with potential use in vulvovaginal candidiasis management. International Journal of Molecular Sciences **2024**, 25(5), 2478.
51. de Souza, M. L.; de Albuquerque Wanderley Sales, V.; Alves, L. P.; Dos Santos, W. M.; de Moura Ferraz, L. R.; de Andrade Lima, G. S.; Dos Santos Mendes, L.M.; Rolim, L. A.; Neto, P. J. R. A Systematic Review of Functionalized Polymeric Nanoparticles to Improve

Intestinal Permeability of Drugs and Biological Products. *Current pharmaceutical design*, **2022**, *28*(5), 410-426.

52. Barras, A.; Mezzetti, A.; Richard, A.; Lazzaroni, S.; Roux, S.; Melnyk, P.; Betbeder, D.; Monfilliette-Dupont, N. Formulation and characterization of polyphenol-loaded lipid nanocapsules. *Int. J. Pharm.* **2009**, 379(2), 270-7.
53. Fazel, M.; Daeihamed, M.; Osouli, M.; Almasi, A.; Haeri, A, Dadashzadeh S. Preparation, *In-Vitro* Characterization and Pharmacokinetic Evaluation of Brij Decorated Doxorubicin Liposomes as a Potential Nanocarrier for Cancer Therapy. *Iran J Pharm Res.* **2018**, *17*, 33-43.
54. Dantas, I.; Bastos, K.; Machado, M.; Galvão, Juliana L. Influence of stearic acid and beeswax as solid lipid matrix of lipid nanoparticles containing tacrolimus. *Journal of Thermal Analysis and Calorimetry.* **2018**, 132.
55. Montenegro, L.; Ottimo, S.; Puglisi, G.; Castelli, F.; Sarpietro, M. G. Idebenone loaded solid lipid nanoparticles interact with biomembrane models: calorimetric evidence. *Molecular pharmaceutics*, **2012**, *9*(9), 2534-2541.
56. Lee, S. H.; Lee, Y. S.; Song, J. G.; Han, H. K. Improved In vivo Effect of Chrysin as an Absorption Enhancer Via the Preparation of Ternary Solid Dispersion with Brij®L4 and Aminoclay. *Current drug delivery*, **2019**, *16*(1), 86-92.
57. Komath, S.; Garg, A.; Wahajuddin, M. Development and evaluation of Chrysin-Phospholipid complex loaded solid lipid nanoparticles - storage stability and in vitro anti-cancer activity. *Journal of Microencapsulation*, **2018**, *35(6)*, 600-617.
58. Silva, M.M.; Calado, R.; Marto, J.; Bettencourt, A.; Almeida, A.J.; Gonçalves, L.M.D. Chitosan Nanoparticles as a Mucoadhesive Drug Delivery System for Ocular Administration. Mar Drugs. **2017**, *15(12)*, 370. doi: 10.3390/md15120370.
59. Novelli, M.; Bolla, J.M. RND Efflux Pump Induction: A Crucial Network Unveiling Adaptive Antibiotic Resistance Mechanisms of Gram-Negative Bacteria. *Antibiotics (Basel)*. **2024**, 13(6), 501.
60. Elbaiomy, R.G.; Luo, X.; Guo, R.; Deng, S.; Du, M.; El-Sappah, A.H.; Bakeer, M.; Azzam, M.M.; Elolimy, A.A.; Madkour, M.; Li, Z.; Zhang, Z. Antibiotic resistance in Helicobacter pylori: a genetic and physiological perspective. *Gut Pathog*. **2025**, 17(1), 35.
61. Al-Haroni, M.; Skaug, N.; Bakken, V.; Cash, P. Proteomic analysis of ampicillin-resistant oral Fusobacterium nucleatum. *Oral Microbiol Immunol*. **2008**, 23(1), 36-42.

62. Gan, Y.; Yang, H.; Wang, M.; Li, J. Advances in drug resistance and resistance mechanisms of four colorectal cancer-associated gut microbiota. *PeerJ*. **2025**, 13, e19535. doi: 10.7717/peerj.19535.
63. Asadi, G. S.; Abdizadeh, R.; Abdizadeh, T. Investigation of a set of flavonoid compounds as *Helicobacter pylori* urease inhibitors: insights from *in silico* studies. *Journal of Biomolecular Structure and Dynamics*, **2023**, *43*(5), 2366-2388.
64. Romero, M.; Freire, J.; Pastene, E.; García, A.; Aranda, M.; González, C. Propolis polyphenolic compounds affect the viability and structure of Helicobacter pylori in vitro, *Revista Brasileira de Farmacognosia*, **2019**, *29*, 325-332.
65. De Rossi, L.; Rocchei, G.; Lucini, L.; Rebecchi, A. Antimicrobial Potential of Polyphenols: Mechanisms of Action and Microbial Responses-A Narrative Review. *Antioxidants* **2025**, 14, 200.
66. Mingoia, M.; Conte, C.; Di Rienzo, A.; Dimmito, M.P.; Marinucci, L.; Magi, G.; Turkez, H.; Cufaro, M.C.; Del Boccio, P.; Di Stefano, A.; Cacciatore, I. Synthesis and Biological Evaluation of Novel Cinnamic Acid-Based Antimicrobials. *Pharmaceuticals* **2022**, *15*, 228.
67. Marinelli, L.; Fornasari, E.; Eusepi, P.; Ciulla, M.; Genovese, S.; Epifano, F.; Fiorito, S.; Turkez, H.; Örtücü, S.; Mingoia, M.; Simoni, S.; Pugnaloni, A.; Di Stefano, A.; Cacciatore, I. Carvacrol prodrugs as novel antimicrobial agents. *European journal of medicinal chemistry* **2019**, *178*, 515-529.
68. Gallorini, M.; Maccallini, C.; Ammazzalorso, A.; Amoia, P.; De Filippis, B.; Fantacuzzi, M.; Giampietro, L.; Cataldi, A.; Amoroso, R. The Selective Acetamidine-Based iNOS Inhibitor CM544 Reduces Glioma Cell Proliferation by Enhancing PARP-1 Cleavage In Vitro. *Int. J. Mol. Sci.* **2019**, *20*, 495.

3.3. Lep(70-89) targeted SLNs as a platform for brain delivery

3.3.1 Introduction

Drug delivery to the central nervous system (CNS) remains one of the greatest challenges in pharmaceutical research. Most therapeutics, even when highly potent *in vitro*, fail to reach effective concentrations in the brain due to the limited permeability of cerebral barriers and the complex neurovascular environment [1]. The impaired delivery of drugs to the brain is primarily due to the presence of the blood-brain barrier (BBB), which represents the main obstacle for CNS drug targeting [2]. The BBB is a specialized system of capillary endothelial cells that protects the brain from harmful substances circulating in the bloodstream, while simultaneously supplying the necessary nutrients to ensure brain functions [3]. Colloidal DDS have emerged as an effective approach to improve drug uptake by the brain [4]. In particular, SLNs have recently been investigated for brain delivery; thanks to their lipidic nature, SLNs are readily taken up by the brain. However, their non-specific uptake and rapid clearance by the reticuloendothelial system (RES) may limit their biodistribution, therapeutic efficiency, and circulation time [5]. To address these challenges, the modification of lipids with polyethylene glycol (PEG) chains, known as PEGylation, has been widely adopted to produce so-called “stealth“ NPs. PEGylated lipids create a hydrophilic steric barrier on the NPs’ surface that reduces serum protein adsorption, minimizes immune recognition, and prolongs systemic circulation. This strategy has been extensively applied to liposomes and to lipid nanoparticles (LNPs) as well, used for RNA or siRNA delivery, which share many physicochemical features with SLNs [6, 7]. By improving colloidal stability and pharmacokinetics, PEGylation enables NPs to better navigate biological environments and reach target tissues such as the BBB [8]. Nevertheless, the so-called “PEG dilemma“ must be considered: while the PEG layer enhances stealth properties and circulation time, it can also partially hinder cellular uptake and endosomal escape [9]. Balancing these opposing effects is therefore critical in the rational design of PEGylated SLNs for brain targeting. Despite these challenges, the PEGylation strategy remains indispensable for achieving an optimized biodistribution profile and reducing off-target accumulation, particularly in clearance organs such as the liver [10].

To overcome these intrinsic limitations, a natural evolution of PEGylation has been the introduction of targeting ligands at the distal ends of PEG chains. This approach preserves the stealth characteristics of PEG while introducing the ability of NPs to interact specifically with target receptors, thereby enhancing cellular uptake and transcytosis efficiency across biological barriers such as the BBB [11].

For successful CNS drug-targeted delivery, identifying receptors expressed on capillary endothelial cells is essential [12]. Neuroactive factors biosynthesized by peripheral tissues are attractive candidates for developing targeted carriers, since their transport into the brain depends on active mechanisms across the BBB. This has been demonstrated for several bioactive peptides and neuropeptides, including insulin, transferrin, lactoferrin, and leptin, which naturally undergo receptor-mediated transport (RMT) [13].

In this context, the surface decoration of NPs with active targeting ligands has garnered growing attention, yielding highly promising results in enhancing site-specific delivery and cellular internalization [14]. For instance, transferrin-functionalized SLNs have been developed for active targeting in breast cancer therapy, improving cellular uptake and therapeutic efficacy, while lactoferrin-conjugated SLNs have been designed as efficient brain-targeting systems for the delivery of docetaxel, exploiting receptor-mediated transcytosis across the BBB [15, 16].

To date, only a few studies have investigated the use of leptin or leptin-derived peptides as targeting ligands in DDS, and their application in SLNs remains poorly explored. Leptin, a 146-amino-acid polypeptide, plays a central role in maintaining body weight homeostasis by regulating food intake and energy expenditure [17]. Secreted primarily by white adipose tissue, leptin acts on neurons expressing the leptin receptor (ObR) within the CNS, particularly in the hypothalamus [18]. Considering leptin's natural affinity for ObR, expressed on the BBB and within the CNS, the use of this molecule represents a rational approach for active brain targeting [19].

Importantly, leptin also acts on peripheral tissues where its receptors are expressed. The ObR family comprises six isoforms (ObRa-ObRf), all sharing the same extracellular domain but differing in signaling capabilities [20]. While ObRb is the main signaling-competent receptor for hypothalamic neurons, the short isoform ObRa plays key roles in transport and membrane trafficking. Notably, ObRa is the isoform predominantly expressed on brain capillary endothelial cells, making it a crucial mediator of leptin

interaction with the BBB and a particularly attractive target for ligand-mediated brain delivery [21]. On this basis, identifying leptin-derived fragments capable of selectively engaging endothelial ObRa could enable more specific and efficient BBB targeting. A recent study has demonstrated that a leptin fragment comprising amino acid residues 61-90, overlapping with ObR-binding site IIb, can cross the BBB to a comparable extent as the wild-type protein [22].

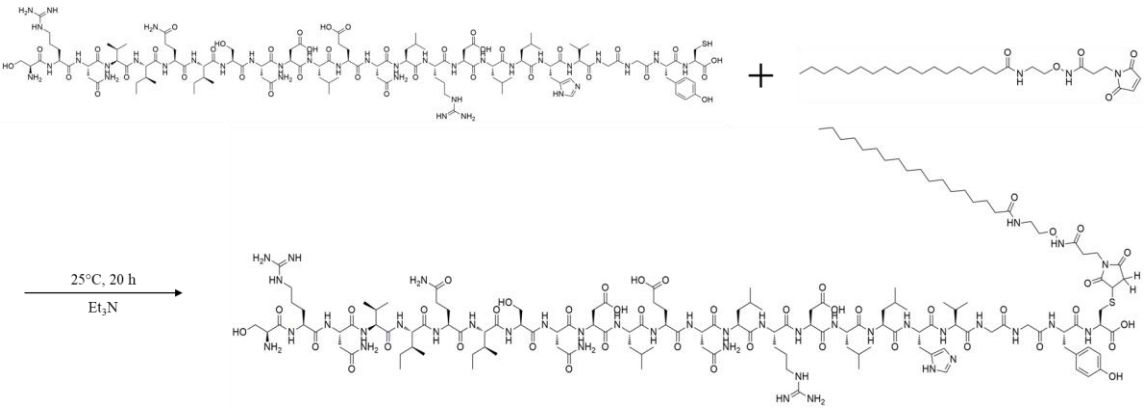
On these bases, this study aimed to develop a novel SLN formulation functionalized with a leptin-derived peptide fragment, Lep(70-89), designed as an active delivery platform for brain targeting. The use of the Lep(70-89) peptide fragment, rather than the full-length leptin protein, offers several key advantages, including lower production costs, improved chemical stability, simplified structural characterization, and more controlled, site-specific conjugation on the SLNs surface. Importantly, this fragment preserves the specific recognition capability toward ObR mesoforms, expressed on brain endothelial cells, enabling selective interaction with the BBB. As a result, Lep(70-89)-functionalized SLNs represent a promising strategy for receptor-mediated transcytosis-based brain delivery.

Such an approach is particularly relevant for the delivery of biotechnological therapeutics, including peptides, proteins, antibodies, and nucleic acids, whose clinical application to CNS disorders is often hindered by poor BBB permeability and high sensitivity to formulation and processing conditions. These molecules strongly suffer from intrinsic limitations such as thermal and chemical instability, susceptibility to enzymatic degradation, short plasma half-life, and large molecular size, which restrict passive diffusion across biological membranes and confine their administration predominantly to parenteral routes [34]. The combination of SLNs with RMT targeting is therefore expected to provide a protective microenvironment for sensitive biotechnological drugs, facilitating their transport across the BBB while preserving their structural integrity and biological activity.

3.3.2. Results and Discussion

Conjugate synthesis and characterization

The synthetic strategy employed in this work was adapted from the procedure reported by Tamaru *et al*., who developed PEG-liposomes functionalized with the leptin fragment [23]. In their study, the maleimide-thiol coupling reaction was exploited to achieve site-specific conjugation between DSPE-PEG-MAL and the peptide, through the Michael addition between the thiol group of the cysteine residue and the maleimide moiety (**Scheme 1**). Following this well-established approach, the present work replaced the phospholipid anchor (DSPE) with a PEGylated stearic acid (SA-PEG-MAL), which maintains the same reactive functionality while being compatible with the solid lipid matrix of SLNs. This reaction pathway ensures a stable thioether linkage and allows the selective orientation of the Lep(70-89) peptide on the SLNs surface for optimal receptor recognition.



Scheme 1. DMF anhydrous, Lep(70-89) (1 eq), SA-PEG-MAL (1.1 eq), Et_3N (5.5 eq), 25°C, 20 h.

The conjugation between SA-PEG-MAL and the Lep(70-89) peptide was confirmed by ^{1}H-NMR spectroscopy. In the spectrum of the SA-PEG-Lep(70-89) conjugate, the disappearance of the characteristic maleimide signal at 7 ppm (**Figure 24B**) indicates the occurrence of a Michael-type addition reaction between the peptide -SH group of the terminal cysteine residue and the maleimide ring of SA-PEG-MAL (**Figure 24A**). This confirmed the successful covalent attachment and the effective synthesis of the desired conjugate. The use of ^{1}H-NMR spectroscopy as a structural characterization method is consistent with the analytical strategy described by Vasconcelos *et al*., who confirmed peptide-polymer conjugation by monitoring the disappearance of the maleimide methine

proton signal and the appearance of new resonances attributed to the peptide amide and aromatic protons [24].

Therefore, the loss of the maleimide resonance in the SA-PEG-Lep(70-89) spectrum, together with the presence of characteristic signals from the peptide moieties, provided clear evidence that the thiol-maleimide reaction had proceeded to completion, resulting in a stable and covalently linked SA-PEG-Lep(70-89) conjugate suitable for nanoparticle functionalization.

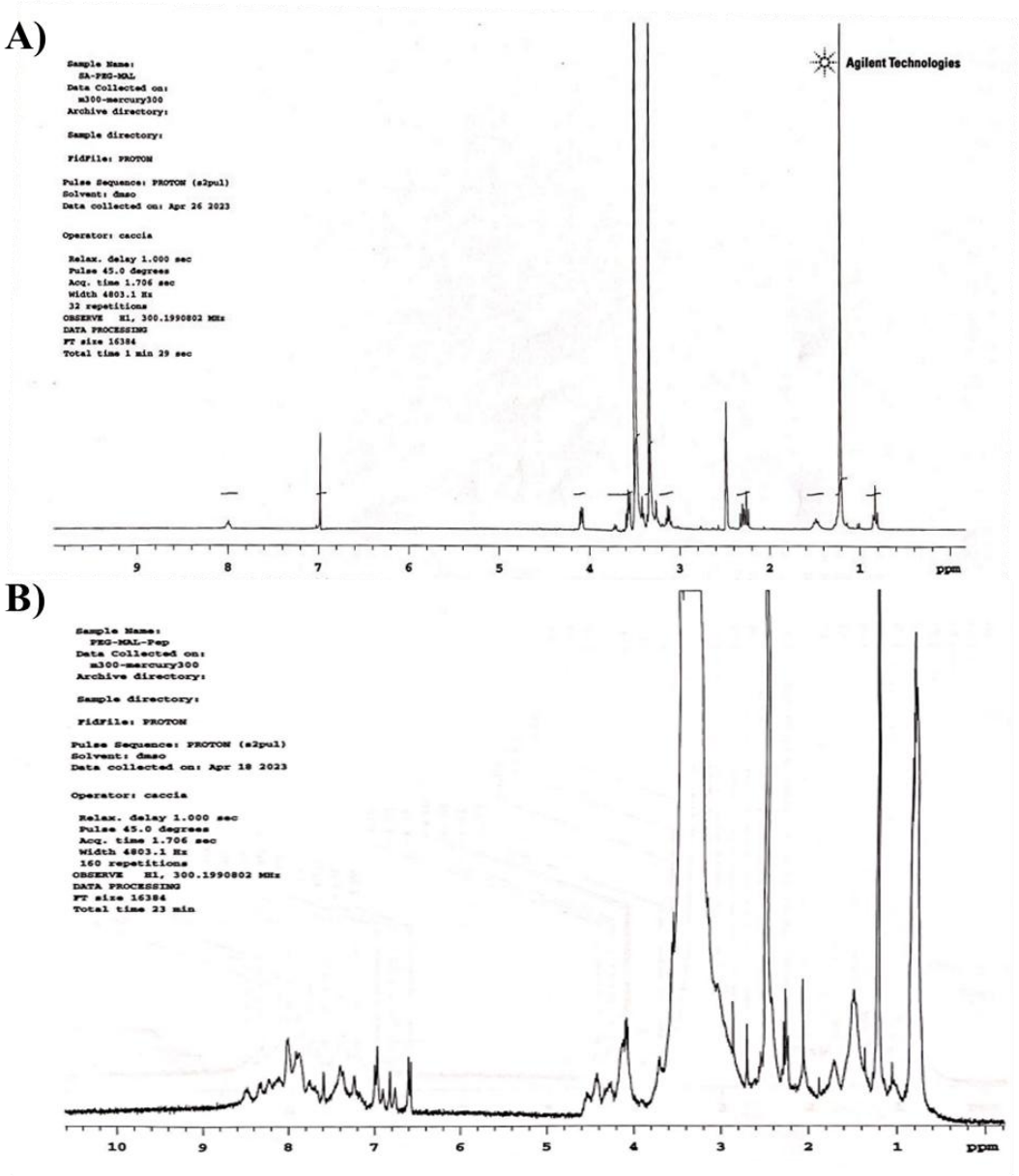


Figure 24. NMR spectras of **A)** SA-PEG-MAL, and **B)** SA-PEG-Lep(70-89) .

Formulation studies

Preformulation studies were carried out to evaluate the suitability of the selected excipients for the emulsification-solvent evaporation method and to identify the optimal composition for obtaining homogeneous SLNs [25]. The formulations (F1-F6) were prepared by varying the surfactant concentration and the lipid composition, and the resulting systems were characterized in terms of particle size, PDI, and ζ-potential, as reported in **Table 10**.

Table 10. Composition and physicochemical characterization of F1-F6.

Formulation	GMS	SA	SL	Tween 80	Surfactant: Lipids Ratio	Size	PDI	ζ-potential (mV)
F1	42.5 mg	7.5 mg	17.5 mg	0.6%*w/v*	1: 1.11	50.89 ± 20.47	0.246 ± 0.009	-3.70 ± 1.0
F2	42.5 mg	7.5 mg	17.5 mg	1.5%*w/v*	1: 2.77	50.21 ± 18.13	0.216 ± 0.003	-5.75 ± 0.9
F3	42.5 mg	7.5 mg	17.5 mg	3%*w/v*	1: 5.55	63.59 ± 31.54	0.245 ± 0.012	-11.90 ± 1.0
F4	42.5 mg	7.5 mg	17.5 mg	5%*w/v*	1: 9.26	44.98 ± 19.92	0.284 ± 0.005	-7.20 ± 0.5
F5	42.5 mg	33.75 mg	17.5 mg	1.5%*w/v*	1: 2	39.08 ± 19.35	0.250 ± 0.007	-15.30 ± 1.0
F6	42.5 mg	65 mg	17.5 mg	1.5%*w/v*	1: 1.5	84.32 ± 3.50	0.248 ± 0.015	-22.53 ± 3.7

The results revealed that variations in the surfactant-to-lipid ratio and the relative lipid content markedly influenced the particle size and surface charge of the SLNs. For formulations F1-F4, prepared using a constant lipid composition and increasing concentrations of Tween 80, the particle size remained within the nanometric range (approximately 45-65 nm) with narrow size distributions (PDI < 0.25), indicating good homogeneity. However, DLS analysis highlighted that Tween 80 concentrations higher than 1.5% resulted in an increase in PDI values and the appearance of two distinct peaks in the size distribution curves (data not shown): one corresponding to the main nanoparticle population and a smaller one around 5 nm, attributable to excess free surfactant micelles. This indicates that an excessive amount of Tween 80 leads to micelle

formation in the aqueous phase, artificially broadening the size distribution and increasing apparent polydispersity [26].

Conversely, at the lowest concentration (0.6%), Tween 80 appeared insufficient to adequately stabilize the emulsion system, resulting in a less uniform particle population. For this reason, the intermediate concentration of 1.5% w/v Tween 80 was selected as the most suitable, ensuring efficient emulsification and stable dispersion while avoiding micelle formation.

To further optimize the surface charge of the SLNs, the amount of charge-modifying lipid in the formulation was increased. Specifically, the concentration of SA was raised to enhance the ζ-potential and improve the electrostatic stabilization of the colloidal system. Therefore, the SA content was adjusted to achieve total lipid amounts corresponding to lipid-to-surfactant ratios of 1:2 (F5) and 1:1.5 (F6). The resulting formulations exhibited hydrodynamic diameter about 39 and 84 nm, respectively, with narrow size distributions. The ζ-potential values showed progressive improvement with increasing SA content, rising from -3.7 mV (F1) to -22.5 mV (F6). As expected, this modification led to a substantial increase in the absolute ζ-potential value (-22.53 ± 3.7 mV for F6), reflecting stronger electrostatic repulsion between particles and, consequently, a reduced tendency to aggregate. Although the higher SA content slightly increased the mean particle size (from 39.08 nm in F5 to 84.32 nm in F6), it remained below 100 nm, and all formulations exhibited PDI values below 0.25, confirming their good uniformity and stable dispersion. These findings indicate that Tween 80 concentrations around 1.5% w/v, combined with a lipid-to-surfactant ratio of 1:2, provided the best compromise between particle size control and formulation homogeneity. Among the tested formulations, F6, characterized by the highest SA content (65 mg), exhibited the most favorable physicochemical profile and was therefore selected as the optimal candidate for subsequent modification and functionalization steps.

Starting from these results, PEGylated SLNs (ELM) were produced by replacing the SA of formulation F6 with SA-PEG-MAL to introduce reactive groups suitable for ligand conjugation, as well as stealth properties. However, due to the higher molecular weight and bulk structure of the PEGylated lipid, a marked increase in particle size was observed: the formulation ELM 1 exhibited an average diameter of 340.20 ± 124.44 nm, significantly larger than that of the non-PEGylated F6 formulation (84.32 ± 3.50 nm).

This enlargement was attributed to the steric hindrance and reduced packing efficiency of PEG chains during nanoparticle solidification, leading to less compact structures.

Table 11. Composition and physicochemical characterization of surface-modified SLNs.

Formulation	GMS (mg)	SA-PEG-MAL (mg)	SA-PEG-Lep(70-89) (mg)	SL (mg)	Tween80 (%*w/v*)	Size (nm)	PDI	ζ-potential (mV)
ELM 1	42.5	65	-	17.5	1.5	340.20 ± 124.44	0.254 ± 0.05	-15.90 ± 0.60
ELM 2	50	1.5	-	15	1.5	65.46 ± 3.87	0.149 ± 0.004	-4.23 ± 2.21
ELM-Lep(70-89)	50	-	4.35	15	1.5	66.75 ± 4.45	0.204 ± 0.010	-19.13 ± 1.23

Based on previous studies performed by Li *et al.,* weight ratios between solid lipid and PEGylated lipid of approximately 100:3 are sufficient to ensure stealth properties while maintaining reduced particle dimensions [27]. On this basis, the amount of SA-PEG-MAL was reduced from 65 mg to 1.5 mg (ELM 2), resulting in a significant reduction in particle size and improved homogeneity (PDI = 0.149 ± 0.004). However, the zeta potential became less negative (-4.23 ± 2.21 mV), reflecting the shielding effect of the PEG layer on the surface charge, a typical feature of PEGylated nanoparticles that enhances colloidal stability and reduces opsonization (**Table 11**).

Finally, conjugation of the Lep(70-89) peptide to the functional groups at the distal ends of the PEG chains led to the formulation of ELM-Lep(70-89), which showed an almost unchanged particle size (66.75 ± 4.45 nm) and a more negative ζ-potential (19.13 ± 1.23 mV) (**Figure 25**).

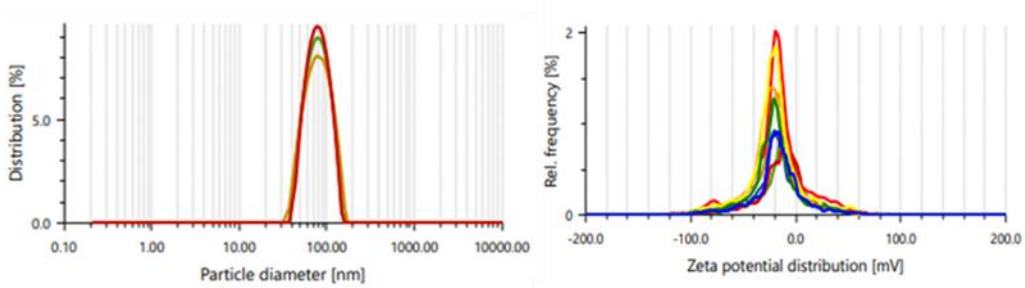


Figure 25. A) Particle size and **B)** ζ-potential distributions of ELM-Lep(70-89).

The limited variation in size may suggest that the peptide is arranged on the nanoparticle surface without affecting the overall colloidal structure. The increase in negative surface charge can be attributed to the Lep(70-89) structure, which contains acidic residues (Asp, Glu) conferring a slightly negative net charge at physiological pH. This explains the

higher absolute ζ-potential observed after conjugation, consistent with the exposure of these ionizable groups at the particle interface. The PDI (0.204 ± 0.010) remained within acceptable limits, indicating that the functionalization preserved nanoparticle uniformity and stability.

Morphological characterization

Atomic Force Microscopy (AFM) images provide insight into the morphology and surface characteristics of the developed SLNs (**Figure 26**): both samples exhibited a spherical morphology and uniform size distribution.

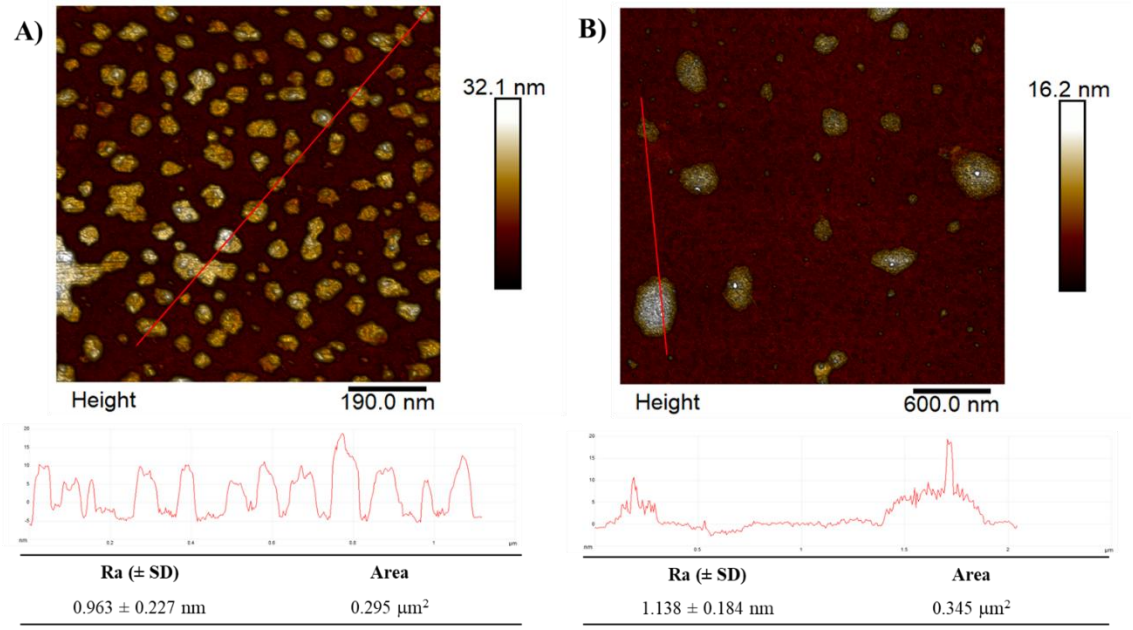


Figure 26. AFM images, height profiles, and roughness values of ELM **A)** and ELM-Lep(70-89) **B)**. The red line represents the section used for line profile analysis, from which the corresponding height profiles were obtained.

Notable differences in surface topography can be observed from the height profiles obtained along the red section lines. The profiles reveal greater height fluctuations for ELM-Lep(70-89) compared to ELM, indicating a less uniform surface at the nanoscale. This suggests that the ELM formulation (**Figure 26A**) possesses a relatively smooth and homogeneous surface, whereas ELM-Lep(70-89) (**Figure 26B**) exhibits a rougher and more irregular morphology. This observation is consistent with the roughness values (Ra), which were higher for ELM-Lep(70-89). The increased roughness can be attributed to the presence of Lep(70-89) peptide fragments on the distal ends of the PEG chains,

introducing additional nanoscale irregularities and slightly altering the lipid packing at the nanoparticle interface.

Raman spectroscopy

Raman spectroscopy provided complementary insights into the molecular organization and structural changes occurring in the lipid matrix after peptide conjugation (**Figure 27**) [28]. The characteristic Raman bands in the region between 2800 and 3000 cm^{-1} are associated with C-H stretching vibrations from the lipid hydrocarbon chains. Specifically, the bands at approximately 2850 cm^{-1} and 2880 cm^{-1} correspond to the symmetric and asymmetric CH_2 stretching modes of the SA alkyl chains, while the peak near 2930 cm^{-1} is attributed to the symmetric stretching of terminal CH_3 groups [29, 30].

A comparative analysis of ELM and ELM-Lep(70-89) spectra revealed evident differences in the relative intensities and positions of these vibrational bands. In particular, a reduction in the intensity ratio of the peaks at 2890 cm^{-1}/2930 cm^{-1} was observed for the functionalized nanoparticles. This change can be attributed to enhanced intermolecular and intramolecular interactions among the lipid chains following conjugation, reflecting a perturbation in the lipid molecular environment due to the presence of the peptide layer on the SLNs surface. Furthermore, the analysis of peak intensity ratios provided deeper information about the structural rearrangements within the lipid matrix. The I_{2930}/I_{2846} ratio (CH_3 terminal / CH_2 symmetric stretching) is a sensitive indicator of rotational disorder in the hydrocarbon chains, while the I_{2930}/I_{2879} ratio (CH_3 terminal / CH_2 asymmetric stretching) reflects variations in chain packing density and gauche/trans conformational transitions. In the case of ELM-Lep(70-89), both ratios showed a clear decrease compared to ELM, indicating a higher degree of molecular disorder and reduced chain alignment within the lipid core [31, 32]. This increased rotational and conformational disorder suggests that the conjugation of Lep(70-89) interferes with the tight packing of the lipid chains by introducing new intermolecular interactions at the interface, possibly through hydrogen bonding and steric effects between the peptide and the lipid headgroups. Such modifications in chain dynamics are

typical of surface-functionalized SLNs and have been previously correlated with the formation of a more flexible and hydrated interfacial layer [33].

Overall, the Raman results corroborate AFM findings, demonstrating that peptide conjugation slightly disrupts the crystalline order of the lipid matrix, increases molecular mobility, and modifies the surface characteristics without compromising the overall structural integrity of the SLNs. These spectral variations thus confirm the successful surface functionalization of PEGylated SLNs with the Lep(70-89) peptide and its impact on lipid molecular organization.

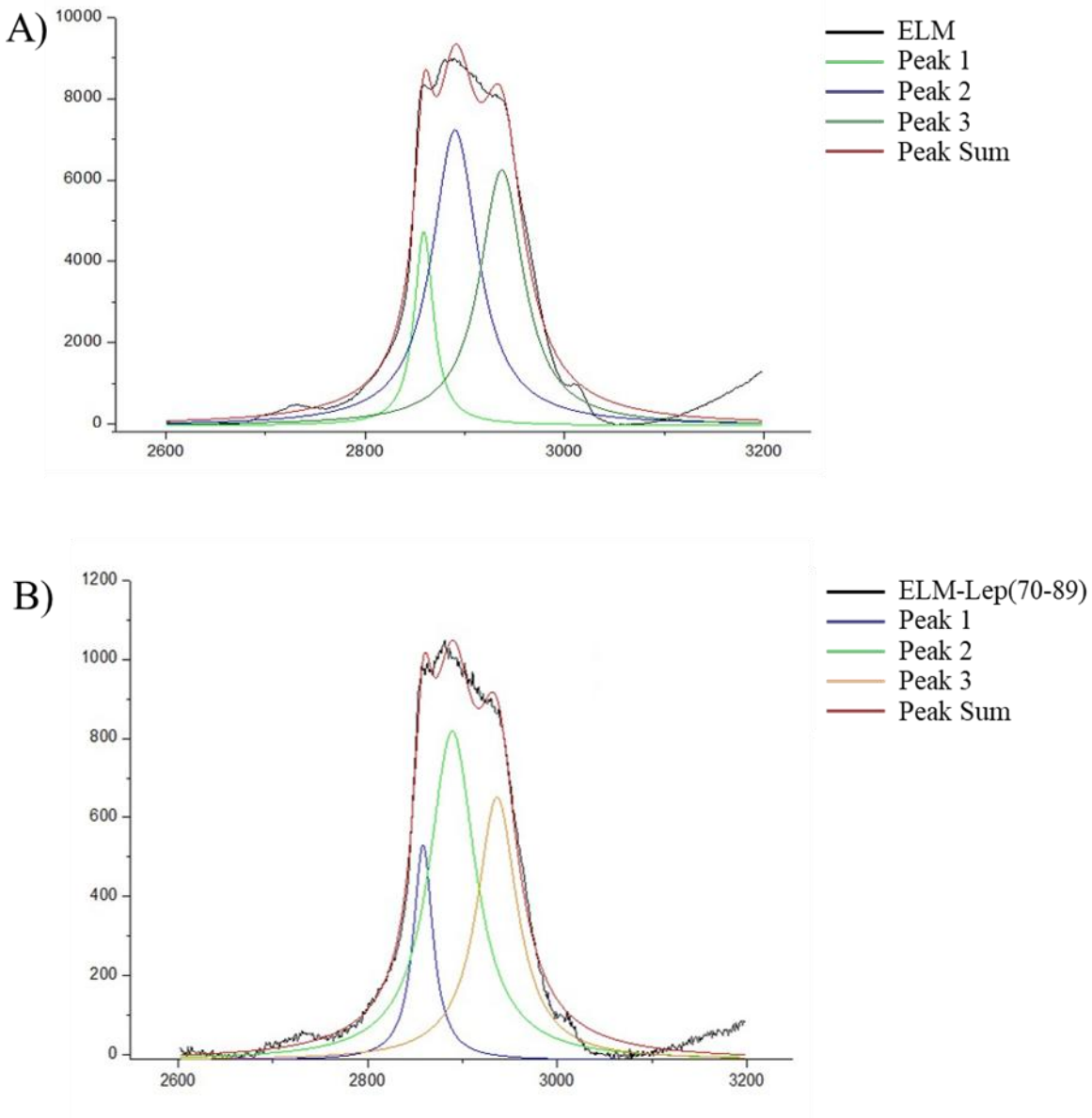


Figure 107. Raman spectra of ELM **A)**, and ELM-Lep(70-89) **B)**.

3.3.3. Experimental Section

Materials

Glyceryl monostearate (GMS), Soy lecithin (SL) and Tween 80 were purchased by Sigma Aldrich (St. Louis, MO, USA). Stearic Acid-PEG_{1000}-MAL (SA-PEG-MAL) was purchased from BroadPharm (San Diego, CA). The leptin-derived peptide, Lep20 with a cysteine on C terminal (96.8% purity, obsd. Mw=2729.4 sequence: SRNVIQISNDLENLRDLLHVGGYC) was synthesized by GenScript (Rijswijk, Netherlands). Ethanol and MilliQ water, and all other solvents of chromatographic grade were obtained from Sigma Aldrich.

Synthesis of SA-PEG-Lep(70-89)

The conjugation of Lep(70-89) peptide to the SA-PEG-MAL lipid was carried out by dissolving 100 mg of peptide into 2 mL of DMF and adding it later to a solution of 58,3 mg of SA-PEG-MAL dissolved in 2 mL of DMF. 20.4 mg of Et_3N was added to permit the cysteine residue to react with the maleimide moiety via Michael addition reaction. The reaction was left for 20 h under magnetical stirring at room temperature. The DMF was then removed by a rotary evaporator. The product was precipitated with 20 mL of cold ether: methanol (1:1) and centrifuged at 10,000 rm 4°C for 10 min. The supernatant was discarded, and the pellet was redissolved in chloroform. The final product was lyophilized and stored at -20°C [2]. Conjugation evaluation was carried out by proton nuclear magnetic resonance (^{1}H-NMR).

NMR spectroscopy

NMR spectroscopy analysis were performed with a Varian VXR-300 MHz spectrometer (Varian Medical Systems, Inc., Palo Alto, CA, USA).

SLNs preparation

The SLNs formulations were prepared according to a slight modification of the emulsification-evaporation-solidifying method previously reported. The SLNs components were selected based on previous studies on brain-targeting formulations [16]. Preliminary trials were performed to confirm the suitability of the selected lipids for the chosen production method. For the preformulation studies of SLN formulations based

GMS, SL, SA, and Tween 80, different ratios of these components were tested, mainly by varying the surfactant-to-lipid ratio and the amount of the charge-modifying excipient.
Briefly, GMS, SL, and SA were completely dissolved in 2.5 mL of ethanol under mild magnetic stirring at 40 ± 2 °C. Simultaneously, a solution of surfactant Tween 80 in deionized water, was prepared and heated at 75 ± 2°C. The organic phase was added dropwise to the aqueous phase under mechanical stirring (750 rpm) to obtain the lipid emulsion, which was subsequently concentrated to 12.5 mL, evaporating the solvents mixture at 75 ± 2 °C. The translucent emulsion system was quickly poured into 12.5 mL of cold deionized water on an ice bath under mechanical stirring (750 rpm) and kept for 30 min. The final suspension was filtered with 1.20 mm filters.
ELM and ELM-Lep(70-89) were prepared as previously reported by replacing SA with SA-PEG-MAL and SA-PEG-Lep(70-89), respectively.

Physical characterization

The average particle size and polydispersity index (PDI) of ELM and ELM-Lep(70-89) SLNs were determined using the dynamic light scattering technique (Anton Paar, Litesizer™ 500). The measurements were carried at 25°C under fixed angle of 90° in disposable polystyrene cuvettes. The formulations were diluted ten times with distilled water prior to measurement. Six measurements were performed in series to calculate the mean value of diameter.
ζ-potential measurements were performed in the DLS instrument operated in the electrophoretic light scattering mode (ELS). The measurements were carried at 25°C under fixed angle of 90° in Omega cuvettes Mat. No. 225288. The formulations were diluted ten times with distilled water prior to measurement. Six measurements were performed in series to calculate the mean value of ζ-potential.

Atomic Force Microscopy (AFM)

AFM images of the SLNs formulations were captured by using MultiMode 8 AFM microscope with Nanoscope V controller (Bruker, Billerica, Massachusetts, US). SLNs solutions were prepared at a concentration of 0.06 mM (27μg/mL) in EtOH and aliquots of 10 μL were placed on SiO2 substrates followed by drying at room temperature overnight. The obtained samples were scanned by the silicon ScanAsyst-Air probe (triangular geometry, cantilever resonance frequency 70 kHz and nominal spring constant

0.4 N/m) in ScanAsyst in Airmode. Images of 512 x 512 pixels were collected with different scan sizes, and the morphological analysis of the AFM data was performed using Nano-Scope Analysis 1.8 software.

Raman spectroscopy

All Raman spectra of were obtained by a confocal and high-performance Raman microscope (XploRA PLUS, HORIBA, Japan) with a deep-cooled CCD detector technology. LabSpec (Horiba, Japan) was employed to control, optimize, and process the acquired data. Furthermore, the Raman spectra were processed through Origin 8.5 to optimize the results. All Raman spectroscopic measurements were performed in the range of 2600-3200 cm^{-1} and with an 1800-line/mm grating. A single spectrum of the sample has been detected with a 532 nm laser, with a time of 10 s and 30 accumulations, to avoid excessive heating of the sample.

3.3.4. Conclusions and future perspectives

The present work describes the rational design of a leptin-derived peptide -functionalized SLNs (ELM-Lep(70-89)) as a promising platform for active drug delivery to the brain. The formulation strategy successfully integrates the stealth behaviour of PEGylated SLNs with the RMT targeting potential of the Lep(70-89) peptide, providing a versatile platform for CNS applications.

In perspective, this nanosystem could serve as a carrier for neuroprotective or neuroactive compounds that require efficient delivery across the BBB, including biotechnological therapeutics relevant to neurodegenerative disorders such as Parkinson's and Alzheimer's diseases. To this end, the translation of the formulation toward microfluidic manufacturing has been considered, since this approach allows nanoparticle production at reduced volumes and under mild processing conditions, avoiding the use of high temperatures. Preliminary studies, focusing on the microfluidic approach, are reported in the next chapter (*Chapter 4.1*).

References

1. Nance, E., S.H. Pun, R. Saigal, D.L. Sellers, Drug delivery to the central nervous system. *Nat Rev Mater*, **2022**. 7(4): p. 314-331.
2. Pardridge, W.M., Drug transport across the blood-brain barrier. *J Cereb Blood Flow Metab*, **2012**. 32(11): p. 1959-72.
3. Pardridge, W.M., The blood-brain barrier and neurotherapeutics. *NeuroRx*, **2005**. 2(1): p. 1-2.
4. Anthony, D.P., M. Hegde, S.S. Shetty, T. Rafic, S. Mutalik, B.S. Rao, Targeting receptor-ligand chemistry for drug delivery across blood-brain barrier in brain diseases. *Life sciences*, **2021**. 274: p. 119326.
5. Satapathy, M.K., T.-L. Yen, J.-S. Jan, R.-D. Tang, J.-Y. Wang, R. Taliyan, C.-H. Yang, Solid lipid nanoparticles (SLNs): an advanced drug delivery system targeting brain through BBB. *Pharmaceutics*, **2021**. 13(8): p. 1183.
6. Suk, J.S., Q. Xu, N. Kim, J. Hanes, L.M. Ensign, PEGylation as a strategy for improving nanoparticle-based drug and gene delivery. *Adv Drug Deliv Rev*, **2016**. 99(Pt A): p. 28-51.
7. Tong, H., Z. Ma, D. Li, J. Yu, Q. Zhu, H. Shi, Y. Zheng, L. Zhou, H. Li, P. Lv, Tuning the Polyethylene Glycol-Lipid Anchor Length of Lipid Nanoparticles to Enhance Brain-Targeted siRNA Delivery. *Acta Biomaterialia*, **2025**.
8. Arduino, I., N. Depalo, F. Re, R. Dal Magro, A. Panniello, N. Margiotta, E. Fanizza, A. Lopalco, V. Laquintana, A. Cutrignelli, PEGylated solid lipid nanoparticles for brain delivery of lipophilic kiteplatin Pt (IV) prodrugs: An in vitro study. *International journal of pharmaceutics*, **2020**. 583: p. 119351.
9. Suzuki, T., Y. Suzuki, T. Hihara, K. Kubara, K. Kondo, K. Hyodo, K. Yamazaki, T. Ishida, H. Ishihara, PEG shedding-rate-dependent blood clearance of PEGylated lipid nanoparticles in mice: Faster PEG shedding attenuates anti-PEG IgM production. *International Journal of Pharmaceutics*, **2020**. 588: p. 119792.
10. Hashimoto, Y., T. Shimizu, A.S.A. Lila, T. Ishida, H. Kiwada, Relationship between the concentration of anti-polyethylene glycol (PEG) immunoglobulin M (IgM) and the intensity of the accelerated blood clearance (ABC) phenomenon against

PEGylated liposomes in mice. *Biological and Pharmaceutical Bulletin*, **2015**. 38(3): p. 417-424.

11. Zalba, S., T.L. Ten Hagen, C. Burgui, M.J. Garrido, Stealth nanoparticles in oncology: Facing the PEG dilemma. *Journal of Controlled Release*, **2022**. 351: p. 22-36.
12. Lajoie, J.M., E.V. Shusta, Targeting receptor-mediated transport for delivery of biologics across the blood-brain barrier. *Annual review of pharmacology and toxicology*, **2015**. 55(1): p. 613-631.
13. Ermisch, A., Peptide receptors of the blood-brain barrier and substrate transport into the brain. *Progress in Brain Research*, **1992**. 91: p. 155-161.
14. Zheng, J., Y. Sun, Y. Shen, Z. Zhou, Surface engineering of nanoparticles for precision medicine. *Precision Medicine and Engineering*, **2025**: p. 100037.
15. Bhagwat, G.S., R.B. Athawale, R.P. Gude, S. Md, N.A. Alhakamy, U.A. Fahmy, P. Kesharwani, Formulation and Development of Transferrin Targeted Solid Lipid Nanoparticles for Breast Cancer Therapy. *Front Pharmacol*, **2020**. 11: p. 614290.
16. Singh, I., R. Swami, D. Pooja, M.K. Jeengar, W. Khan, R. Sistla, Lactoferrin bioconjugated solid lipid nanoparticles: a new drug delivery system for potential brain targeting. *J Drug Target*, **2016**. 24(3): p. 212-23.
17. Banks, W.A., M.L. Niehoff, D. Martin, C.L. Farrell, Leptin transport across the blood-brain barrier of the Koletsky rat is not mediated by a product of the leptin receptor gene. *Brain Res*, **2002**. 950(1-2): p. 130-6.
18. Banks, W.A., Leptin transport across the blood-brain barrier: implications for the cause and treatment of obesity. *Curr Pharm Des*, **2001**. 7(2): p. 125-33.
19. Münzberg, H., C.D. Morrison, Structure, production and signaling of leptin. *Metabolism*, **2015**. 64(1): p. 13-23.
20. Pan, W., H. Hsuchou, H. Tu, A.J. Kastin, Developmental changes of leptin receptors in cerebral microvessels: unexpected relation to leptin transport. *Endocrinology*, **2008**. 149(3): p. 877-85.
21. Hileman, S.M., J. Tornøe, J.S. Flier, C. Bjørbaek, Transcellular transport of leptin by the short leptin receptor isoform ObRa in Madin-Darby Canine Kidney cells. *Endocrinology*, **2000**. 141(6): p. 1955-61.
22. Barrett, G.L., J. Trieu, T. Naim, The identification of leptin-derived peptides that are taken up by the brain. *Regul Pept*, **2009**. 155(1-3): p. 55-61.

23. Tamaru, M., H. Akita, T. Fujiwara, K. Kajimoto, H. Harashima, Leptin-derived peptide, a targeting ligand for mouse brain-derived endothelial cells via macropinocytosis. *Biochem Biophys Res Commun*, **2010**. 394(3): p. 587-92.
24. Vasconcelos, A., E. Vega, Y. Pérez, M.J. Gómara, M.L. García, I. Haro, Conjugation of cell-penetrating peptides with poly (lactic-co-glycolic acid)-polyethylene glycol nanoparticles improves ocular drug delivery. *International journal of nanomedicine*, **2015**: p. 609-631.
25. Mehnert, W., K. Mäder, Solid lipid nanoparticles: production, characterization and applications. *Adv Drug Deliv Rev*, **2001**. 47(2-3): p. 165-96.
26. Khaleseh, F., M. Barzegar-Jalali, P. Zakeri-Milani, Z. Islambulchilar, H. Valizadeh, Optimum surfactant concentration for preparation of amiodarone loaded solid lipid nanoparticles: Theoretical estimation versus experimental results by box-behnken design. *J Rep Pharm Sci*, **2023**. 12: p. e146155.
27. Li, R., J.S. Eun, M.K. Lee, Pharmacokinetics and biodistribution of paclitaxel loaded in pegylated solid lipid nanoparticles after intravenous administration. *Arch Pharm Res*, **2011**. 34(2): p. 331-7.
28. Bunaciu, A.A., H.Y. Aboul-Enein, Ş. Fleschin, Vibrational spectroscopy in clinical analysis. *Applied Spectroscopy Reviews*, **2015**. 50(2): p. 176-191.
29. Movasaghi, Z., S. Rehman, I.U. Rehman, Raman spectroscopy of biological tissues. *Applied Spectroscopy Reviews*, **2007**. 42(5): p. 493-541.
30. Jores, K., A. Haberland, S. Wartewig, K. Mäder, W. Mehnert, Solid lipid nanoparticles (SLN) and oil-loaded SLN studied by spectrofluorometry and Raman spectroscopy. *Pharmaceutical research*, **2005**. 22(11): p. 1887.
31. Giancaspro, J., P. Scollan, J. Rosario, E. Miller, S. Braziel, S. Lee, Structural determination of model phospholipid membranes by Raman spectroscopy: Laboratory experiment. *Biochemistry and Molecular Biology Education*, **2022**. 50(2): p. 181-192.
32. Saupe, A., K.C. Gordon, T. Rades, Structural investigations on nanoemulsions, solid lipid nanoparticles and nanostructured lipid carriers by cryo-field emission scanning electron microscopy and Raman spectroscopy. *International journal of pharmaceutics*, **2006**. 314(1): p. 56-62.

33. Lang, X., X. Gao, M. Wei, N. Qian, W. Min, Bioorthogonal chemical imaging of solid lipid nanoparticles with minimal labeling by stimulated Raman scattering microscopy. *Natural Sciences*, **2023**. 3(2): p. e202103304.
34. Conti S., Polonelli L., Frazzi R., Artusi M., Bettini R., Cocconi D., Colombo P., Controlled delivery of biotechnological products. *Curr Pharm Biotechnol*., **2000.** 1(4): p. 313-23.

Chapter 4.
Experimental Investigation of Microfluidic and Hierarchical Structures

4.1. From Batch to Microfluidics Production of SLNs

4.1.1. Introduction

Microfluidic technology has emerged as an innovative approach for the fabrication of SLNs, offering a robust alternative to conventional bulk production methods [1]. By exploiting laminar flow conditions, microfluidic systems enable precise control over mixing dynamics, residence time, and solvent-antisolvent interactions, resulting in SLNs with uniform and tunable sizes, low polydispersity, improved encapsulation efficiency, and superior batch-to-batch reproducibility [2-5]. In addition to these formulation advantages, microfluidics reduces solvent and reagent consumption, minimizing waste generation and improving the sustainability and cost-effectiveness of nanoparticle manufacturing processes [6, 7]. Microfluidic manufacturing is especially advantageous for biotechnological therapeutics, such as peptides and proteins, whose formulation is often limited by sensitivity to harsh processing conditions. The ability to operate at reduced volumes and under mild, controlled conditions, without the use of high temperatures, makes microfluidic SLN fabrication suitable for preserving molecular integrity and biological activity. Recent studies have demonstrated the versatility of microfluidic platforms for encapsulating a wide range of therapeutic agents, including small molecules, peptides, proteins, enzymes, and chemotherapeutics, often achieving enhanced stability and biological performance relative to bulk-prepared SLNs. Representative examples include tristearin-based ovalbumin-loaded SLNs produced using a benchtop NanoAssemblr™ system [8], iRGD-functionalized paclitaxel-loaded SLNs manufactured via 3D-printed microfluidic chips for tumour targeting [9], and lysozyme-loaded SLNs obtained using custom microfluidic devices that preserved enzyme structure and activity [10]. Despite these promising results, the application of microfluidics to SLN fabrication remains relatively recent, and further systematic studies are required to fully establish its robustness, scalability, and translational potential.

From a mechanistic perspective, microfluidic SLN preparation relies on the controlled mixing of an organic phase containing the molten lipid dissolved in a water-miscible solvent and an aqueous phase containing stabilizing surfactants. The final physicochemical properties of SLNs are governed by a complex interplay of process-related parameters, including total flow rate (TFR), flow rate ratio (FRR), device

geometry, temperature, and pressure, all of which regulate nucleation and growth kinetics [11-14]. In parallel, formulation-related factors such as lipid concentration, drug loading, and phase introduction sequence further influence encapsulation efficiency and nanoparticle stability [15]. The choice of microfluidic chip material and fabrication method is equally critical, as surface-fluid interactions can affect mixing efficiency and particle formation. Various mixer designs, such as hydrodynamic flow focusing, staggered herringbone mixers, T- and Y-junctions, and baffle-based geometries, have been developed to enhance mixing efficiency and control nanoprecipitation, directly impacting SLN size and uniformity [16-18].

This work aimed to investigate the feasibility of transferring the preparation of SLNs based on glyceryl monostearate (GMS), soybean lecithin (SL), and stearic acid-PEG_{1000} (SA-PEG), a lipid composition previously employed for conventional batch-based SLN formulations, from a classical bulk method to a microfluidic manufacturing approach.

From a translational perspective, processing a previously validated SLNs composition using microfluidic technology could be attractive, as it enables the preservation of established formulation performance while exploiting the enhanced controllability and reproducibility of microfluidic processing. However, this transition is not trivial, since differences in mixing regime, solvent exchange rates, and hydrodynamic conditions may alter lipid self-assembly and stabilization mechanisms, ultimately affecting particle size, homogeneity, and colloidal stability. Accordingly, a systematic investigation was undertaken to assess the robustness of this translation and to identify the critical process and formulation parameters governing SLN formation under microfluidic conditions. To this end, a comprehensive screening of key microfluidic variables (including FRR, TFR, chip geometry, surfactant concentration, lipid concentration, and lipid composition) was performed in a stepwise manner to elucidate their individual and combined effects on the main quality attributes of SLNs, namely particle size, polydispersity index, and short-term colloidal stability.

Overall, this work establishes a rational framework for translating conventional SLN formulations into microfluidic processes, providing mechanistic insights into parameter property relationships and laying the groundwork for future formulation optimization, drug loading, and scalable SLN production using microfluidic technology.

4.1.2. Results and Discussion

First Parameter Screening for SLNs Optimization

Dynamic light scattering (DLS) analysis of Runs 1-5, with sizes ranging from 52 to 133 nm, showed that decreasing the FRR from 12 to 4, corresponding to an increase in the organic solvent fraction during microfluidic mixing, led to a progressive increase in particle size, while the PDI remained relatively unchanged (**Table 1**).

Table 1. Size and PDI of experimental Runs 1-20.

Run	Size (nm)	PDI	Peak 1 by Intensity (nm)	Peak 2 by Intensity (nm)
1	52*	0.32	82	10
2	69*	0.30	94	10
3	75*	0.29	104	12
4	107	0.33	-	-
5	133	0.36	-	-
6	90	0.44	-	-
7	81	0.34	-	-
8	80*	0.30	105	15
9	102*	0.39	142	27
10	51*	0.30	73	10
11	60*	0.27	80	11
12	63	0.25	-	-
13	71*	0.32	94	12
14	71	0.29	-	-
15	59	0.25	-	-
16	57	0.25	-	-
17	77*	0.38	109	13
18	60*	0.32	81	10
19	54	0.24	-	-
20	54*	0.43	86	11

*multiple populations. Peak 1 and Peak 2 are reported for formulations exhibiting bimodal or multimodal particle size distributions.

Alongside the main SLN population, a secondary population at approximately 10-15 nm was observed in several formulations and attributed to the formation of Tween 80 micelles, likely arising from excess surfactant not involved in nanoparticle self-assembly. Deng *et al*. performed DLS and TEM analyses on aqueous Tween 80 solutions and reported the presence of empty micelles with sizes around 10 nm at concentrations exceeding the critical micelle concentration, closely matching the secondary population observed in the present study [20]. Considering the absence of this population from FRR

ratio values lower than 6, a second experimental set (Runs 6-9) was designed by fixing the Tween 80-to-lipid mass ratio to the value calculated for this condition; however, the micellar population was still intermittently detected, suggesting that micelle formation is not strictly governed by the Tween-to-lipid ratio and may instead result from dynamic self-assembly processes. To further improve particle homogeneity, a micromixer chip was introduced (Run 10-20), leading to overall smaller and more homogeneous SLNs, with Run 12 exhibiting the lowest PDI value. Variations in total flow rate (±0.5 mL/min around 2 mL/min) and lipid concentration (15, 10, and 5 g/L) did not produce significant changes in size or PDI, and therefore standard values of 2.0 mL/min and 15 g/L were selected for subsequent experiments (Runs17-20).

Short-term stability studies revealed a pronounced increase in particle size over time, as observed for Runs 12 and 20 after 16 h of storage at room temperature (**Table 2**).

Overall, the first optimization phase defined a set of fixed process parameters for SLN production at T0, which were subsequently used as reference conditions in the following phase. Keeping together the increase in size and the meanwhile reduction of PDI, suggests that formulation required a maturation time probably corresponding to the arrangement of Tween on the SLNs surface.

Table 2. Short-term stability study

Run	Time (h)	Size (nm)	PDI
12	**0**	63	0.25
	16	155	0.18
20	**0**	66	0.28
	16	116	0.18

Second phase

Under the reference process conditions identified in the first phase, Runs 2_1 to 2_5 were performed to investigate the effect of different final Tween 80-to-lipid ratios on SLN formation and short-term stability. At T0, when the formulations were stored *as is*, all formulations exhibited particle sizes of approximately 70 nm with PDI values around 0.4 (**Table 3**). Notably, the absence of Tween 80 (Run 2_1) did not result in significant differences in either particle size or PDI, and no clear correlation was observed between Tween 80 concentration and the measured parameters. Meanwhile, the same formulation subjected to exchange in Milli-Q water (2_1W, 2_2W, 2_3W, 2_4W, 2_5W) exhibited particle sizes in the range of 100-120 nm, with PDI values between 0.2 and 0.3.

After 24 h, the samples 21, 22, 23, stored as is exhibited dimension increase to around 170 nm and a reduction in PDI. Runs 24 and 25 displayed evident opalescence, and DLS measurements were no longer considered reliable. When stored for 24 h, after water treatment, particle sizes exceeded 130 nm for all samples, accompanied by increased PDI values and the appearance of pronounced opalescence. Buffer exchange in PBS was not feasible, as it induced rapid precipitation of the samples, preventing reliable DLS analysis.

Table 3. Size and polydispersity index of Runs 21-25, analysed *as is*, and after water exchange 21W-25W).

As is	Time (h)	Size (nm)	PDI	Peak 1 (nm)	Peak 2 (nm)
21	0	68*	0.27	95	8
	24	169	0.17	-	-
22	0	67	0.23	-	-
	24	164	0.18	-	-
23	0	69	0.26	-	-
	24	170	0.19	-	-
24	0	68*	0.27	95	13
	24	923	0.98	-	-
25	0	68*	0.28	89	13
	24	231*	0.38	212	48
Water exchanged	**Time (h)**	**Size (nm)**	**PDI**	**Peak 1 (nm)**	**Peak 2 (nm)**
21W	0	102	0.19	-	-
	24	140	0.26	-	-
22W	0	113	0.25	-	-
	24	561	0.49	-	-
23W	0	107	0.22	-	-
	24	145	0.25	-	-
24W	0	104	0.22	-	-
	24	168	0.24	-	-
25W	0	100	0.22	-	-
	24	209	0.34	-	-

*multiple populations. Peak 1 and Peak 2 are reported for formulations exhibiting bimodal or multimodal particle size distributions.

Evaluation of the Amicon-based purification procedure showed that samples subjected to exchange in Milli-Q water exhibited a slightly larger particle size at T0 (approximately 100 nm) compared to *as is* samples (approximately 70 nm). However, despite this initial size increase, water-exchanged samples displayed a more moderate particle growth over time. These results indicate that, although purification in water induces a slight increase in particle size immediately after processing, it contributes to a partial stabilization of SLN dispersions over time by slowing down particle growth. Nevertheless, particle size

continued to increase upon prolonged storage, suggesting that solvent exchange alone is not sufficient to fully stabilize the system.

Third phase

In the third optimization phase, the molar ratios of the lipid components were modified. All formulations were diluted to final organic solvent fractions of 8%, 2% *v/v*. Different conditions were applied to assess the effect of dilution on particle size and stability over time.

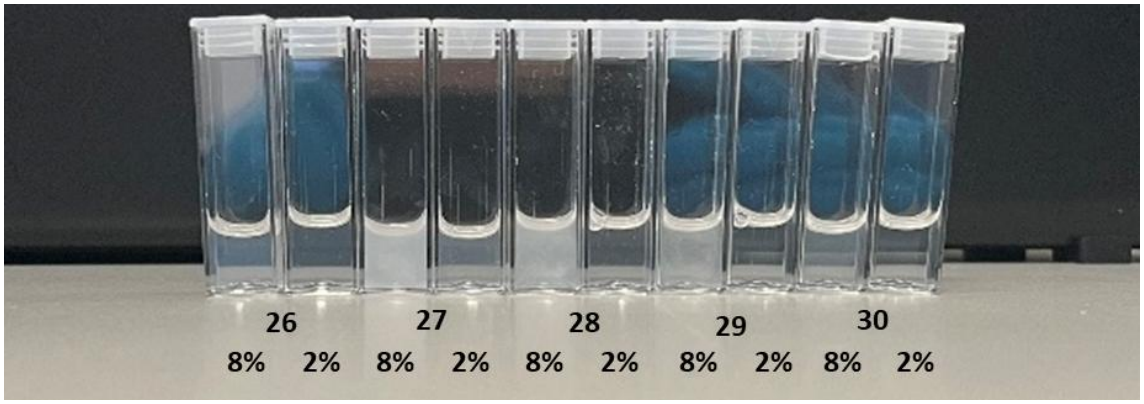


Figure 1. Visual aspect of Runs 26-30 at concentrations of 8 and 2% *v/v*.

At T0, all exhibited comparable particle size, and PDI, indicating that dilution within this range did not significantly affect the measured hydrodynamic diameter. Dispersions at higher organic solvent content (8%) were excluded from the comparative analysis, as they were consistently visually cloudy and therefore unsuitable for reliable particle size determination (**Figure 1**). For this reason, the 2% dilution condition was selected as the reference for evaluating formulation features and short-term stability.

In Runs 26-30, performed at a fixed FRR of 4 while varying the incoming Tween 80 concentration from 3 to 150 g/L, acceptable particle size and PDI values were obtained only for Run 26, corresponding to the lowest Tween 80 concentration (**Table 4**). Increasing the Tween 80 concentration resulted in larger apparent particle sizes and in the appearance of an additional population attributed to Tween micelles again, as indicated by the increasing intensity of the peak in the 10-15 nm range. These findings suggest that excessive Tween 80 does not improve SLNs' characteristics and instead contributes to increased system heterogeneity.

Table 4. Size and polydispersity index of Runs 26-30, at different dilutions of organic fraction(8, 2% *v/v*).

Runs	**26**		**27**		**28**		**29**		**30**	
Conc (%*v/v*)	Size (nm)	PDI	Size (nm)	PDI	Size (nm)	PDI	Size (nm)	PDI	Size (nm)	PDI
8%	105	0.23	144	0.46	110*	0.44*	36*	0.61*	14*	0.29*
2%	94	0.22	116	0.37	80*	0.39*	32*	0.61*	12*	0.31*

*multiple populations.

Stability studies

Holding-time studies were performed to evaluate the short-term stability of the SLN formulation at 2% *v/v* of organic content. To ensure a meaningful comparison among formulations, only data obtained from samples that remained sufficiently clear to allow reliable DLS measurements were considered in the discussion. Therefore, 8% *v/v* was discarded from the study due to the cloudiness previously mentioned. This effect was described by Gordillo-Galeano *et al.*, who demonstrated that dilution of lipid nanoparticle dispersions, within an appropriate concentration range and without altering formulation composition, does not necessarily result in significant changes in mean particle size, while it can markedly improve colloidal stability by reducing interparticle interactions and aggregation during storage [21]. Similarly, Mehnert *et al.* reported that lower particle concentrations in SLNs reduce particle-particle contact and time-dependent growth phenomena, leading to enhanced physical stability while maintaining comparable initial particle sizes [22].

At T0, run 26 showed particle size of 94 nm with low PDI values (0.22), whereas Runs 27-30 already exhibited broader size distributions and higher PDI values. After 24 h, Run 26 displayed only a moderate increase in particle size (30 nm), indicating a relatively stable behaviour (**Table 6**). In contrast, Runs 27-30 showed a rapid and uncontrolled increase in particle size, with high PDI values and pronounced sample cloudiness. As a result, DLS measurements for these runs were excluded from quantitative comparison.

Table 6. Holding time results for Runs 26-30, at concentrations 2% *v/v*.

Runs	**26**		**27**		**28**		**29**		**30**	
Time (h)	Size (nm)	PDI	Size (nm)	PDI	Size (nm)	PDI	Size (nm)	PDI	Size (nm)	PDI
0	94	0.22	116	0.37	80	0.39	32	0.61	12	0.31
24	124	0.29	-		-		-		-	

Based on these results, Run 26 was identified as the most promising formulation and was selected for reproducibility and extended stability studies. Replicate experiments confirmed the reproducibility of Run 26. The influence of storage temperature was further investigated by storing it at 5 and -20 °C for up to 5 days. As shown in **Table 7**, lower storage temperatures resulted in reduced particle growth. Conversely, instability at room temperature is a well-recognized characteristic of SLN systems, mainly associated with ongoing lipid recrystallization and increased molecular mobility. In this regard, Shah *et al*. reported that stearic acid-based SLNs exhibited pronounced particle growth when stored at room temperature, whereas refrigerated storage effectively preserved particle size and colloidal stability, highlighting the strong temperature dependence of SLNs' stability and the intrinsic susceptibility of these systems to destabilization under ambient conditions [23].

Overall, the performed stability studies demonstrated that SLNs' stability is strongly formulation-dependent and controlled by low-temperature storage.

Table 7. Size and PDI of Run 26 before and after 5 days of storage at 5, and -20 °C.

	Day 0	**Day 5**	
Storage Temperature	**25°C**	**5°C**	**-20 °C**
Size	90	113	95
PDI	0.20	0.26	0.28

4.1.3. Experimental section

Materials

Soybean lecithin (SL), glyceryl monostearate (GMS), and Tween 80 were purchased from Sigma-Aldrich (St. Louis, MO, USA). Stearic acid-PEG_{1000} (SA-PEG) was purchased from Tebubio (Île-de-France, France). Dimethyl sulfoxide (DMSO) and Milli-Q water were of HPLC grade.

Preparation of precursor solutions for microfluidic device

The lipid solution was prepared by dissolving SL and GMS in DMSO at proper concentrations. The mixture was stirred at room temperature for 5 h and subsequently heated to 40 °C for the last 15 min to ensure complete solubilization. The solution was then maintained under magnetic stirring overnight.

After this step, SA-PEG_{1000} was added and solubilized at 40 °C for an additional 20 min. The final lipid solution was filtered through a 0.2 µm nylon membrane filter before use.

An aqueous solution of Tween 80 was prepared as a stock solution at 30 g/L and subsequently diluted to working concentrations. The solution was filtered through a 0.2 µm PES membrane filter before microfluidic processing.

First optimization phase of SLNs

The influence of microfluidic parameters on SLNs size and PDI was systematically investigated. The parameters explored included flow rate ratio (FRR), Tween 80 concentration, chip geometry, total flow rate (TFR), and lipid concentrations. After production, all samples were quenched with Milli-Q water to standardize the organic solvent fraction to approximately 8% *v/v* (**Table 8**).

Effect of Flow Rate Ratio

The first experimental set consisted of five microfluidic runs (Runs 1-5) in which the FRR varied from 12 to 4, while maintaining constant conditions: TFR 2 mL/min, lipids concentrations 15 g/L, Tween 80 concentration 2 g/L; droplet Junction chip geometry (**Figure 2**).

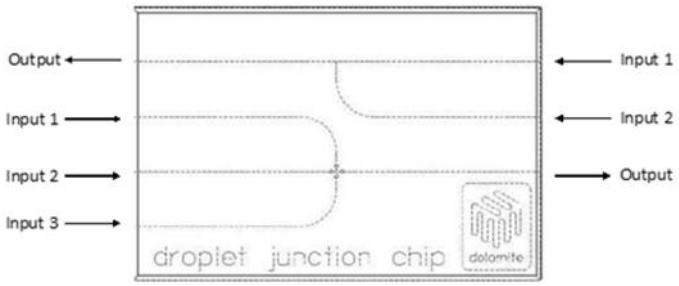


Figure 2. Droplet Junction Chip.

Effect of surfactant concentration

A second set of experiments (Runs 6-9) was designed to maintain a constant Tween/lipid mass ratio equivalent to that calculated for FRR 6, while varying the surfactant amount. Therefore, Tween 80 stock solutions with concentrations of 3, 1.50, 1.20, and 1.0 g/L were prepared starting from the 30 g/L stock solution. Fixed parameters were the TFR 2 mL/min, the lipid stock solution concentration 15 g/L, and droplet junction chip geometry.

Effect of chip geometry

To investigate the influence of chip geometry on SLN production, two microfluidic geometries were used: a droplet junction chip (Runs 1-9) and a micromixer chip (Runs 10-20) (**Figure 3**). Runs 10-14 were carried out at FRR values between 12 and 4, with a fixed TFR of 2 mL/min, a lipids stock solution concentration of 15 g/L, droplet junction chip geometry.

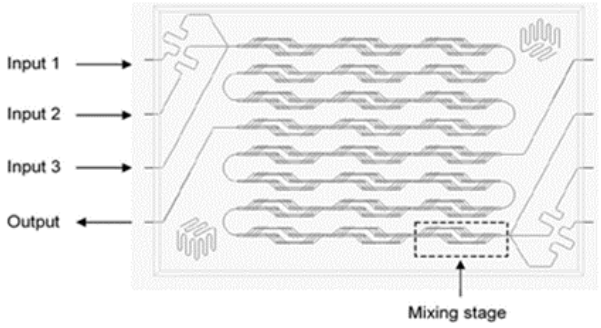


Figure 3. Micromixer chip.

Effect of TFR variation

The effect of TFR was investigated by varying the TFR around the reference value of 2 mL/min (± 0.5 mL/min). Runs 15-17 were performed under the following constant conditions: FRR 8, lipid stock solution concentration 15 g/L, micromixer chip geometry.

Effect of lipids concentration

The influence of lipid concentration was then evaluated by performing Runs 18-20 using lipid concentrations of 5, 10, and 15 g/L, while maintaining the following parameters: FRR 8, TFR 2 mL/min, and micromixer chip geometry.

Table 8. Microfluidic process parameters for Runs 1-20.

Run	TFR (mL/min)	FRR	Lipids (g/L)	Tween 80 (g/L)	FR(o) mL/min	FR(w) mL/min	Tween 80 /Lipid Ratio (*w/w*)
1	2	12	15	2	0.15	1.85	1.60
2	2	10	15	2	0.18	1.82	1.33
3	2	8	15	2	0.22	1.78	1.07
4	2	6	15	2	0.29	1.71	0.80
5	2	4	15	2	0.40	1.60	0.53
6	2	12	15	1.00	0.15	1.85	0.80
7	2	10	15	1.20	0.18	1.82	0.80
8	2	8	15	1.50	0.22	1.78	0.80
9	2	4	15	3.00	0.40	1.60	0.80
10	2	12	15	1.00	0.15	1.85	0.80
11	2	10	15	1.20	0.18	1.82	0.80
12	2	8	15	1.50	0.22	1.78	0.80
13	2	6	15	2.00	0.29	1.71	0.80
14	2	4	15	3.00	0.40	1.60	0.80
15	1.5	8	15	1.50	0.17	1.33	0.80
16	2.0	8	15	1.50	0.18	1.82	0.80
17	2.5	8	15	1.50	0.22	1.78	0.80
18	2.0	8	10	1.0	0.22	1.78	0.80
19	2.0	8	5	0.5	0.22	1.78	0.80
20	2.0	8	15	1.5	0.18	1.82	0.80

Short-term stability studies

Runs 12 and 20 were stored at room temperature for 16 h and subsequently analyzed in terms of particle size and PDI to evaluate their stability.

Second phase of SLNs optimization

Evaluation of Tween 80/Lipid Ratios

Based on the first optimization phase, the preparation parameters were fixed at a TFR of 2.0 mL/min, an FRR of 8, a lipids concentration of 15 g/L, and a micromixer chip. Subsequent experiments (Runs 21-25) were performed to evaluate different final Tween 80-to-lipid ratios, aiming to identify Tween 80 concentrations compatible with its critical micelle concentration (CMC). Tween 80 stock solutions were diluted to final concentrations of 0.1, 0.35, 0.80, and 1.50 g/L for use in microfluidic production (**Table 9**).

Table 9. Microfluidic process parameters for Runs 21-25.

Run	FR(o) mL/min	FR(w) mL/min	Lipids (g/L)	Tween 80 (g/L)	Tween/Lipid Ratio *w/w*
21	0.22	1.78	15	0	0
22	0.22	1.78	15	0.1	0.05
23	0.22	1.78	15	0.35	0.19
24	0.22	1.78	15	0.80	0.43
25	0.22	1.78	15	1.50	0.80

Sample Purification and Buffer Exchange

For each microfluidic run, three aliquots of 1 mL were collected and quenched with Milli-Q water to reach a final organic solvent fraction of 8% *v/v*, as in the first optimization phase.

Each aliquot was then subjected to a different post-processing treatment. One aliquot was analyzed by DLS immediately after preparation and during storage at room temperature, *as is*. A second aliquot was concentrated four-fold and subjected to washing with Milli-Q water by diafiltration over five diavolumes (5 DV) using Amicon centrifugal filters with a molecular weight cut-off of 10 kDa. Centrifugation was performed at 7250 rpm for 5 min per cycle, and the samples were subsequently analyzed by DLS over time. A third aliquot was processed in the same manner but exchanged with PBS, pH 7.4.

DLS measurements were performed at T0 and 24 h for all treated and untreated aliquots to monitor particle size and PDI over time.

Third phase of SLNs optimization

The lipid components were combined according to a different molar ratio of stearic SA-PEG: SL: GMS (1:3:10), as selected from literature data [19], maintaining a total concentration of 15 g/L. Tween 80 aqueous solutions were prepared at different concentrations, covering a range from 3 to 150 g/L, to investigate the effect of surfactant concentration during microfluidic processing. A total of 5 runs were performed.

In Runs 26-30, the FRR was set at 4, while the Tween 80 stock concentration was varied between 3 and 150 g/L (**Table 10**).

Table 10. Microfluidic process parameters for Runs 26-30.

Run	TFR (mL/min)	FRR	Lipids (g/L)	Tween 80 (g/L)	FR(o) mL/min	FR(w) mL/min
26	2	4	15	3.00	0.40	1.60
27	2	4	15	12.38	0.40	1.60
28	2	4	15	37.50	0.40	1.60
29	2	4	15	75.00	0.40	1.60
30	2	4	15	150.00	0.40	1.60

Stability Studies

Short-term stability studies were conducted up to 24 h after preparation. Subsequently, selected formulations were subjected to temperature-dependent stability assessment by storage at -20 °C and 5 °C for 5 days.

4.1.4. Conclusions

This work demonstrates the applicability of microfluidic technology for producing SLNs using lipid and surfactant components previously employed in a conventional batch preparation technique. The successful transfer of these established excipients to a microfluidic platform highlights the potential of this approach as a controllable manufacturing strategy for SLNs intended for pharmaceutical applications.

Through a systematic screening of key formulation and process parameters, this study identified the main variables governing SLN quality features, including particle size and PDI. FRR, surfactant concentration, chip geometry, and lipid composition emerged as critical factors for setting nanoparticle characteristics, enabling the definition of suitable operating conditions for process optimization and subsequent scale-up.

This study establishes a solid methodological framework for the development of microfluidic SLNs as drug delivery systems. The insights gained from parameter screening and stability assessment provide a basis for future investigations focused on the introduction of functional lipid conjugates, such as the SA-PEG-Lep(70-89) previously developed, as well as on the inclusion of biotechnological compounds and formulation tailoring for specific administration routes and therapeutic applications.

The experimental work presented in this chapter was conducted with the support of the Research and Development team at BSP Pharmaceuticals, which provided scientific advice, technical assistance, and access to facilities.

References

1. Khoshnood, A., S. Iranpour, S. Khaksari, S.A.M. Shaegh, K. Abnous, S.M. Taghdisi, Liposome/AZIF-8 Janus nanoplatforms: Promising nanocarriers for improving chemotherapeutic outcomes in breast cancer treatment. *International Journal of Pharmaceutics*, **2025**: p. 125702.
2. Bezelya, A., B. Küçüktürkmen, A. Bozkır. *Microfluidic devices for precision nanoparticle production*. in *Micro*. 2023. MDPI.
3. Osouli-Bostanabad, K., S. Puliga, D.R. Serrano, A. Bucchi, G. Halbert, A. Lalatsa, Microfluidic manufacture of lipid-based nanomedicines. *Pharmaceutics*, **2022**. 14(9): p. 1940.
4. Liu, D., S. Cito, Y. Zhang, C.F. Wang, T.M. Sikanen, H.A. Santos, A versatile and robust microfluidic platform toward high throughput synthesis of homogeneous nanoparticles with tunable properties. *Adv Mater*, **2015**. 27(14): p. 2298-304.
5. Fontana, F., M.P. Ferreira, A. Correia, J. Hirvonen, H.A. Santos, Microfluidics as a cutting-edge technique for drug delivery applications. *Journal of Drug Delivery Science and Technology*, **2016**. 34: p. 76-87.
6. Gdowski, A., K. Johnson, S. Shah, I. Gryczynski, J. Vishwanatha, A. Ranjan, Optimization and scale up of microfluidic nanolipomer production method for preclinical and potential clinical trials. *Journal of nanobiotechnology*, **2018**. 16(1): p. 12.
7. Liu, Z., F. Fontana, A. Python, J.T. Hirvonen, H.A. Santos, Microfluidics for production of particles: mechanism, methodology, and applications. *Small*, **2020**. 16(9): p. 1904673.
8. Anderluzzi, G., Y. Perrie, Microfluidic manufacture of solid lipid nanoparticles: A case study on tristearin-based systems. *Drug Delivery Letters*, **2020**. 10(3): p. 197-208.
9. Arduino, I., Z. Liu, R.M. Iacobazzi, A.A. Lopedota, A. Lopalco, A. Cutrignelli, V. Laquintana, L. Porcelli, A. Azzariti, M. Franco, H.A. Santos, N. Denora, Microfluidic preparation and in vitro evaluation of iRGD-functionalized solid lipid nanoparticles for targeted delivery of paclitaxel to tumor cells. *Int J Pharm*, **2021**. 610: p. 121246.
10. Sommonte, F., I. Arduino, R.M. Iacobazzi, M. Tiboni, F. Catalano, R. Marotta, M. Di Francesco, L. Casettari, P. Decuzzi, A.A. Lopedota, N. Denora, Microfluidic assembly of "Turtle-Like" shaped solid lipid nanoparticles for lysozyme delivery. *Int J Pharm*, **2023**. 631: p. 122479.
11. Prakash, G., A. Shokr, N. Willemen, S.M. Bashir, S.R. Shin, S. Hassan, Microfluidic fabrication of lipid nanoparticles for the delivery of nucleic acids. *Advanced drug delivery reviews*, **2022**. 184: p. 114197.

12. Jaradat, E., E. Weaver, A. Meziane, D.A. Lamprou, Microfluidics Technology for the Design and Formulation of Nanomedicines. *Nanomaterials*, **2021**. 11(12): p. 3440.
13. Mudugamuwa, A., U. Roshan, S. Hettiarachchi, H. Cha, H. Musharaf, X. Kang, Q.T. Trinh, H.M. Xia, N.T. Nguyen, J. Zhang, Periodic Flows in Microfluidics. *Small*, **2024**. 20(50): p. e2404685.
14. Maeki, M., Y. Fujishima, Y. Sato, T. Yasui, N. Kaji, A. Ishida, H. Tani, Y. Baba, H. Harashima, M. Tokeshi, Understanding the formation mechanism of lipid nanoparticles in microfluidic devices with chaotic micromixers. *PLoS One*, **2017**. 12(11): p. e0187962.
15. Vogelaar, A., S. Marcotte, J. Cheng, B. Oluoch, J. Zaro, Use of Microfluidics to Prepare Lipid-Based Nanocarriers. *Pharmaceutics*, **2023**. 15(4): p. 1053.
16. Lu, M., A. Ozcelik, C.L. Grigsby, Y. Zhao, F. Guo, K.W. Leong, T.J. Huang, Microfluidic Hydrodynamic Focusing for Synthesis of Nanomaterials. *Nano Today*, **2016**. 11(6): p. 778-792.
17. Cheung, C.C.L., W.T. Al-Jamal, Sterically stabilized liposomes production using staggered herringbone micromixer: Effect of lipid composition and PEG-lipid content. *Int J Pharm*, **2019**. 566: p. 687-696.
18. Chen, D., Z. Liu, L. Guo, L. Yang, Y. Zhao, M. Yang, Controlled preparation of lipid nanoparticles in microreactors: Mixing time, morphology and mRNA delivery. *Chemical Engineering Journal*, **2025**. 505: p. 159318.
19. Li, R., J.S. Eun, M.K. Lee, Pharmacokinetics and biodistribution of paclitaxel loaded in pegylated solid lipid nanoparticles after intravenous administration. *Arch Pharm Res*, **2011**. 34(2): p. 331-7.
20. Deng, L.L., M. Taxipalati, F. Que, H. Zhang, Physical characterization and antioxidant activity of thymol solubilized Tween 80 micelles. *Sci Rep*, **2016**. 6: p. 38160.
21. Gordillo-Galeano, A., C.E. Mora-Huertas, Hydrodynamic diameter and zeta potential of nanostructured lipid carriers: Emphasizing some parameters for correct measurements. *Colloids and surfaces A: Physicochemical and engineering aspects*, **2021**. 620: p. 126610.
22. Mehnert, W., K. Mäder, Solid lipid nanoparticles: production, characterization and applications. *Advanced drug delivery reviews*, **2012**. 64: p. 83-101.
23. Shah, R., D. Eldridge, E. Palombo, I. Harding, Optimisation and stability assessment of solid lipid nanoparticles using particle size and zeta potential. *Journal of physical science*, **2014**. 25(1).

4.2. Bridging Microfluidics and Design of Experiments for the Development of SLNs-based Artificial Tears

4.2.1. Introduction

Dry eye disease (DED) is a multifactorial disorder affecting the ocular surface characterized by a disruption of tear film homeostasis. It currently represents a growing public health concern due to its impact on both visual function and quality of life, leading to a significant socioeconomic burden [1]. Recent clinical data emphasize that conventional tear substitutes often fail to fully relieve symptoms in patients with chronic DED, reflecting the multifactorial and persistent nature of the disease [2]. Clinically, DED manifests as ocular discomfort, visual disturbances, and tear film instability, often accompanied by increased osmolarity, inflammation, and, in some cases, neurosensory abnormalities [3]. DED is typically classified into two main subtypes: evaporative dry eye, characterized by excessive tear evaporation, and aqueous-deficient dry eye, resulting from inadequate tear production. Both forms lead to a hyperosmolar environment, which triggers inflammation via increased matrix metalloproteinase expression and cytokine activation [4], resulting in epithelial cell apoptosis and a self-perpetuating vicious cycle of ocular surface damage [5]. More recently, a third type has been proposed, including a globet cell dysfunction [6]. Given the hyperosmolarity conditions occurring in the disease mechanisms, the development of novel pharmaceutical systems incorporating osmoprotective substances represents a promising approach for mitigating ocular surface damage, not only in DED but also in related pathologies [7]. These agents help protect cells against osmotic stress, contributing to improved cell viability and overall ocular surface homeostasis [8]. Osmoprotectant substances, such as betaine, taurine, and L-carnitine have been demonstrated to prevent and decelerate the initiation of DED and can additionally be utilised after manifestation of damage [9].

The tear film is constituted by an aqueous-mucin gel, which protects the internal corneal epithelium, being also responsible for lubrication and maintenance of physiological osmolarity, and the external lipid layer, which prevents evaporation in physiological conditions [10, 11]. The latter have been reported to function as a barrier preventing evaporation of the aqueous tear fluid and to avoid the entry of microorganisms and organic matter [12]. In particular, it is composed of a thin layer of polar lipids interfacing

with the underlying secretory mucus layer and a thicker layer of non-polar lipids at the air interface [13]. When the tear film integrity is compromised and DED is triggered, the preocular tear film may benefit from supplementation with the above-mentioned lipid and aqueous components through the instillation of artificial tears [14].

Artificial tears (ATs) represent the mainstay therapy for dry eye disease (DED), as they supplement the natural tear film, improve its stability, and provide symptomatic relief while supporting ocular surface health [15]. Although widely available as over-the-counter products, their efficacy is limited by the absence of lipid components and a rapid clearance from the ocular surface due to tear turnover, blinking, and nasolacrimal drainage [16]. To overcome this limitation, nanoparticle-based drug delivery systems (DDS) have been explored to prolong residence time and enhance mucoadhesion [17]. A variety of DDSs have been developed so far, for the ophthalmic application [18]. In particular, lipid-based DDs have been proposed for DED treatments, since the lipid nanostructure may help to restore and reinforce the tear film lipid layer [19]. Among them, solid lipid nanoparticles (SLNs) stand out as a promising carrier for ocular drug delivery [20]. They offer several advantages, including enhanced encapsulation efficiency, biocompatibility, and protection of the drug from degradation [21, 22]. Their lipid matrix mimics physiological lipids, improving tolerability and potentially enhancing corneal penetration [23]. However, conventional SLN preparation methods, such as high-pressure homogenization or ultrasonication, often result in batch-to-batch variability, broad size distributions, and limited scalability [24].

In this regard, microfluidics has emerged as a precise, reproducible, and scalable alternative for SLNs fabrication, addressing the limitations of traditional techniques [25]. Although successfully applied to other lipid-based nanocarriers, the use of microfluidic systems for SLN production remains relatively underexplored. Given the novelty of applying microfluidics to SLN production, there is a growing need for systematic strategies that can accelerate formulation development and process optimization. In this context, the use of Design of Experiments (DoE), particularly the central composite design (CCD), represents a valuable tool [26]. CCD, as a form of response surface methodology (RSM), enables the efficient evaluation of complex interactions among key formulation and process parameters, such as lipid concentration, surfactant ratio, and flow rate, to identify conditions that optimize critical quality attributes [27]. By integrating

microfluidic methodology with statistical design approaches, researchers can significantly reduce experimental workload, shorten development timelines, and enhance the overall efficiency and reproducibility of SLN formulations [28].

Moreover, the addition of mucoadhesive polymers in eye-drop formulations has been widely proposed as an effective strategy to increase the residence time of topically applied ocular drugs. These polymers, such as hydroxypropyl methylcellulose (HPMC) and hyaluronic acid (HA), enhance viscosity and hydration, contributing to the formation of a protective, tear-like layer that coats the ocular surface and reduces drainage [29]. Beyond its rheological role, HA plays a biological function in maintaining tear film stability and epithelial health [30]. Naturally present in the tear film and extracellular matrix, it provides lubrication, osmoprotection, and anti-inflammatory activity, promoting corneal epithelial healing and comfort after instillation [31, 32]. Previous studies conducted by our group demonstrated that incorporating HA into liposomal-based eye drops improved both ocular surface tolerance and therapeutic efficacy upon topical administration [33, 34].

Building on these principles, this study integrates microfluidic production and RSM optimization to develop novel solid lipid nanoparticles dispersed in hyaluronic acid (HA-SLNs) intended as advanced artificial tears. Osmoprotectants (taurine and ribitol) and HA were incorporated into the aqueous phase to improve the conditions generated by osmotic stress in DED by enhancing hydration and comfort, while the lipidic core ensured structural stability and physiological compatibility. The resulting formulations were optimized for ocular physicochemical parameters, tested for *in vitro* cytocompatibility, and their long-term tolerance was comprehensively evaluated *in vivo*.

4.2.2. Results and discussion

Central composite design development and analysis

All formulations were produced by a microfluidic-assisted nanoprecipitation process using a 5-input chip, where nanoprecipitation is driven by hydrodynamic flow focusing [50]. In this configuration, the central organic stream is confined by surrounding aqueous streams, enabling rapid mixing and controlled nanoparticle formation [51, 52]. The stearic acid was dissolved in ethanol, forming the inner phase (organic phase), while an aqueous Brij 78 solution acts as the outer continuous phase.

Table 12. Experimental Runs and corresponding responses included in the CCD.

Run	Block	Brij 78 (mg/mL)	Stearic acid (mg/mL)	FRR	Size (nm)	PDI
1	2	0.75	3.00	18.00	276.5 ± 1.304	0.1697 ± 0.02310
2	2	1.25	3.00	22.00	192.3 ± 3.690	0.1636 ± 0.03059
3	2	0.75	2.00	22.00	209.3 ± 4.366	0.1377 ± 0.03589
4	2	1.25	2.00	18.00	179.5 ± 2.120	0.1794 ± 0.00665
5	2	1.00	2.50	20.00	215.6 ± 3.252	0.1247 ± 0.03753
6	2	1.00	2.50	20.00	215.4 ± 2.174	0.1603 ± 0.03395
7	3	0.59175	2.50	20.00	238.4 ± 13.76	0.3451 ± 0.07331
8	3	1.00	2.50	20.00	200.1 ± 7.161	0.1614 ± 0.03138
9	3	1.00	2.50	16.734	220.1 ± 5.089	0.1865 ± 0.04980
10	3	1.40825	2.50	20.00	176.1 ± 3.755	0.1588 ± 0.02489
11	3	1.00	2.50	23.266	203.9 ± 2.212	0.1211 ± 0.03537
12	3	1.00	2.50	20.00	233.2 ± 1.751	0.1378 ± 0.04639
13	3	1.00	3.3165	20.00	292.1 ± 3.289	0.1741 ± 001726
14	3	1.00	1.6835	20.00	206.3 ± 2.781	0.2174 ± 0.01963
15	1	0.75	2.00	18.00	279.1 ± 1.949	0.2454 ± 0.01742
16	1	1.00	2.50	20.00	219.3 ± 1.691	0.1320 ± 0.07293
17	1	1.00	2.50	20.00	225.2 ± 0.940	0.1938 ± 0.04311
18	1	1.25	3.00	18.00	244.5 ± 1.269	0.1889 ± 0.06005
19	1	0.75	3.00	22.00	287.9 ± 1.324	0.2261 ± 0.02325
20	1	1.25	2.00	22.00	200.0 ± 1.094	0.1606 ± 0.01053

The variation in size and PDI of SLNs was investigated within the framework of a CCD, applying response surface methodology (RSM) to describe the interactions and the effects of formulation conditions on nanoparticle characteristics obtained through the microfluidic process. The CCD approach has been widely employed for the optimization of SLN formulations, as it enables the identification of robust conditions that satisfy critical quality attributes while requiring a reduced number of experimental runs compared with conventional one-factor-at-a-time strategies [53, 54].

Preformulation studies highlighted working phase concentrations and the flow rate ratio (FRR) as the main factors influencing the mixing process and the resulting nanoparticle size. A previous study performed by Terada *et al.* demonstrated, through a DoE-based statistical evaluation, that lipid concentration and FRR represent critical process parameters that must be carefully monitored to achieve robust LNP-siRNA formulations [55].

Therefore, a total of 20 randomized runs were performed, and for each experimental run, the hydrodynamic diameter, expressed as Size (nm), and PDI values were evaluated. **Table 12** lists the value obtained as mean ± SD of three experiments. The observed sizes ranged from 176.1 to 292.1 nm, and the PDI values were all lower than 0.2 except for two formulations.

According to the analysis of variance (ANOVA) results calculated by Minitab software (version 19.1.0.1) for choosing the best model to fit the data, a quadratic second-order polynomial model was found to be appropriate when the particle size was considered as the response. The results of fitting the polynomial equation to the data are shown in **Table 13**. The model obtained was highly statistically significant without lack of fit ($F = 0.89$, $p > 0.05$). In addition, three linear (concentration of Brij 78, concentration of Stearic acid, and FRR value) and one quadratic (Stearic acid concentration) were significant. Other factors that had *p*-values of more than 0.05 resulted not significant. Therefore, the mathematical model describing the relationship between variables (A, B, and C) and response (Y_1) was reduced to that shown in **Equation 1:**

$$Y_1 = 656.2 - 101.5A - 241.4B - 4.37C + 56.5B^2 \qquad \textbf{(1)}$$

Where Y_1 is the particle size and A, B, and C are Brij 78, stearic acid concentrations, and FRR, respectively. The negative coefficients for A and B suggest that an increase in either

Brij 78 or stearic acid concentration results in a reduction in particle size, indicating their significant inverse effect on the response. The quadratic term B^2 with a positive coefficient reflects a non-linear relationship between stearic acid concentration and particle size, implying that beyond a certain point, further increases in stearic acid may lead to particle growth. This effect has been previously described in experimental studies based on a central composite design approach. In fact, Babu *et al*. reported that stearic acid concentration exerted both a significant linear and quadratic effect on particle size, with particle growth observed at higher lipid levels [37].

Table 13. ANOVA results for Size (nm) as the response (Y_1).

Source	*df*	Sum of squares	Mean squares	F-value	p-value	
Model	6	20465.9	3411.0	19.78	0.0000077639	Significant
Blocks	2	2601.1	1300.5	7.54	0.0066992947	
Linear	3	15205.6	5068.5	29.39	0.0000046262	
A	1	8580.2	8580.2	49.75	0.0000086310	
B	1	5606.5	5606.5	32.51	0.0000727687	
C	1	1018.9	1018.9	5.91	0.0303047055	
Square	1	2659.3	2659.3	15.42	0.0017368004	
B*B	1	2659.3	2659.3	15.42	0.0017368004	
Error	13	2242.3	172.5			
Lack-of-Fit	10	1677.0	167.7	0.89	0.6145902426	Not significant
Pure Error	3	565.2	188.4			
Total	19	22708.2				

A: Brij 78; B: Stearic acid; C: FRR.

The model exhibited a coefficient of determination (R^2) of 0.9013 and an adjusted R^2 of 0.8557, indicating that nearly 90% of the variability in particle size was explained by the selected factors. The correspondence between R^2 and adjusted R^2 values highlights the reliability of the model and suggests that overfitting is unlikely [56]. Moreover, the predicted R^2 value of 0.7576 confirmed the model's predictive capability, demonstrating that it is sufficiently robust for forecasting particle size within the investigated design space.

The 3D response surface plots of the combination of solid lipid and surfactant further explained the interaction between the factors in the design (**Figure 4**).

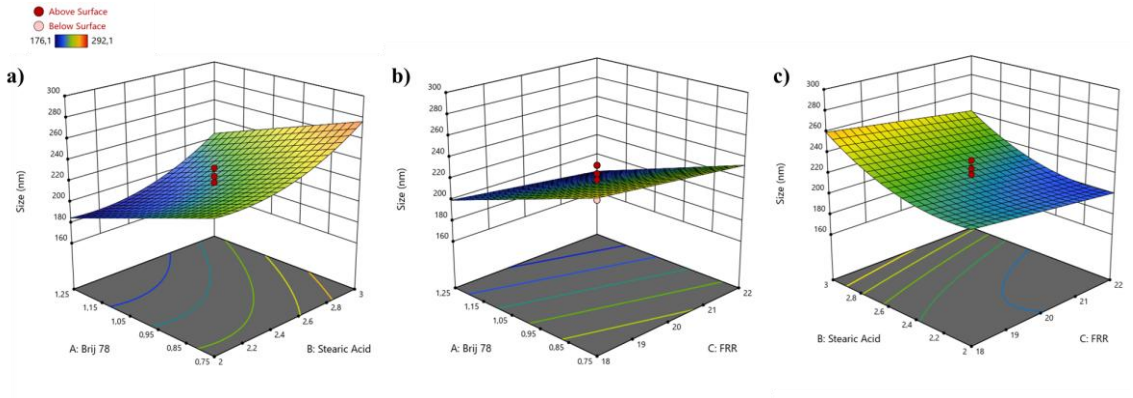


Figure 4. The 3D response surface plots generated from the fitted quadratic model (Eq. 4), illustrating the effects and interactions of Brij 78 (A), stearic acid (B), and flow rate ratio (FRR, C) on particle size (Y_1).

In plot **a)**, the interaction between Brij 78 and stearic acid is shown. The curved surface emphasizes the non-linear effect of stearic acid, consistent with the quadratic term (B^2) in the model: particle size decreases at moderate stearic acid levels and rises again at higher concentrations, while Brij 78 contributes to a general size reduction. The size-decreasing effect observed at higher concentrations of Brij 78 has already been reported, suggesting that surfactant concentration plays a dominant role within the explored design space. Dong *et al*. developed lipid-based nanoparticles composed of a wax core stabilized with the non-ionic surfactant Brij 78 to improve the delivery of anticancer drugs and overcome P-glycoprotein-mediated multidrug resistance. Within this framework, they demonstrated that increasing the Brij 78 concentration from 2 to 4 mg/mL resulted in a pronounced reduction in particle size. This behaviour was attributed to enhanced surface coverage by Brij 78, which increases steric stabilization at the particle interface and limits particle growth and fusion during nanoparticle formation [57]. Similar findings were also reported by Tang et al., who investigated the effects of different Brij surfactants and Brij-to-drug ratios on the formation and physicochemical properties of paclitaxel nanocrystals. In their study, increasing the Brij-to-drug ratio from 1:2 to 1:5 (w/w) led to smaller and more stable nanocrystals, an effect attributed also to enhanced surface coverage and steric stabilization provided by PEG-based Brij surfactants, effectively limiting particle growth during nanocrystal formation [58].

Plot **b)** illustrates the interaction between Brij 78 and FRR. Both factors have negative linear effects, causing a steady decrease in particle size with increasing levels, and the flat surface confirms the absence of quadratic or interaction terms involving FRR. This indicates that, within the investigated range, FRR primarily modulates particle size through a linear hydrodynamic effect rather than complex interactions.

In plot **c)**, the combined effect of stearic acid and FRR is visualized. Particle size reaches a minimum at moderate stearic acid levels, while FRR has only a mild, nearly linear influence. The observed role of FRR is consistent with previously reported microfluidic fabrication studies, in which increasing FRR promotes faster solvent exchange and nucleation, ultimately limiting particle growth. Forbes *et al.* investigated the microfluidic manufacture of protein-loaded liposomes, formulated using phosphatidylcholine-based lipids in combination with cholesterol, to identify the key process parameters governing liposome size and homogeneity. They demonstrated that increasing the aqueous-to-organic FRR from 1:1 to 3:1 led to a consistent reduction in liposome size, from approximately 100-200 nm to 50-60 nm, while maintaining low polydispersity [59]. Comparable conclusions were drawn by Kastner et al., who employed a design of experiments approach to study the microfluidic production of cationic DOPE/DOTAP liposomes, identifying FRR as the dominant parameter controlling vesicle size, with a marked decrease in diameter observed when the FRR was increased from 1:1 to 1:5 [60]. Though the experimental design included the polydispersity index (PDI) as a response variable, the mathematical model obtained for PDI exhibited limited predictive capability, with determination coefficients lower than 0.50 (model not shown). This limitation is not uncommon in response surface modelling of nanoparticle systems, as also reported in the literature. Uche *et al*. investigated the adequacy and predictive performance of first- and second-order regression models applied to the optimization of sonicated SLNs of bedaquiline using a CCD. Their study specifically aimed to assess whether high goodness-of-fit metrics necessarily correspond to reliable predictive performance. Despite a high R^2 value (0.895) for the quadratic PDI model, the adjusted R^2 (0.7317), the near-zero predicted R^2 (0.0111) revealed poor external predictability [61]. Similarly, in the present study, the PDI model showed only modest predictive capability (R^2 = 0.5032, adjusted R^2 = 0.4448, predicted R^2 = 0.4056). Taking together, these findings

suggest that PDI, owing to its intrinsic variability and sensitivity to minor formulation or process changes, is particularly challenging to model accurately using RSM.

In the present study, the impossibility of obtaining a reliable model may be attributed to the low variability that was captured within the design space: as highlighted in classical DoE literature, an adequate spread of factor levels is required to reliably estimate model coefficients and detect quadratic or interaction effects, whereas narrow response ranges inherently reduce the model's discriminating power [62-63]. Nevertheless, it is important to note that all PDI values obtained during the experimental runs remained below 0.2, which is generally considered the upper threshold for monodisperse nanoparticle systems. From a technological perspective, given that all formulations demonstrated acceptable homogeneity, the need for a predictive model for PDI was deprioritized, as the values consistently met the target quality specifications. Therefore, the optimization effort was primarily focused on particle size, which exhibited more variability and had a greater influence on the final performance of the SLNs.

Response optimization and model validation

Further optimization and validation process was undertaken (Minitab software) to obtain the optimal SLNs with a minimum particle size and PDI. The composition of the optimum formulation for each component was determined as 1.4082 mg/mL of Brij 78, 2.12886 mg/mL of Stearic acid, and FRR at 23.266 (**Table 14**).

Table 14. Response optimization and model validation

Goal	**Minimize Size (nm)**
Independent Variables	**Solution Value**
A: Brij 78 (mg/mL)	1.40825
B: Stearic Acid (mg/mL)	2.12886
C: FRR	23.266
Responses	**Size (nm)**
Predicted	153.68 ± 9.22
Observed	167.55 ± 4.97
Bias (%)	9
p-value	0.108

According to the model, the predicted values of Y_1 (Size(nm)) were 153.68 ± 9.22 nm. In the previously cited conditions, the optimized formulation, F-SLNs, had a particle size of 167.55 ± 4.97 nm, which fell within the interval confidence value, calculated by the software [95% CI (133.75; 173.61)]. A Student's t-test confirmed the absence of a statistically significant difference between the predicted and experimental values (p > 0.05). Moreover, the reduced model showed a percentage error of 9%, indicating a high level of predictive accuracy [64]. These findings support the robustness of the mathematical model developed through the CCD. The formulation F-SLNs exhibited a PDI value of about 0.174 ± 0.01, a narrow dispersity as highlighted by the DLS analysis displayed in **Figure 6**. This finding confirms that, despite no regression model describing the response, PDI was obtained, it had an overall acceptable value within the design space.

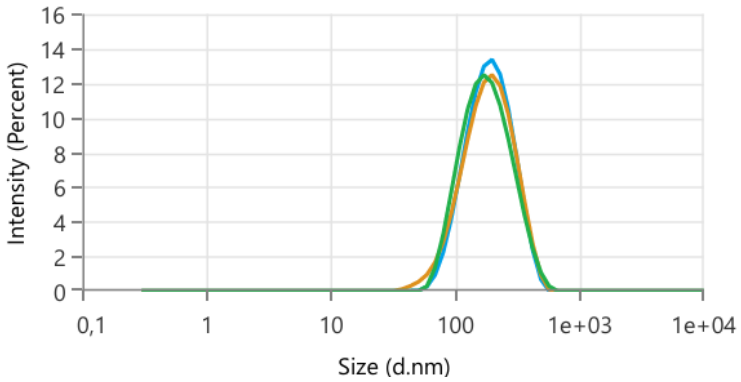


Figure 6. Experimental Size distribution graph for the optimized formulation F-SLNs.

Characterization of SLNs-based ATs

The optimized F-SLNs were combined with Buffers 1 and 2 to formulate osmoprotectant-enriched SLN-based ATs, with or without hyaluronic acid (HA), obtaining B-SLNs and HA-SLNs, respectively. Once prepared, the physicochemical attributes relevant for ocular instillation were evaluated, as summarized in **Table 15.** Following buffer incorporation, in both cases, a slight increase in particle size was observed, being attributable to the presence of salts and other solutes interacting at the nanoparticle surface, thereby increasing the hydrodynamic diameter. This phenomenon is commonly observed in lipid-based nanodispersions upon electrolyte addition and has been previously described. Gordillo-Galeano *et al.* performed a systematic study on the effect of key experimental variables on the size distribution of nanostructured lipid carriers prepared from a binary mixture of trimyristin and medium-chain triglycerides, stabilized with the non-ionic

surfactant Poloxamer 188. They demonstrated that increasing the ionic strength of the dispersion medium through electrolyte addition led to an increase in the measured hydrodynamic diameter, an effect attributed to electric double-layer compression and ion-induced rearrangement of the stabilizing layer at the nanoparticle surface [65].

Table 15. Characterization of B-SLNs and HA-SLNs by size, PDI, pH, surface tension, osmolarity, and viscosity.

Formulation	Size [nm]	PDI	pH	Surface tension [mN/m]	Osmolarity [mOsm/L]	Viscosity [mPa/s]
B-SLNs	227.9 ± 1.5	0.1302 ± 0.008	6.83 ± 0.03	40.93 ± 0.61	288.33 ± 1.53	0.98 ± 0.02
HA-SLNs	258.5 ± 0.8	0.2541 ± 0.022	6.81 ± 0.02	40.73 ± 1.40	297.33 ± 2.08	2.08 ± 0.02

Despite the size increase, the final dimensions of SLNs were still below 300 nm, indicating that the formulation maintained suitable characteristics for ocular application. It has been previously described that nanoparticles close to 300 nm are accumulated in the cornea and conjunctiva without detectable intraocular or systemic exposure supporting the suitability of this nanoparticle size range for topical ophthalmic delivery [66]. Furthermore, both formulations exhibited physicochemical properties compatible with ophthalmic use with pH and surface tension values close to those of natural tears, along with isotonicity [11]. As described by several authors, ATs drop tensions around 44 mN/m have been shown to enhance spreadability onto the ocular surface [67].

A more detailed comparison between the two formulations highlights the role of HA on the final physicochemical profile. In particular, B-SLNs exhibit a tighter size distribution (PDI 0.1302 ± 0.008) and low viscosity (0.98 ± 0.02 mPa·s), features that favor immediate comfort but may also promote rapid elimination. As expected, the addition of the polymer increased the particle hydrodynamic size (258.5 ± 0.84 nm vs 227.9 ± 1.48 nm) and slightly broadened the distribution (PDI 0.2541 ± 0.022), reflecting the formation of a hydrated HA layer around the lipid core. These results are in good agreement with previously reported HA-modified lipid nanocarriers. Ruiz et al. investigated SLN-based multicomponent vectors functionalized with hyaluronic acid of different molecular weights and demonstrated that HA incorporation led to a significant increase in particle diameter, with sizes shifting from approximately 220-240 nm for non-coated SLNs to

values above 300 nm for HA-containing systems. Importantly, this size increase was accompanied by enhanced cellular uptake and transfection efficiency, highlighting the role of HA as a surface-modifying polymer capable of modulating nanoparticle-cell interactions [68].

Bulk physicochemical properties, including pH and surface tension, were essentially preserved. More importantly, the viscosity doubled to 2.08 ± 0.02 mPa·s, a favorable adjustment expected to enhance residence time without impairing visual clarity.

TEM images of SLNs-based ATs revealed uniform and spherical morphologies, with no evidence of aggregation or structural disruption. B-SLNs appeared darker and more electron-dense (**Figure 7a**), whereas HA-SLNs exhibited a lighter contrast and less sharply defined contours (**Figure 7b**). This difference in staining behaviour is consistent with the presence of a hydrated HA layer at the nanoparticle surface, which can hinder uranyl acetate adsorption and thereby reduce image contrast, as previously observed for HA-coated nanocarriers [69].

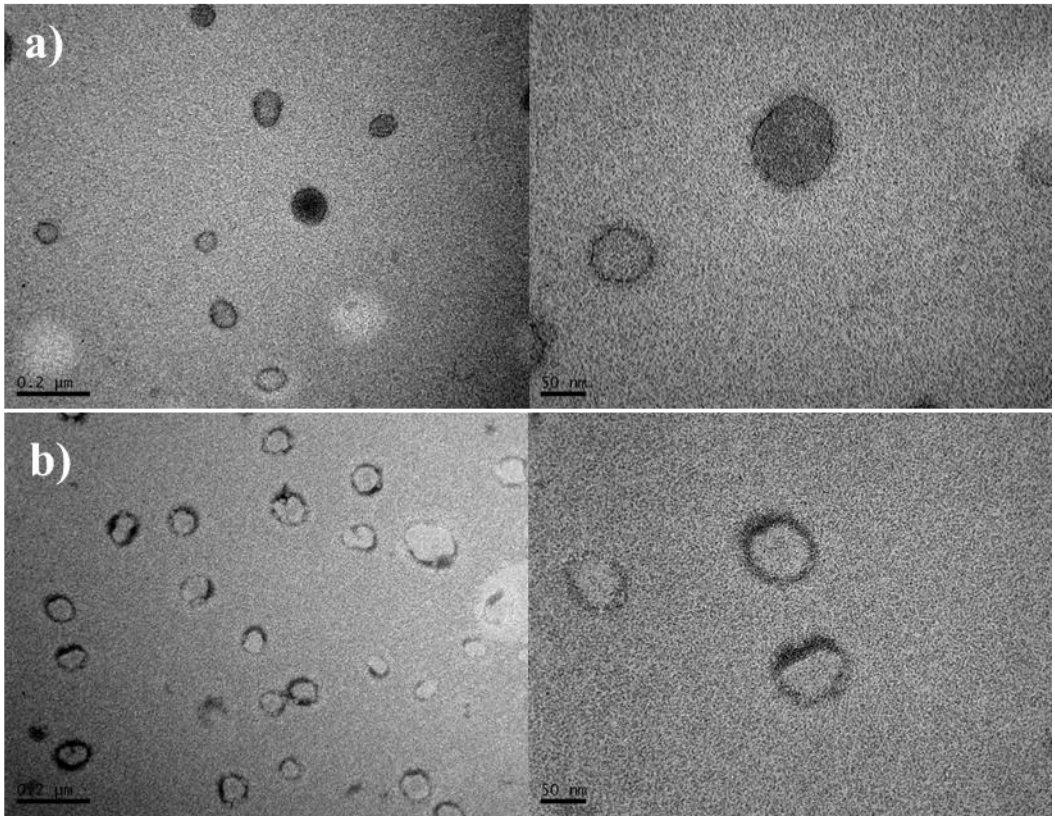


Figure 7. TEM images of B-SLNs **a)** and HA-SLNs **b),** at magnifications of 100x (left), and 250x (right).

Cellular biocompatibility

Tolerance studies were performed on J774A.1 cell cultures under simulated conditions of acute (1 h) and chronic (4 h) exposure conditions, as suggested by previously established and validated protocols of other topical ophthalmic formulations [70]. Macrophages use as a stress-sensitive model is a common strategy to screen nanocarrier-induced cytotoxicity [71]. In particular, dose-response studies were performed exposing cell lines to SLN formulations concentrations ranging from 0.01 to 5 mg/mL. According to ISO 10993-5 criteria, a reduction in cell viability greater than 20% compared to untreated controls indicates cytotoxicity. Therefore, formulations maintaining cell viability above 80% are considered non-cytotoxic and well-tolerated *in vitro* [72]. As shown in **Figure 8A,** B-SLNs were well tolerated at 0.01 mg/mL; however, increasing concentrations resulted in a pronounced and statistically significant loss of cell viability, with viability values dropping below 40%. Interestingly, HA-SLNs exhibited a significantly improved cytocompatibility profile, maintaining cell viability above 80% up to 0.1 mg/mL, regardless of exposure time (**Figure 8B)**.

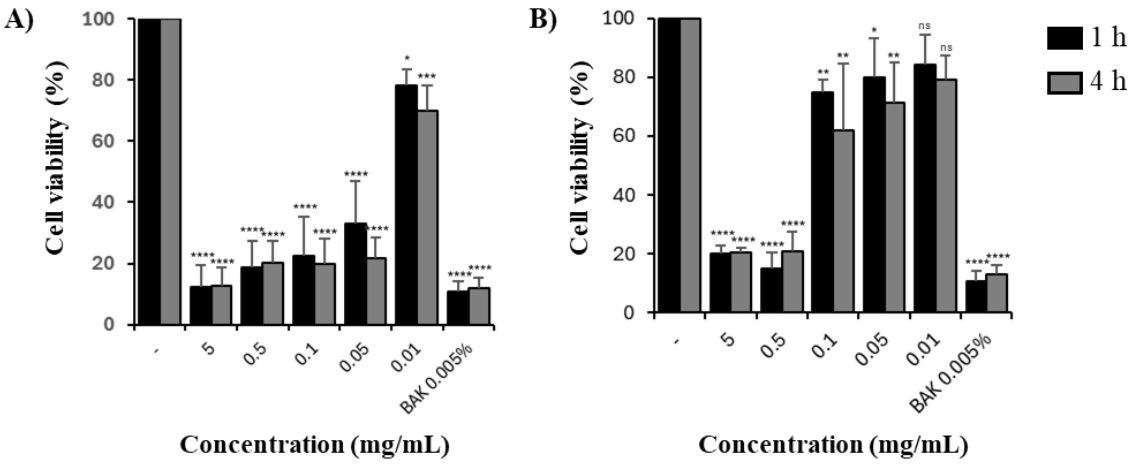


Figure 8. Cell viability was determined by the MTT assay. J774A.1 macrophages were treated with formulations including 5, 0.5, 0.1, 0.05, and 0.01 mg/mL of B-SLNs **a)**, and HA-SLNs **b)** for 1 and 4 h. Results are reported as mean of cell viability (% of non-treated cells) of n = 2-3 independent experiments ± SD. Statistical differences between treatments and control were evaluated by one-way ANOVA (**p*<0.05, ***p*<0.01, ****p*<0.001, and *****p*<0.00001).

The increase of cytocompatibility of HA-SLNs can be mainly attributed to the presence of hyaluronic acid in the surrounding aqueous phase, which can transiently associate with the nanoparticle surface. This hydrated HA environment likely reduces direct contact between surfactant molecules present in the SLNs and cellular membranes, thereby

minimizing membrane perturbation and oxidative stress. Our results are consistent with the observations described by Apaolaza *et al.* reporting that HA-functionalized SLNs maintained full viability of retinal pigment epithelial cells after 72 h exposure, confirming their excellent biocompatibility [73].

Furthermore, the mucoadhesive nature of HA also contributes to improved nanoparticle stability and compatibility with ocular surface tissues. As reported by De la Fuente *et al*. and Contreras-Ruiz *et al.*, HA-based nanocarriers adhere to mucosal epithelia without inducing irritation or altering tear production, emphasizing their safety for ophthalmic use [74, 75]. Overall, HA clearly improved the tolerability of SLNs, allowing their safe use at higher nanoparticle concentrations during *in vivo* testing. Therefore, its incorporation not only enhanced viscosity, hydration, and mucoadhesion, key features for ocular comfort and tear film stability, but also significantly expanded the safety margin of the formulation, reinforcing the rationale for using HA-SLNs as next-generation ATs.

***In vivo* chronic tolerance studies**

In order to confirm the usefulness of the novel ATs an evaluation of the ocular safety and long-term tolerability of HA-SLNs was performed in rabbits. These studies allow to simulate a chronic use of the ATs in closer conditions to the clinical situation. To this, animals were monitored daily for 15 days after one instillation/day through the modified Draize test (**Table 19**), in combination with standard diagnostic parameters of tear film stability and ocular surface integrity. The HA-SLNs was compared to the well tolerated isotonic solution of 0.9% w/v NaCl. All the Draize test scores, reported as the mean ± SEM, are summarized in **Table 16** of the supporting materials. At time zero, score values indicated minimal to no signs of ocular irritation or inflammation in rabbits (1.00 ± 0.58 for 0.9% w/v NaCl and 0.25 ± 0.25 for HA-SLNs). Throughout the study period, ocular surface assessments revealed no significant changes or adverse effects compared to baseline (0.00 ± 0.00 for 0.9% w/v NaCl and 0.25 ± 0.25 for HA-SLNs at day 15) and average scores consistently remained below the predefined threshold of ten. Discomfort or redness was absent during the entire observation study. No statistical differences were observed between the control and the test formulation ($p > 0.05$), confirming the good chronic tolerability of HA-SLNs.

Table 16. Draize test results.

	Draize score ± SEM	
Day	**0.9 % NaCl**	**HA-SLN**
0	1 ± 0.5773	0.25 ± 0.25
1	0 ± 0	0 ± 0
2	0 ± 0	0 ± 0
3	1 ± 1	0 ± 0
4	0 ± 0	0.5 ± 0.3273
5	0 ± 0	0.5 ± 0.3273
6	0 ± 0	0 ± 0
7	0 ± 0	0 ± 0
8	1 ± 0.5773	0 ± 0
9	0 ± 0	0 ± 0
10	1 ± 0.5773	0 ± 0
11	0 ± 0	0 ± 0
12	0 ± 0	0.25 ± 0.25
13	0 ± 0	0 ± 0
14	0 ± 0	0 ± 0
15	0 ± 0	0.25 ± 0.25
Overall Mean	0.25 ± 0.4472	0.1093 ± 0.1818

All the DED diagnostic parameters systematically monitored at time 0, 8 days, and 15 days of the study are summarized in **Figure 10**. Tear secretion, as measured by the Schirmer's test, was comparable between the groups both at baseline (9.25 ± 0.41 for 0.9% w/v NaCl and 9.88 ± 0.94 for HA-SLNs) and after treatment (11.25 ± 1.63 for 0.9% w/v NaCl and 10.88 ± 0.41 for HA-SLNs at day 15), with no significant differences ($p >$ 0.05). Similarly, TBUT remained stable over the study period (9.00 ± 0.35 for 0.9% w/v NaCl and 8.88 ± 0.60 for HA-SLNs at time zero; 7.50 ± 0.25 for 0.9% w/v NaCl and 7.63 ± 0.35 for HA-SLNs on day 15). Following the application of the fluorescent dye, which is useful not only for performing the TBUT but also for assessing ocular surface damage. The evaluation of representative slit lamp photos (**Figure 9**), was performed according to the OXGS; highlighted a slight increment from a mild to a minimal level of staining when HA-SLNs was administered (0.75 ± 0.41 for 0.9% w/v NaCl, 1.13 ± 0.33 for HA-SLNs at time zero; 1.00 ± 0.00 for 0.9% w/v NaCl, 2.00 ± 0.40 for HA-SLNs at day 15), with no statistical significance with the control. Lissamine green staining, evaluated by the Van Bijsterveld scale, indicated minimal ocular surface involvement in both groups. HA-SLNs presented slightly higher scores than the control at day 0 and 15, but these differences were not statistically significant. HA-SLNs showed slightly higher scores than

the NaCl control, yet without statistical significance ($p > 0.05$) (0.25 ± 0.22 for NaCl vs 0.63 ± 0.17 for HA-SLNs at time zero; 0.50 ± 0.25 for NaCl vs 1.38 ± 0.25 for HA-SLNs at day 15). All these results confirmed the good tolerance of HA-SLNs in a long-term situation.

Lipid-based nanocarriers have been recently proposed as innovative ATs to restore tear film stability through lipid supplementation. In this context, Zhang *et al.* developed a nanoscale lipid eye ointment based on nanostructured lipid carriers, aiming to reinforce the lipid layer of the tear film and reduce tear evaporation. In a murine DED model, repeated topical administration for 14 days resulted in a significant improvement in TBUT, reduced corneal staining, and good ocular tolerability, supporting the suitability of lipid-based nanocarriers as ATs [76].

Beyond lipid layer instability, tear hyperosmolarity represents a key pathogenic factor in DED, as it induces osmotic stress, inflammation, and epithelial damage to the ocular surface. Accordingly, the incorporation of osmoprotective substances into ATs represents a rational strategy to complement lipid supplementation and preserve ocular surface homeostasis. Among the osmoprotective agents proposed for ocular applications, taurine and ribitol have received particular attention. López-Cano et al. demonstrated, in a comprehensive study under DED-related hyperosmotic conditions, that taurine effectively protects corneal epithelial cells by improving cell viability and reducing stress-induced cellular damage [77]. Ribitol, a sugar alcohol belonging to the polyol family, is likewise a well-established compatible osmolyte, reported to protect cells from osmotic stress by stabilizing cellular structures and maintaining intracellular osmotic balance without interfering with normal cellular functions [78].

Consistent with these findings, several lipid-based nanocarrier systems enriched with osmoprotective agents have been proposed as advanced ATs. This is the case of osmoprotective ophthalmic microemulsions incorporating amino acid-based osmoprotectants (betaine and leucine) or a protein-lipid combination (clusterin and oleanolic acid), further combined with hyaluronic acid or dextran as functional polymers with excellent ocular safety in rabbits [9]. Similarly, González-Cela-Casamayor et al. developed osmoprotective liposomes containing ribitol and taurine, demonstrating effective *in vitro* protection and good *in vivo* tolerance [79].

According to the advantage of including osmoprotectants in ophthalmic preparations, we proposed a novel ATs combining SLNs as lipid nanocarriers with osmoprotective agents. This system maintained ocular comfort and tear film stability over 15 days of daily application in rabbits, confirming good chronic tolerability across multiple clinical endpoints.

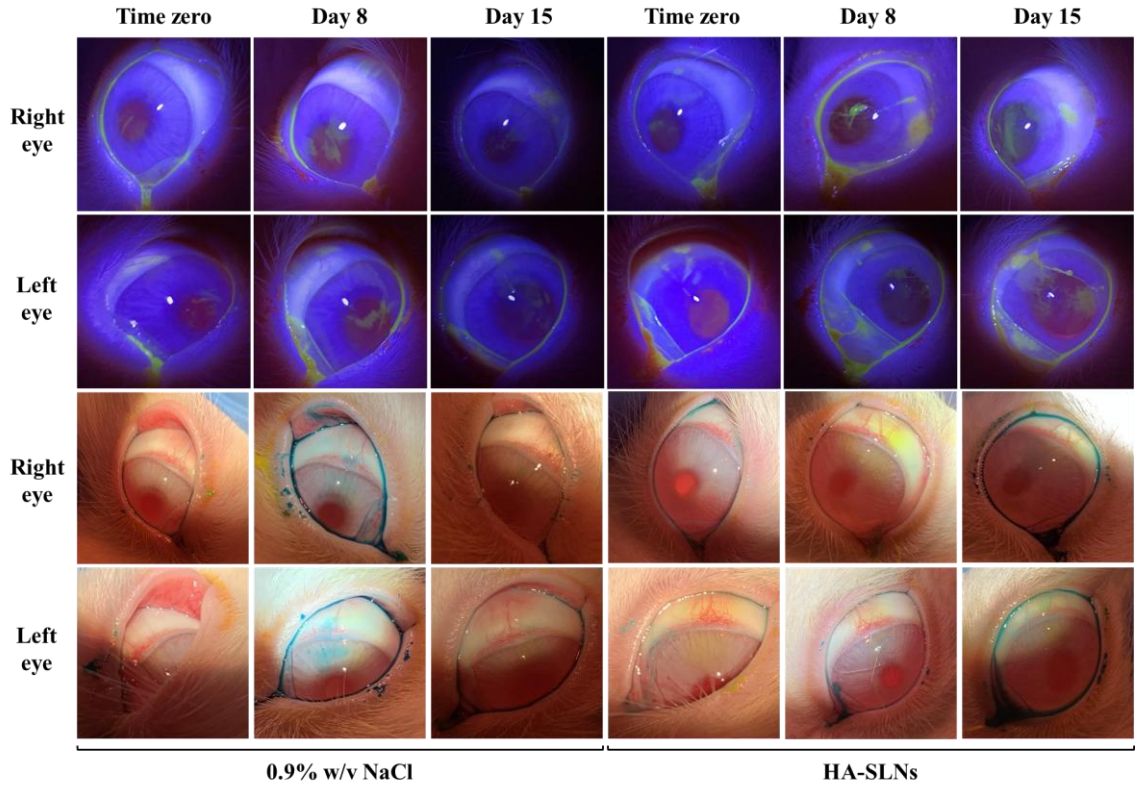


Figure 9. Representative slit lamp pictures of rabbits' left and right eyes after either HA-SLNs (n = 8) or 0.9% w/v NaCl (n = 4) daily administration. The first and second rows show corneal and conjunctival fluorescein staining under cobalt blue light, highlighting epithelial damage before and after treatment, evaluated through the OXGS. The third and fourth rows display lissamine green staining under white light, used to assess conjunctival integrity and cell damage, evaluated through Van Bijsterveld score.

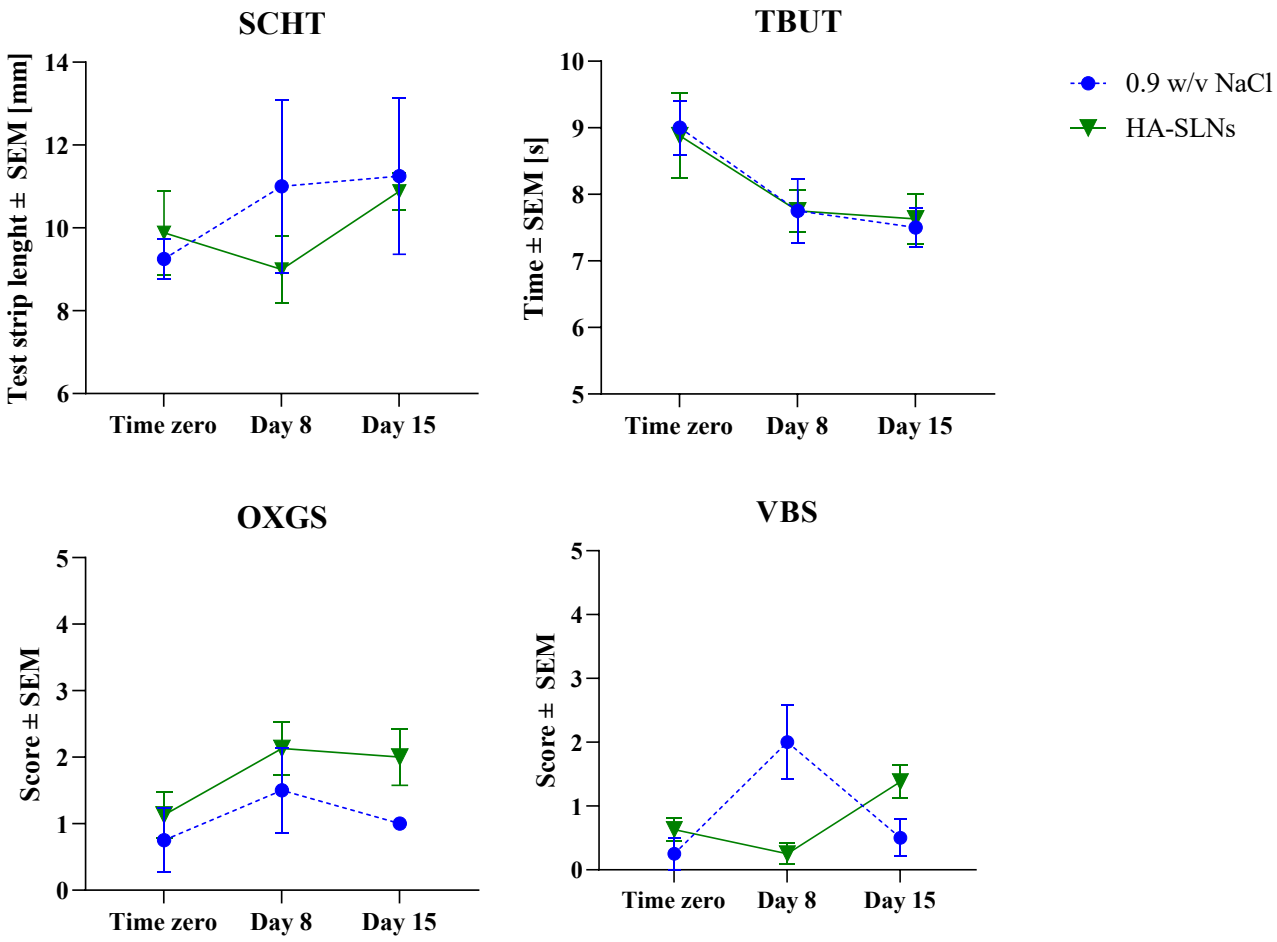


Figure 10. DED diagnostic parameters measurements over time (time zero, day 8, and day 15) regarding Shirmer's test (SCHT), tear breakup time (TBUT), fluorescence staining evaluated through Oxford grading scale (OXGS), and lissamine green staining evaluated through the Van Bijsterveld scale, during 15 days of consecutive daily administration of HA-SLNs (n = 8, green line), and 0.9% w/v NaCl (n = 4, blue dotted line).

4.2.3. Experimental Section

Materials

Stearic acid (CAS 57-11-4), Brij 78 (CAS 9005-00-9), and ethanol were purchased from Sigma-Aldrich (St. Louis, MO, USA) as well as the compounds Ribitol (Adonitol, CAS 488-81-3, 99%), Taurine (CAS 107-35-7, 99%), Sodium tetraborate decahydrate ($Na_2B_4O_7 \cdot 10H_2O$, CAS 1303-35-3, 99.5%), and Boric Acid (H_3BO_3, CAS 10043-35-3, 99.5%). D-(+)-trehalose dihydrate (CAS 6138-23-4) was purchased from Fisher Scientific (Geel, Belgium). Sodium hyaluronate ophthalmic grade (HA) (molecular weight 400-800 kDa) was supplied by Abaran Materias Primas S.L. (Villaviciosa de Odon, Spain). All chemicals used were of analytical grade.

Central Composite Design

First, a factorial design approach was applied to optimize the temperatures for the microfluidic chip (70 °C) and the SLN hardening phase (2-4 °C), respectively (data not shown). After that, a three-factor Central Composite Design (CCD) was applied to investigate the effect and the optimum levels of variables [35]. A CCD has three groups of design points, including two-level factorial design points, axial or star points, and center points, which have been selected after a preliminary optimization. Therefore, selected variables [Brij 78 concentration (A), Stearic acid concentration (B), and Flow Rate Ratio (FRR) (C)] were studied at five different concentrations coded as -α, -1, 0, 1, and +α. The value for alpha (-1.683) is calculated to fulfill orthogonality in the design. The coded and actual values of the variables are given in **Table 17**.

Table 17. The coded and actual values of the variables used in the CCD.

		Levels				
Independent variables	**Symbol**	**-α**	**-1**	**0**	**+1**	**+α**
Brij 78 (mg/mL)	A	0.591	0.75	1.0	1.25	1.40825
Stearic Acid (mg/mL)	B	1.6835	2.0	2.5	3.0	3.3165
Flow Rate Ratio (FRR)	C	16.734	18	20	22	23.266
Dependent variables						
Y_1= Size (nm)						
Y_2= Polydispersity index (PDI)						

According to the CCD matrix generated using Minitab 19 (version 19.1.0.1), a total of 20 experiments, including 8 factorial points, 6 axial points, and 6 replicates at the center point for estimation of pure error sum of squares, were performed (**Table 12**). The design was blocked into three blocks to control nuisance variability and enhance the precision and reliability of the estimated effects [36].

Statistical Analysis

The optimum values of the independent variables for SLN formulation were chosen based on the conditions that yielded the minimum particle size and the minimum polydispersity index. The response surface behaviour was investigated for the response function (Y) using the polynomial **Equation 2** and the generalized response surface model as shown:

$$Y_i = \beta_0 + \beta_1 x_1 + \beta_2 x_2 + \beta_3 x_3 + \beta_{11} x_1^2 + \beta_{22} x_2^2 + \beta_{33} x_3^2 + \beta_{12} x_1 x_2 + \beta_{13} x_1 x_3 + \beta_{23} x_2 x_3 \qquad \textbf{(2)}$$

where Y is the predicted response; 0 is a constant; 1, 2, and 3 are the linear, quadratic, and interaction coefficients, respectively. The analysis of variance (ANOVA) was used to determine the significance of the differences between the independent variables. All significant independent variables' effects ($p < 0.05$) were included in the reduced model. To visualize the interaction effect of the variables on the responses, three-dimensional response surface plots were composed. The R^2 should be at least 0.8 for models with a good fit [37].

Verification of the reduced model

The reduced model was validated by preparing an additional SLN batch under the predicted optimal conditions obtained as reported above. The experimental responses were compared with the model-predicted values, and the percentage bias, **Equation 3**, was calculated to assess the predictive accuracy [38].

$$Bias\ (\%) = \frac{Observed\ response - Predicted\ response}{Predicted\ response} \times 100 \qquad \textbf{(3)}$$

Moreover, statistical comparison between predicted and experimental data was performed using Student's *t*-test, with $p < 0.05$ considered significant.

Microfluidic Preparation of SLNs

SLNs were prepared using a microfluidic system (Dolomite, Royston, UK) equipped with a 5-input chip (150 µm channel width, Part No. 3200711). The aqueous phase, organic phase, and ethanol were filtered through 0.2 µm filters and loaded into three pressure pumps (Part No. 3200016), which were designated as Pump 1 (P1), Pump 2 (P2), and Pump 3 (P3), respectively. These pumps were connected to flow rate sensors with ranges of 30-1000 µL/min (P1, Part No. 3200097), 1-50 µL/min (P2, Part No. 3200098), and 0.2-5 mL/min (P3, Part No. 3200096), respectively. The fluids were conveyed from the pressure pumps to the chip using FEP tubing (OD 1.6 mm, ID 0.25 mm, Part No. 3200302). To control fluid flow through the chip, 2-way in-line valves (Part No. 3200087) were installed. T-connectors (Part No. 3000397) were integrated to join the organic and ethanol phases and to facilitate system cleaning. The chip was assembled using the H Interface 7-way (Part No. 3200297) and two Linear Connectors 7-way (Part No. 3200148) and was mounted on a Meros TCU-100 thermostat (Part No. 3200428) for temperature control (**Figure 11**).

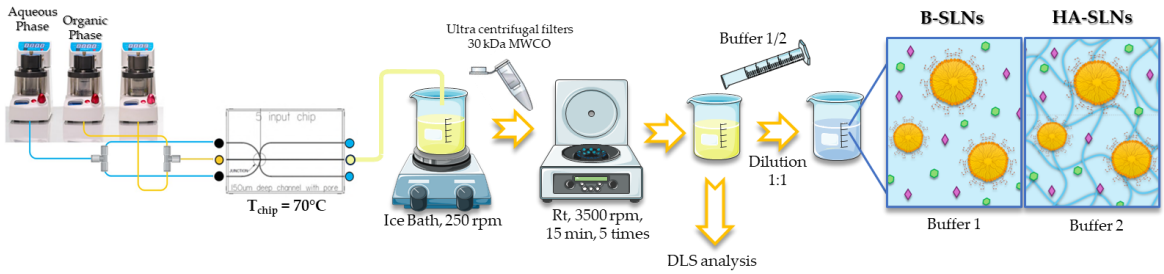


Figure 11. Schematic representation of the microfluidic platform utilizing a 5-input flow-focusing chip.

The SLNs preparation process was optimized, based on the DoE previously described, by varying the concentrations of Brij 78 and stearic acid, as well as the flow rate ratio (FRR). Flow rates were controlled using the Flow Control Center software. The FRR (Flow Rate Ratio) was defined as the ratio between the aqueous and organic phase flow rates (FR)(**Equation 4**):

$$FRR = FR_{Aqueous\ Phase} / FR_{Organic\ Phase} \quad \textbf{(4)}$$

Once a steady flow was established, the resulting SLNs were collected into a secondary container placed in an ice bath. The formulation was then centrifuged (5 times, 15 min, 3500 rpm, 20°C) using Amicon® Ultra centrifugal filters (30 kDa MWCO) to completely

remove the organic solvent and eventual excess of surfactant [39]. Once the optimal formulation was obtained through the statistical analysis of the CCD, it was named F-SLNs.

Preparation of SLNs-based Artificial Tears

To confer suitable and enhanced physicochemical properties for ophthalmic instillation, F-SLNs were prepared and then diluted 1:1 with two different buffers. The buffers were prepared in order to reach final concentrations as reported in **Table 18**. The developed SLNs-based ATs were nominated B-SLNs and HA-SLNs. Prior to dilution, additional ultracentrifugation cycles were carried out to eliminate trace amounts of residual organic solvent that might influence the resulting osmolarity.

Table 18. Aqueous phase composition.

Formulation	Aqueous phase composition (% w/v)
B-SLNs	H_3BO_3 0.84%
	$Na_2B_4O_7 \cdot 10\ H_2O$ 0.14%
	Ribitol 0.5%
	Taurine 0.5%
	Trehalose $\cdot 2\ H_2O$ 2.65%
HA-SLNs	H_3BO_3 0.84%
	$Na_2B_4O_7 \cdot 10\ H_2O$ 0.14%
	Ribitol 0.5%
	Taurine 0.5%
	Trehalose $\cdot\ 2\ H_2O$ 2.0%
	Hyaluronic Acid 0.2%

SLNs characterization

Size and Polydispersity Index Analysis

SLNs' sizes and polydispersity index (PDI) were determined at 25 °C by diluting the samples in Milli-Q® water at a ratio of 1:10. Both parameters were evaluated, respectively, in disposable transparent polystyrene cuvettes (batch 67.754, Sarstedt, Nümbrecht, Germany) and disposable folded capillary cells (DTS1070, Zetasizer Nano Series®, Malvern Panalytical Ltd, Malvern, United Kingdom) using the ZS Xplorer® software and Zetasizer Lab® (Malvern Panalytical Ltd, Malvern, United Kingdom). Material refractive index and absorption were correspondingly set at 1.35 and 0.001,

whereas water refractive index, viscosity, and dielectric constant were respectively set at 1.33, 1.05, and 78.5.

Morphological characterization

The morphology of B-SLNs and HA-SLNs was evaluated by transmission electron microscopy (Jeol, JEM-1010). A drop of SLNs suspension was placed on a Formvar-coated, 200-mesh copper grid and negatively stained with 2% (w/v) uranyl acetate. The grids were examined at an accelerating voltage of 80 kV using an Erlangshen ES500W camera (Gatan, Model 782).

pH

The pH was measured in triplicate using a pH meter (model GLP-2, Crison Instruments SA, Barcelona, Spain) calibrated with standards at pH equal to 7.00 and 9.00 and equipped with a microelectrode (InLab, Mettler, Barcelona, Spain).

Surface tension

SLNs formulation surface tensions were measured as per the Wilhelmy plate method. Briefly, all measurements were taken in triplicate using a K-11 digital tensiometer (Kruss GmbH, Hamburg, Germany) previously calibrated with Milli-Q® water (70.0 ± 2.0 mN/m) at 33 °C to simulate ocular surface temperature [40]. Before each analysis, the SLNs formulations were pre-heated to 33 °C and equilibrated for 3 min.

Osmolarity

Osmolarity was measured by the freezing point depression technique using a Fiske® single-sample micro osmometer (model 210, Fiske® Associates, Norwood, Massachusetts, United States). Three standard solutions of 50, 290, and 850 mOsm/L were employed to calibrate the equipment.

Rheological studies

Viscosity was measured by a parallel plate system linked to a Discovery HR1 hybrid rheometer (TA Instruments, New Castle, Delaware, United States). Measurements were carried out by gradually increasing the shear rate from 0 to 1000 s^{-1} in 30 steps at 33 °C.

In vitro cell viability

J774A.1 murine macrophage cells were purchased from American Type Cell Culture (ATCC, Manassas, VA, USA) and were cultured in Dulbecco's modified Eagle medium (DMEM, Sigma) containing 10% fetal bovine serum (FBS), 100 U/ml penicillin, and 100 µg/ml streptomycin, at 37 ºC in a humidified incubator containing 5% CO_2. For cytotoxic determinations, J774A.1 macrophages were seeded into 96-well plates ($7x10^3$ cells/well) and incubated with various concentrations of B-SLNs and HA-SLNs, or BAK 0.005 % for 1 and 4 h. Cell viability was measured using 3-(4,5-dimethylthiazol-2-yl)-2,5-diphenyltetrazolium bromide dye (MTT, 2 mg/mL, Sigma), incubated at 37 ºC for additional 1 h. The reaction product, formazan, was extracted with dimethyl sulfoxide (DMSO), and the absorbance was read at 570 nm. Each assay was conducted in duplicate or triplicate, where each data point shown in the figures represents the mean of, at least, 7 technical replicates from a single independent experiment, performed on separate days with different biological samples, but under the same experimental conditions. The results were expressed as the percent reduction in cell viability compared to untreated cells.

In vivo studies

Animals

In vivo experiments were performed fulfilling the Spanish Regulation on Experimental Studies with Animals (RD 53/2013 of 1 February 2013, modified by RD 118/2021 of 23 February 2021), the European Council Directive (86/609/EEC) and the Association for Research in Vision and Ophthalmology (ARVO) Statement for the Use of Animals in Ophthalmic Vision Research. The Animal Experimentation Ethics Committee of the Complutense University of Madrid granted approvals for the procedures under the codes PROEX 091.5/21 (February 24, 2021), and PROEX 114.4/21 (March 16, 2021). The experiments were conducted at the animal facility of the Complutense University of Madrid, in normotensive albino male New Zealand rabbits (n = 6; 4.95 kg ± 0.57) from Granja San Bernardo (Tulebras, Spain). The sample size was determined by adhering to the principles of the 3Rs principle. Animals were housed individually in standard cages, with free access to rabbit pellets and water *ad libitum*, and the housing conditions maintained a room temperature of 22 °C in a controlled atmosphere and kept under 12-h

light-dark cycles (with lights on from 8:00 pm to 8:00 am). Based on the results discussed in Section 3.4, the formulation HA-SLNs (0.1 mg/mL) was selected for the *in vivo* studies.

Chronic tolerance studies

Chronic tolerance studies were conducted following the EMA/CHMP/SWP/2145/2000 guidelines, which are typically applied to ophthalmic medicinal products, to assess the long-term local tolerance of the formulation intended for repeated ocular administration (European Medicines Agency, 2015). Although the proposed HA-SLNs formulation is classified as a medical device rather than a medicinal product, the same experimental protocol was previously employed for drug-based eye drop formulations [7]. Briefly, HA-SLNs, previously filtered through 0.22 μm cellulose acetate filters, was topically instilled (25 μL) once per day for 15 consecutive days at the same time each day (10 am) to avoid diurnal fluctuations of the estimated parameters (n = 8 eyes). Ocular surface status and animals' discomfort were evaluated by the Draize test before the beginning of the study and each day before HA-SLNs administration until the end of the follow-up period. As control, 0.9 % w/v NaCl was utilised (n = 4 eyes). Inflammatory responses were graded according to a modified Draize scoring system, adapted in alignment with ISO 10993-10:2021 guidelines (**Table 19**). Prior to initiating the study, the authors set a threshold of a cumulative score of 10, including the 'discomfort' factor, to define good tolerance of HA-SLNs [41, 42].

Table 19. Scoring system for the Draize test, employed for determining the ocular signs severity during *in vivo* chronic tolerance studies of the proposed liposomal formulation.

CORNEA Score = A × B × 5 (range 0-80)	A. Opacity/Degree of density (most dense area taken for reading) - Scattered or diffuse area; details of iris clearly visible = 1 - Easily discernible translucent areas; details of iris slightly obscured = 2 - Opalescent areas; no details of iris visible, size of pupil barely discernible = 3 - Opaque; iris invisible = 4 B. Area of cornea involved - One quarter (or less), but not zero = 1 - Greater than one quarter, less than one half = 2 - Greater than one half, less than three quarters = 3 - Greater than three quarters, up to whole area = 4
IRIS Score = A × 5 (range 0-10)	A. Values Folds above normal, congestion, swelling, and/or circumcorneal injection; iris still reacting to light (sluggish reaction is positive) = 1 No reaction to light, haemorrhage, and/or gross destruction = 2

CONJUNCTIVA Score = (A + B + C) × 2 (range 0-20)	A. Redness of palpebral conjunctiva - Vessels definitely injected above normal = 1 - More diffuse, deeper crimson red; individual vessels not easily discernible = 2 - Diffuse beefy red = 3 B. Chemosis - Any swelling above normal (includes nictitating membrane) = 1 - Obvious swelling with partial eversion of the lids = 2 - Swelling with lids about half closed = 3 - Swelling with lids about half closed to completely closed = 4 C. Discharge - Any amount different from normal = 1 - Discharge with moistening of the lids and hairs adjacent to the lids = 2 - Discharge with moistening of the lids and considerable area around the eye
DISCOMFORT Score = A × 5 (range 0-10)	A. Values - No reaction = 0 - Blinking = 1 - Enhanced blinking; vocalisations = 2
Total score	= Sum of all scores obtained for the cornea, iris, conjunctiva, and discomfort

Evaluation of dry eye disease diagnostic parameters

As the SLNs proposed have been designed with the inclusion of osmoprotective agents, the onset, evolution, or reduction of DED has been evaluated throughout the study, concomitantly with chronic tolerance studies. Tear secretion, tear film stability and eventual ocular surface damage were the DED diagnostic parameters evaluated throughout the whole study [43].

Tear secretion was assessed through the Schirmer's test (SCHT), without anaesthesia. Sterile Schirmer's test strips (Contacare Ophthalmics and Diagnostics, Gujarat, India) were placed on the temporal tarsal conjunctiva of the lower lid for 60 s with closed eyes. Tear volume was recorded as the length of the moistened area (in millimetres) on the strip [44, 45]. To minimize potential cross-assay interference, a washout period of five minutes was observed between successive SCHT and subsequent evaluations.

Afterwards, sterile fluorescein sodium ophthalmic strips (Contacare Ophthalmics and Diagnostics, Gujarat, India) were moistened with 0.9% w/v NaCl and gently applied to the inferior conjunctival fornix of each rabbit. Animals were allowed to blink to evenly distribute the dye over the ocular surface. Following fluorescein application, the corneal epithelium was examined using a handheld slit-lamp microscope (SL-15 L, Kowa

Optimed Deutschland GmbH, Düsseldorf, Germany) with a cobalt blue filter at 16× magnification. The extent of corneal epithelial damage was evaluated using the Oxford grading scale (OXGS), which divides corneal staining into six levels of severity ranging from 0 (no staining) to 5 (extensive staining), as previously described [46].

Additionally, tear film stability was assessed by performing the tear breakup time (TBUT) test, under a broad beam of Cobalt blue light. Briefly, TBUT was measured using a stopwatch by determining the duration in seconds from the moment of the last blink to the appearance of the first dry area within the tear film [47, 48].

Finally, conjunctival epithelial integrity was evaluated by applying lissamine green dye. Lissamine green sterile ophthalmic strips (Contacare Ophthalmics and Diagnostics, India) containing approximately 1.5 mg of dye were moistened with 0.9% w/v NaCl and gently applied to the inferior conjunctival fornix. After blinking, the ocular surface was examined under slit-lamp white light, and the degree of conjunctival staining was scored according to the Van Bijsterveld scale, which divides the surface into three zones (nasal conjunctiva, cornea, and temporal conjunctiva). Each zone was scored from 0 (no staining) to 3 (confluent staining), for a maximum cumulative score of 9 per eye [49].

Evaluations of DED diagnostic parameters were performed following the same order as they were described at the following timepoints: right before the first application and at 8, 15 days after the beginning of the studies (n = 8 eyes). The same procedures were followed for 0.9 % w/v NaCl, which was used as a control (n = 4 eyes).

Data Analysis

Statistical modeling and rationalization of the experimental data were performed using Minitab 19 (19.1.0.1, Minitab, LLC, State College, PA, USA), which enabled a robust evaluation of the regression parameters and the predictive performance of the model. Response surface and contour plots were generated with Stat-Ease® 360 (version 25.0.2; Stat-Ease, Inc., Minneapolis, MN, USA) to explore the design space and visualize the model behaviour. All data presented in text and tables are reported as mean value ± SD. *In vitro* statistical significance was determined using one-way ANOVA followed by Dunnett's post-hoc test. *In vivo* chronic tolerance measurements were reported as the average value ± SEM. The significance of the differences in the *in vivo* tolerance results was assessed using a one-tailed Student's t-test. Prism 8.4.3 software (GraphPad, San

Diego, CA, USA) was used for the statistical determinations, considering statistically significant probability value lower than 0.05 ($p < 0.05$).

4.3.4. Conclusions

Overall, the integration of DoE-guided microfluidic manufacturing with a rational and systematic *in vitro-in vivo* evaluation provides strong evidence of the safety and suitability of HA-SLNs as advanced ATs formulations. By combining the structural advantages of SLNs with the mucoadhesive and viscoelastic functions of hyaluronic acid, the osmoprotective activity of ribitol and taurine, this system effectively targets the main pathophysiological mechanisms of DED while maintaining excellent ocular tolerability. Moreover, the lipid nanoparticle platform of HA-SLNs offers intrinsic versatility for the incorporation of therapeutic agents, enabling their potential use as drug-loaded ATs for the management of ocular diseases commonly associated with DED, such as glaucoma or inflammatory conditions, where tear film instability and chronic surface stress coexist.

Our approach extends previous nanocarrier-based strategies in two important ways: first, by providing a long-term rabbit safety dataset supported by comprehensive tear-film diagnostics, and second, by applying microfluidic hydrodynamic flow focusing combined with DoE optimization to ensure precise control, reproducibility, and scalability. Collectively, these results highlight HA-SLNs as a next-generation artificial tear platform, bridging nanotechnology, tear-film physiology, and translational design principles toward future clinical validation and comparative trials with marketed formulations.

References

1. Uchino, M., D.A. Schaumberg, Dry Eye Disease: Impact on Quality of Life and Vision. *Curr Ophthalmol Rep*, **2013**. 1(2): p. 51-57.
2. Benitez-del-Castillo, J.M., B. Burgos-Blasco, Prevalence of dry eye disease in Spain: A population-based survey (PrevEOS). *The Ocular Surface*, **2025**. 36: p. 126-133.
3. Zemanová, M., Dry Eye Disease. A Review. *Cesk Slov Oftalmol*, **2021**. 77(3): p. 107–119.
4. Craig, J.P., K.K. Nichols, E.K. Akpek, B. Caffery, H.S. Dua, C.-K. Joo, Z. Liu, J.D. Nelson, J.J. Nichols, K. Tsubota, TFOS DEWS II definition and classification report. *The ocular surface*, **2017**. 15(3): p. 276-283.
5. Messmer, E.M., The pathophysiology, diagnosis, and treatment of dry eye disease. *Dtsch Arztebl Int*, **2015**. 112(5): p. 71-81; quiz 82.
6. Stapleton, F., P. Argüeso, P. Asbell, D. Azar, C. Bosworth, W. Chen, J.B. Ciolino, J.P. Craig, J. Gallar, A. Galor, TFOS DEWS III: Digest. *American Journal of Ophthalmology*, **2025**. 279: p. 451-553.
7. Brugnera, M., M. Vicario-de-la-Torre, M.A. González-Cela-Casamayor, F.M. Gonzalez-Fernandez, I. Ferraboschi, V. Andrés-Guerrero, S. Nicoli, C. Sissa, S. Pescina, R. Herrero-Vanrell, Disclosing long-term tolerance, efficacy and penetration properties of hyaluronic acid-coated latanoprost-loaded liposomes as chronic glaucoma therapy. *Journal of Controlled Release*, **2025**. 379: p. 730-742.
8. Bucolo, C., A. Fidilio, C.B.M. Platania, F. Geraci, F. Lazzara, F. Drago, Antioxidant and Osmoprotecting Activity of Taurine in Dry Eye Models. *J Ocul Pharmacol Ther*, **2018**. 34(1-2): p. 188-194.
9. López-Cano, J.J., M. González-Cela-Casamayor, V. Andrés-Guerrero, M. Vicario-de-la-Torre, J.B. Del Castillo, R. Herrero-Vanrell, I.T. Molina-Martínez, Development of an osmoprotective microemulsion as a therapeutic platform for ocular surface protection. *International journal of pharmaceutics*, **2022**. 623: p. 121948.
10. Scarpellini, C., A. Ramos Llorca, C. Lanthier, G. Klejborowska, K. Augustyns, The potential role of regulated cell death in dry eye diseases and ocular surface dysfunction. *International journal of molecular sciences*, **2023**. 24(1): p. 731.

11. Torrent-Burgués, J., Tear film constituents and medicines for eyes investigated as Langmuir films. *BioNanoScience*, **2023**. 13(3): p. 1324-1338.
12. McCulley, J.P., W.E. Shine, The lipid layer: the outer surface of the ocular surface tear film. *Bioscience reports*, **2001**. 21(4): p. 407-418.
13. Pflugfelder, S.C., M.E. Stern, Biological functions of tear film. *Experimental eye research*, **2020**. 197: p. 108115.
14. Jones, L., L.E. Downie, D. Korb, J.M. Benitez-Del-Castillo, R. Dana, S.X. Deng, P.N. Dong, G. Geerling, R.Y. Hida, Y. Liu, K.Y. Seo, J. Tauber, T.H. Wakamatsu, J. Xu, J.S. Wolffsohn, J.P. Craig, TFOS DEWS II Management and Therapy Report. *Ocul Surf*, **2017**. 15(3): p. 575-628.
15. Kim, M., Y. Lee, D. Mehra, A.L. Sabater, A. Galor, Dry eye: why artificial tears are not always the answer. *BMJ open ophthalmology*, **2021**. 6(1).
16. Akhter, M.H., I. Ahmad, M.Y. Alshahrani, A.I. Al-Harbi, H. Khalilullah, O. Afzal, A.S.A. Altamimi, S.N.M. Najib Ullah, A. Ojha, S. Karim, Drug Delivery Challenges and Current Progress in Nanocarrier-Based Ocular Therapeutic System. *Gels*, **2022**. 8(2).
17. Kamaleddin, M.A., Nano-ophthalmology: Applications and considerations. *Nanomedicine*, **2017**. 13(4): p. 1459-1472.
18. Coco, G., G. Buffon, A. Taloni, G. Giannaccare, Recent Advances in Nanotechnology for the Treatment of Dry Eye Disease. *Nanomaterials (Basel)*, **2024**. 14(8).
19. Garrigue, J.-S., M. Amrane, M.-O. Faure, J.M. Holopainen, L. Tong, Relevance of lipid-based products in the management of dry eye disease. *Journal of ocular pharmacology and therapeutics*, **2017**. 33(9): p. 647-661.
20. Seyfoddin, A., J. Shaw, R. Al-Kassas, Solid lipid nanoparticles for ocular drug delivery. *Drug Deliv*, **2010**. 17(7): p. 467-89.
21. Marinelli, L., M.P. Dimmito, I. Cacciatore, E.C. Toto, A. Di Rienzo, F. Palmerio, V. Puca, E.S. Di Filippo, S. Fulle, A. Di Stefano, Solid lipid nanoparticles for efficient delivery of capsaicin-rich extract: Potential neuroprotective effects in Parkinson's disease. *Journal of Drug Delivery Science and Technology*, **2024**. 91: p. 105097.
22. Laserra, S., A. Basit, P. Sozio, L. Marinelli, E. Fornasari, I. Cacciatore, M. Ciulla, H. Türkez, F. Geyikoglu, A. Di Stefano, Solid lipid nanoparticles loaded with lipoyl-

memantine codrug: preparation and characterization. *Int J Pharm*, **2015**. 485(1-2): p. 183-91.

23. Liang, Z., Z. Zhang, P. Lu, J. Yang, L. Han, S. Liu, T. Zhou, J. Li, J. Zhang, The effect of charges on the corneal penetration of solid lipid nanoparticles loaded Econazole after topical administration in rabbits. *Eur J Pharm Sci*, **2023**. 187: p. 106494.
24. Khairnar, S.V., P. Pagare, A. Thakre, A.R. Nambiar, V. Junnuthula, M.C. Abraham, P. Kolimi, D. Nyavanandi, S. Dyawanapelly, Review on the Scale-Up Methods for the Preparation of Solid Lipid Nanoparticles. *Pharmaceutics*, **2022**. 14(9).
25. Carvalho, B.G., B.T. Ceccato, M. Michelon, S.W. Han, L.G. de la Torre, Advanced Microfluidic Technologies for Lipid Nano-Microsystems from Synthesis to Biological Application. *Pharmaceutics*, **2022**. 14(1).
26. González-Fernández, F.M., A. Bianchera, P. Gasco, S. Nicoli, S. Pescina, Lipid-Based Nanocarriers for Ophthalmic Administration: Towards Experimental Design Implementation. *Pharmaceutics*, **2021**. 13(4): p. 447.
27. Hassan, H., S.K. Adam, E. Alias, M.M.R. Meor Mohd Affandi, A.F. Shamsuddin, R. Basir, Central Composite Design for Formulation and Optimization of Solid Lipid Nanoparticles to Enhance Oral Bioavailability of Acyclovir. *Molecules*, **2021**. 26(18): p. 5432.
28. Guo, W.P., Z.B. Rong, Y.H. Li, Y.S. Fung, G.Q. Gao, Z.M. Cai, Microfluidic chip capillary electrophoresis coupled with electrochemiluminescence for enantioseparation of racemic drugs using central composite design optimization. *Electrophoresis*, **2013**. 34(20-21): p. 2962-9.
29. Esteban-Pérez, S., V. Andrés-Guerrero, J.J. López-Cano, I. Molina-Martínez, R. Herrero-Vanrell, I. Bravo-Osuna, Gelatin nanoparticles-HPMC hybrid system for effective ocular topical administration of antihypertensive agents. *Pharmaceutics*, **2020**. 12(4): p. 306.
30. Marinelli, L., I. Cacciatore, E. Costantini, M.P. Dimmito, F. Serra, A. Di Stefano, M. Reale, Wound-Healing Promotion and Anti-Inflammatory Properties of Carvacrol Prodrugs/Hyaluronic Acid Formulations. *Pharmaceutics*, **2022**. 14(7).
31. Aragona, P., P.A. Simmons, H. Wang, T. Wang, Physicochemical properties of hyaluronic acid–based lubricant eye drops. *Translational Vision Science & Technology*, **2019**. 8(6): p. 2-2.

32. Abusharha, A., A.A. Shbear, R. Fagehi, M.A. Alanazi, A. Alsaqr, G.A. El-Hiti, A.M. Masmali, Assessment of the efficiency of hp-guar and hyaluronic acid tear supplements to control tear film evaporation rate in dry eye subjects. *The Open Ophthalmology Journal*, **2021**. 15(1).
33. Brugnera, M., M. Vicario-de-la-Torre, M.A. González-Cela Casamayor, J.J. López-Cano, I. Bravo-Osuna, F. Huete-Toral, M.L. González Rubio, G. Carracedo, I.T. Molina-Martínez, V. Andrés-Guerrero, Enhancing the hypotensive effect of latanoprost by combining synthetic phosphatidylcholine liposomes with hyaluronic acid and osmoprotective agents. *Drug Delivery and Translational Research*, **2024**. 14(10): p. 2804-2822.
34. González-Cela-Casamayor, M.A., J.J. López-Cano, I. Bravo-Osuna, V. Andrés-Guerrero, M. Vicario-de-la-Torre, M. Guzmán-Navarro, J.M. Benítez-Del-Castillo, R. Herrero-Vanrell, I.T. Molina-Martínez, Novel Osmoprotective DOPC-DMPC Liposomes Loaded with Antihypertensive Drugs as Potential Strategy for Glaucoma Treatment. *Pharmaceutics*, **2022**. 14(7).
35. Szpisják-Gulyás, N., A.N. Al-Tayawi, Z.H. Horváth, Z. László, S. Kertész, C. Hodúr, Methods for experimental design, central composite design and the Box–Behnken design, to optimise operational parameters: A review. *Acta Alimentaria*, **2023**. 52(4): p. 521-537.
36. Varshosaz, J., S. Ghaffari, M.R. Khoshayand, F. Atyabi, S. Azarmi, F. Kobarfard, Development and optimization of solid lipid nanoparticles of amikacin by central composite design. *Journal of liposome research*, **2010**. 20(2): p. 97-104.
37. Babu, V.N., G.S.K. Rao, R.R. Budha, R.R. Alavala, P.K. Desu, G.K. Babu, A.D. Prasad, Development, characterization and optimization of solid lipid nanoparticles of alpha-mangostin by central composite design approach. *Journal of Applied Pharmaceutical Science*, **2023**. 13(8): p. 140-150.
38. Ali, H., S.K. Singh, Preparation and characterization of solid lipid nanoparticles of furosemide using quality by design. *Particulate Science and Technology*, **2018**. 36(6): p. 695-709.
39. Arduino, I., Z. Liu, A. Rahikkala, P. Figueiredo, A. Correia, A. Cutrignelli, N. Denora, H.A. Santos, Preparation of cetyl palmitate-based PEGylated solid lipid nanoparticles by microfluidic technique. *Acta Biomater*, **2021**. 121: p. 566-578.

40. Purslow, C., J.S. Wolffsohn, Ocular surface temperature: a review. *Eye Contact Lens*, **2005**. 31(3): p. 117-23.
41. Lambert, L.A., W.A. Chambers, S. Green, K.C. Gupta, R.N. Hill, P.M. Hurley, C.C. Lee, J.K. Lee, P.T. Liu, D.K. Lowther, et al., The use of low-volume dosing in the eye irritation test. *Food Chem Toxicol*, **1993**. 31(2): p. 99-103.
42. Wilhelmus, K.R., The Draize eye test. *Surv Ophthalmol*, **2001**. 45(6): p. 493-515.
43. Wolffsohn, J.S., R. Arita, R. Chalmers, A. Djalilian, M. Dogru, K. Dumbleton, P.K. Gupta, P. Karpecki, S. Lazreg, H. Pult, B.D. Sullivan, A. Tomlinson, L. Tong, E. Villani, K.C. Yoon, L. Jones, J.P. Craig, TFOS DEWS II Diagnostic Methodology report. *Ocul Surf*, **2017**. 15(3): p. 539-574.
44. Carracedo, G., C. Pastrana, M. Serramito, C. Rodriguez-Pomar, Evaluation of tear meniscus by optical coherence tomography after different sodium hyaluronate eyedrops instillation. *Acta Ophthalmol*, **2019**. 97(2): p. e162-e169.
45. Versura, P., M. Frigato, M. Cellini, R. Mulè, N. Malavolta, E.C. Campos, Diagnostic performance of tear function tests in Sjogren's syndrome patients. *Eye (Lond)*, **2007**. 21(2): p. 229-37.
46. Bron, A.J., V.E. Evans, J.A. Smith, Grading of corneal and conjunctival staining in the context of other dry eye tests. *Cornea*, **2003**. 22(7): p. 640-50.
47. Paugh, J.R., J. Tse, T. Nguyen, A. Sasai, E. Chen, M.T. De Jesus, J. Kwan, A.L. Nguyen, M. Farid, S. Garg, J.V. Jester, Efficacy of the Fluorescein Tear Breakup Time Test in Dry Eye. *Cornea*, **2020**. 39(1): p. 92-98.
48. Doughty, M.J., Tear Film Stability and Tear Break Up Time (TBUT) in Laboratory Rabbits-A Systematic Review. *Curr Eye Res*, **2018**. 43(8): p. 961-964.
49. Wahyu, T., Examination for Dry Eyes. *Dry Eye Syndrome: Modern Diagnostic Techniques and Advanced Treatments*, **2022**: p. 3.
50. Adediran, E., S. Vijayanand, A. Kale, M. Gulani, J.C. Wong, A. Escayg, K.S. Murnane, M.J. D'Souza, Microfluidics-Assisted Formulation of Polymeric Oxytocin Nanoparticles for Targeted Brain Delivery. *Pharmaceutics*, **2025**. 17(4): p. 452.
51. Truong, N., S.K. Black, J. Shaw, B.L. Scotland, R.M. Pearson, Microfluidic-Generated Immunomodulatory Nanoparticles and Formulation-Dependent Effects on Lipopolysaccharide-Induced Macrophage Inflammation. *Aaps j*, **2021**. 24(1): p. 6.

52. Leung, M.H., A.Q. Shen, Microfluidic assisted nanoprecipitation of PLGA nanoparticles for curcumin delivery to leukemia jurkat cells. *Langmuir*, **2018**. 34(13): p. 3961-3970.
53. Wang, F.-z., M.-w. Zhang, D.-s. Zhang, Y. Huang, L. Chen, S.-m. Jiang, K. Shi, R. Li, Preparation, optimization, and characterization of chitosan-coated solid lipid nanoparticles for ocular drug delivery. *Journal of Biomedical Research*, **2018**. 32(6): p. 411.
54. Talarico, L., S. Pepi, S. Susino, G. Leone, C. Bonechi, M. Consumi, I. Clemente, A. Magnani, Design and optimization of solid lipid nanoparticles loaded with triamcinolone acetonide. *Molecules*, **2023**. 28(15): p. 5747.
55. Terada, T., J.A. Kulkarni, A. Huynh, S. Chen, R. van der Meel, Y.Y.C. Tam, P.R. Cullis, Characterization of lipid nanoparticles containing ionizable cationic lipids using design-of-experiments approach. *Langmuir*, **2021**. 37(3): p. 1120-1128.
56. Montgomery, D.C., *Design and analysis of experiments*. 2017: John wiley & sons.
57. Dong, X., C.A. Mattingly, M.T. Tseng, M.J. Cho, Y. Liu, V.R. Adams, R.J. Mumper, Doxorubicin and paclitaxel-loaded lipid-based nanoparticles overcome multidrug resistance by inhibiting P-glycoprotein and depleting ATP. *Cancer research*, **2009**. 69(9): p. 3918-3926.
58. Tang, J., Y. Wang, D. Wang, Y. Wang, Z. Xu, K. Racette, F. Liu, Key structure of brij for overcoming multidrug resistance in cancer. *Biomacromolecules*, **2013**. 14(2): p. 424-430.
59. Forbes, N., M.T. Hussain, M.L. Briuglia, D.P. Edwards, J.H. Ter Horst, N. Szita, Y. Perrie, Rapid and scale-independent microfluidic manufacture of liposomes entrapping protein incorporating in-line purification and at-line size monitoring. *International journal of pharmaceutics*, **2019**. 556: p. 68-81.
60. Kastner, E., R. Kaur, D. Lowry, B. Moghaddam, A. Wilkinson, Y. Perrie, High-throughput manufacturing of size-tuned liposomes by a new microfluidics method using enhanced statistical tools for characterization. *International journal of pharmaceutics*, **2014**. 477(1-2): p. 361-368.
61. Uche, C.U., M.A. Okezue, I. Amidu, S.R. Byrn, Model Adequacy in Assessing the Predictive Performance of Regression Models in Pharmaceutical Product

Optimization: The Bedaquiline Solid Lipid Nanoparticle Example. *Scientia Pharmaceutica*, **2024**. 92(4): p. 64.

62. Oehlert, G.W., A first course in design and analysis of experiments. **2010**.
63. Barton, R.R., *Designing Experiments Graphically*, in *Graphical Methods for the Design of Experiments*. 1999, Springer. p. 93-131.
64. Metwally, A.A., R.M. Hathout, Computer-Assisted Drug Formulation Design: Novel Approach in Drug Delivery. *Mol Pharm*, **2015**. 12(8): p. 2800-10.
65. Gordillo-Galeano, A., C.E. Mora-Huertas, Hydrodynamic diameter and zeta potential of nanostructured lipid carriers: Emphasizing some parameters for correct measurements. *Colloids and surfaces A: Physicochemical and engineering aspects*, **2021**. 620: p. 126610.
66. De Campos, A.M., A. Sánchez, M.J. Alonso, Chitosan nanoparticles: a new vehicle for the improvement of the delivery of drugs to the ocular surface. Application to cyclosporin A. *Int J Pharm*, **2001**. 224(1-2): p. 159-68.
67. Hotujac Grgurević, M., M. Juretić, A. Hafner, J. Lovrić, I. Pepić, Tear fluid-eye drops compatibility assessment using surface tension. *Drug development and industrial pharmacy*, **2017**. 43(2): p. 275-282.
68. Ruiz de Garibay, A.P., M.A. Solinís, A. del Pozo-Rodríguez, P.S. Apaolaza, J.S. Shen, A. Rodríguez-Gascón, Solid Lipid Nanoparticles as Non-Viral Vectors for Gene Transfection in a Cell Model of Fabry Disease. *J Biomed Nanotechnol*, **2015**. 11(3): p. 500-11.
69. Liu, D., Y. Lian, Q. Fang, L. Liu, J. Zhang, J. Li, Hyaluronic-acid-modified lipid-polymer hybrid nanoparticles as an efficient ocular delivery platform for moxifloxacin hydrochloride. *International journal of biological macromolecules*, **2018**. 116: p. 1026-1036.
70. Vicario-de-la-Torre, M., M. Caballo-González, E. Vico, L. Morales-Fernández, P. Arriola-Villalobos, B. De Las Heras, J.M. Benítez-del-Castillo, M. Guzmán, T. Millar, R. Herrero-Vanrell, Novel nano-liposome formulation for dry eyes with components similar to the preocular tear film. *Polymers*, **2018**. 10(4): p. 425.
71. Niu, Y., M. Tang, In vitro review of nanoparticles attacking macrophages: Interaction and cell death. *Life Sciences*, **2022**. 307: p. 120840.

72. Iso, I., 10993-5: 2009 Biological evaluation of medical devices-part 5: tests for in vitro cytotoxicity. *International Organization for Standardization, Geneva*, **2009**. 34.
73. Apaolaza, P., A. del Pozo-Rodríguez, J. Torrecilla, A. Rodríguez-Gascón, J. Rodríguez, U. Friedrich, B.H. Weber, M. Solinís, Solid lipid nanoparticle-based vectors intended for the treatment of X-linked juvenile retinoschisis by gene therapy: In vivo approaches in Rs1h-deficient mouse model. *Journal of Controlled Release*, **2015**. 217: p. 273-283.
74. Contreras-Ruiz, L., M. de la Fuente, C. García-Vázquez, V. Sáez, B. Seijo, M.J. Alonso, M. Calonge, Y. Diebold, Ocular tolerance to a topical formulation of hyaluronic acid and chitosan-based nanoparticles. *Cornea*, **2010**. 29(5): p. 550-8.
75. De La Fuente, M., B. Seijo, M.J. Alonso, Novel hyaluronan-based nanocarriers for transmucosal delivery of macromolecules. *Macromolecular bioscience*, **2008**. 8(5): p. 441-450.
76. Zhang, W., Y. Wang, B.T.K. Lee, C. Liu, G. Wei, W. Lu, A novel nanoscale-dispersed eye ointment for the treatment of dry eye disease. *Nanotechnology*, **2014**. 25(12): p. 125101.
77. López-Cano, J.J., M.A. González-Cela-Casamayor, V. Andrés-Guerrero, R. Herrero-Vanrell, J.M. Benítez-Del-Castillo, I.T. Molina-Martínez, Combined hyperosmolarity and inflammatory conditions in stressed human corneal epithelial cells and macrophages to evaluate osmoprotective agents as potential DED treatments. *Exp Eye Res*, **2021**. 211: p. 108723.
78. Tran, K.N., N. Pham, S.H. Jang, C. Lee, Purification and characterization of a novel medium-chain ribitol dehydrogenase from a lichen-associated bacterium Sphingomonas sp. *PLoS One*, **2020**. 15(7): p. e0235718.
79. Gonzalez Cela Casamayor, M.A., J.J. Lopez Cano, V. Andres Guerrero, R. Herrero Vanrell, J.M. Benitez del Castillo, I.T. Molina Martinez, A novel osmoprotective liposomal formulation from synthetic phospholipids to reduce in vitro hyperosmolar stress in dry eye treatments. *Journal of Liposome Research*, **2023**. 33(2): p. 117-128.
80. European Medicines Agency, Guideline on non-clinical local tolerance testing of medicinal products (EMA/CHMP/SWP/2145/2000) Rev 1, Corr 1, in, 2015.

4.3. Exploring Nano-in-Micro Architectures: SLNs Incorporation into PLGA Microspheres

4.3.1 Introduction

Glaucoma is a chronic, progressive optic neuropathy and one of the leading causes of irreversible blindness worldwide [1]. It encompasses a group of eye diseases characterized by the progressive degeneration of retinal ganglion cells (RGCs) and the retinal nerve fiber layer (RNFL). The most prevalent form, primary open-angle glaucoma (POAG), accounts for approximately 74% of all glaucoma cases, and arises from impaired aqueous humor outflow through the trabecular meshwork, resulting in elevated intraocular pressure (IOP) and subsequent optic nerve damage [2]. Although IOP reduction remains the cornerstone of glaucoma therapy, and topical medications represent the first-line treatment in most clinical settings, visual function may continue to deteriorate despite adequate pressure control [3]. Moreover, optic nerve degeneration also occurs in normotensive individuals, highlighting the multifactorial nature of the disease and the need for therapeutic strategies that extend beyond IOP lowering [4]. RGC loss is driven by an intricate interplay of pathological mechanisms, including oxidative stress, neuroinflammation, excitotoxicity, glial cell activation, mitochondrial dysfunction, and trophic factor deprivation [5, 6]. Increasing evidence also implicates both microglia and macroglia in modulating the inflammatory environment of the glaucomatous retina [7]. The convergence of these damaging pathways underscores the need for multitarget neuroprotective approaches [8].

Conventional ocular drug delivery, particularly topical administration, is severely hindered by the anatomical and physiological barriers and physiological tear turnover, blinking, nasolacrimal drainage, and poor corneal and conjunctival permeability, resulting in less than 5% intraocular bioavailability [9, 10]. Intraocular injections are more effective for targeting the posterior segment, but they carry risks, including detachment, endophthalmitis, and patient discomfort due to the need for frequent reinjections [11]. Therefore, long-acting intraocular drug delivery systems (IODDS) have emerged as promising solutions to sustain drug levels, reduce injection frequency, and mitigate safety concerns [12]. Biodegradable platforms, particularly poly(lactic-co-glycolic acid) (PLGA) systems approved by the FDA and EMA, are widely explored because they

naturally degrade after releasing their therapeutic payload [13]. Among IODDS, microspheres (MSs) have gained considerable interest for ocular applications [22]. They can be administered as suspensions through standard 25G-32G needles and maintain therapeutic drug levels for extended periods, thereby reducing the need for repeated injections [14]. Notably, MSs can sustain drug release for weeks to months, depending on the clinical requirements, and allow the co-encapsulation of multiple agents within a single platform [15].

In recent years, the combination of micro- and nanoscale carriers has led to the development of advanced hierarchical architectures known as nanoparticle-in-microparticle (NiM) or "Trojan" systems [16]. These platforms consist of microspheres encapsulating nanoparticles, which can subsequently be released in a controlled manner, protecting them from the surrounding environment and enabling sustained therapeutic action [17]. Such architectures allow controlled and sequential drug delivery, enhanced stability of labile molecules, co-loading of agents with different physicochemical properties, prolonged intravitreal residence, deeper tissue penetration, and reduced burst-related toxicity [18]. Owing to these features, NiM systems have attracted growing interest in ocular drug delivery, where overcoming physiological barriers and achieving long-lasting posterior segment exposure remain major challenges [19].

Within this framework, we propose a multi-agent microsystem containing ketorolac, a nonsteroidal anti-inflammatory drug (NSAID) that inhibits cyclooxygenase (COX)-mediated inflammatory pathways, and ursodeoxycholic acid (UDCA), a bile acid with antioxidant, anti-apoptotic, and anti-inflammatory properties known for its neuroprotective effects in models of retinal degeneration and optic neuropathy [20, 21]. This combinatorial strategy is designed to counteract inflammatory processes while protecting RGCs from degeneration, thus addressing multiple aspects of glaucomatous pathology within a single formulation.

To explore the potential of a NiM configuration for ocular therapy, we developed and characterized a PLGA-based Trojan system for intraocular administration in which plain solid lipid nanoparticles (SLNs) were co-encapsulated with ketorolac and UDCA. Blank SLNs were introduced to investigate how a lipid nanostructured compartment influences microsphere properties, including encapsulation efficiency, release behaviour, and internal organization. Although unloaded in the present work, the inclusion of SLNs

represents a first technological step toward the development of a versatile delivery platform in which lipid nanosystems could be loaded with active compounds in future studies. This strategy would enable the incorporation of drugs that are incompatible with the PLGA matrix, display poor encapsulation efficiency when directly embedded in polymeric microspheres, or require distinct microenvironments for optimal stabilization and release. The resulting data provide insight into the role of SLNs as modulatory elements within PLGA -MSs and contribute to the rational design of long-acting delivery systems for chronic ocular diseases.

4.3.2. Results and discussion

SLNs preparation and characterization

SLNs were produced using a microfluidic flow-focusing technique, a highly controlled and reproducible method that enables the generation of homogeneous nanoparticle batches by applying robust operating parameters previously optimized through a systematic experimental design. Blank SLNs consistently displayed hydrodynamic diameters around 189-199 nm, narrow PDI values (<0.22), and a negative ζ-potential (-43/-46 mV), confirming the formation of a stable colloidal system with suitable electrostatic repulsion to prevent aggregation. As expected, the incorporation of the fluorescent lipid SA-PEG-FITC slightly modified the SLNs' features, leading to a modest reduction in mean diameter (166.01 ± 3.32 nm) and a decrease in surface charge intensity (**Table 20**). This change is consistent with the presence of PEGylated moieties at the particle interface and further supports the successful incorporation of the fluorescent tracer. Such variation could also arise from the interaction between FITC and the PEG chains, which may promote a more compact arrangement of the PEG corona [27].

Table 20. Size distributions and ζ-potential of blank SLNs loaded into Trojan MSs**.**

Formulation	Size (nm)	PDI	ζ-potential (mV)
Blank SLN I	191.00 ± 1.06	0.220 ± 0.007	- 46.36 ± 1.97
Blank SLN II	199.60 ± 0.38	0.190 ± 0.010	- 46.76 ± 1.50
Blank SLN III	189.20 ± 5.21	0.170 ± 0.008	- 43.00 ± 1.52
FITC-SLN	166.01 ± 3.32	0.200 ± 0.010	- 31.89 ± 5.26

To enable high loading of SLNs into PLGA microspheres, lyophilization was essential to obtain a dry and concentrated SLN powder. However, freeze-drying inherently stresses SLNs due to the formation of ice crystals, dehydration forces, and the reorganization of lipids [28]. The results clearly showed that SLNs freeze-dried without cryoprotectant underwent marked size growth after lyophilization, confirming nanoparticle destabilization (**Figure 12**) [29]. These findings are consistent with different literature references. Timothy *et al*. have reported a comparative study in which several osmoprotectants were evaluated for the lyophilization of SLNs, demonstrating that trehalose was the most effective agent in preserving the original particle size and ensuring optimal redispersibility after freeze-drying [30]. Similarly, Schwarz *et al*. also employed

trehalose at concentrations ranging from 1% to 15%, confirming its superior ability to minimize particle growth and aggregation during both freezing and drying steps [31]. Based on this evidence, trehalose was selected as the cryoprotectant of choice in the present study and was employed at concentrations of 2.5%, 5%, and 10% w/v. A clear concentration-dependent protective effect was observed, with 10% trehalose providing the most efficient stabilization. This formulation maintained SLNs' size, PDI, and morphology close to the pre-lyophilized controls. TEM imaging further corroborated these results: SLNs freeze-dried with 10% trehalose retained a spherical morphology and good dispersion, with smaller apparent dimensions compared to DLS measurements (**Figure 13**) [32]. Overall, these findings validate the cryoprotectant strategy and confirm that SLNs can be successfully converted into a dry form while preserving their original physicochemical properties suitable for subsequent encapsulation into PLGA microspheres.

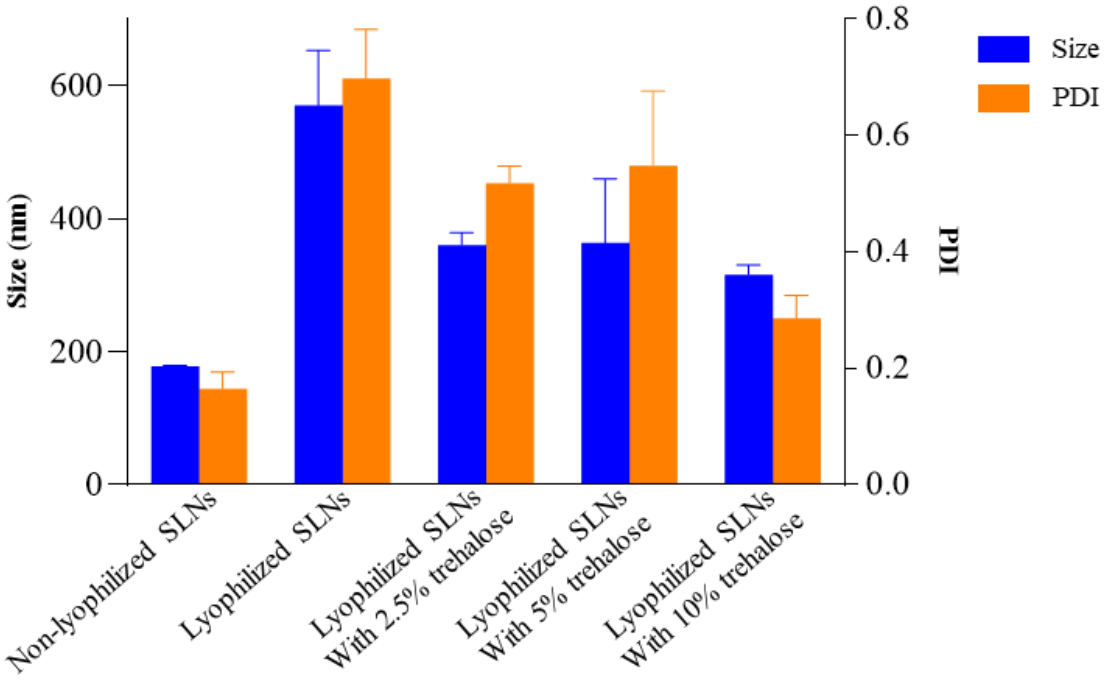


Figure 122. Size and polydispersity index of SLNs pre-, post-lyophilization, and post-lyophilization in the presence of 2.5, 5, and 10 %w/v of trehalose.

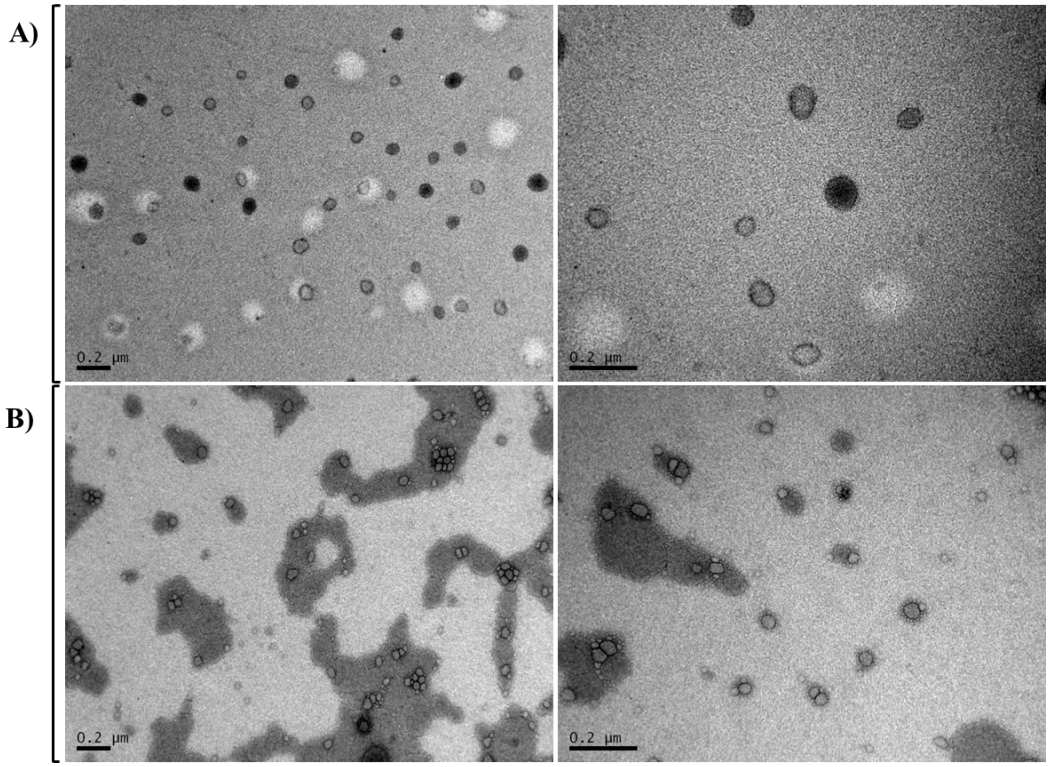


Figure 13. TEM images of **A)** blank SLN pre-lyophilization, and **B)** after lyophilization in the presence of trehalose 10% *w/v,* at magnifications of 50x (left), and 100x (right).

SLNs distribution within PLGA microspheres

Trojan MSs were prepared using the double emulsion technique, as summarized in **Figure 14.**

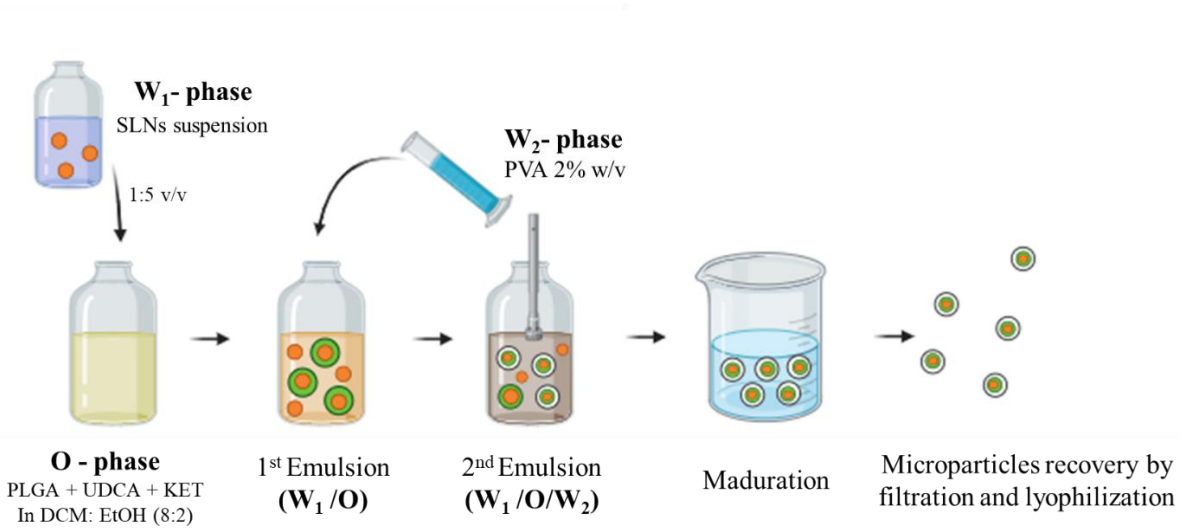


Figure 14. Schematic representation of the double emulsion technique for the preparation of Trojan MSs.

To visually demonstrate the successful internalization of SLNs into the polymeric matrix, FITC-SLNs were first encapsulated with PLGA, stained using Nile Red. The dual-fluorescence approach is a well-established imaging strategy for assessing the spatial distribution of nanoparticles within polymeric microspheres, as it enables clear discrimination between the polymer matrix and the embedded particles [33].

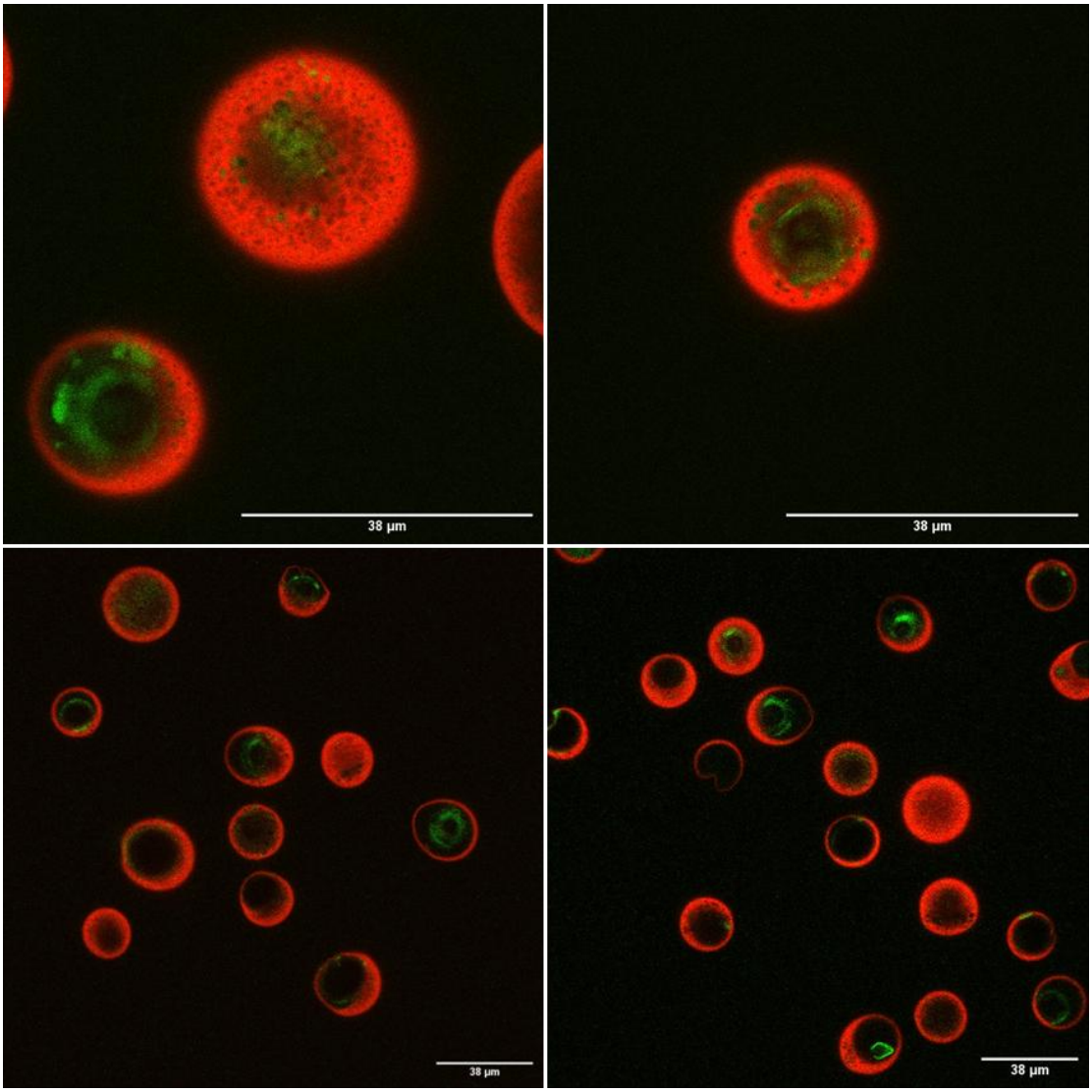


Figure 15. Confocal images of FITC SLNs Red Nile Trojan MSs.

Confocal imaging demonstrated the presence of green, fluorescent domains well distributed throughout the red matrix (**Figure 15**). These green domains clearly correspond to FITC-SLNs and were visible both near the particle core and within the intermediate concentric layers of the matrix. Through z-stack acquisition, confocal

microscopy allows the microsphere to be visualized from the exterior toward the interior [34]. Remarkably, no green fluorescence was detected in the outermost optical sections, whereas the signal progressively appeared only within deeper layers. This confirms that SLNs were not merely adsorbed or trapped on the MSs surface but were effectively incorporated within the polymeric matrix during emulsion formation. Such evidence supports the reliability of the double-emulsion method and validates the feasibility of achieving an authentic NiM configuration. The presence of internalized SLNs across multiple microspheres further demonstrates the robustness and reproducibility of the encapsulation process.

Physicochemical characterization of drug-loaded microspheres

Three batches of Trojan MSs dual drug loaded were prepared using increasing amounts of blank SLNs, nominated as TB-MSs 1, TB-MSs 2, and TB-MSs 3. SLNs were co-loaded with UDCA and KET, and the resulting Trojan systems were characterized and compared with a control MSs batch in which just the two drugs, KET and UDCA, were encapsulated into the polymer matrix, named MSs (**Table 21**). All formulations exhibited mean diameters within the 29.37-31.10 μm range, fully matching the granulometric window considered optimal for intravitreal administration and minimizing the risk of post-injection aggregation or sedimentation [35].

Table 21. Mean particle size and encapsulation efficiency data for each formulation. Data are shown as mean ± SD.

Formulation	MEAN Size (μm)	Encapsulation efficiency (EE)			
		UDCA μg X/mg MSs	KET μg X/mg MSs	UDCA (%)	KET (%)
MSs	30.80 ± 2.10	41.95 ± 1.87	51.15 ± 2.96	52.40 ± 2.34	42.60 ± 2.48
TB-MSs 1	29.37 ± 7.23	31.43 ± 3.92	32.98 ± 2.68	47.45 ± 5.94	32.90 ± 2.67
TB-MSs 2	30.48 ± 7.71	30.83 ± 0.25	25.15 ± 3.16	47.45 ± 0.39	25.83 ± 3.25
TB-MSs 3	31.10 ± 2.14	26.23 ± 1.06	38.83 ± 3.73	42.34 ± 1.72	41.70 ± 4.01

SEM analysis confirmed that all microspheres were spherical and displayed good monodispersity. However, superficial irregularities were consistently observed across formulations. Comparison with unloaded particles (**Figure 16 A1**) and single-drug microspheres revealed that KET-MSs retained a smooth and homogeneous surface (**Figure 16 A2**), whereas UDCA-MSs exhibited shallow surface marks and a slightly textured appearance (**Figure 16 A3**). This effect can be attributed to the amphiphilic nature of UDCA, which might tend to migrate toward the particle periphery during solvent extraction, locally perturbing shell formation. The use of ethanol as cosolvent in UDCA-containing formulations further influences polymer precipitation, favouring the development of these surface imprints rather than true porosity. Consequently, the irregularities seen in multi-loaded MSs can be primarily ascribed to the presence of UDCA [36]. Notably, no structural elements attributable to SLNs were detected on the microsphere surface, consistent with confocal microscopy observations indicating that SLNs were efficiently incorporated within the polymeric matrix rather than exposed on the exterior.

Huang *et al*. prepared PLGA microspheres co-loaded with rifapentine and linezolid and demonstrated that their surface morphology varied considerably depending on the physicochemical properties of the encapsulated drugs. The resulting particles displayed shallow concavities and subtle surface deformations, attributed to drug-dependent redistribution within the polymer matrix and its effects on solidification dynamics. The strong resemblance between their SEM micrographs and the superficial marks observed in our formulations supports the interpretation that these features represent normal morphological outcomes driven by drug-polymer interactions rather than structural defects [37].

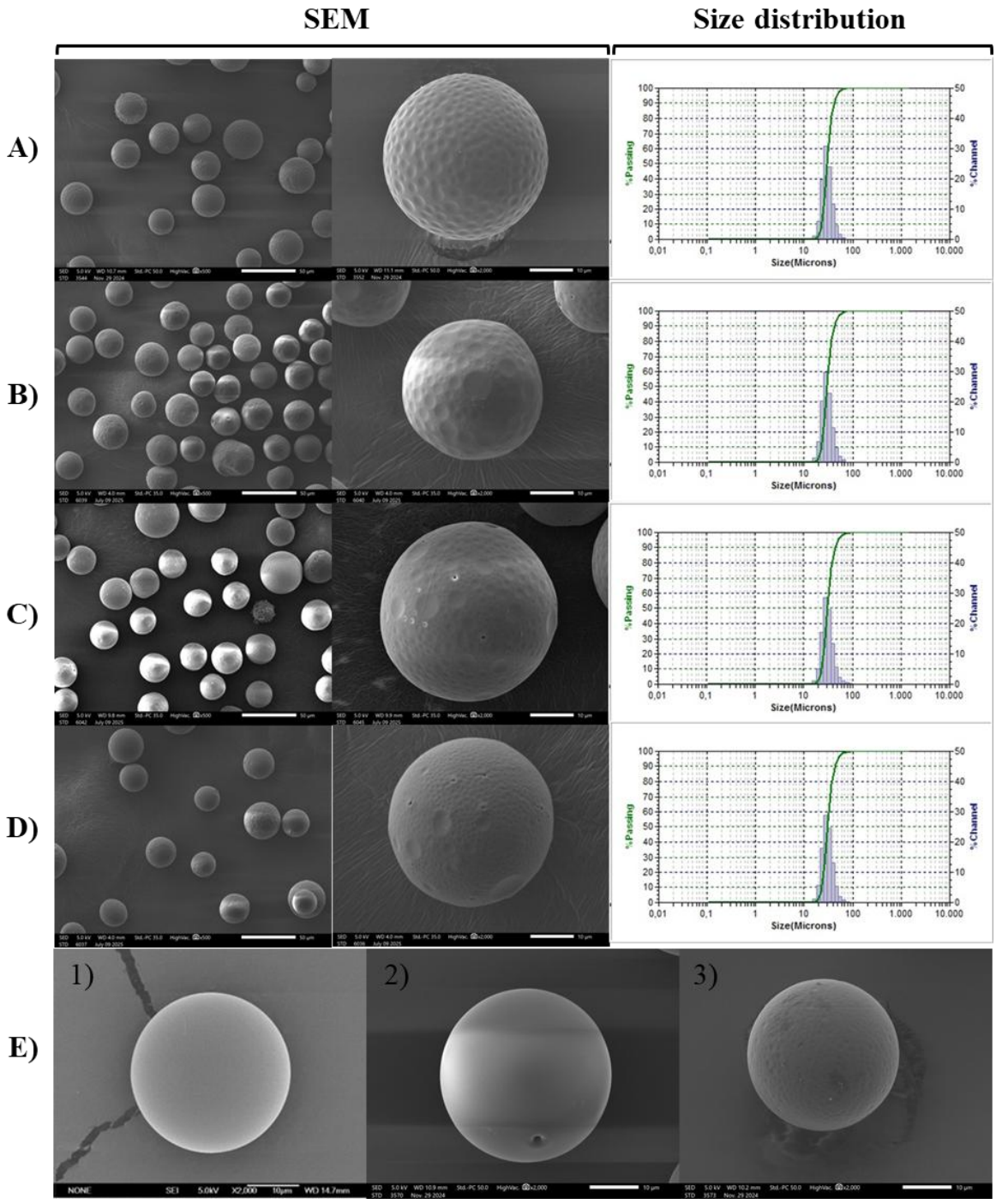


Figure 16. Size distributions and SEM images 500x and 2000x of **A)** MSs, **B)** TB-MSs 1, **C)** TB-MSs 2, **D)** TB-MSs 3. **E)** SEM images of **1)** unloaded MSs, **2)** KET-MSs, and **3)** UDCA-MSs

Encapsulation efficiency is a critical parameter for multi-loaded delivery systems, particularly when free drugs are combined with nanoscale carriers. MSs exhibited good EE% values for both drugs, approximately 42-52%, depending on the molecule, reflecting

the solubility and affinity of KET and UDCA for the PLGA matrix. This batch was prepared as a control to evaluate the impact of SLN inclusion on microsphere EE.

After SLN incorporation, a decrease in EE% was observed for both molecules. For UDCA, this reduction was limited and remained almost unchanged across the TB-MSs. In contrast, KET showed a more marked and less predictable drop, which is consistent with the behaviour of more hydrophilic drugs that tend to partition into aqueous domains during the double-emulsion process [38].

Interestingly, EE% did not further decrease in TB-MSs 3, despite this formulation containing the highest SLN amount. Because the internal aqueous phase volume was kept constant, the increased SLN loading likely made this compartment more crowded, reducing its capacity to extract additional free drug from the polymer-rich domains. Zhou *et al*. demonstrated that, in double-emulsion systems, a reduction in the viscosity of the primary emulsion (W_1/O) decreases the stability of internal droplets and promotes drug loss to the external aqueous phase, ultimately lowering EE [39]. Conversely, higher primary-emulsion viscosity enhances droplet integrity and drug retention. In TB-MSs 3, the higher SLNs content increased the effective viscosity of the W_1 compartment, potentially contributing to the internal droplets stabilization and limiting further drug partitioning, which could explain the absence of an additional decline in EE.

Furthermore, it is important to note that the SLN suspension dispersed in the internal aqueous phase contains trehalose. This detail is not trivial, as other authors such as Park *et al*. have shown that adding sucrose, a hydrophilic sugar closely related to trehalose, to the inner aqueous phase can significantly influence encapsulation efficiency by modifying the viscosity and osmotic environment of W_1, ultimately altering drug-retention behaviour in double-emulsion systems [40]. In our case, the presence of trehalose within the SLNs might have exerted a similar effect, increased the structuring and viscosity of the internal phase and reinforced the stabilizing behaviour observed in TB-MSs 3, thereby maintaining an EE comparable to that obtained with the single-emulsion system.

Release studies

Current drug delivery research aims to develop systems capable of maintaining drug concentrations within the therapeutic window for extended periods [41]. Accordingly, the goal of IODDS in retinal and intraocular diseases is to achieve long-acting injectable formulations with controlled and sustained release to the target tissue [42]. In this study, both active agents, KET and UDCA, were released in a controlled manner *in vitro* throughout the 30-day assay.

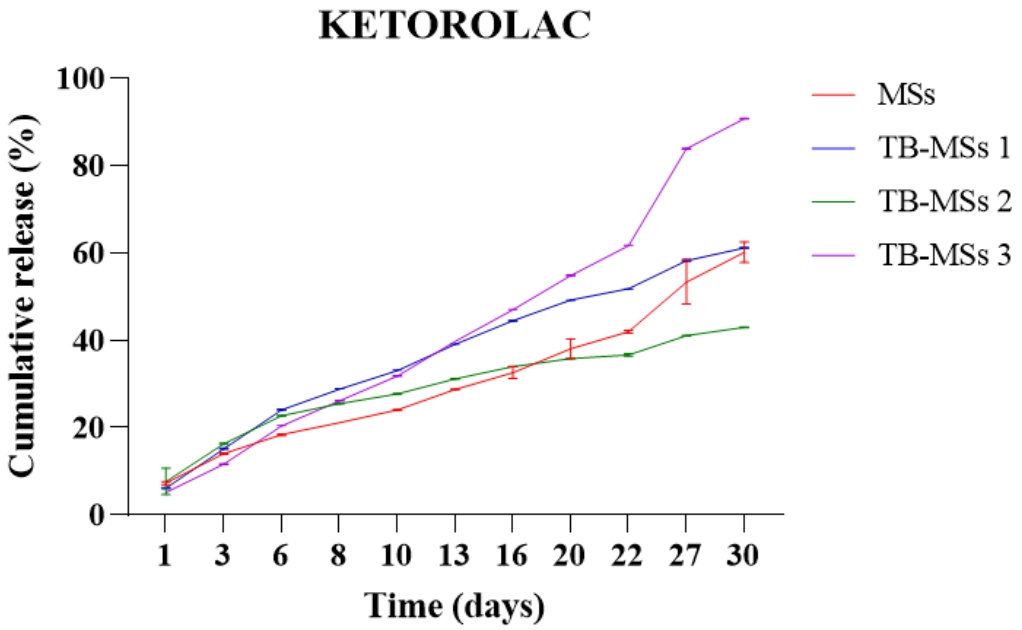


Figure 113. Drug release profiles of KET from microspheres.

Starting from KET (**Figure 17**), MSs displayed a sustained release profile, with a burst release of 7.26 ± 0.34 % and 60.17 ± 2.38 % released on day 30, corresponding to a release rate of about 1.82 %/day. Such a release profile closely resembles the study performed by González-Cela-Casamayor *et al.*, who reported that ketorolac-loaded PLGA 85:15 MSs dictate a slow, well-controlled release profile extending over four weeks [43]. This behaviour is consistent with a release mechanism governed by a combination of drug diffusion through the hydrated PLGA matrix and the progressive relaxation and erosion of the polymer chains, which are typical of PLGA systems with relatively high lactic acid content.

Among the Trojan formulations, TB-MSs 1 exhibited the slowest and least extensive release. The burst was similar to MSs (7.64 ± 3.06 %, $p = 0.85$), but the cumulative release

was significantly lower on day 30 (42.94 ± 0.08 %, $p < 0.01$), with a release rate of 1.22 %/day. The f_2 value calculated with respect to MSs (65.71) confirmed similarity.

This behaviour suggests that, in this formulation, the internal SLN-rich aqueous domains may act as additional diffusional barriers, locally hindering KET mobility and delaying its migration toward the external medium. However, since trehalose is co-introduced together with SLNs in the internal aqueous phase, it cannot be excluded that trehalose itself contributes to this effect by modifying local hydration and internal microstructure.

TB-MSs 2 presented a slightly lower burst (6.16 ± 0.09 %) and reached 61.13 ± 0.06 % on day 30, showing a release behaviour comparable to MSs at both times ($p = 0.033$; $p = 0.373$). Its f_2 value relative to MSs (55.27) and release rate (1.89 %/day) suggest borderline similarity. This intermediate behaviour could be indicative that SLN-induced hydration domains may facilitate early diffusion while having a limited impact on the PLGA-driven erosion occurring at later stages. Thus, in this formulation, the nano-in-micro architecture appears to modulate the initial accessibility of the drug without significantly perturbing the intrinsic polymer-controlled release mechanism, although a contribution of trehalose-induced porosity cannot be ruled out.

The fastest and most extensive KET release was obtained with TB-MSs 3, which reached 90.73 ± 0.07 % on day 30, releasing 2.96 %/day. Differences between MSs and controls were significant at 24 h ($p = 0.008$) and even more pronounced at day 30 ($p = 0.002$), with a very low f_2 value relative to MSs (42.27). This acceleration can be attributed to the high SLNs and trehalose content, which likely increased internal porosity and water uptake, promoting faster polymer hydration, channel formation, and, consequently, enhanced KET diffusion.

Overall, the four formulations seem to show a common KET release pattern driven mainly by the PLGA 85:15 matrix, with differences emerging from the extent of SLN and trehalose incorporation. MSs and TB-MSs 2 displayed very similar behaviour, confirming that moderate SLN loading does not markedly affect polymer-controlled erosion. TB-MSs 1 released KET more slowly, while TB-MSs 3, containing the highest amount of SLNs and trehalose, showed the fastest and most extensive release. These results support the concept that the Trojan architecture allows fine-tuning of diffusional pathways while preserving the long-acting nature of the PLGA matrix, which is a key requirement for injectable intraocular drug delivery systems. However, because trehalose is intrinsically

associated with SLNs incorporation in the present formulation, the relative contribution of the lipid nanocarrier and of the cryoprotectant to these effects cannot be discriminated at this stage.

UDCA exhibited markedly slower release than KET, reflecting its stronger affinity for the PLGA matrix and diffusion-limited behaviour in hydrophobic environments. MSs released only 0.092 ± 0.01 % on day 1 and 9.25 ± 0.96 % on day 30 (**Figure 18**).

Trojan formulations significantly increased UDCA release compared to MSs. Among them, TB-MSs 1 showed the highest burst and cumulative release (34.22 ± 0.42 % and 45.50 ± 0.01 %, respectively), with strong statistical significance at both 24 h and 30 days. TB-MSs 3 and TB-MSs 2 also exhibited higher cumulative release than MSs (28.18 ± 0.01 % and 18.61 ± 0.03 %, respectively). Comparison of the release profiles using the similarity factor f_2, calculated relative to MSs, revealed clear dissimilarity for TB-MSs 1 (20.58) and TB-MSs 3 (34.55), whereas TB-MSs 2 retained a release profile like that of MSs (65.20).

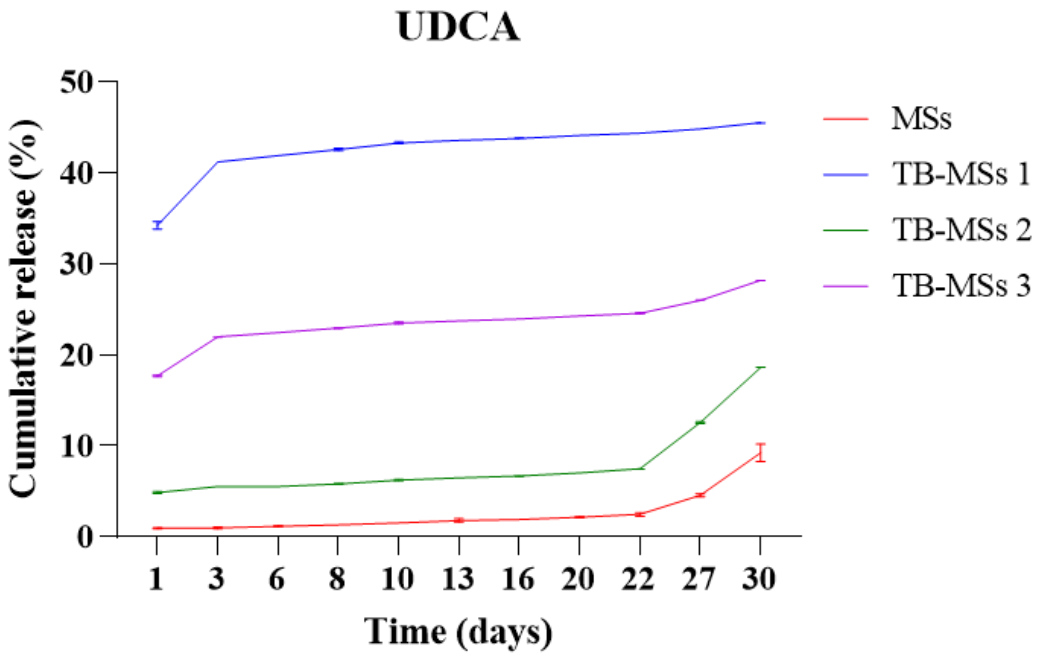


Figure 18. Drug release profiles of UDCA from microspheres.

SEM analysis suggests that UDCA tends to localize closer to the particle surface, making it particularly susceptible to early outward diffusion. In this context, the marked variability observed in the burst release among Trojan formulations is likely influenced by formulation-related factors rather than by SLN loading alone. In W/O/W systems, the

presence of trehalose in the internal aqueous phase increases osmotic pressure, promoting water influx during emulsification and solvent extraction. This process can induce early pore formation and enlarged internal cavities, thereby enhancing the initial release of surface-associated amphiphilic molecules such as UDCA [40]. Consistently, no direct proportional relationship was observed between the amount of encapsulated SLNs and the magnitude of the UDCA burst, indicating that the early release reflects a complex interplay between drug distribution, internal microstructure, and cryoprotectant-induced porosity rather than a direct effect of nanoparticle content. Therefore, the UDCA burst likely reflects a combined effect of drug localization, SLN-induced heterogeneities, and trehalose-driven porosity, rather than the presence of nanoparticles alone.

Despite these differences in the burst phase, all Trojan formulations converged toward comparable sustained release rates between days 1 and 30 (0.32-0.47 %/day), closely overlapping with that of MSs (0.32 %/day), which is particularly relevant for long-acting intraocular drug delivery, where stable drug exposure over extended periods is required. Taken together, these findings indicate that the incorporation of SLNs does not compromise the ability of PLGA 85:15 to sustain long-term drug release, a key requirement for injectable intraocular drug delivery systems, while still allowing modulation of the early release phase for molecules with distinct physicochemical properties, in agreement with previous reports on PLGA-based multi-loaded delivery systems [25, 44].

While the overall release behaviour is predominantly governed by the PLGA matrix, targeted studies in which SLN loading and cryoprotectant content are independently varied would enable a more precise understanding of their respective roles in modulating the release behaviour of the microspheres.

Considering the objective of developing a Trojan system capable of providing a delayed and well-controlled release over time, TB-MSs 2 emerged as the most suitable formulation. Notably, it exhibited release profiles for both KET and UDCA that were highly comparable to those of conventional MSs, confirming its ability to preserve the intrinsic sustained-release behaviour of PLGA 85:15 while integrating the advantages associated with SLN inclusion.

Thermal and Structural Analysis

The selected Trojan formulation, TB-MSs 2, was further characterized by performing thermal and structural analysis. In particular, DSC and XRD analyses were performed to evaluate the physical state of the components and to assess whether drug crystallinity was preserved or lost upon incorporation into microspheres [47].

In the DSC thermograms (**Figure 19**), pure UDCA and KET exhibited sharp endothermic peaks at approximately 203-207 °C and 157 °C, respectively, corresponding to their melting transitions [48, 49]. These characteristic signals were completely absent in the thermograms of the MSs and TB-MSs, confirming the good distribution of drugs within the polymer matrix and the absence of drug crystals, in accordance with the SEM images [50]. A similar conclusion can be drawn for the SLNs. When analysed alone, blank SLNs displayed a low-temperature lipid transition at around 35 °C, while SLNs lyophilized in the presence of 10% trehalose showed an additional endothermic peak at 93 °C, attributable to trehalose, in agreement with the melting event observed in the pure excipient (99 °C). Notably, none of these peaks were detectable in the thermograms of the selected microspheres, indicating that the nanocarriers were effectively embedded within the polymeric matrix, without residual crystalline trehalose or isolated SLNs. Moreover, the typical PLGA glass transition was not clearly evidenced in any microsphere formulation, suggesting that the double-emulsion technique led to the formation of a complex and fully amorphous system comprising KET, UDCA, and SLNs lyophilized with trehalose [51].

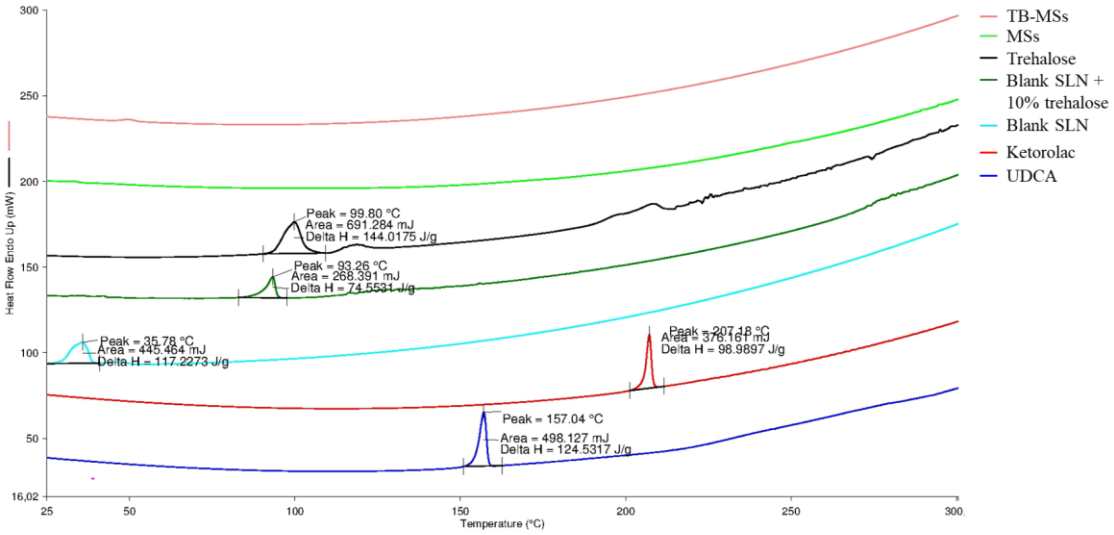


Figure 19. DSC thermograms of microspheres and loaded compounds.

XRD analysis further corroborated these findings (**Figure 20**). Pure UDCA and KET displayed numerous intense diffraction peaks, confirming their highly crystalline nature. Conversely, the diffractograms of blank SLNs, MSs, and TB-MSs 2 were characterized by broad halos with no detectable crystalline reflections attributable to the drugs. This loss of long-range molecular order demonstrates that neither UDCA nor KET recrystallized after encapsulation [52]. Together, DSC and XRD results unequivocally demonstrate that both drugs underwent complete amorphization or molecular dispersion within the SLN and PLGA matrices. The absence of crystalline domains supports the notion of homogeneous drug distribution throughout the Trojan nano-in-micro system.

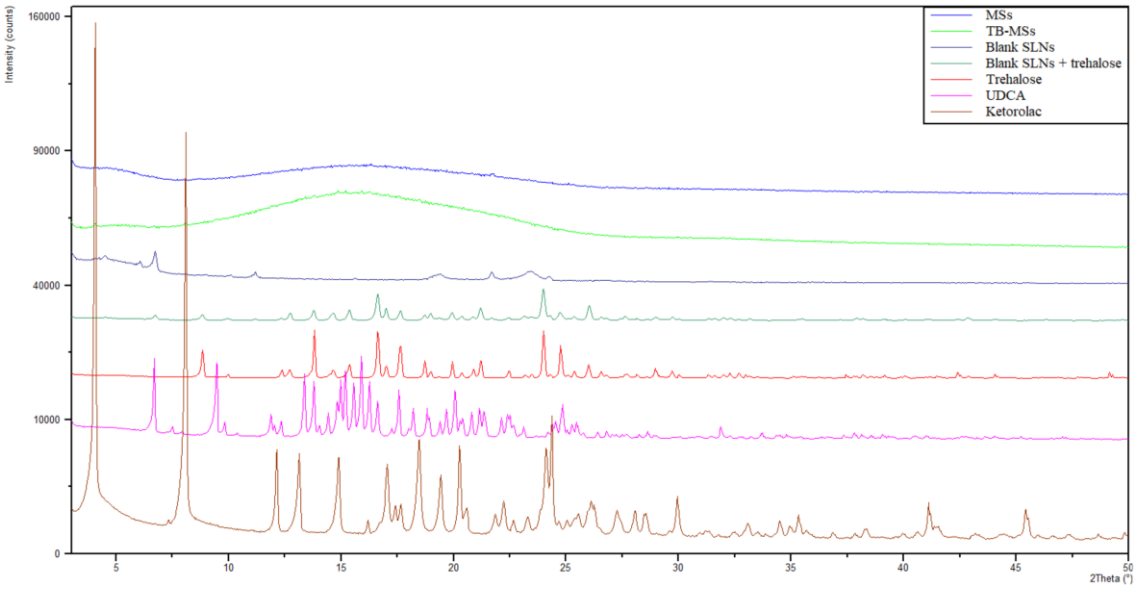


Figure 20. XRD patterns of microspheres and loaded compounds.

4.3.3. Experimental section

Materials

PLGA (85:15) polymer was obtained from Evonik Nutrition & Care GmbH (Darmstadt, Germany). Ursodeoxycholic acid (UDCA) (purity > 99%) was obtained from Alfa Aesar (Haverhill, Massachusetts, USA) and Ketorolac (KET) (purity > 98%), Stearic Acid, and Brij 78 were provided by Sigma-Aldrich (St. Louis, Mo., USA). Polyvinyl alcohol 72000 g/mol (PVA) was purchased from Panreac Química (Castellar del Vallès, Spain). D-(+)-trehalose dihydrate was purchased from Fisher Scientific (Geel, Belgium). Stearic Acid-PEG_{1000}-FITC was purchased by CD bioparticles (Shirley, New York). All organic solvents, MilliQ water, acetonitrile (ACN), dichloromethane (DCM), ethanol (EtOH), and methanol (MeOH), were HPLC-grade and used without further purification.

Microfluidic Preparation of SLNs Through Hydrodynamic Flow

SLNs were prepared using a microfluidic system (Dolomite, Royston, UK) equipped with a 5-input chip (150 μm channel width, Part No. 3200711). Lipid, surfactant, and ethanol solutions were sterile filtered through 0.2 μm filters and loaded into three pressure pumps (Part No. 3200016), designated Pump 1 (P1), Pump 2 (P2), and Pump 3 (P3). These pumps were connected to flow rate sensors with ranges of 30–1000 μL/min (P1, Part No. 3200097), 1–50 μL/min (P2, Part No. 3200098), and 0.2–5 mL/min (P3, Part No. 3200096), respectively. The fluids were conveyed from the pressure pumps to the chip using FEP tubing (OD 1.6 mm, ID 0.25 mm, Part No. 3200302). To control fluid flow through the chip, 2-way in-line valves (Part No. 3200087) were installed. T-connectors (Part No. 3000397) were integrated to join the organic and ethanol phases and to facilitate system cleaning. The chip was assembled using the H Interface 7-way (Part No. 3200297) and two Linear Connectors 7-way (Part No. 3200148) and was mounted on a Meros TCU-100 thermostat (Part No. 3200428) for temperature control.

The SLNs were prepared by nanoprecipitation using a three-inlet flow-focusing microfluidic device [22]. The SLN preparation parameters were optimized employing Design of Experiments (DoE) described previously. The aqueous phase consisted of a Brij 78 solution at a concentration of 1.4081 mg/mL, serving as the surfactant, and was delivered using Pump 1. The organic phase consisted of a stearic acid solution at 2.1286 mg/mL, acting as the solid lipid, and was delivered using Pump 2. The theoretical Flow

Rate Ratio (FRR) was set at 23.233. Once a steady flow was established, the resulting SLNs were collected into a secondary container placed in an ice bath. The formulation was then centrifuged using Amicon® Ultra centrifugal filters (30 kDa MWCO) to completely remove the organic solvent, excess surfactant, and any unencapsulated drug [23].

To prepare fluorescent-labeled SLNs (FITC-SLN), 0,06 mg/mL of SA-PEG-FITC was added to the aqueous phase before mixing. Finally, the SLN blank and FITC-SLN were freeze-dried and stored at -30°C in a dry conditions.

Lyophilization studies

Lyophilization studies were conducted by adding different concentrations of trehalose as a cryoprotectant. The SLNs formulations were diluted with trehalose solution at 2.5, 5, and 10% *w/v*, then frozen at -60 °C for 1 hour, and dried at -60 °C, 0.1 mBar for 16 hours [24]. Variations in particle size dimensions were assessed through Zetasizer analysis.

SLNs characterization

Size, ζ-Potential, and Polydispersity Index Analysis

SLNs' sizes and ζ-potential were determined at 25 °C by diluting the samples in Milli-Q® water at a ratio of 1:10. Both parameters were evaluated, respectively, in disposable transparent polystyrene cuvettes (batch 67.754, Sarstedt, Nümbrecht, Germany) and disposable folded capillary cells (DTS1070, Zetasizer Nano Series®, Malvern Panalytical Ltd, Malvern, United Kingdom) using the ZS Xplorer® software and Zetasizer Lab® (Malvern Panalytical Ltd, Malvern, United Kingdom). Material refractive index and absorption were correspondingly set at 1.35 and 0.001, whereas water refractive index, viscosity, and dielectric constant were respectively set at 1.33, 1.05, and 78.5.

Microsphere elaboration

In an initial step, the dual-loaded MSs were prepared following the Oil/Water (O/W) emulsion solvent extraction-evaporation technique. Briefly, 400 mg of PLGA and 40 mg UDCA were dissolved in 1.2 mL of a mixture of DCM: EtOH (8:2), as optimized in a previous work [25]. 60 mg of KET were incorporated into the polymeric dissolution and dispersed by ultrasonication (Ultrasons; J.P. Selecta, Barcelona, Spain) in an ice-water bath for 5 min. Next, the organic phase was emulsified by adding 5 mL of PVA MilliQ®

water solution (2% w/v) through a homogenizer (Polytron®RECO, Kinematica, GmbHT PT3000, Lucerna, Switzerland) for 1 min at 8500 rpm. The obtained emulsion was incorporated into 100 mL of PVA MilliQ® water solution (0.1% w/v), and it was stirred for 3 h to harden the MSs. Once MSs matured, they were washed and sieved, collecting the 20-38 μm granulometric fraction. Finally, MSs were freeze-dried (Freezing: -60 °C /15 min, drying: -60°C/12 h/0.1 mBar) and stored at -30 °C in dry conditions.

In the second step of the optimization process, three batches of Trojan MSs (TB-MSs 1, TB-MSs 2, TB-MSs 3) were produced by incorporating various amounts of the third component, SLN blank formulations (106.3 mg, 117.3 mg, 156.1 mg, respectively), using the Water-in-Oil-in-Water ($W_1/O/W_2$) double emulsion solvent extraction/evaporation method. The initial dissolution phase of the polymer and drugs to create the organic phase was carried out as described above. The weighed amounts of lyophilized SLNs were resuspended in 240 μL of an H_2O: propylene glycol (1:1, v/v) mixture, obtaining a homogeneous SLN suspension. This suspension was then added to the organic phase. The first (W_1/O) emulsion was formed using a vortex mixer (D-051, Dinko, Barcelona, Spain) at 1000 rpm for 1 minute. All subsequent steps followed the same procedure described above.

Microspheres physicochemical characterization

Mean particle size and particle size distribution

The mean particle size and particle size distribution of each formulation were measured by dual light scattering in a Microtrac®S3500 Series Particle Size Analyser (Montgomeryville, PA, USA) by suspending MSs in MilliQ® water. The particle size results are expressed as the mean ± standard deviation (SD) (n = 3).

Morphological evaluation by scanning electron microscopy (SEM) and transmission electron microscopy (TEM)

The external morphology of MSs was observed by scanning electron microscopy (Jeol, JSM-6335F, Tokyo, Japan). Prior to observation, freeze-dried MSs were coated with a gold sputter-coating.

The morphology of freshly prepared SLNs and lyophilized and resuspended SLNs formulations was evaluated by transmission electron microscopy (Jeol, JEM-1010). A drop of SLNs suspension was placed on a formvar carbon, 200 mesh, copper grid and

negatively stained with 2% (w/v) of uranyl acetate. Grids were viewed at an accelerating voltage of 80 kV.

Components distribution

To evaluate the SLNs' distribution through the MS matrix, a formulation was developed incorporating fluorescently labelled SLNs (FITC-SLNs) and a fluorescent stain with affinity for PLGA (Nile Red). To this, 3 μL of a Nile Red solution (4 mg/mL) was added to the organic phase, and the MSs' elaboration was carried out as explained before. These MSs were observed by confocal fluorescence microscopy (Leica TCS SP8, Wetzlar, Germany). For the preparation of samples, ProLong™ Gold antifade was placed in the center of the slides, followed by the addition of a small amount of the formulations previously prepared on top of them. The samples were then carefully covered with a glass coverslip and protected from light. Therefore, the samples were observed at 481 nm of emission wavelength and 644 nm of emission one. Unloaded Ms were submitted to the same procedure to use them as controls.

Quantification methods

UDCA quantification by LC/MS

The chromatographic system was made of a High-Performance Liquid Chromatography (Waters 1525 binary HPLC pump and Waters 2707 autosampler) coupled to a mass detector (Waters 3100 single quadrupole mass spectrometer). The quantification was performed by employing a Nova-Pak C18 column (4 μm, ID 2.1 mm × 150 mm) connected previously to a guard column (4 μm, 3.9 mm × 20 mm), both were maintained at 45 °C. The mobile phase was composed of acetonitrile/ammonium acetate in water 15 mM (2:1 v/v), adjusted to pH 5.0 with formic acid, and the flow rate was 0.15 mL/min. Electrospray ion source (ESI) operated in a negative ionization mode. The parameters were set as follows: 3 kV for spray voltage, 80 °C for the capillary temperature, and 3 V extractor voltage. Desolvation (925 L/h flow rate, 180 °C desolvation temperature) was performed employing nitrogen gas (> 99.999%).

Ketorolac quantification by HPLC

High-performance liquid chromatography coupled with ultraviolet detection (HPLC-UV) was employed to quantify the KET in the formulations produced. The apparatus used to

perform the analyses was a Waters® Acquity Arc Bio UHPLC device (Waters, Madrid, Spain) paired with a Waters® Photodiode Array 2998 detector; samples were analysed with the HPLC line of the instrument. The Empower 3® software was used to collect and process the chromatographic results.

For the quantification of KET, analyses were based on a pre-existing method employing an Ascentis® C18 HPLC Column (25 cm × 4.6 mm, 5 µm) (Supelco®, Sigma-Aldrich, Madrid, Spain) as the stationary phase. The reversed-phase HPLC column was kept at 45.0 ± 0.2 °C throughout the analysis. The injection volume was 10 µL, and the flow rate was set at 1 mL/min. The composition of the mobile phase was MeOH + 0.1% v/v TFA in Milli Q® water (60:40% v/v). The isocratic elution was examined for 8.00 min, and KET was detected at 313.5 nm. Several standard dilutions were prepared from a 5 mg/mL KET stock solution in MeOH (10, 25, 40, 50, 60, µg/mL) to calculate the regression line.

Encapsulation efficiency (%)

For UDCA quantification, 1 mg of MSs or TB-MSs was dissolved in 2.5 mL of methylene chloride. UDCA was extracted with 6 mL of ethanol, which also promotes polymer precipitation. Then, the so-treated samples were vortex mixed and centrifuged to separate the polymer (5000 rpm, 5 min, 20 °C) and filtered through a 0.22 µm pore size nylon filter (JNY022013N, Filter-lab®, Barcelona, Spain). The supernatant was filtered and analysed in LC/MS as described before for UDCA quantification. Each batch was quantified in duplicate.

For KET quantification, 5 mg of MSs or TB-MSs, 1 ml of DCM was added and vortex-mixed for 30 seconds to dissolve the PLGA. Subsequently, 10 ml MeOH was added, and then mixed for 1 minute to precipitate the PLGA. The resulting solution of the active compounds in the DCM: MeOH mixture was centrifuged at 5000 rpm for 10 minutes and filtered through a 0.22 µm pore size nylon filter (JNY022013N, Filter-lab®, Barcelona, Spain). Finally, the samples were quantified by HPLC.

The EE(%) of the drugs were calculated individually as the ratio of the actual amount of drug per weight of Mss to the total weight of drug added during the processing of the microspheres, as reported in **Equation 5:**

$$EE(\%) = \frac{\frac{mg\ Drug}{mg\ MSs\ weighted}}{\frac{mg\ Drug\ added}{mg\ Drug\ added + mg\ PLGA\ added}}\ x\ 100 \qquad \textbf{(5)}$$

***In vitro* release studies**

Triplicate samples of 5 mg MSs, TB-MSs 1, TB-MSs 2, TB-MSs 3, were suspended in 2 mL of phosphate-buffered saline (PBS, pH 7.4, isotonized with NaCl). The samples were kept at 37 °C under constant agitation in a water shaker bath (WNB Memmert Shaking Bath, Memmert, Schwabach, Germany). At pre-set times (24 h, 3, 6, 8, 10, 13, 16, 20, 22, 27, 30 days), the MSs were gently centrifuged (5000 rpm, 5 min, 20 °C). The supernatants were recovered, filtered (0.22 μm), and replaced with 2 mL of fresh PBS to continue with the release study. The UDCA and KET concentrations of the aforementioned filtered supernatants were analysed by LC/MS and HPLC as described previously.

To compare the release profiles, we use the similarity factor (f_2), as reported in **Equation 6**. This equation is a logarithmic transformation of the sum-squared error of differences between the reference (Rt) and the test (Tt) formulations over all time points:

$$f_2 = 50\ log\left[\frac{100}{\sqrt{1+\frac{\sum_{t-t}^{t-n}[R(t)-T(t)]^2}{n}}}\right] \qquad \textbf{(6)}$$

Where n is the number of experimental points, t is the time points, and Rt and Tt are the mean percentages of the dissolved drugs in the reference and test formulations, respectively. Using f_2, it can be established that the difference between the two release profiles is lower than 10% when values are between 50 and 100.

Differential Scanning Calorimetry (DSC)

Thermal analysis of raw materials and the prepared SLNs and MSs formulation was made by a differential scanning calorimeter (DSC, Diamond-Perkin Elmer). Between 5–10 mg samples were employed, and an empty aluminum pan was used as a reference standard. The samples were placed in the DSC furnace, and thermograms were recorded by subjecting the sample to a thermal program using a heating rate of 10 °C/min in the temperature range of 25 to 300 °C under nitrogen purge gas maintained at a flow rate of 20 mL/min.

X-Ray diffractometry analysis

MSs and the compound's crystalline structure were assessed by an X-ray diffractometer (Philips X'Pert, USA). The angular range employed was from 5.0° to 50.0° (2θ) with a step size of 0.033° and a scan rate of 100.0 s/step.

Statistical Analysis

Results were expressed as mean values ± standard deviation (SD) of at least three replicates. Values of $p < 0.05$ were considered statistically significant, and values of $p < 0.01$ were considered highly significant. Statistical analysis was performed using Student's t-test. Minitab 19 (19.1.0.1, Minitab, LLC, State College, PA, USA) and GraphPad (Prism 8.0.0 Software; GraphPad Software Inc., San Diego, CA, USA) software were used for statistical determinations.

4.3.4. Conclusions and future perspectives

This study demonstrates the feasibility of engineering a PLGA-based nano-in-micro system incorporating SLNs within dual-drug microspheres, establishing a robust platform capable of integrating multiple therapeutic functions within a single injectable depot. The successful dispersion of SLNs inside the polymeric matrix, together with the preservation of microsphere integrity and long-acting release behaviour, confirms the suitability of this architecture for intraocular delivery in chronic diseases.

Beyond its current configuration, this system offers significant opportunities for future development. SLNs could be exploited not only as structural modulators but also as active nanoacarriers enabling the incorporation of additional drugs, biologics, or sensitive neuroprotective agents requiring enhanced stabilization. Such hierarchical loading would allow spatial and temporal control over multi-phase release, opening the way to true multitarget therapies capable of simultaneously addressing inflammation, oxidative stress, and neurodegeneration.

Overall, the nano-in-micro approach represents a versatile and evolvable platform for long-acting ophthalmic drug delivery and holds strong potential for translation into next-generation treatments for glaucoma and other retinal disorders.

References

1. Meier-Gibbons, F., M. Töteberg-Harms, Influence of Cost of Care and Adherence in Glaucoma Management: An Update. *J Ophthalmol*, **2020**. 2020: p. 5901537.
2. Kass, M.A., D.K. Heuer, E.J. Higginbotham, C.A. Johnson, J.L. Keltner, J.P. Miller, R.K. Parrish, 2nd, M.R. Wilson, M.O. Gordon, The Ocular Hypertension Treatment Study: a randomized trial determines that topical ocular hypotensive medication delays or prevents the onset of primary open-angle glaucoma. *Arch Ophthalmol*, **2002**. 120(6): p. 701-13; discussion 829-30.
3. Matlach, J., S. Bender, J. König, H. Binder, N. Pfeiffer, E.M. Hoffmann, Investigation of intraocular pressure fluctuation as a risk factor of glaucoma progression. *Clin Ophthalmol*, **2019**. 13: p. 9-16.
4. Lee, H.P., T.H. Tsung, Y.C. Tsai, Y.H. Chen, D.W. Lu, Glaucoma: Current and New Therapeutic Approaches. *Biomedicines*, **2024**. 12(9).
5. Salkar, A., R.V. Wall, D. Basavarajappa, N. Chitranshi, G.E. Parilla, M. Mirzaei, P. Yan, S. Graham, Y. You, Glial Cell Activation and Immune Responses in Glaucoma: A Systematic Review of Human Postmortem Studies of the Retina and Optic Nerve. *Aging Dis*, **2024**. 15(5): p. 2069-2083.
6. Tezel, G., Oxidative stress in glaucomatous neurodegeneration: mechanisms and consequences. *Progress in retinal and eye research*, **2006**. 25(5): p. 490-513.
7. Chrysostomou, V., F. Rezania, I.A. Trounce, J.G. Crowston, Oxidative stress and mitochondrial dysfunction in glaucoma. *Current opinion in pharmacology*, **2013**. 13(1): p. 12-15.
8. Zhang, Z.-Q., Z. Xie, S.-Y. Chen, X. Zhang, Mitochondrial dysfunction in glaucomatous degeneration. *International Journal of Ophthalmology*, **2023**. 16(5): p. 811.
9. Akhter, M.H., I. Ahmad, M.Y. Alshahrani, A.I. Al-Harbi, H. Khalilullah, O. Afzal, A.S.A. Altamimi, S.N.M. Najib Ullah, A. Ojha, S. Karim, Drug Delivery Challenges and Current Progress in Nanocarrier-Based Ocular Therapeutic System. *Gels*, **2022**. 8(2).
10. Actis, A.G., T. Rolle, Ocular surface alterations and topical antiglaucomatous therapy: a review. *Open Ophthalmol J*, **2014**. 8: p. 67-72.
11. Lin, B., P. Shi, D. Li, Intravitreal drug injection for glaucoma: mechanisms, clinical efficacy, and future horizons. *Frontiers in Pharmacology*, **2025**. 16: p. 1660401.
12. Bravo-Osuna, I., V. Andrés-Guerrero, A. Arranz-Romera, S. Esteban-Pérez, I.T. Molina-Martínez, R. Herrero-Vanrell, Microspheres as intraocular therapeutic tools in chronic diseases of the optic nerve and retina. *Adv Drug Deliv Rev*, **2018**. 126: p. 127-144.

13. Andres-Guerrero, V., I. Bravo-Osuna, P. Pastoriza, I.T. Molina-Martinez, R. Herrero-Vanrell, Novel technologies for the delivery of ocular therapeutics in glaucoma. *Journal of Drug Delivery Science and Technology*, **2017**. 42: p. 181-192.
14. De Hoz, R., B. Rojas, A. Ramírez, J. Salazar, B. Gallego, A. Triviño, V. Andrés-Guerrero, R. Herrero-Vanrell, G. Mihov, A. Dias, Assessment of polyesteramide of PEA Microparticles for in vivo intraocular injections. *Acta Ophthalmologica*, **2013**. 91.
15. García-Caballero, C., B. Lieppman, A. Arranz-Romera, I.T. Molina-Martínez, I. Bravo-Osuna, M. Young, P. Baranov, R. Herrero-Vanrell, Photoreceptor preservation induced by intravitreal controlled delivery of GDNF and GDNF/melatonin in rhodopsin knockout mice. *Molecular vision*, **2018**. 24: p. 733.
16. Anton, N., A. Jakhmola, T.F. Vandamme, Trojan microparticles for drug delivery. *Pharmaceutics*, **2012**. 4(1): p. 1-25.
17. Carvalho, S.G., A.M. Dos Santos, A.L. Polli Silvestre, A.G. Tavares, M. Chorilli, M.P. Daflon Gremião, Multifunctional systems based on nano-in-microparticles as strategies for drug delivery: advances, challenges, and future perspectives. *Expert Opinion on Drug Delivery*, **2023**. 20(9): p. 1231-1249.
18. Spessot, E., X. Bai, D. Moranduzzo, C. Zhao, S. Butterworth, D. Maniglio, A. Tirella, Exploiting nano-in-micro-technologies to couple PLGA-hydroxyl-FK866 nanoparticles to a hydrogel network for local drug release. *RSC Pharmaceutics*, **2025**.
19. Esteban-Pérez, S., I. Bravo-Osuna, V. Andrés-Guerrero, I.T. Molina-Martínez, R. Herrero-Vanrell, Trojan Microparticles Potential for Ophthalmic Drug Delivery. *Curr Med Chem*, **2020**. 27(4): p. 570-582.
20. Shaila, B., B. Vaishnavi, N.Y. Jadhav, A review of ketorolac as a potential therapeutic agent. *World J Pharm Res*, **2023**. 13(1): p. 539-560.
21. Ikegami, T., Y. Matsuzaki, Ursodeoxycholic acid: mechanism of action and novel clinical applications. *Hepatology Research*, **2008**. 38(2): p. 123-131.
22. Truong, N., S.K. Black, J. Shaw, B.L. Scotland, R.M. Pearson, Microfluidic-Generated Immunomodulatory Nanoparticles and Formulation-Dependent Effects on Lipopolysaccharide-Induced Macrophage Inflammation. *Aaps j*, **2021**. 24(1): p. 6.
23. Arduino, I., Z. Liu, A. Rahikkala, P. Figueiredo, A. Correia, A. Cutrignelli, N. Denora, H.A. Santos, Preparation of cetyl palmitate-based PEGylated solid lipid nanoparticles by microfluidic technique. *Acta Biomater*, **2021**. 121: p. 566-578.
24. Schwarz, C., W. Mehnert, Freeze-drying of drug-free and drug-loaded solid lipid nanoparticles (SLN). *Int J Pharm*, **1997**. 157(2): p. 171-179.

25. Aragón-Navas, A., M.J. Rodrigo, I. Munuera, D. García-Herranz, M. Subías, P. Villacampa, J. García-Feijoo, L. Pablo, E. Garcia-Martin, R. Herrero-Vanrell, I. Bravo-Osuna, Multi-loaded PLGA microspheres as neuroretinal therapy in a chronic glaucoma animal model. *Drug Deliv Transl Res*, **2025**. 15(5): p. 1660-1684.
26. Costa, P., J.M.S. Lobo, Modeling and comparison of dissolution profiles. *European journal of pharmaceutical sciences*, **2001**. 13(2): p. 123-133.
27. Cao, F., Y. Li, J. Wu, W. Liu, T. Ngai, Measurements of interactions between fluorescent molecules and polyethylene glycol self-assembled monolayers. *Soft Matter*, **2022**. 18(1): p. 236-243.
28. Abdelwahed, W., G. Degobert, S. Stainmesse, H. Fessi, Freeze-drying of nanoparticles: formulation, process and storage considerations. *Advanced drug delivery reviews*, **2006**. 58(15): p. 1688-1713.
29. Bustos Araya, M.E., A.N. Ricart, A.C. Calpena Campmany, R. Prohens, M. Miñarro Carmona, Development and Characterization of Lyophilized Chondroitin Sulfate-Loaded Solid Lipid Nanoparticles: Encapsulation Efficiency and Stability. *Pharmaceutics*, **2025**. 17(1).
30. Amis, T.M., J. Renukuntla, P.K. Bolla, B.A. Clark, Selection of cryoprotectant in lyophilization of progesterone-loaded stearic acid solid lipid nanoparticles. *Pharmaceutics*, **2020**. 12(9): p. 892.
31. Schwarz, C., W. Mehnert, Freeze-drying of drug-free and drug-loaded solid lipid nanoparticles (SLN). *International journal of pharmaceutics*, **1997**. 157(2): p. 171-179.
32. Akbaba, H., D.D. Dora, A.G. KANTARCI, The effects of lyophilization and cryoprotectants on solid lipid nanoparticle-DNA systems. *Romanian Biotechnological Letters*, **2017**. 22(6): p. 13186.
33. Liu, Z., W. Ye, J. Zheng, Q. Wang, G. Ma, H. Liu, X. Wang, Hierarchically electrospraying a PLGA@ chitosan sphere-in-sphere composite microsphere for multi-drug-controlled release. *Regenerative Biomaterials*, **2020**. 7(4): p. 381-390.
34. Elliott, A.D., Confocal Microscopy: Principles and Modern Practices. *Curr Protoc Cytom*, **2020**. 92(1): p. e68.
35. Herrero-Vanrell, R., M.F. Refojo, Biodegradable microspheres for vitreoretinal drug delivery. *Adv Drug Deliv Rev*, **2001**. 52(1): p. 5-16.
36. Arranz-Romera, A., B.M. Davis, I. Bravo-Osuna, S. Esteban-Pérez, I.T. Molina-Martínez, E. Shamsher, N. Ravindran, L. Guo, M.F. Cordeiro, R. Herrero-Vanrell, Simultaneous co-

delivery of neuroprotective drugs from multi-loaded PLGA microspheres for the treatment of glaucoma. *Journal of Controlled Release*, **2019**. 297: p. 26-38.

37. Huang, J., Z. Chen, Y. Li, L. Li, G. Zhang, Rifapentine-linezolid-loaded PLGA microspheres for interventional therapy of cavitary pulmonary tuberculosis: preparation and in vitro characterization. *Drug Design, Development and Therapy*, **2017**: p. 585-592.
38. Zhang, C., R. Zhang, L. Liu, M. Yang, Designing long-acting injectable formulations using PLGA via spray-drying. *International Journal of Pharmaceutics*, **2025**: p. 126083.
39. Zhou, J., R. Schutzman, N.-Q. Shi, R. Ackermann, K. Olsen, Y. Wang, S.P. Schwendeman, Influence of encapsulation variables on formation of leuprolide-loaded PLGA microspheres. *Journal of Colloid and Interface Science*, **2023**. 636: p. 401-412.
40. Park, H., D.-H. Ha, E.-S. Ha, J.-S. Kim, M.-S. Kim, S.-J. Hwang, Effect of Stabilizers on Encapsulation Efficiency and Release Behaviour of Exenatide-Loaded PLGA Microsphere Prepared by the W/O/W Solvent Evaporation Method. *Pharmaceutics*, **2019**. 11(12): p. 627.
41. Park, K., Controlled drug delivery systems: past forward and future back. *Journal of Controlled Release*, **2014**. 190: p. 3-8.
42. Herrero-Vanrell, R., I. Bravo-Osuna, V. Andrés-Guerrero, M. Vicario-de-la-Torre, I.T. Molina-Martínez, The potential of using biodegradable microspheres in retinal diseases and other intraocular pathologies. *Progress in retinal and eye research*, **2014**. 42: p. 27-43.
43. Ana González-Cela-Casamayor, M., M.J. Rodrigo, M. Brugnera, I. Munuera, T. Martínez-Rincón, C. Prats-Lluís, P. Villacampa, J. García-Feijoo, L.E. Pablo, I. Bravo-Osuna, E. Garcia-Martin, R. Herrero-Vanrell, Ketorolac, melatonin and latanoprost tri-loaded PLGA microspheres for neuroprotection in glaucoma. *Drug Deliv*, **2025**. 32(1): p. 2484277.
44. Arranz-Romera, A., S. Esteban-Pérez, I.T. Molina-Martínez, I. Bravo-Osuna, R. Herrero-Vanrell, Co-delivery of glial cell-derived neurotrophic factor (GDNF) and tauroursodeoxycholic acid (TUDCA) from PLGA microspheres: potential combination therapy for retinal diseases. *Drug Deliv Transl Res*, **2021**. 11(2): p. 566-580.
45. Korsmeyer, R.W., R. Gurny, E. Doelker, P. Buri, N.A. Peppas, Mechanisms of solute release from porous hydrophilic polymers. *International journal of pharmaceutics*, **1983**. 15(1): p. 25-35.
46. Higuchi, T., Mechanism of sustained-action medication. Theoretical analysis of the rate of release of solid drugs dispersed in solid matrices. *J Pharm Sci*, **1963**. 52: p. 1145-9.
47. Zhang, Z., X. Wang, B. Li, Y. Hou, Z. Cai, J. Yang, Y. Li, Paclitaxel-loaded PLGA microspheres with a novel morphology to facilitate drug delivery and antitumor efficiency. *RSC advances*, **2018**. 8(6): p. 3274-3285.

48. Yonemochi, E., Y. Ueno, T. Ohmae, T. Oguchi, S.-i. Nakajima, K. Yamamoto, Evaluation of amorphous ursodeoxycholic acid by thermal methods. *Pharmaceutical research*, **1997**. 14(6): p. 798-803.
49. Sohn, Y.-T., H.O. Seo, Crystal forms of ketorolac. *Archives of pharmacal research*, **2004**. 27(3): p. 357-360.
50. Yang, F., D. Chen, Z.-f. Guo, Y.-m. Zhang, Y. Liu, S. Askin, D.Q. Craig, M. Zhao, The application of novel nano-thermal and imaging techniques for monitoring drug microstructure and distribution within PLGA microspheres. *International Journal of Pharmaceutics*, **2017**. 522(1-2): p. 34-49.
51. Yang, C., D. Plackett, D. Needham, H.M. Burt, PLGA and PHBV microsphere formulations and solid-state characterization: possible implications for local delivery of fusidic acid for the treatment and prevention of orthopaedic infections. *Pharmaceutical research*, **2009**. 26(7): p. 1644-1656.
52. Masaeli, R., S.J.K. T, R. Dinarvand, M. Tahriri, V. Rakhshan, M. Esfandyari-Manesh, Preparation, Characterization and Evaluation of Drug Release Properties of Simvastatin-loaded PLGA Microspheres. *Iran J Pharm Res*, **2016**. 15(Suppl): p. 205-211.

Conclusions

This thesis focused on the experimental development and technological advancement of SLNs, with particular attention to formulation versatility and advanced manufacturing strategies. The experimental work presented in **Chapter 3** demonstrated the flexibility of SLNs as nanocarriers for a broad range of bioactive compounds. SLNs were successfully developed to encapsulate natural extracts and poorly soluble molecules, achieving homogeneous formulations with good colloidal stability and high encapsulation efficiency. Moreover, formulation strategies oriented toward brain targeting highlighted the potential of SLNs for the selective treatment of CNS disorders, supporting their relevance in addressing complex therapeutic challenges.

- In *Chapter 3.1*, we demonstrated that **CPS-ext SLNs** are an effective delivery system, providing controlled release and significant neuroprotective activity by reducing ROS levels induced by H_2O_2. PAMPA-BBB results indicated their potential to cross the BBB, supporting further *in vivo* investigation for Parkinson's disease therapy.
- In *Chapter 3.2*, we demonstrated that SLNs effectively address the main limitations of PEE by improving stability, permeability, and controlling the delivery of propolis polyphenols and flavonoids. The optimized **PEE-SLN10** ensured robust encapsulation and enhanced resistance to physiological and thermal stress, supporting its potential for *H. pylori* treatment and warranting further mechanistic and *in vivo* investigations.
- In *Chapter 3.3*, we developed that leptin-derived peptide functionalized, PEGylated SLNs (**ELM-Lep(70-89)**), proposing a promising strategy for active brain targeting, combining stealth properties with receptor-mediated transport potential. This platform lays the groundwork for the delivery of neuroactive compounds across the BBB and supports further *in vitro* and *in vivo* evaluation for neurodegenerative disease therapy.

Building on the formulation and biological innovations discussed in Chapter 3, **Chapter 4** introduces an additional technological advance by translating SLNs production to microfluidic technology. By employing widely used lipid and surfactant components, this approach enabled the achievement of multiple formulation goals.

- In *Chapter 4.1*, we demonstrated that microfluidic technology enables the reproducible production of SLNs using pharmaceutically established lipids and

surfactants, with precise control over particle size and polydispersity. Systematic parameter screening identified FRR, surfactant concentration, chip geometry, and lipid composition as key levers for process optimization, supporting the scalability and translational potential of microfluidic SLN manufacturing.

- In *Chapter 4.2*, the microfluidic hydrodynamic flow focusing combined with an RSM approach led to a rapid, robust, and scalable optimization of SLNs. Then, a multi-strategy artificial tear based on SLNs dispersed in hyaluronic acid and enriched with osmoprotectants (**HA-SLNs**) was developed for DED treatment. The resulting HA-SLNs showed excellent physicochemical properties for ophthalmic application and *in vitro* biocompatibility. A deep investigation of *in vivo* ocular long-term tolerance evidenced their good tolerability and potential for long-term DED treatment.
- In *Chapter 4.3*, we developed Trojan microspheres as a multiscale delivery system combining the advantages of SLNs and polymeric microspheres. **TB-MSs** successfully co-encapsulated SLNs, KET, and UDCA with high encapsulation efficiency, preserved structural integrity, and enabled sustained drug release for up to 30 days. Release studies confirmed that SLNs incorporation modulates release kinetics, supporting the potential of this platform for multitarget therapy in chronic retinal diseases.

This thesis represents an evolutionary technological pathway centered on SLNs, with a strong application-driven focus. The work progresses from the formulation of SLNs for the delivery of natural bioactive compounds, to surface functionalization strategies enabling active targeting, followed by the implementation of microfluidic manufacturing for enhanced process control and scalability, and finally to the development of multilevel delivery architectures such as Trojan systems. Together, these results demonstrate how SLNs can be systematically engineered across multiple technological layers, supporting their translation into robust, controllable, and application-oriented nanomedicines.

Curriculum Vitae

CURRENT POSITION:

PhD student in Biomolecular and Pharmaceutical Sciences, XVIII Cycle, University "G. d'Annunzio", Chieti-Pescara, November 2022-November 2025.

EDUCATION:

- **Visiting PhD student,** University Complutense, Madrid, Spain, from the 10th of September 2024 to the 11th of July 2025.
- **Pharmacist Professional Qualification**, University "G. d'Annunzio", Chieti-Pescara, November 2022.
- **Master's Degree in Pharmaceutical Chemistry and Technology (LM-13)**, University "G. d'Annunzio", Chieti-Pescara, Italy. (Graduation grade: 110/110 with honors). Experimental thesis's title: "Preparation and characterization of calcium phosphate nanoparticles", 22 July 2022.
- **High School Diploma,** Liceo Scientifico, opzione Scienze Applicate "Luigi di Savoia", Chieti (CH), Italy (grade: 88/100), 2017.

LIST OF PUBLICATIONS:

1. Balaha M., De Filippis B., Rapino M., Kazimierczak P., Przekora A., Esmail T., **Toto E.C.,** Petrucci G., Canal C., Cataldi A., Di Giacomo V., *CAPE Derivatives as Potent Agents for Induction of Osteogenic Differentiation in DPSCs and Biomaterial Development* (**2025**) Biomedicines, 13(12), 3039. DOI: 10.3390/biomedicines13123039
2. Dimmito M. P., Marinelli L., **Toto E.C.**, Di Biase G., Cacciatore I., Toto P., Ciulla M., Monti B., Santoleri F., Costantini A., Di Stefano A., *A Methodological Proposal for Health Technology Assessments: A Case Study on Biosimilar Drugs* (**2025**) Journal of Market Access & Health Policy, *13*(2), 12. DOI: 10.3390/jmahp13020012
3. Di Rienzo A., Marinelli L., Dimmito M.P., **Toto E.C.,** Di Stefano A., Cacciatore I. *Advancements in Inflammatory Bowel Disease Management: From Traditional Treatments to Monoclonal Antibodies and Future Drug Delivery Systems* (**2024**) Pharmaceutics. 16(9):1185. DOI: 10.3390/pharmaceutics16091185.
4. Dimmito M.P., Marinelli L., Cacciatore I., **Toto E.C**, Albertini B., Fontana A., Pilato S., Reale M., Costantini E., Pesce C., Di Stefano A., Caliceti P. *From self-Assembly to healing: Engineering ultra-Small peptides into supramolecular hydrogels for controlled drug release* (**2024**) International Journal of Pharmaceutics, Volume 663, 124562, DOI: 10.1016/j.ijpharm.2024.124562.
5. Marinelli L., Dimmito M.P., Cacciatore I., **Toto E.C**., Di Rienzo A., Palmerio F., Puca V., Di Filippo E.S., Fulle S., Di Stefano A. *Solid lipid nanoparticles for*

efficient delivery of capsaicin-rich extract: Potential neuroprotective effects in Parkinson's disease (**2024**) Journal of Drug Delivery Science and Technology, 91, art. no. 105097. DOI: 10.1016/j.jddst.2023.105097.

SUBMITTED MANUSCRIPT:

Dimmito M.P., Puca V., Di Stefano A., **Toto E.C**., Corfiati G., Appignani M., Grande R., Marinacci B., Gallorini M., Santolo F., Robuffo I., Cacciatore I., Marinelli L., *Propolis-Loaded Solid Lipid Nanoparticles Targeting Pathogens Associated with Gastrointestinal Diseases*. Submitted to the Journal of Functional Foods.

POSTER PRESENTATIONS AT SCIENTIFIC CONFERENCES IN ITALY OR ABROAD

- Cabeza-Vàzquez C., **Toto E.C**., Morilla-Lomeña C., Brugnera M., Di Stefano A., Andrés-Guerrero V., Vicario-de-la-Torre M., Bravo-Osuna I., Herrero-Vanrell R., *Solvent removal and Lyophilization Strategies to optimize Solid Lipid Nanoparticles with Microfluidics*, SPLC CRS Chapter, Albacete, Spain, 14-16 January 2026.
- **Toto E.C.,** Brugnera M., Marinelli L., M.P. Dimmito, Cacciatore I., Di Stefano A., Bravo-Osuna I., Herrero-Vanrell R., *Optimization of Solid Lipid Nanoparticles Manufacturing through Microfluidic technique.* 23rd International Symposium on Microencapsulation, Ferrara, Italy, 10-12 September 2025.
- **Toto E.C.,** Brugnera M., Di Stefano A., Bravo-Osuna I., Herrero-Vanrell R., *Solid Lipid Nanoparticles Enriched with the Osmoprotectant Taurine for Enhanced Glaucoma Therapy. Preliminary studies.* IX International Congress of Research in Retina and Vision, Alcalà de Henares/Madrid, 13-14 June 2025.
- Dimmito M.P., Marinelli L., Cacciatore I., **Toto E.C.,** Corfiati G., Appignani M., Belfiglio V., Baccari G., Di Stefano, A., *Chitosan nanoparticles for the delivery of terpenoid prodrugs in inflammatory bowel diseases (IBD).* CRS Italy Workshop, Bari, Italy, 15-17 May 2025.
- **Toto E.C.,** Marinelli L., M.P. Dimmito, I. Cacciatore, S. Pilato, M. Ciulla, Bravo-Osuna I., Herrero-Vanrell R., Di Stefano A. *Surface modification of solid lipid nanoparticles with peptide fragments for the brain delivery.* XVII Congreso SEFIG, Santa Cruz de Tenerife, Spain, 22-24 January 2025.
- **Toto E.C.,** Marinelli L., Dimmito M.P., Cacciatore I., Pilato S., Ciulla M., Di Stefano A**.,** *Lep(20) targeted solid lipid nanoparticles as platform for brain delivery.* 1st SITELF PhD National Summer School, Pavia, Italy, 2-4 September 2024.
- Dimmito, M.P., Di Stefano, A., Marinelli, L., Carraro, G., Albertini, R., Rapino, A., **Toto, E.C.,** Cacciatore, I*., Lipidated peptide hydrogels: a platform for the delivery of inflammatory bowel disease therapeutics.* CRS Italy Local Chapter Workshop, Palermo, Italy, 5-7 October 2023.
- Rapino A., Romeo T., Dragania M.C., Di Stefano A., Cacciatore I., Marinelli L., Dimmito M.P., **Toto E.C.,** *Characterization of ketoprofen, lysine and gabapentin co-*

crystal: preformulation studies of a new chemical entity. XXIII Simposio ADRITELF, Trieste, Italy, 11-13 September 2023.

- Di Stefano A., Marinelli L., Dimmito M.P., **Toto E.C**., Rapino A., Palmerio F., Spaccapaniccia E., Lardo M., Di Rienzo A., Cacciatore I., *Brain delivery of therapeutics for neurodegenerative diseases.* XXIII Simposio ADRITELF, Trieste, Italy, 11-13 September 2023.
- Dimmito M.P., Di Stefano A., Marinelli L., Di Rienzo A., Carraro G., Albertini R., Rapino A., **Toto E.C.,** Cacciatore, I., *Lipidated peptide hydrogels: a platform for the delivery of therapeutics for the treatment of inflammatory bowel diseases.* 62° SIMPOSIO AFI, Rimini, 7-9 June 2023.
- Dimmito M.P., Cacciatore I., Di Stefano A., Di Rienzo A., **Toto E.C**., Rapino A., Fulle S., Di Filippo E.S., Marinelli L., *Solid lipid nanoparticles as drug delivery carriers for capsaicin extract.* Marseille, France, 20-21 March 2023.
- Dimmito M.P., Cacciatore I., Marinelli L., Di Rienzo A., Agostini M., Garocchio B., **Toto E.C**., Vicaretti G., Palmerio F., Di Stefano A., *Solid lipid nanoparticles as a potential tool for the delivery of natural compounds.* 61° SIMPOSIO AFI, Rimini, Italy, 8-10 June 2022.

ORAL PRESENTATIONS:

- *"Smart Formulation of SLNs: Integrating Microfluidics and Design of Experiments Tools"*. 2nd SITELF National PhD Summer School - XXIV ADRITELF National PhD School, 4th September 2025.
- Invited speaker at the webinar "New advances in Medicinal Chemistry: bioactive compounds and exploitable targets". Presentation title: *"Lipidated peptide hydrogels: a platform for the delivery of biological active compounds",* 21st June 2024.

SUBSCRIPTION TO SCIENTIFIC SOCIETIES:

- **SCI**, Italian Chemical Society (S.S.D. CHIM-09), since 2023.
- **AFI**, Associazione Farmaceutici Industria, since 2023.
- **CRS,** Controlled Release Society Italy Local Chapter, since 2023.
- **SITELF,** Società italiana di Tecnologia e Legislazione Farmaceutiche, since 2023.
- **SEFIG,** Sociedad Española de Farmacia Industrial y Galénica, since 2024

PARTICIPATIONS IN CONGRESSES AND CONFERENCES:

- 4th European Conference on Pharmaceutics, Marseille 20-21 March 2023.
- 62° SIMPOSIO AFI: Rimini, Italy, 7-9 June 2023.
- XXIII Simposio ADRITELF, Trieste, Italy, 11-13 September 2023.
- XXII Scuola Dottorale di Tecnologia Farmaceutica, 13-15 September 2023.
- CRS Italy Workshop, Palermo, Italy, 5-7 October 2023.

- 1st SITELF National PhD Summer School, Pavia, Italy, 2-4 September 2024.
- XVII Congreso SEFIG, Santa Cruz de Tenerife, Spain, 22-24 January 2025.
- IX International Congress of Research in Retina and Vision, Alcalà de Henares/Madrid, 13-14 June 2025.
- 2nd SITELF National PhD Summer School – XXIV ADRITELF National PhD School, 2-4 September 2025.
- 23rd International Symposium on Microencapsulation, Ferrara, Italy, 10-12 September 2025.

Third Mission Activities

Valorization of intellectual or industrial property:

- **PATENT**: Industrial Invention Patent, Title: "Platform for the Delivery of Biologically Active Substances". Patent Holder: Algo Biotechnologies S.r.l., Via dei Vestini 1, Chieti Scalo (CH), 66100 – VAT: 2692030691. Designated Inventors: Antonio Di Stefano, Ivana Cacciatore, Lisa Marinelli, Marilisa Pia Dimmito, Annalisa Di Rienzo, **Eleonora Chiara Toto**. Patent Number: IT102023000007812. Grant Date: April 10, 2025.

Activities of engagement and interaction with the school community:

- **23-10-2025:** Workshop: "Carenza dei medicinali e filiere del farmaco: impatti e prospettive occupazionali per laureati in Farmacia e CTF".
- **26-09-2025**: "ImAgine: la Notte Europea dei Ricercatori 2025".
- **12-04-2024**: "Un viaggio virtuale alla scoperta della produzione, delle nuove figure in campo farmaceutico", Johnson & Johnson.
- **22-11-2023**: "Lecture: La garanzia della Qualità dei Medicinali e l'attività di Contrasto del Crimine Farmaceutico", Dr. Domenico Di Giorgio, AIFA.
- **29-09-2023**: "Notte europea dei Ricercatori 2023: One world, One health, One thousand cultures" with laboratory activities at the Department of Pharmacy, "La scienza che genera dolcezza".